THÈSE

Pour obtenir le grade de

DOCTEUR DE L'UNIVERSITÉ GRENOBLE ALPES

École doctorale : PHYS - Physique
Spécialité : Physique Théorique
Unité de recherche : Modélisation et Exploration des Matériaux

De la lecture d'un qubit à celle d'un état à N corps dans les plateformes d'électrodynamique quantique de circuit

From single qubit to many-body readout in Circuit Quantum Electrodynamics platforms

Présentée par :

Alessandro CHESSARI

Direction de thèse :

Yann-Michel NIQUET DIRECTEUR DE RECHERCHE, CEA CENTRE DE GRENOBLE	Directeur de thèse
Michele FILIPPONE DIRECTEUR DE RECHERCHE, CEA CENTRE DE GRENOBLE	Co-directeur de thèse

Rapporteurs :

TOMMASO ROSCILDE
MAITRE DE CONFERENCES HDR, ENS DE LYON
ALFREDO LEVY YEYATI
FULL PROFESSOR, UNIVERSIDAD AUTONOMA DE MADRID

Thèse soutenue publiquement le **19 novembre 2025**, devant le jury composé de :

JULIA MEYER, PROFESSEURE DES UNIVERSITES, UNIVERSITE GRENOBLE ALPES	Présidente
TOMMASO ROSCILDE, MAITRE DE CONFERENCES HDR, ENS DE LYON	Rapporteur
ALFREDO LEVY YEYATI, FULL PROFESSOR, UNIVERSIDAD AUTONOMA DE MADRID	Rapporteur
BENJAMIN HUARD, PROFESSEUR DES UNIVERSITES, ENS DE LYON	Examinateur
ALEXANDRU PETRESCU, CHARGE DE RECHERCHE, MINES PARIS PSL	Examinateur

Invités :

ANNA KAUCH
SCIENTIST, TECHNISCHE UNIVERSITÄT WIEN
MARKUS WALLERBERGER
SCIENTIST, TECHNISCHE UNIVERSITÄT WIEN

Abstract

Robust manipulation and control of quantum systems require a fast and efficient way to read out their state. After cavity quantum electrodynamics (cavity QED) pioneered the manipulation of neutral atoms and ions with light, circuit quantum electrodynamics (circuit QED) became the dominant readout paradigm for artificial atoms such as superconducting circuits, with dispersive readout widely adopted for its stability and efficiency. Recently, longitudinal readout has emerged as a potentially faster readout protocol, but relies on sophisticated parametric modulation, whose underlying mechanisms have remained unclear so far. Longitudinal interactions have been demonstrated across platforms ranging from superconducting qubits to quantum dots, and rely on driving the qubit at the resonator frequency. In different regimes, the coupling emerges parametrically in the drive strength, growing linearly as the drive increases. In this manuscript, we experimentally demonstrate the breakdown of this parametric regime in a two-level quantum dot charge qubit and devise a unifying Floquet theory to establish a universal connection between AC Stark shift, longitudinal coupling and dispersive readout in cQED. We derive analytical results supported by exact numerical simulations that we apply to superconducting and spin-hybrid cQED systems, showcasing the flexibility of faster-than-dispersive longitudinal readout.

Inspired by cQED's readout capabilities in single qubit measurements, we address many-body state readout in quantum simulators. Since the dynamical structure factor (DSF) encodes key information about density excitations in quantum systems, we propose Many-Body Admittance Spectroscopy (MADS) as a weakly invasive method to probe the DSF by analyzing the transmission coefficients of microwave signals coupled to the quantum simulator. We demonstrate the approach on a one-dimensional spinless fermionic chain, representative of quantum dot implementations of the Heisenberg model, and we discuss, supported by numerical simulations obtained using exact diagonalization and density matrix renormalization group (DMRG), the possibility to measure the qualitative modifications of the DSF caused by interactions. Our results highlight the potential of MADS for characterizing the dynamical properties in highly tunable solid-state quantum simulators, extending the toolbox for the readout of quantum simulators.

Résumé

La manipulation et le contrôle robustes des systèmes quantiques nécessitent une méthode rapide et efficace pour lire leur état. Après que l'électrodynamique quantique en cavité (cavity QED) a ouvert la voie à la manipulation d'atomes neutres et d'ions à l'aide de la lumière, l'électrodynamique quantique en circuit (circuit QED) est devenue le paradigme dominant pour la lecture d'atomes artificiels tels que les circuits supraconducteurs, la lecture dispersive étant largement adoptée pour sa stabilité et son efficacité.
Récemment, la lecture longitudinale est apparue comme un protocole de lecture potentiellement plus rapide, mais elle repose sur une modulation paramétrique sophistiquée dont les mécanismes sous-jacents demeurent encore mal compris.
Les interactions longitudinales ont été démontrées sur diverses plateformes allant des qubits supraconducteurs aux boîtes quantiques, et reposent sur l'excitation du qubit à la fréquence du résonateur. Dans différents régimes, le couplage apparaît de manière paramétrique en fonction de l'amplitude de l'excitation, croissant linéairement avec celle-ci.
Dans ce manuscrit, nous démontrons expérimentalement la rupture de ce régime paramétrique dans un qubit de charge à deux niveaux basé sur une boîte quantique, et nous développons une théorie de Floquet unifiée établissant une connexion universelle entre le décalage AC Stark, le couplage longitudinal et la lecture dispersive en cQED.
Nous dérivons des résultats analytiques, appuyés par des simulations numériques exactes, que nous appliquons à des systèmes cQED supraconducteurs et hybrides spin-charge, illustrant la flexibilité de la lecture longitudinale plus rapide que la lecture dispersive.
Inspirés par les capacités de lecture de la cQED pour les mesures sur un seul qubit, nous abordons la lecture d'états à plusieurs corps dans les simulateurs quantiques. Puisque le facteur de structure dynamique (DSF) encode des informations essentielles sur les excitations de densité dans les systèmes quantiques, nous proposons la spectroscopie d'admittance multi-corps (MADS) comme une méthode faiblement invasive pour sonder le DSF en analysant les coefficients de transmission des signaux micro-ondes couplés au simulateur quantique. Nous démontrons cette approche sur une chaîne unidimensionnelle de fermions sans spin, représentative des implémentations du modèle de Heisenberg à base de boîtes quantiques, et nous discutons, à l'aide de simulations numériques obtenues par diagonalisation exacte et par la méthode du groupe de renormalisation de la matrice de densité (DMRG), de la possibilité de mesurer les modifications qualitatives du DSF induites par les interactions. Nos résultats mettent en évidence le potentiel de la MADS pour la caractérisation des propriétés dynamiques des simulateurs quantiques à semi-conducteurs hautement réglables, élargissant ainsi la boîte à outils dédiée à la lecture des simulateurs quantiques.

Acknowledgments

As I look at the final version of this manuscript, I cannot help but think about these three years spent in Grenoble. My first thoughts go to my family, who supported me especially during the second year, which was by far the most stressful, both because of personal issues and because my first project was finally coming to an end.

What naturally follows is Matthieu. What can I say: friends at university, then roommates, and also colleagues. When I think back to all the stories we have shared, I don't even know where to begin. But I believe the anecdote that best captures our personalities and our friendship is the fact that at home we switched rooms every six months to avoid the other ending up with the "better" one (and we are still not entirely sure which one that actually was). I will leave the *Mouchariu*m and the *Pastarium* as memorable anecdotes reserved only for the finest connoisseurs of *la Poubelle*.

Esteban, even through our ups and downs, the difficult moments are eclipsed by the fact that you were always there. You have put up with my complaints and frustrations since the very beginning. You also had the patience to put up with all my ideas during this time. I agree, most of them were very bad, but there were some good ones, as the dinners at the CEA, where you had the chance to hear, usually in the good company of Prasoon, the newest ideas of *Chessari Labs*. I still don't know how you manage to collect the craziest stories I have ever heard, but they certainly helped bring humor into the office. I owe it in part to you if I was able to complete these three years with serenity.

But a boat does not set sail unless it is pushed out of the harbor, and this is where the captain of my boat comes into the picture: Michele. I have often heard that choosing a good supervisor is crucial during a PhD, and whenever I think of that, I cannot help but feel that Michele has been a great guide, and not only scientifically. I hope he will never stop telling the story of when he overheard Matthieu and me arguing about the Christmas bonus, or about my own delay... at my very first talk. And Yann-Michel, I hope you will forgive me for mentioning Michele before you, but I would like to thank you for fostering such a positive atmosphere within the group. Many thanks also to Markus and Anna, who have welcomed me in Vienna for my period abroad.

Nicholas, Giovani, I am glad we managed to stay in touch, even if in Lyon we used to steal each other's chairs. And you may be at the end, but I have not forgotten you, Camilla. Since you like to joke and tell me that I only look for you when I need food, I am putting you last. We may not have as many hilarious stories as I do with the guys, but I know I can count on you. You have been a constant presence, and I am sure we will keep seeing each other even after I move to Vienna, where there is Davide, who still manages to put up with me and still has a hard time admitting when I am right.

Contents

1 Introduction **1**
- 1.1 cQED readout protocols . . . 4
- 1.2 Quantum simulation . . . 6
- 1.3 Outline of this thesis . . . 9
- 1.4 List of publications . . . 9

2 Circuit Quantum Electrodynamics **10**
- 2.1 The LC circuit . . . 11
- 2.2 The coplanar waveguide . . . 13
  - 2.2.1 The transmission line . . . 13
  - 2.2.2 The resonator . . . 16
  - 2.2.3 Coupling between the transmission line and the resonator . . . 17
- 2.3 Input-output theory . . . 19
  - 2.3.1 Input-output relations . . . 20
  - 2.3.2 Input-output relations from the Heisenberg equation . . . 24
  - 2.3.3 Eliminating the bath Hamiltonian . . . 25
- 2.4 Hybrid cQED . . . 27
  - 2.4.1 An artificial atom: the charge qubit . . . 27
  - 2.4.2 Coupling of a double quantum dot to a resonator . . . 28
- 2.5 Chapter 2 in a nutshell . . . 30

3 cQED readout protocols in qubits **31**
- 3.1 Dispersive readout . . . 32
  - 3.1.1 Dispersive regime . . . 32
  - 3.1.2 Semiclassical approach . . . 34
  - 3.1.3 Review of a classical harmonic oscillator . . . 36
- 3.2 Field detection and quality of readout . . . 39
  - 3.2.1 Homodyne and heterodyne detection . . . 40
  - 3.2.2 Signal-to-noise ratio . . . 40
- 3.3 Longitudinal readout . . . 41
  - 3.3.1 Ideal longitudinal coupling . . . 42
  - 3.3.2 Synthetic longitudinal coupling . . . 42
- 3.4 Analytical integration of the equations of motion . . . 46
- 3.5 Chapter 3 in a nutshell . . . 48

4 Experimental realization of longitudinal coupling in a charge qubit **49**
- 4.1 The device . . . 49
  - 4.1.1 Experimental setup . . . 50
  - 4.1.2 The model . . . 50

4.2 Transmission measurement of dispersive and longitudinal readout 51
4.3 Qubit state displacement 53
4.4 Breakdown of the parametric regime 55
4.4.1 Parametric dependence of the longitudinal interaction 55
4.5 Chapter 4 in a nutshell 55

5 Unifying Floquet Theory of readout **57**
5.1 Floquet theorem 58
5.2 Spatial periodic potentials 61
5.2.1 Bloch's theorem as a consequence of the Floquet theorem 61
5.2.2 The band spectrum 63
5.3 Time periodic Hamiltonians 64
5.4 cQED readout protocols using Floquet theory 67
5.4.1 Semiclassical approach : the quantum Rabi model 67
5.4.2 Beyond the semiclassical approach 71
5.4.3 Purcell effect 76
5.5 Limiting cases 77
5.6 Dispersive readout 78
5.7 Discussion of longitudinal readout 78
5.7.1 Change of sign across resonance 79
5.7.2 Deviations from parametric longitudinal coupling at strong drives 79
5.8 Chapter 5 in a nutshell 80

6 Applications to realistic multi-level systems **82**
6.1 Extension of Floquet Theory to multi-level systems 82
6.2 Spin qubits 86
6.2.1 The model 88
6.2.2 The Floquet spectrum 91
6.2.3 Longitudinal readout of flopping-mode qubits 93
6.3 Superconducting qubits 94
6.3.1 The Josephson junction 94
6.3.2 The Transmon qubit 95
6.3.2.1 From the Cooper pair box to the transmon regime 96
6.3.2.2 Floquet spectrum 98
6.3.2.3 Longitudinal readout of a transmon qubit 100
6.3.3 The Fluxonium qubit 100
6.3.3.1 The model 101
6.3.3.2 The Floquet spectrum 102
6.3.3.3 Longitudinal readout for a fluxonium qubit 102
6.4 Polarizability contributions 103
6.5 Chapter 6 in a nutshell 104

7 Many-Body Admittance Spectroscopy **105**
7.1 Experimental protocol for MADS 106
7.1.1 The model 107
7.1.2 Input-output relations 107
7.2 MADS for spinless fermions in 1D 110
7.2.1 Non-interacting fermions 111
7.2.2 Interacting gapless regime 115

7.3 Chapter 7 in a nutshell . . . 121

8 Conclusions and perspectives **122**

A Input-output theory **137**

B Active and passive transformations in physics **138**
B.1 Active and passive transformations . . . 138
B.1.1 Active interpretation . . . 138
B.1.2 Passive interpretation . . . 139
B.1.2.1 Application to the dipole operator . . . 139
B.2 Diagonalization of an operator . . . 140
B.3 Schrödinger, Heisenberg and interacting picture . . . 142
B.4 Rotating frame . . . 143

C Schrieffer-Wolff transformations **145**
C.1 The dispersive Hamiltonian . . . 146
C.2 The Floquet Hamiltonian . . . 147

D Kubo linear response **149**
D.1 The interaction picture . . . 149
D.2 The Dyson series . . . 149
D.3 The linear response function . . . 150

E Supplementary material for Chapter 7 **151**
E.1 Change of basis in second quantization . . . 151
E.2 The Lehmann representation . . . 151
E.2.1 Application to the DSF . . . 153
E.2.2 Application to the fermionic Green's function in the tight-binding chain . 153
E.2.3 Analytical evaluation of the Green's functions in coordinate space . . . 154
E.3 The Matsubara formalism . . . 156
E.3.1 Connection between Matsubara and retarded functions . . . 157
E.3.2 Derivation of Eq. (7.36) . . . 158

Chapter

1 Introduction

Contents

1.1 cQED readout protocols **4**
1.2 Quantum simulation **6**
1.3 Outline of this thesis **9**
1.4 List of publications **9**

The transistor, invented at Bell Labs in 1947 [1], is one of the first widely implemented quantum-enabled devices and the basis of the twentieth-century revolution in information technology. At the circuit level, it defines two stable voltage ranges, labeled 0 and 1, which constitute the classical bit. While quantum mechanics is at the base of the band theory that sets the transistor's operating principles, the information is encoded and manipulated classically.

Only in the 1980s was the measurement and control of individual quantum systems demonstrated using Rydberg atoms and trapped ions coupled to optical cavities, a breakthrough recognized with the 2012 Physics Nobel Prize awarded to Serge Haroche and David Wineland [3–5]. In such *cavity quantum electrodynamics* (cavity QED) experiments, the coherent interaction between a single atom and a single electromagnetic mode could be prepared, monitored, and read out (see Fig. 1.1). These experiments showed for the first time that quantum systems could be isolated, manipulated and read out, providing evidence that information could be stored and manipulated in a *quantum computer*.

Although the idea of a quantum computer as an isolated quantum system whose internal degrees of freedom can be measured dates to 1982 [6], the race to build a large-scale quantum

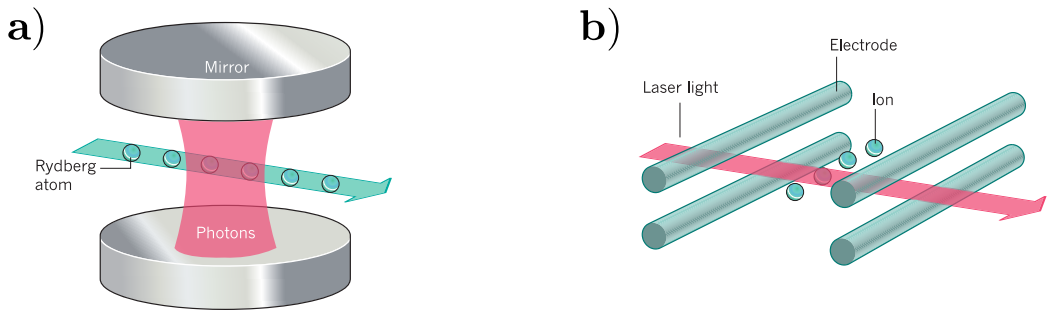

Figure 1.1: Control and measurement of single particle quantum states in cavity QED. a) Haroche method. Microwave photons are placed between two highly reflective mirrors that enable an individual photon to bounce back and forth between them many times. Rydberg atoms are sent through the system to measure and manipulate the photon's quantum state. b) Wineland method. An electric field produced by an arrangement of electrodes holds one or several ions inside a trap. Laser light is shone on the ion, suppressing its thermal vibration and allowing its quantum state to be measured and controlled. Figure adapted from Ref. [2].

computer accelerated only after Peter Shor introduced the first quantum algorithms that made quantum computing appealing for the general public. First, he showed that a quantum computer could be used to factorize large numbers, a challenge inaccessible to classical computers and crucial for modern cryptosecurity [7]. Second, he showed that errors in a quantum computer could be mitigated by quantum error correction algorithms [8].

At the heart of a quantum computer are its qubits, the quantum analog of classical bits. Just as a classical bit has a computational basis defined by the value 0 or 1, a qubit has a computational basis defined by the states $|0\rangle$ and $|1\rangle$. In a qubit, however, not only the quantum states $|0\rangle$ and $|1\rangle$ are available, but also any superposition

$$|\psi\rangle = \alpha\,|0\rangle + \beta\,|1\rangle\ , \qquad\qquad |\alpha|^2 + |\beta|^2 = 1\,. \tag{1.1}$$

Still, just as for a classical bit, the measurement of a single qubit has only two possible outcomes, with $|\alpha|^2$ and $|\beta|^2$ only providing the probability of those outcomes. Quantum advantage emerges from state superposition when the number of qubits increases. For two qubits, the quantum state can be any superposition of the states $|00\rangle$, $|01\rangle$, $|10\rangle$ and $|11\rangle$,

$$|\psi\rangle = \alpha\,|00\rangle + \beta\,|01\rangle + \gamma\,|10\rangle + \delta\,|11\rangle\ . \tag{1.2}$$

Consequently, the space of parameters needed to describe the state grows faster with the number of qubits than with the number of classical bits. While in the two-bits case the system is fully characterized by the value of each bit, in the two-qubit case the system is described by the four-parameter space spanned by the complex parameters $\alpha, \beta, \gamma, \delta$. This scalability allows a quantum computer composed of N qubits to operate within a computational space of dimension 2^N, a sharp contrast to the linear scaling of classical bits which gives an idea of the appeal of quantum computing.

Figure 1.2 illustrates an example of a quantum computation with two qubits. It shows the three stages of a computation: (1) Initialization: the qubits are usually prepared in the basis states $|0\rangle$ or $|1\rangle$. (2) Manipulation: a quantum algorithm is executed and modifies the quantum state, possibly entangling the qubits. (3) Readout: the final state of the qubit is revealed. Ideally, the readout stage consists in a quantum non-demolition measurement (QND) of the qubits, in which the measurement apparatus is engineered so that its Hamiltonian commutes with the qubit Hamiltonian. In this way, QND measurements project the qubit on states $|0\rangle$

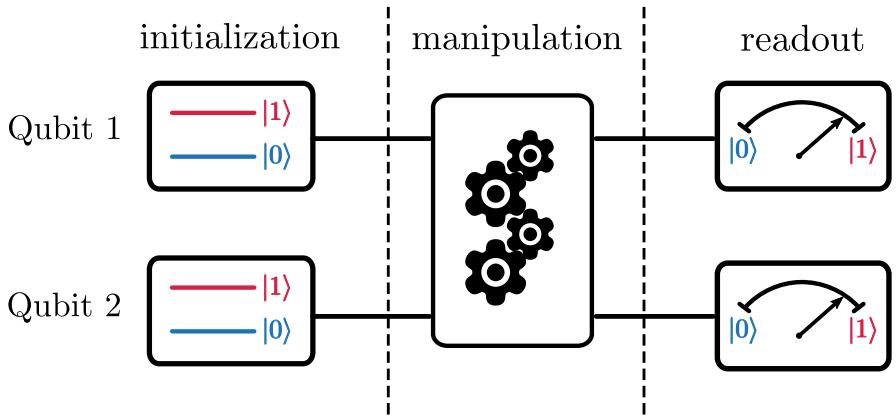

Figure 1.2: Example of a basic quantum computation circuit diagram for two qubits showing the three stages of a quantum computation: initialization, manipulation and read out of qubits. Time flows from left to right.

or $|1\rangle$ by avoiding relaxation or excitation during readout. This allows the measurement to be repeated an arbitrary number of times to improve the signal-to-noise ratio and leaves the qubit immediately available to be reused.

Shortly after the work of Shor, the first quantum processors were realized using ensembles of nuclear spins in a single molecule as the qubits [9], up to ultimately a seven-qubit quantum computer capable of factoring the number 15 [10]. Unfortunately, scaling here was ultimately limited by readout. Nuclear spins cannot be addressed and measured independently, and the signal arising from multi-qubit entanglement decreases exponentially, limiting the size of the processor.

After the nuclear spin quantum processor, many other physical implementations for quantum information technologies have been proposed, including ions [11, 12], neutral atoms [13], superconducting quantum circuits [14] and semiconductor quantum dots [15]. Among these, arrays of more than 200 Rydberg atoms have recently been manipulated with extraordinary control [16] while superconducting qubits have proven their great potential notably with the Google 105-qubit chip [17], but also with the 127-qubit processor of IBM [18]. However, in the perspective of large-scale quantum computations requiring millions of physical qubits [19], the large size of these devices limits their scalability.

In Grenoble, the presence of major players in the semiconductor industries has motivated the development of coherent semiconductor spin qubits, where information is encoded in the spin of a particle in a quantum dot [20]. Although spin qubits are harder to address than superconducting qubits, due to their strong isolation from the environment, their nanometer-scale offers an alternative route to dense integration [21].

While each architecture has its advantages and limitations, hybrid circuit quantum electrodynamics (cQED) platforms are promising versatile solutions for fast QND readout.

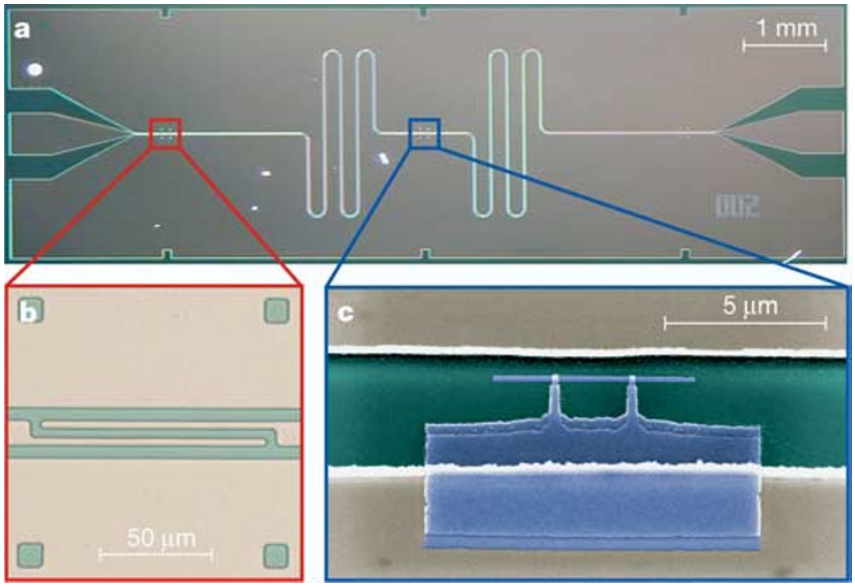

Figure 1.3: Superconducting qubit coupled to a resonator in circuit QED. a) A coplanar microwave resonator is coupled at each of its ends to an input and output feedline. b) The capacitive coupling to the input and output lines is controlled by adjusting the length and separation of the capacitors formed in the centre conductor. c) A superconducting qubit, the Cooper pair box (blue), is fabricated onto the silicon substrate (green) into the gap between the centre conductor (top) and the ground plane (bottom) of a resonator (beige). Figure adapted from Ref. [22].

1.1 cQED readout protocols

While for ions and neutral atoms, readout is naturally implemented within cavity QED, for superconducting and semiconductor qubits[1], the story is more complicated.

The first superconducting circuit, the Cooper pair box, was first investigated in the nineties [23] with coherent manipulation demonstrated in 1999 by Nakamura using a destructive measurement [14]. Its issue was the susceptibility to charge noise. The situation changed in 2004 with the advent of *circuit quantum electrodynamics* (cQED) [24] and the first demonstrations of quantum non-demolition (QND) measurement (see Fig. 1.3). These readout methods were faster and enabled operation in new regimes more robust towards charge noise, leading to the development of the transmon, which is the prevailing design in most modern superconducting chips.

For spin qubits in quantum dots, the magnetic moment is typically too small to measure directly, so the spin degree of freedom is mapped onto a charge state to produce a larger signal. Readout therefore relies on spin-to-charge conversion, with the charge state detected by a charge sensor. There are two main types of spin-to-charge conversion for semiconductor spin qubits. The first, known as Elzerman readout, involves spin selective tunnelling between a quantum dot and a reservoir. The second is based on the Pauli exclusion principle and is called Pauli spin blockade (PSB). In PSB, a spin state in one quantum dot is read out using the spin state of another quantum dot. Despite enabling initialization, control, and measurement, spin-to-charge conversion techniques are intrinsically quantum destructive and require additional charge sensors and extra wiring, limiting scalability.

Only in 2012 hybrid systems of superconducting circuits and quantum dots (see the left panel in Fig. 1.4) led to the first QND measurements in spin qubits [25], where the intrinsic spin-orbit coupling of electrons in InAs allowed the coupling of the spin degrees of freedom to the electric

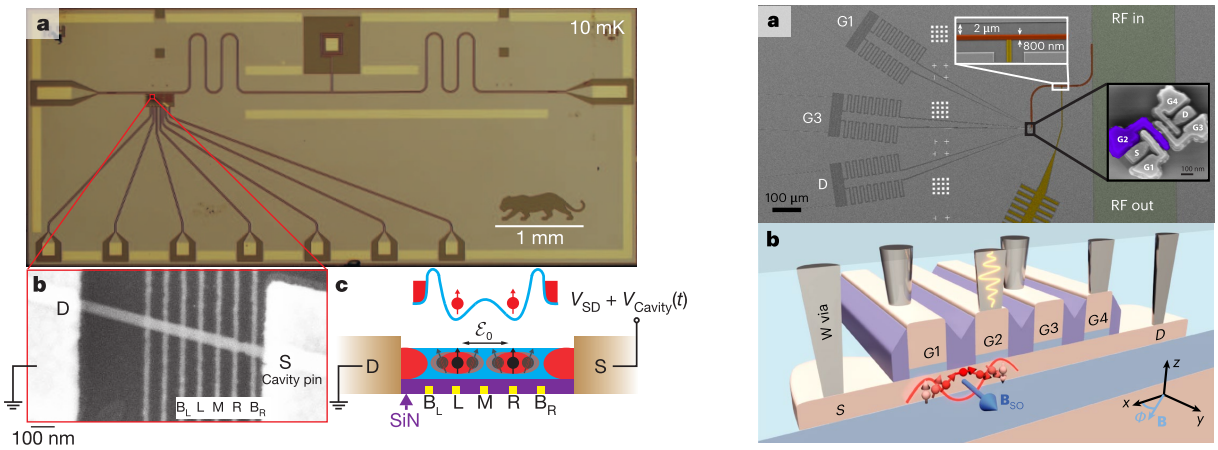

Figure 1.4: (Left) First Hybrid DQD/superconducting resonator device in InAs. a) Circuit schematic and micrograph of the hybrid device design. Scanning electron micrograph (b) and cross-sectional schematic view (c) of a typical nanowire DQD. The left and right barrier gates (BL and BR), left and right plunger gates (L and R), and middle gate (M) are biased to create a double-well potential within the nanowire. Figure adapted from Ref. [25]. (Right) Hybrid cQED implementation for readout of a coherent hole spin-qubit in Silicon. a) False-colour top-view scanning electron micrograph of a representative circuit. The resonator (red) is galvanically connected to the gate electrode G2. b) Schematic of the cross section of the DQD device. The orange wavepacket on G2 pictures the photon in the microwave cavity. Figure adapted from Ref. [26].

[1] More detailed introductions to these qubits are contained in Chapter 6.

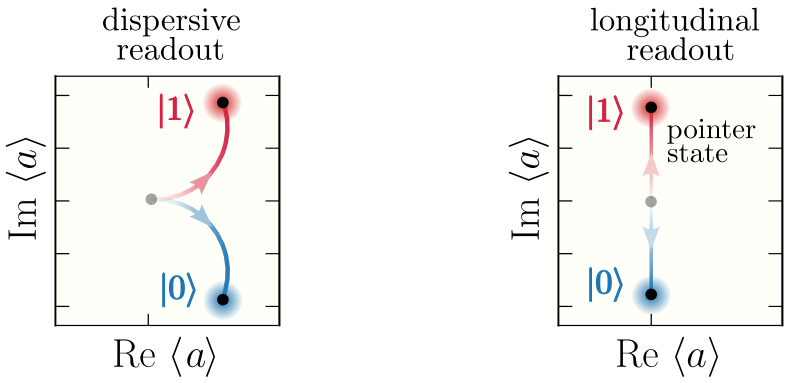

Figure 1.5: Time evolution of the cavity expectation value $\langle a \rangle$ in the phase space defined by the real and imaginary part of $\langle a \rangle$. The pointer state is the cavity expectation value when the qubit is initialized in $|0\rangle$ or $|1\rangle$. For longitudinal readout, the pointer states separate immediately while for dispersive readout the separation is minimal at short times.

field of resonators. InAs devices were quickly limited by the large number of nuclear spins while the more promising purified silicon realizations require additional magnetic control lines that are not very scalable [27]. On the other hand, holes exhibit naturally stronger spin-orbit coupling and their coherent control in Silicon has recently been demonstrated in Grenoble [28], paving the way for the record in intrinsic spin-photon coupling reached in 2023 [26] (see the right panel in Fig. 1.4).

Motivated by the recent implementations of cQED in spin qubits and the recent achievements in hole spin-qubits in Grenoble, we addressed the problem of readout in cQED, its limitations and regimes. Traditional quantum non-demolition (QND) readout in circuit QED relies on a transverse coupling

$$\mathcal{H}_\perp = \hbar g_\perp \left(a + a^\dagger\right) \sigma_x \,,$$

where $a^{(\dagger)}$ annihilates (creates) photons in the resonator and σ_x flips the qubit state. In the dispersive regime, this interaction leads to the σ_z-state dependent shift of the cavity frequency $\chi\sigma_z$, providing approximately QND readout capability. When the resonator is populated by a coherent drive, the evolution of the cavity follows different trajectories in the phase space, which serve as *pointer states* of the qubit levels, as illustrated in Fig. 1.5. While this approach maintains the approximately non-destructive nature of measurements, the coherent drive at the input first pushes the two pointer states in the same direction in phase space before pulling them apart. Therefore, achieving sufficient separation of the cavity pointer states can require integration times comparable to or exceeding the qubit relaxation time.

In contrast, a longitudinal coupling interaction

$$\mathcal{H}_\parallel = \hbar g_\parallel(t) \left(a + a^\dagger\right) \sigma_z \,, \tag{1.3}$$

has emerged as an alternative solution for faster QND readout [29–32]. This interaction acts as a drive which immediately separates the pointer states in the phase space (see Fig. 1.5). However, implementing effective longitudinal coupling requires sophisticated parametric modulation schemes and it remains unclear which circuit properties control the strength of the coupling. In different regimes, the coupling emerges parametrically in the drive, growing linearly with its strength. However, existing theories rely on small-drive approximations, leaving open the question of whether this parametric scaling persists at strong drive. This raises a fundamental

scientific question that will be addressed and answered in this manuscript

Is there a generic mechanism to implement a longitudinal interaction? (1.4)

Our approach is based on a Floquet theory of readout which unifies the adiabatic limit, where the cavity dynamics is so slow that the longitudinal coupling results from the static spectrum curvature of the qubit, with the diabatic one, where the static spectrum plays no role. We find that the longitudinal coupling arises from the slope of the Floquet spectrum and is equal to the static curvature only in the adiabatic regime. The usual parametric description breaks down at strong drive, where it overestimates the longitudinal coupling emerging from the Floquet spectrum. In particular, we find sudden degradations of the readout at very particular frequencies in the adiabatic regime. These arise from anticrossings in the Floquet spectrum due to couplings between distant replicas in the Floquet spectrum which cause the suppression of the longitudinal coupling. On the other hand, these suppressions are absent in the diabatic regime, where higher replica processes at strong drives play no role.

1.2 Quantum simulation

So far, we have focused on single-qubit measurement. We turn now our attention to *analog quantum simulators*, devices whose interest lies in the many-body state of multiple qubits.

Even though Shor's algorithm attracted public attention to quantum computing, the first quantum algorithms were meant for quantum simulations, following Richard Feynman's idea developed in 1982 [6]. By quantum simulation we mean reproducing the behavior of a targeted

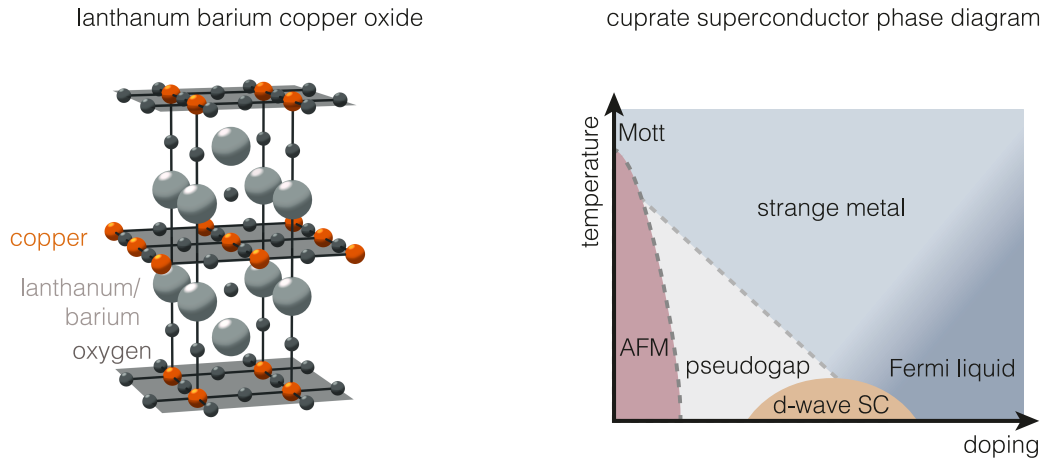

Figure 1.6: Cuprates. Lathanum barium copper oxide (LBCO) was the first high-temperature superconductor discovered [33]. It is one in a family of cuprate materials which exhibit this phenomenon. While these materials have been studied extensively and phase diagrams have been mapped out (here a representative schematic is shown), many open questions remain. The underlying physics stems from the valence electrons of the copper atoms which rearranged in two-dimensional (2D) planes. In a simplified picture, a copper oxygen plane can be viewed as a square lattice where every site contains one hole. The hole concentration can be altered by hole doping p from the charge reservoir layers. With no doping, the system is a Mott insulator, where holes cannot move around because of the large Coulomb energy associated with two of them occupying the same site. At very high doping, correlation effects weaken, and the system approaches a normal metal described by Fermi liquid theory. While these two limits are relatively well understood, superconductivity and many other fascinating phenomena emerging in between are objects of debate. Figure adapted from Ref. [34].

quantum system by implementing appropriate operations on a controllable quantum system. There are two main approaches to quantum simulation. The first uses universal quantum computers, which encode the target Hamiltonian in a quantum algorithm and solve the problem by executing that algorithm on multiple qubits, much like digital computation. The second one uses *analog quantum simulators.* These simulators are not universal and are built to emulate a target system by engineering a Hamiltonian that mimics the physics of interest. Such devices do not need the same efficiency as general-purpose quantum computers, since they target specific problems. Nevertheless, they can be leveraged to simulate strongly correlated materials, where intricate quantum effects predominate.

Among these materials, cuprate high-temperature superconductors are surely among the most intriguing ones. As shown in Fig. 1.6, cuprates have a layered crystal structure consisting of copper oxygen planes and charge reservoir layers. At present, it is strongly believed that holes in

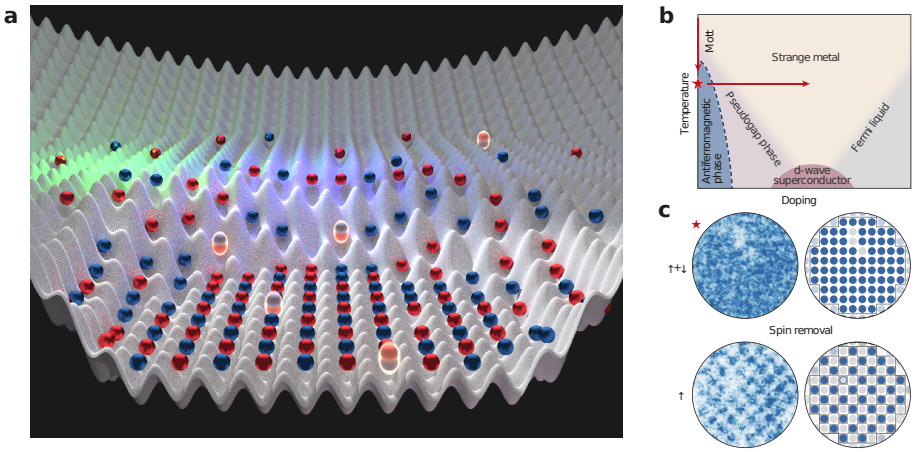

Figure 1.7: A quantum simulator implementing the Fermi-Hubbard Hamiltonian. a) Ultra-cold atoms are arranged in an ordered lattice. The array of lattice sites is produced in experiments by laser light. b) Schematic of the two-dimensional Hubbard phase diagram, including predicted phases. The explored trajectories in the phase space are traced by the red arrows. The strongest anti-ferromagnetic order is observed at the starred point. c) Exemplary raw (left) and processed (right) images of the atomic distribution of single experimental realizations. The observed checkerboard pattern in the spin-removal images indicates the presence of an anti-ferromagnet. Figure adapted from Ref. [35].

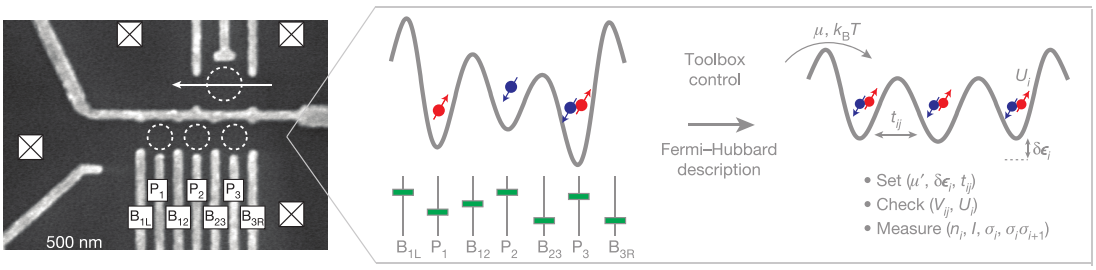

Figure 1.8: Quantum dots Fermi-Hubbard simulator. The bottom three dashed circles indicate the triple-quantum-dot array, whose Hamiltonian parameters derive from the local potential landscape controlled by the seven gates under (B_{1L} to B_{3R}). The top dashed circle and arrow indicate the sensing dot channel, which is monitored to enable real-time charge sensing. Crossed squares indicate distinct Fermi reservoirs that are contacted using ohmic contacts. The diagram shows how a Fermi-Hubbard model is set up. In particular, the system is engineered to allow for the independent calibration of the parameters that governs the Fermi-Hubbard Hamiltonian. Figure adapted from Ref. [36].

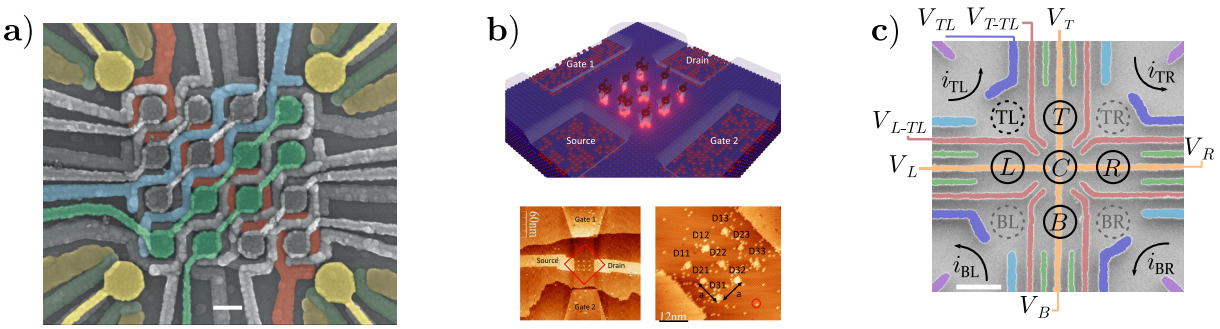

Figure 1.9: Two-dimensional arrays of quantum dots. The a) 16 dots plaquette in planar germanium from Ref. [43], the b) 9 dots plaquette in silicon from Ref. [44] and the c) 9 dots plaquette in a GaAs heterostructure from Ref. [45] are all suitable experimental platforms to simulate the two-dimensional Fermi-Hubbard model.

cuprates are described by the 2D Fermi-Hubbard model, first introduced in the '60s to describe electrons in transition metals. Although the model contains only a tunnelling term between neighboring sites and an on site interaction, the full description of its low temperature behavior in two dimensions remains beyond current analytical and classical computational methods. This combination of broad relevance and numerical intractability makes the Fermi–Hubbard model an ideal target for quantum simulation.

A natural platform for such simulations is ultracold fermionic atoms, which can natively implement the requisite fermionic degrees of freedom to simulate the Fermi-Hubbard model. In such systems, a standing wave of light serves as the periodic potential and a gas of atoms is cooled to very low temperatures using optical techniques and magnetic traps [37, 38]. To extract information from the cloud of the atomic gas, quantum gas microscopy had been used to explore its phase diagram (see Fig. 1.7) [35, 39–41] and with cryogenic temperature recently reached [42], the region of the phase space where a superconductive phase could be demonstrated is now potentially experimentally available.

Beyond ultracold atoms, the intrinsic fermionic nature of electrons and holes in quantum dots also makes them a suitable platform to simulate the Fermi-Hubbard Hamiltonian. These devices scale readily with state-of-the-art semiconductor processes, and their small size makes cryogenic temperatures readily accessible in compact cryostats. However, as for spin qubits, measurement of such platforms relies on spin-to-charge conversion techniques, which require sensors and extra wiring at each site creating cross-talk and limiting the size of the simulator. Coulomb blockade transition, analogous to the Mott transition in one dimension, had been demonstrated in 2017 in an array of three dots (see Fig. 1.8) [36] while the Nagaoka ferromagnetism (a zero measure point in the phase space of the Hubbard model) had been explored in a two-dimensional plaquette of four dots [46]. Recent demonstrations of full control and manipulation in two dimensional arrays of quantum dots [43–45] (Fig. 1.9) are currently laying the ground to explore the phases of the two dimensional Hubbard model on this kind of platform.

As cQED platforms have been implemented for single-qubit readout, a natural question is whether similar techniques can extract information from the many-body state of a quantum simulator. We focus on the admittance, an electrically measurable observable, whose imaginary part is the dynamical structure factor (DSF), which is a sensitive probe of strongly-correlated dynamics. The second question addressed in this manuscript is therefore:

Can cQED enable efficient measurements of the DSF in analog quantum simulators? (1.5)

1.3 Outline of this thesis

This dissertation is organized as follows. Chapter 2 introduces and reviews the circuit QED concepts needed for the readout protocols developed in the rest of the manuscript. Chapter 3 presents dispersive and longitudinal readout and reviews the theoretical state of the art behind these protocols. Chapter 4 reports on an experimental realization of longitudinal coupling in charge qubits and explains how to distinguish longitudinal from dispersive readout even when coherent qubit control is unavailable. Chapter 5 introduces Floquet theory, which forms the core of our answer to the first fundamental question (1.4). Chapter 6 extends the Floquet framework to multilevel qubits. Chapter 7 introduces Many-Body Admittance Spectroscopy as an answer to question (1.5), with an application to a one-dimensional spinless chain of quantum dots.

1.4 List of publications

This thesis has led to the publication of two articles, with a third one currently being finalized.

- [47] V. Champain, S. Zihlmann, **A. Chessari**, B. Bertrand, H. Niebojewski, É. Dumur, X. Jehl, V. Schmitt, B. Brun et al., "Parametric longitudinal coupling of a semiconductor charge qubit and an rf resonator" in *Phys. Rev. Applied 23, 034067* (2025) is covered in Chapter 4.
- [48] **A. Chessari**, E. A. Rodríguez-Mena, J. C. Abadillo-Uriel, V. Champain, S. Zihlmann, R. Maurand, Y.-M. Niquet, and M. Filippone, "Unifying Floquet Theory of Longitudinal and Dispersive Readout" in *Phys. Rev. Lett. 134, 037003* (2025) is covered in Chapters 5 and 6.
- [49] **A. Chessari** and M. Filippone, "Many-Body Admittance Spectroscopy", *in preparation*, is covered in Chapter 7.

Chapter

2 Circuit Quantum Electrodynamics

Contents

2.1 The LC circuit 11
2.2 The coplanar waveguide 13
2.2.1 The transmission line 13
2.2.2 The resonator 16
2.2.3 Coupling between the transmission line and the resonator 17
2.3 Input-output theory 19
2.3.1 Input-output relations 20
2.3.2 Input-output relations from the Heisenberg equation 24
2.3.3 Eliminating the bath Hamiltonian 25
2.4 Hybrid cQED 27
2.4.1 An artificial atom: the charge qubit 27
2.4.2 Coupling of a double quantum dot to a resonator 28
2.5 Chapter 2 in a nutshell 30

As discussed in Chapter 1, cavity quantum electrodynamics (QED) has been the reference framework for exploring light-matter interaction at the most fundamental level [5]. In free space, the cross-section for interactions between a single atom and a photon is quite small, making it difficult to observe their effect on one another. In cavity QED, a very different environment is created, in which photons confined in a reflective cavity bounce back and forth between the mirrors before they leak out. In this way, the cavity confines photons to a small volume, increasing their energy density and giving them many chances to interact with the atom, hence enhancing the light-matter coupling. As it will be discussed in Section 5.6, the light-matter

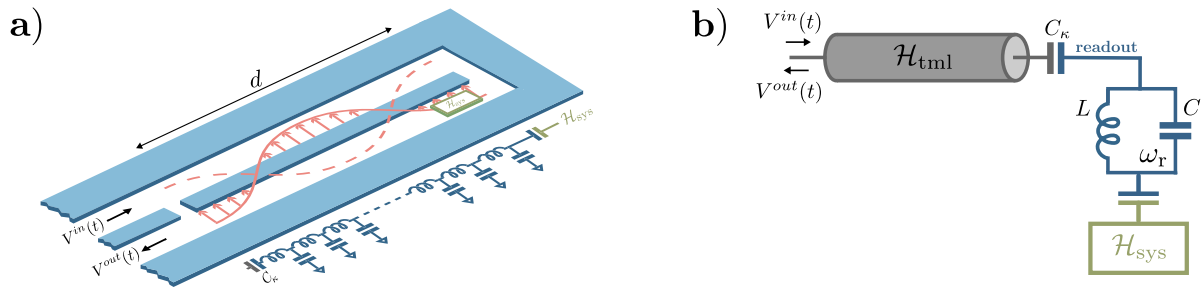

Figure 2.1: Typical cQED platform with input and output voltages used to read out the state of the resonator. a) A coplanar waveguide resonator is coupled to a transmission line to perform readout on a qubit ($\mathcal{H}_{\text{sys}}$). b) Schematic circuit representation of a). The resonator is represented as an effective LC circuit. Figure adapted from Ref. [50].

interaction also reshapes the atom's spontaneous emission rate through the Purcell effect [51]. As the detuning between the atom and the cavity decreases, the atom can relax and emit a photon that fits inside the cavity, and the spontaneous decay is enhanced.

The prototypical cavity QED system is an atom modeled as a two-level system coupled to a cavity. In the strong coupling regime, characterized by a profound mutual influence between single atoms and the photonic states confined within the cavity, the presence of even a single atom can significantly alter the behavior of photons. An initially excited two level atom in an empty cavity would coherently emit and absorb a single photon, provided that the cavity resonance frequency matches the atom's transition frequency and the rate at which this energy quantum is lost is sufficiently small [52]. This process is called a vacuum Rabi oscillation and was first observed in 1996 with Rydberg atoms [53].

While in this regime cavity QED became for a long time the ideal testing ground of fundamental quantum effects [5], the advent of quantum information theory [54, 55] opened up new possibilities. Ions and Rydberg atoms with photons in cavities became experimental implementations of qubits leading to early demonstrations of quantum gates and simple quantum algorithms [56].

In this chapter, we give the key elements of *circuit quantum electrodynamics* (cQED) [22, 24, 50]. In this paradigm, qubits are realized as artificial atoms in quantum circuits that offer a flexible tunability that is not readily available in natural atom systems. The typical cQED platform is sketched in Fig. 2.1. In the first cQED experiments, the standard configuration consisted of a superconducting qubit strongly coupled to an on-chip resonator. Qubit sensitive resonator state is read out via microwave coplanar waveguide (CPW) feedlines, transmission lines which route coherent microwave drives to the resonator and carry away the emitted field. Building on this, cQED has been extended to hybrid platforms, in which the cavity can be coupled to other solid state devices or qubits. Coupling the qubit to the feedline via a resonator provides strong, controllable interaction while protecting the qubit from external sources of noise coming from the feedlines.

This Chapter is structured as follows. In Sec. 2.1 we review the LC circuit. Distributed LC circuits, used to model transmission lines and resonators, are analyzed in Sec. 2.2. The coupling between a transmission line and a resonator, which enables readout of the resonator state via input–output theory, is discussed in Sec. 2.3. In Sec. 2.4, we turn to hybrid cQED, detailing how resonators couple to qubits. As a demonstrative example, we consider the charge states of a double quantum dot acting as the qubit. This example will accompany us until Chap. 6, where other qubits are discussed.

2.1 The LC circuit

Consider the LC oscillator of Figure 2.2. This circuit combines a capacitor C in parallel with an inductor L and realizes a harmonic oscillator that behaves as a mass-spring system: energy oscillates between the kinetic energy $p^2/2m$ and the potential energy $x^2/2k^{-1}$. For the LC circuit this corresponds to a flow between a charging energy $T = Q^2/2C$ and an inductive energy $V(\Phi) = \Phi^2/2L$, where the flux Φ through the inductor is defined from the voltage V by

$$\Phi(t) \equiv \int_{-\infty}^{t} V(t')dt' \,, \tag{2.1}$$

and is related to the current across it by Faraday's law

$$\Phi(t) = LI \,. \tag{2.2}$$

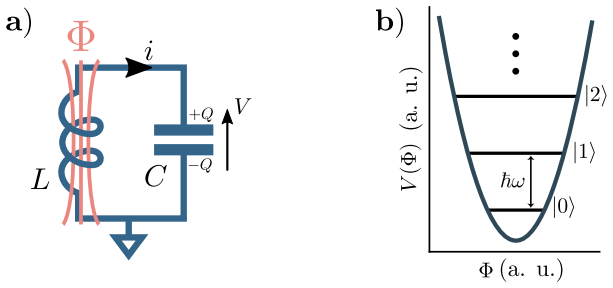

Figure 2.2: LC circuit and its energy levels. a) Scheme of the LC circuit. During an oscillating cycle the energy flows from the flux Φ in the inductor L to the charge Q in the capacitor C and vice versa. b) The parabolic potential (in arbitrary units) gives rise to bounded eigenstates spaced by $\hbar\omega = \hbar/\sqrt{LC}$. Figure adapted from Ref. [50].

Combining Eq. (2.1) with the definition of capacitance $Q = CV$ leads to the classical Lagrangian $\mathcal{L} = T - V(\Phi)$ of the LC circuit

$$\mathcal{L} = \frac{C\dot{\Phi}^2}{2} - \frac{\Phi^2}{2L}\,. \tag{2.3}$$

Classically, the momentum conjugated to Φ is

$$\frac{\partial \mathcal{L}}{\partial \dot{\Phi}} = C\dot{\Phi} = Q\,, \tag{2.4}$$

so the flux Φ and the charge Q are conjugate variables with $\{\Phi, Q\} = 1$, where $\{f, g\}$ is the classical Poisson bracket

$$\{f, g\}_{\Phi,Q} = \frac{\partial f}{\partial \Phi}\frac{\partial g}{\partial Q} - \frac{\partial f}{\partial Q}\frac{\partial g}{\partial \Phi}\,. \tag{2.5}$$

As for a harmonic oscillator, both conjugate variables oscillate sinusoidally at a frequency $\omega = 1/\sqrt{LC}$.

The Hamiltonian of the system follows from the Legendre transformation [57]

$$\mathcal{H} = \frac{\partial \mathcal{L}}{\partial \dot{\Phi}}\dot{\Phi} - \mathcal{L} = \frac{Q^2}{2C} + \frac{\Phi^2}{2L}\,. \tag{2.6}$$

Quantization proceeds by promoting Φ, Q to operators and replacing the Poisson bracket $\{\cdot,\cdot\}$ by the commutator $[\cdot,\cdot]/i\hbar$

$$\mathcal{H} = \frac{Q^2}{2C} + \frac{\Phi^2}{2L}\,, \qquad \text{with} \quad [\Phi, Q] = i\hbar\,. \tag{2.7}$$

It is convenient to introduce the ladder operators a and $a^\dagger$. These operators satisfy the bosonic commutation relations $\left[a, a^\dagger\right] = 1$ and define a Hilbert space, the *Fock space*, constituted by the family of eigenstates $\{|n\rangle\}_{n\geq 0}$ of the occupation number operator $N = a^\dagger a$, which satisfy $N|n\rangle = n|n\rangle$. The physical interpretation of the ladder operators is apparent considering the commutation relations

$$\left[N, a^\dagger\right] = a^\dagger\,, \qquad [N, a] = -a\,. \tag{2.8}$$

From these, we see that $a^\dagger|n\rangle$ is an eigenstate of N with eigenvalue $n+1$ and thus creates an excitation. A similar consideration shows that a is the annihilation operator.

For the LC circuit, the bosonic commutation relation is obtained defining the ladder operators through[1]

$$\Phi = i\Phi_{\text{zpf}}\left(a - a^\dagger\right), \qquad Q = Q_{\text{zpf}}\left(a + a^\dagger\right), \tag{2.9}$$

where $\Phi_{\text{zpf}} = \sqrt{\hbar/2C\omega}$ and $Q_{\text{zpf}} = \sqrt{\hbar C\omega/2}$ are known as the *zero-point fluctuations*. These quantities correspond to the variance of the flux and charge operators in the vacuum state of the circuit

$$\left\langle 0|\hat{\Phi}^2|0\right\rangle = \Phi_{\text{zpf}}^2, \qquad \left\langle 0|\hat{Q}^2|0\right\rangle = Q_{\text{zpf}}^2.$$

Finally, expressing the Hamiltonian in terms of the ladder operators we recognize the Hamiltonian of a simple harmonic oscillator

$$H = \hbar\omega\left(a^\dagger a + \frac{1}{2}\right). \tag{2.10}$$

While this quantization procedure is correct, the practical question is whether an LC oscillator can be operated so that quantum effects are observable. That requires temperatures low enough to suppress thermal excitations and coupling to environmental degrees of freedom weak enough that each level's linewidth, set by its relaxation rate, remains much smaller than the spacing between levels (∼GHz). Low temperatures (∼mK) are achieved by operating in a cryostat, while the exceptionally low dissipation of superconducting materials keeps linewidths narrow, making them especially well suited to reach the quantum regime.

2.2 The coplanar waveguide

Coplanar waveguides play a key role in a cQED platform. They not only carry signals between components (Sec. 2.2.1), acting as quantum optical "buses", but they may also take the form of resonators (Sec. 2.2.2), depending on their size and boundary conditions. Coplanar waveguide transmission lines and resonators can be coupled by capacitive couplings realized "tapping" their conductor centers (Sec. 2.2.3) [50].

2.2.1 The transmission line

The typical setup of a transmission line is illustrated in Fig. 2.3a. It consists of a coplanar waveguide formed by a center conductor of width w and thickness σ, separated on both sides by a distance s from a ground plane of the same thickness. Both conductors are typically deposited on a low-loss dielectric substrate [58]. The coplanar waveguide confines the electromagnetic field to a small volume between its center conductor and the ground, Fig. 2.3b, and supports quasi–Transverse Electromagnetic (quasi-TEM) modes in which the transverse electric field scales with the local voltage [58]. Ideally, the loss of coplanar waveguides is only limited by the conductivity of the center conductor and the ground plane, and by the losses of the dielectric medium. To minimize losses, superconducting metals such as aluminum, niobium or niobium titanium nitride (NbTiN), are used in combination with dielectrics of low loss tangent, such as sapphire or high-resistivity silicon [50].

[1] The ladder operators are defined only up to a phase: the transformation $a \to ae^{i\theta}$ leaves both the Hamiltonian (2.10) and the commutation relation $\left[a, a^\dagger\right]$ invariant. Equation (2.9) therefore fixes a phase convention by specifying how the operators are defined in terms of physical observables.

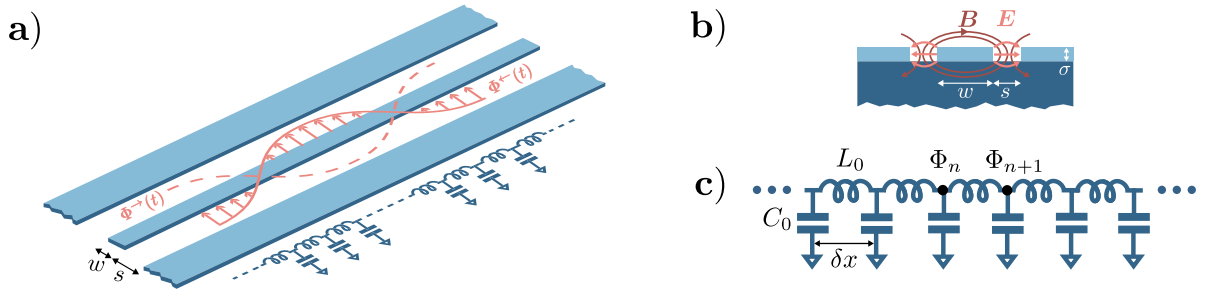

Figure 2.3: Circuit configuration of an infinite transmission line realized as a coplanar waveguide. (a) Schematic layout of a coplanar waveguide with center conductor width w, and ground plane separation s. The guide hosts both travelling waves going to the right ($\Phi^{\rightarrow}$) and to the left ($\Phi^{\leftarrow}$) (b) Cross-section cut of the coplanar waveguide resonator showing the substrate (dark blue), the two ground planes, and the center conductor of thickness σ (light blue) as well as schematic representations of the E and B field distributions. The electric field is confined inside the waveguide while the magnetic field is solenoidal to the conductor center. (c) A coplanar waveguide can be modeled by a series of capacitors C_0 and inductors L_0. The flux associated to the n-th node is Φ_n, so that the energy associated to the n-th inductance is $(\Phi_{n+1} - \Phi_n)^2/2L_0$. Figure adapted from Ref. [50].

Figure 2.3c shows the telegrapher model for such a system where the distributed inductance of the resonator's center conductor is represented by the series of lumped inductances L_0 while the capacitance to ground by a parallel combination of capacitances C_0 [50]. Denoting Φ_n the flux associated to the n-th node and with Q_n the charge at that node, the classical Hamiltonian is a generalization of Eq. (2.6)

$$\mathcal{H}_{\text{tml}} = \sum_{n=0}^{\infty} \frac{Q_{n+1}^2}{2C_0} + \frac{1}{2L_0}(\Phi_n - \Phi_{n-1})^2 \,, \tag{2.11}$$

where $\Phi_{n+1} - \Phi_n$ is the flux across the n-th inductor which defines the current across it $I_n = (\Phi_{n+1} - \Phi_n)/L_0$. To take the continuum limit we send the size of the unit cell δx to zero. For this purpose, we define the capacitance and the inductance per unit length c_0 and l_0, such that we can write $C_0 = c_0 \delta x$ and $L_0 = l_0 \delta x$. Introducing the fields $\Phi(x_n, t) = \Phi_n(t)$ and $Q(x_n, t) = Q_n(t)/\delta x$ the Hamiltonian becomes

$$\mathcal{H}_{\text{tml}} = \int_{-\infty}^{\infty} dx \left(\frac{1}{2c} Q(x,t)^2 + \frac{1}{2l} \left[\partial_x \Phi(x,t)\right]^2 \right) \,, \tag{2.12}$$

where $\partial_x \Phi(x_n, t) = \lim_{\delta x \to 0} (\Phi_{n+1} - \Phi_n)/\delta x$ sets the current propagating along the line

$$I(x,t) = \frac{\partial_x \Phi(x,t)}{l} \,.$$

The Hamilton equations provide the equations of motion of the conjugate variables

$$\dot{\Phi}(x,t) = \frac{Q(x,t)}{c} \,, \qquad \dot{Q}(x,t) = \frac{\partial_x^2 \Phi(x,t)}{l} \,, \tag{2.13}$$

where $\dot{Q}(x,t)$ is the current flowing in the capacitors to the common ground. The Hamilton equations can be recast in the wave equation

$$\ddot{\Phi}(x,t) - v^2 \partial_x^2 \Phi(x,t) = 0 \,, \tag{2.14}$$

with $v = 1/\sqrt{lc}$ the speed of light in the medium.

Solutions in momentum space To solve the wave equation we expand the fields in spatial Fourier modes

$$\begin{aligned}\Phi(x,t) &= \frac{1}{\sqrt{2\pi}}\int_{-\infty}^{\infty} dk \Phi_k(t) e^{-ikx}\,,\\ Q(x,t) &= \frac{1}{\sqrt{2\pi}}\int_{-\infty}^{\infty} dk Q_k(t) e^{-ikx}\,.\end{aligned} \tag{2.15}$$

In momentum space the wave equation decouples into independent harmonic oscillators

$$\ddot{\Phi}_k(t) + \omega_k^2 \Phi_k(t) = 0\,, \tag{2.16}$$

with $\omega_k = v|k|$. To quantize the solutions of (2.16), we promote the mode amplitudes to operators and we choose a normalization that enforces hermiticity, and reproduces the canonical commutator $[\Phi_k(x), Q_k(x')] = i\hbar\delta(x-x')$. Introducing the bosonic operators b_k satisfying

$$[b_k, b_{k'}] = 0\,, \qquad \left[b_k, b_{k'}^\dagger\right] = \delta(k-k')\,, \tag{2.17}$$

a convenient mode expansion is

$$\Phi_k(t) = i\sqrt{\frac{\hbar}{2c\omega_k}}\left(b_k e^{-i\omega_k t} - b_{-k}^\dagger e^{i\omega_k t}\right)\,, \tag{2.18}$$

which implies, through Eq. (2.13),

$$Q_k(t) = \sqrt{\frac{\hbar c\omega_k}{2}}\left(b_{-k}^\dagger e^{i\omega_k t} + b_k e^{-i\omega_k t}\right)\,. \tag{2.19}$$

With these definitions, we can rewrite Eq. (2.15) as

$$\begin{aligned}\Phi(x,t) &= \frac{i}{2}\sqrt{\frac{\hbar}{\pi c}}\int_{-\infty}^{\infty}\frac{dk}{\sqrt{\omega_k}}\left(b_k(t)e^{-ikx} - b_k^\dagger(t)e^{ikx}\right)\,,\\ Q(x,t) &= \frac{1}{2}\sqrt{\frac{\hbar c}{\pi}}\int_{-\infty}^{\infty}\sqrt{\omega_k}dk\left(b_k(t)e^{-ikx} + b_k^\dagger(t)e^{ikx}\right)\,,\end{aligned} \tag{2.20}$$

with

$$b_k(t) = b_k e^{-i\omega_k t}\,.$$

The Hamiltonian becomes a continuum of decoupled oscillators,

$$\mathcal{H}_{\text{tml}} = \hbar\int_{-\infty}^{\infty} dk\omega_k\left(b_k^\dagger b_k + \frac{1}{2}\delta(0)\right)\,, \tag{2.21}$$

where the last term accounts for the zero point energy of all the modes. In practice, one normal orders $\mathcal{H}_{\text{tml}}$ and discards this additive constant.

Solutions as travelling waves We can rewrite Eq. (2.20) making the right and left moving components explicit as

$$\Phi(x,t) = \Phi^{\rightarrow}(t - x/v) + \Phi^{\leftarrow}(t + x/v)\,. \tag{2.22}$$

The two components (see Fig. 2.3a) are

$$\Phi^{\overleftarrow{\rightarrow}}(t) = \frac{i}{2}\sqrt{\frac{\hbar}{\pi c}}\int_0^{\infty}\frac{dk}{\sqrt{\omega_k}}\left(b_k^{\overleftarrow{\rightarrow}} e^{-i\omega_k t} - \text{h. c.}\right)\,, \tag{2.23}$$

with right and left movers field defined only for $k > 0$ as

$$b_k^{\leftarrow} \equiv b_k\,, \quad b_k^{\rightarrow} \equiv b_{-k}\,. \tag{2.24}$$

Similar considerations apply to $Q(x,t)$ and therefore the Hamiltonian separates into independent right and left movers,

$$\mathcal{H}_{\text{tml}} = \hbar \int_0^\infty dk\omega_k \left(b_k^{\rightarrow,\dagger} b_k^{\rightarrow} + b_k^{\leftarrow,\dagger} b_k^{\leftarrow} \right). \tag{2.25}$$

2.2.2 The resonator

As illustrated in Figure 2.4, sections of a coplanar waveguide form resonators. Since the coplanar waveguide is now confined to $x \in [0,d]$, the electromagnetic modes are quantized. This means that we need to write the decomposition in Eq. (2.15) as a Fourier series

$$\Phi(x,t) = \sqrt{\frac{2}{d}} \sum_m \Phi_m(t) \cos\left(k_m x\right)\,, \quad Q(x,t) = \sqrt{\frac{2}{d}} \sum_m Q_m(t) \cos\left(k_m x\right)\,, \tag{2.26}$$

where k_m and ϕ are fixed by the boundary conditions.

To probe the cavity, one of its end may be capacitively coupled to a transmission line. At $x = 0$, the coupling to the feedline is typically designed to have a very large impedance (C_κ very small), so the current there is nearly zero and the port behaves as an open circuit. From Eq. (2.13), this implies $I(0,t) = \partial_x \Phi(x=0,t)/l = 0$. Thus $x = 0$ is a stationary point for $\Phi(x,t)$ and hence a voltage antinode. At $x = d$, we consider two cases

- $\lambda/2$ resonator (Fig. 2.4a): the far end is also an open circuit. This implies that no current can exist the end node, $\partial_x \Phi(x = d, t) = 0$, yielding standing wave solutions with $k_m = (m+1)\pi/d$ with $m = 0, 1 \ldots d-1$.
- $\lambda/4$ resonator (Fig. 2.4a): the far end is shorted to ground. This implies that the voltage vanishes at the boundary, $V(d,t) = \partial_t \Phi(x,t) = 0$, yielding $k_m = (m + 1/2)\,\pi/d$ with $m = 0, 1 \ldots d-1$.

Using the normal mode decomposition of Eq. (2.26), the resonator Hamiltonian is

$$\mathcal{H}_{\text{res}} = \sum_{m=0}^{\infty} \frac{Q_m^2}{2c} + \frac{\Phi_m^2}{2L_m}, \tag{2.27}$$

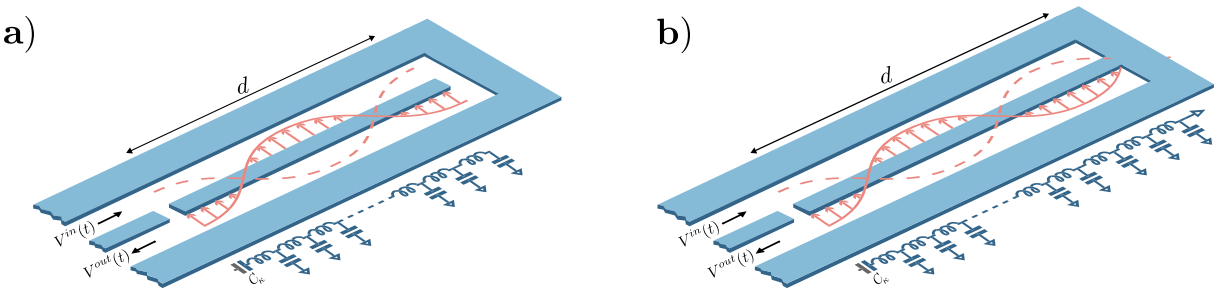

Figure 2.4: Coplanar waveguide resonator of length d coupled to a transmission line through a capacitance C_κ. V^{in} and V^{out} are the input and output signals at one port. The opposite end of the resonator is either left open or shorted to ground. a) Half-wave ($\lambda/2$) resonator with the far end open. b) Quarter-wave ($\lambda/4$) resonator with the far end grounded. Figure adapted from Ref. [50]. In orange, the electric field configuration for both boundary conditions.

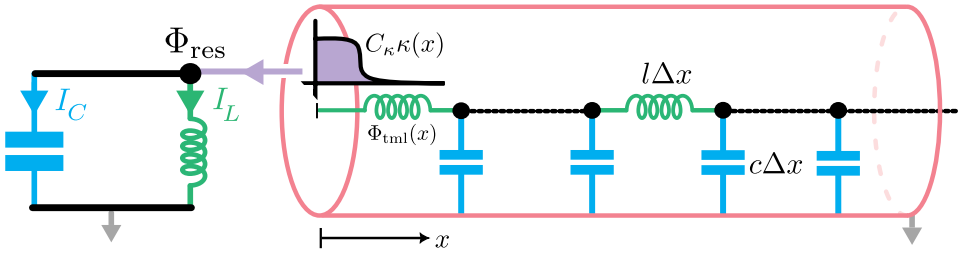

Figure 2.5: Semi-infinite transmission line coupled to a resonator. The coupling envelope $C_\kappa\kappa(x)$ nodes the voltage at the resonator node $\dot{\Phi}_{\rm res}$ and the voltage in the transmission line $\dot{\Phi}_{\rm tml}$. The resonator is represented as a LC circuit. Figure adapted from Ref. [61].

where $L_m^{-1} = c\omega_m^2$ with the angular velocity $\omega_m = k_m/v$. Following once more the canonical quantization and introducing the ladder operators a_m for each mode, we obtain

$$\Phi_m = i\sqrt{\frac{\hbar}{2c\omega_m}}(a_m - a_m^\dagger)\,, \qquad Q_m = \sqrt{\frac{\hbar c\omega_m}{2}}(a_m + a_m^\dagger)\,. \tag{2.28}$$

Using these expressions the Hamiltonian takes once again the form

$$\mathcal{H}_{\rm res} = \hbar\sum_{m=0}^{\infty}\omega_m\left(a_m^\dagger a_m + \frac{1}{2}\right). \tag{2.29}$$

In practice, since the level spacing ω_m is inversely proportional to the resonator length d, a single-mode resonator can be obtained reducing d. In this limit, Eq. (2.26) reduces to

$$\Phi(x,t) = f_m(x)\Phi_m(t)\,, \qquad Q(x,t) = f_m(x)Q_m(t)\,, \tag{2.30}$$

with all the spatial dependency contained in $f_m(x) = \sqrt{2/d}\cos(k_m x)$. A system coupled to the resonator at position $x = x_0$ therefore "sees" a LC circuit with flux and charge given by

$$\Phi_{\rm res} = \Phi(x_0,t) = f_m(x_0)\Phi_m(t)\,, \qquad Q_{\rm res} = Q(x_0,t) = f_m(x_0)Q_m(t)\,. \tag{2.31}$$

The effective capacitance and inductance of the LC circuit are given by $C = cf_m(x_0)^2$ and $L = L_m f_m(x_0)^2$.

2.2.3 Coupling between the transmission line and the resonator

In this Section we discuss the coupling between a transmission line and a resonator. We revisit Ref. [50] by considering a spatially extended capacitive coupling. Working with a smooth coupling envelope regularizes the theory, avoids ill-defined products of distributions [59, 60] and introduces a high-energy cutoff in the density of state of the transmission line (see Chapter 7). The limiting case of a point-like coupling is discussed at the end of the Section.

For a spatially extended capacitive coupling (see Fig. 2.5), the Lagrangian contribution can be written as

$$\mathcal{L}_{\rm int} = \frac{C_\kappa}{2}\int_0^\infty dx\kappa(x)\left(\dot{\Phi}_{\rm tml}(x) - \dot{\Phi}_{\rm res}\right)^2, \tag{2.32}$$

where $\kappa(x)$ is a spatial envelope normalized on the half-line[2]. This reduces the Lagrangian to the familiar form $\mathcal{L}_{\rm int} = C_\kappa\left(\dot{\Phi}_{\rm tml}(0) - \dot{\Phi}_{\rm res}\right)^2/2$, which described the energy stored in the capacitor

[2]This means $\int_0^\infty dx\kappa(x) = 1$.

C_κ due to the voltage drop across it. As usual, the semi-infinite transmission line is described by the Lagrangian

$$\mathcal{L}_{\text{tml}} = \int_0^\infty dx \left(\frac{c\dot{\Phi}^2_{\text{tml}}(x,t)}{2} - \frac{(\partial_x \Phi(x,t))^2}{2l} \right) , \tag{2.33}$$

while the resonator is modeled as an effective LC circuit (see Sec. (2.2.2)) with

$$\mathcal{L}_{\text{res}} = \frac{C\dot{\Phi}^2_{\text{res}}}{2} - \frac{\Phi^2_{\text{res}}}{2L} . \tag{2.34}$$

The full Lagrangian is therefore

$$\mathcal{L} = \mathcal{L}_{\text{tml}} + \mathcal{L}_{\text{res}} + \mathcal{L}_{\text{int}} . \tag{2.35}$$

The Hamiltonian To construct the Hamiltonian we compute the conjugate momentum density of the line $Q_{\text{tml}} = \delta_{\dot{\Phi}_{\text{tml}}} \mathcal{L}$ and the conjugate charge of the resonator $Q_{\text{res}} = \partial_{\dot{\Phi}_{\text{res}}} \mathcal{L}$.

$$Q_{\text{tml}} = c\dot{\Phi}_{\text{tml}} + C_\kappa \kappa(x) \left(\dot{\Phi}_{\text{tml}} - \dot{\Phi}_{\text{res}} \right) , \tag{2.36}$$

$$Q_{\text{res}} = C\dot{\Phi}_{\text{res}} - C_\kappa \int_0^\infty dx \kappa(x) \left(\dot{\Phi}_{\text{tml}} - \dot{\Phi}_{\text{res}} \right) . \tag{2.37}$$

The charge density Q_{tml} corresponds to the total charge density accumulated by the capacitors attached to the line at x, while Q_{res} is the total charge energy accumulated at the resonator's coupling node (see Fig. 2.5). In Appendix A, these relations are inverted so that up to linear order in C_κ we can write

$$\dot{\Phi}_{\text{tml}} = \frac{1}{\bar{c}(x)} \left(Q_{\text{tml}} + \frac{C_\kappa}{\bar{C}} \kappa(x) Q_{\text{res}} \right) , \tag{2.38}$$

$$\dot{\Phi}_{\text{res}} = \frac{1}{\bar{C}} \left(Q_{\text{res}} + \int_0^\infty dx \frac{C_\kappa}{\bar{c}(x)} \kappa(x) Q_{\text{tml}}(x) \right) , \tag{2.39}$$

with the normalized capacitances $\bar{c}(x) = c + C_\kappa \kappa(x)$ and $\bar{C} = C + C_\kappa$. The Hamiltonian up to linear order in C_κ then reads

$$\mathcal{H} = \int_0^\infty \frac{dx}{2\bar{c}(x)} \left(Q_{\text{tml}}(x,t) + \frac{C_\kappa}{\bar{C}} \kappa(x) Q_{\text{res}} \right)^2 + \int_0^\infty dx \frac{[\partial_x \Phi(x,t)]^2}{2l} + \frac{Q^2_{\text{res}}}{2\bar{C}} + \frac{\Phi^2_{\text{res}}}{2L} . \tag{2.40}$$

The Hamiltonian captures the effects of the coupling. First, it induces a shift of the line momentum density, analogous to the minimal-coupling substitution in cavity QED ($p \to p - eA$). Second, it normalizes the capacitance along the line and for the resonator.

Equations of motion For the resonator, Hamilton's equation provide two relations: Eq. 2.39 and

$$\dot{Q}_{\text{res}}(t) = -\frac{\partial \mathcal{H}}{\partial \Phi_{\text{res}}} = -\frac{\Phi_{\text{res}}(t)}{L} . \tag{2.41}$$

Combining these gives

$$I_C + I_L = C_\kappa \int_0^\infty dx \kappa(x) \left(\ddot{\Phi}_{\text{tml}}(x,t) - \ddot{\Phi}_{\text{res}}(t) \right) , \tag{2.42}$$

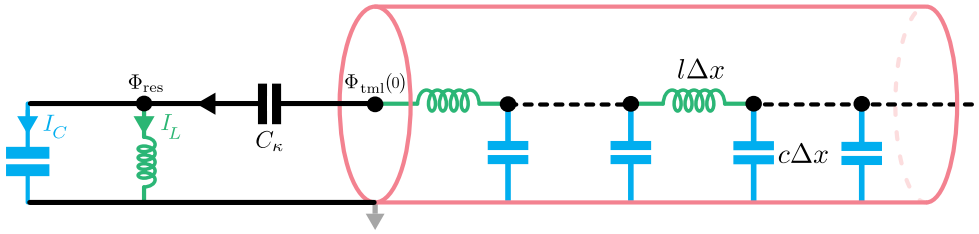

Figure 2.6: Semi-infinite transmission line coupled to a resonator through the point-like capacitive coupling C_κ. The resonator is represented as a LC circuit. The flux at the resonator node and at the end of the line are $\Phi_{\rm res}$ and $\Phi_{\rm tml}(0)$, respectively. The current flows from the end of the line towards both the inductor and the capacitor of the resonator. Figure adapted from Ref. [61].

which is Kirchhoff's current law at the resonator node, with $I_C = C\ddot{\Phi}_{\rm res}(t)$ the current flowing in the capacitor and $I_L = \Phi_{\rm res}/L$ the current in the inductor, as illustrated in Fig. 2.5. For the line, Hamilton's equations provide Eq. 2.38 and

$$\dot{Q}_{\rm tml}(x,t) = -\frac{\delta\mathcal{H}}{\delta\Phi_{\rm tml}} = \frac{1}{l}\partial_x\Phi_{\rm tml}(x,t) + \frac{1}{2l}\delta_+(x)\partial_x\Phi_{\rm tml}(x,t)\,.$$

Combining them yields the wave equation with source for $x \geq 0$

$$\ddot{\Phi}_{\rm tml}(x,t) - \frac{1}{l\bar{c}(x)}\left(\partial_x^2\Phi_{\rm tml}(x,t) + \delta_+(x)\partial_x\Phi_{\rm tml}(0,t)\right) = \kappa(x)\frac{C_\kappa}{\bar{c}(x)\bar{C}}\dot{Q}_{\rm res}(t)\,, \tag{2.43}$$

where we introduced the one-sided delta function $\delta_+(x)$. Integrating this equation over $x \in [0,\epsilon]$ and taking the limit $\varepsilon \to 0$ provides the Neumann boundary condition for $\Phi_{\rm tml}$. If the coupling is a smooth function, $\kappa(x)$ has no singularity in $x = 0$ (κ a smooth function) and the boundary condition reads

$$\frac{1}{l}\partial_x\Phi_{\rm tml}(0,t) = 0\,, \tag{2.44}$$

which reflects the open circuit termination at $x = 0$. If the coupling is the point-like capacitor in Fig. 2.6, $\kappa(x) = \delta(x)$ and the integration of the right hand side in Eq. (2.43) gives

$$\frac{1}{l}\partial_x\Phi_{\rm tml}(0,t) = -\frac{C_\kappa}{\bar{C}}\dot{Q}_{\rm res}\,, \tag{2.45}$$

which is the Kirchhoff's current law at $x = 0$: the line current at the boundary of the transmission line equals the current through the coupling capacitor (C_κ in Fig. 2.6).

We conclude this section by remarking that in the experimentally relevant regime $C_\kappa \ll c, C$ we the approximations $\bar{c} \approx c$ and $\bar{C} \approx C$ are valid[3].

2.3 Input-output theory

Transmission lines are widely used to probe quantum systems within input-output theory. A signal is sent into the line at a time t_0 and retrieved at time t_1. Because of the coupling between the system and the line, the measured signal carries information about the system. This is the effective description employed in Chap. 3, where resonator sensitive to the qubit state are

[3] In the case of a point-like coupling the renormalization term proportional to C_κ in $\bar{c}$ cannot be formally dropped since it contains a $\delta(x)$ contribution. However, in this case $\bar{c}(x) \neq c$ only at $x = 0$ and that term would be relevant only for the boundary condition at $x = 0$. In practice, Eq. (2.45) does not contain $\bar{c}$ so we take $\bar{c} = C$.

read out via capacitively coupled transmission lines, and in Chap. 7 to introduce Many-Body Admittance Spectroscopy (MADS).

In Secs. 2.3.1,2.3.2 we review input–output theory, building on Refs. [50, 62] and laying the groundwork for MADS. Section 2.3.3 shows how to solve the resonator dynamics by integrating out the feedline: the average input mode becomes a drive Hamiltonian while the residual fluctuations set the damping rate of the cavity.

2.3.1 Input-output relations

Here we derive the input-output relations for a cavity coupled to a transmission line. To not lose generalities and lay the groundwork for Many-Body Admittance Spectroscopy (Chap. 7), we consider a more general setup in which the transmission line is coupled to an unspecified charge degree of freedom X via a spatially extended coupling envelope $\alpha\kappa(x)$. The results are analogous to those of scattering theory.

The wave equation with source We consider the Hamiltonian [50, 62–64]

$$\mathcal{H} = \mathcal{H}_{\text{sys}} + \int_0^\infty dx \left\{ \frac{1}{2c} \left[Q(x,t) + \alpha\kappa(x) X(t) \right]^2 + \frac{1}{2l} \left[\partial_x \Phi(x,t) \right]^2 \right\} , \tag{2.46}$$

which is Eq. (2.40) with $\alpha = C_\kappa$ and $X = Q_{\text{res}}$.

As discussed in the previous section, Hamilton equations provide

$$\begin{aligned} \dot{Q} &= \frac{1}{l} \partial_x^2 \Phi(x,t) \,, \\ \dot{\Phi} &= \frac{Q}{c} + \frac{\alpha\kappa(x) X(t)}{c} \,, \end{aligned} \tag{2.47}$$

which can be recast in the wave equation for any $x > 0$

$$\ddot{\Phi}(x,t) - v^2 \partial_x^2 \Phi(x,t) = \frac{\alpha\kappa(x)\dot{X}(t)}{c} \,, \tag{2.48}$$

with $v = 1/\sqrt{lc}$. Since $X(t)$ appears in the wave equation as a source term, we refer to X as the source. This is the system coupled to the transmission line that injects a signal into the line.

The infinite line We start by considering the wave equation on the entire line (see Fig. 2.7), with $\kappa(x)$ supported on $[-x^*, x^*]$. This allows us to forget about the spatial boundary condition for the moment. Solutions on the half-line, with the boundary conditions discussed in Sec. 2.2.3, will then be obtained via the method of images from this solution. For the temporal boundary condition, we write the Fourier expansion of the general solution to the Hamilton equations (2.47) as in (2.20). At time t_0, before any wave packet has reached the source, we set the fields b_k to the input fields

$$b_k(t_0) = b_k^{in}(t_0) \,, \tag{2.49}$$

which evolve freely as

$$b_k^{in}(t) = b_k^{in}(t_0) e^{-i\omega_k (t - t_0)} \,. \tag{2.50}$$

The condition (2.49) is enforced by fixing both the flux at t_0,

$$\Phi(x, t_0) = \Phi_{in}(x, t_0) \,, \tag{2.51}$$

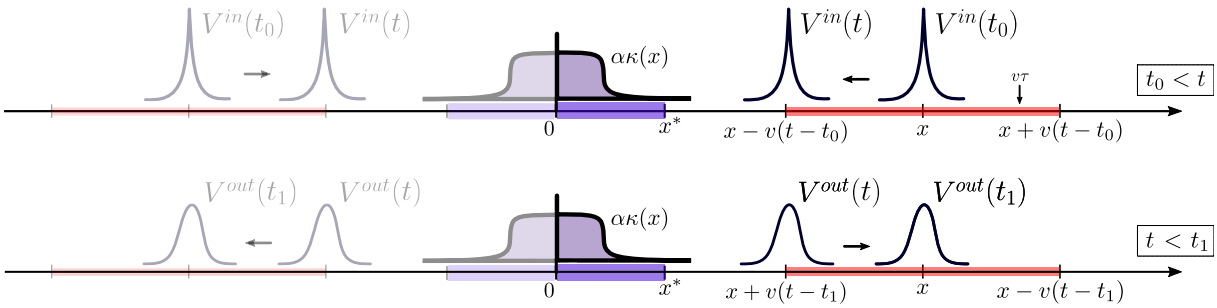

Figure 2.7: Boundary condition used to solve the wave equation on the infinite transmission line. At t_0 an input voltage, decomposes in left and right movers, is imposed on the line. As t grows, the fields b_k in the wave packet evolves freely. When $x - v(t - t_0) = x^*$, the wave packet has reached the interacting region, and the signal radiated from the source at t_0 has reached x, adding to the output field. At t_1 all the wave packets had already interacted with the source and are leaving from the interacting region.

and the conjugated momentum $Q(x, t_0) = Q_{in}(x, t_0)$. The latter sets the line voltage

$$\dot{\Phi}(x, t_0) = \dot{\Phi}_{in}(x, t_0) + \frac{\alpha\kappa(x)X(t_0)}{c}\,, \tag{2.52}$$

which is the sum of the input-mode voltage and the electrostatic profile generated by the source at t_0.

To gain physical insights, it is useful to decompose the input field Φ^{in} into left and right movers as

$$\Phi_{in}(x,t) = \Phi_{in}^{\rightarrow}\left(t - \frac{x}{v}\right) + \Phi_{in}^{\leftarrow}\left(t + \frac{x}{v}\right)\,,$$

with $\overrightarrow{\Phi_{in}^{\leftarrow}}(t)$ given by (2.23). The homogeneous solution of the wave equation is simply this input field

$$\Phi_{\rm hom}(x,t) = \Phi_{in}(x,t)\,, \tag{2.53}$$

while the general solution reads

$$\Phi(x,t) = \Phi_{in}^{\rightarrow}\left(t - \frac{x}{v}\right) + \Phi_{in}^{\leftarrow}\left(t + \frac{x}{v}\right) + \frac{\alpha}{2c}\int_{\frac{x}{v}-(t-t_0)}^{\frac{x}{v}+(t-t_0)} d\tau\kappa(v\tau)X\left(t - \left|\tau - \frac{x}{v}\right|\right)\,. \tag{2.54}$$

On the other hand, we could also enforce the field at a time t_1 in the distant future, after all the wave packets have already interacted with the source

$$b_k(t_1) = b_k^{out}(t_1)\,. \tag{2.55}$$

This is enforced by

$$\Phi(x,t_1) = \Phi_{out}^{\rightarrow}\left(t_1 - \frac{x}{v}\right) + \Phi_{out}^{\leftarrow}\left(t_1 + \frac{x}{v}\right)\,, \tag{2.56}$$

$$\dot{\Phi}(x,t_1) = \dot{\Phi}_{out}^{\rightarrow}\left(t_1 + \frac{x}{v}\right) + \dot{\Phi}_{out}^{\leftarrow}\left(t_1 - \frac{x}{v}\right) + \frac{\alpha\kappa(x)X(t_1)}{c}\,. \tag{2.57}$$

According to these boundary conditions, the general solution then reads

$$\Phi(x,t) = \Phi_{out}^{\rightarrow}\left(t - \frac{x}{v}\right) + \Phi_{out}^{\leftarrow}\left(t + \frac{x}{v}\right) - \frac{\alpha}{2c}\int_{\frac{x}{v}+(t-t_1)}^{\frac{x}{v}-(t-t_1)} d\tau\kappa(v\tau)X\left(t + \left|\tau - \frac{x}{v}\right|\right)\,. \tag{2.58}$$

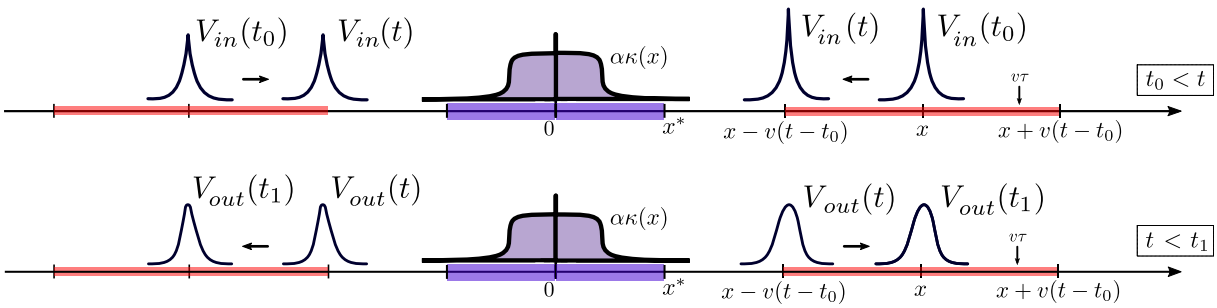

Figure 2.8: Boundary conditions to solve the half-line through the method of the image. The situation is similar to the one of Figure 2.7, with an imposed reflection symmetry over the x axis.

For x outside the source support, we always have $v\tau < x$ for non vanishing $\kappa(v\tau)$ and we can write $|\tau - x/v| = x/v - \tau$ for both integrals. Taking $t_0 \to -\infty$ and $t_1 \to \infty$ extends also the limits of the integrals to $\pm\infty$. Combining Eq. (2.54-2.58) we then obtain the input-output (IO) relations

$$\begin{aligned}\Phi^{\rightarrow}_{out}\left(t - \frac{x}{v}\right) &= \Phi^{\rightarrow}_{in}\left(t - \frac{x}{v}\right) + \frac{\alpha}{2c}\int_{-\infty}^{\infty} d\tau\kappa(v\tau)X\left(t - \frac{x}{v} + \tau\right) ,\\ \Phi^{\leftarrow}_{out}\left(t + \frac{x}{v}\right) &= \Phi^{\leftarrow}_{in}\left(t + \frac{x}{v}\right) + \frac{\alpha}{2c}\int_{-\infty}^{\infty} d\tau\kappa(v\tau)X\left(t + \frac{x}{v} - \tau\right) .\end{aligned} \tag{2.59}$$

Plugging the IO into (2.54) gives

$$\Phi(x,t) = \Phi^{\rightarrow}_{out}\left(t - \frac{x}{v}\right) + \Phi^{\leftarrow}_{in}\left(t + \frac{x}{v}\right) , \tag{2.60}$$

making explicit that, outside the interaction region, $\Phi(x,t)$ is a sum of an incoming input field and an outgoing output field.

Since (2.59) holds for any t, even though x must be outside the range of $\kappa(x)$, we can write the time evolution of the output mode as [62]

$$\begin{aligned}\Phi^{\rightarrow}_{out}(t) &= \Phi^{\rightarrow}_{in}(t) + \frac{\alpha}{2c}\int_{-\infty}^{\infty} d\tau\kappa(v\tau)X(t+\tau) ,\\ \Phi^{\leftarrow}_{out}(t) &= \Phi^{\leftarrow}_{in}(t) + \frac{\alpha}{2c}\int_{-\infty}^{\infty} d\tau\kappa(v\tau)X(t-\tau) .\end{aligned} \tag{2.61}$$

This expression of the output field shows that it is itself given by the sum of a reflection of the input field and a radiated field $\frac{\alpha}{2c}\int_{-\infty}^{\infty} d\tau\kappa(v\tau)X(t+\tau)$, whose behaviour is determined by $\mathcal{H}_{\text{sys}}$ [62].

Voltages IO relations follow by taking time derivatives Eqs. (2.60-2.61).

The semi-infinite line To obtain the half-line solution, we match the boundary conditions at $x = 0$ via the method of images (see Fig. 2.8).

- Neumann homogeneous boundary condition corresponds to a free end $\partial_x\Phi(0,t) = 0$. This condition is automatically satisfied extending the wave equation to the entire line and enforcing an even solution $\Phi(x,t) = \Phi(-x,t)$. This is achieved by imposing the even extension of the fields $\Phi^{\rightarrow}_{in}(t) = \Phi^{\leftarrow}_{in}(t)$, $\dot{\Phi}^{\rightarrow}_{in}(t) = \dot{\Phi}^{\leftarrow}_{in}(t)$ and of the source $\kappa(-x) = \kappa(x)$.

- Neumann inhomogeneous boundary condition corresponds to a pointlike coupling at $x = 0$. As we have seen, this imposes a non-zero current $\partial_x \Phi(0,t)/l = -\alpha \dot{X}(t)$. This boundary condition is automatically implemented considering the even extension of the source $\kappa(x) = 2\delta(x)$. (see Eq. (2.43)). Still, one needs to enforce $\Phi(x,t) = \Phi(-x,t)$ to prevent other terms in the boundary current.

In both cases, the condition $\Phi(x,t) = \Phi(-x,t)$ enforces $b_k = b_{-k}$. This means that modes with negative k are no more independent physical modes ($\left[b_k, b_{-k}^\dagger\right] \neq 0$) and must be replaced by the physical modes in the Fourier decomposition (2.20). Keeping these redundant modes explicit in the Fourier decomposition implies $[\Phi(x,t), Q(x',t)] = 2i\hbar\delta(x-x')$. Expressed only using the physical modes, the fields write

$$\begin{aligned} \Phi(x,t) &= i\sqrt{\frac{\hbar}{\pi c}} \int_0^\infty \frac{dk}{\sqrt{\omega_k}} \left(b_k(t) - b_k^\dagger(t)\right) \cos(kx) \,, \\ Q(x,t) &= \sqrt{\frac{\hbar c}{\pi}} \int_0^\infty \sqrt{\omega_k} dk \left(b_k(t) + b_k^\dagger(t)\right) \cos(kx) \,. \end{aligned} \tag{2.62}$$

and the Hamiltonian reduces to

$$\mathcal{H}_{\mathrm{tml}} = \hbar \int_0^\infty dk \omega_k b_k^\dagger b_k \,. \tag{2.63}$$

Dirichlet boundary condition

- Dirichlet boundary condition corresponds to a grounded end $\Phi(0,t) = 0$. This condition would enforce an odd extension of the fields $\Phi_{in}^{\rightarrow}(t) = -\Phi_{in}^{\leftarrow}(t)$, $\dot{\Phi}_{in}^{\rightarrow}(t) = -\dot{\Phi}_{in}^{\leftarrow}(t)$ and of the source $\kappa(-x) = -\kappa(x)$.

As a side note, Dirichlet boundary condition are incompatible with the assumption $C_\kappa \ll c$, since a grounded end implies $C_\kappa \to \infty$.

Input-output relations in momentum space Consider the Fourier transform of the coupling envelope

$$\kappa(x) = \frac{1}{\sqrt{2\pi}} \int_{-\infty}^\infty dk \kappa(k) e^{ikx} \,. \tag{2.64}$$

From the Fourier decomposition of $\Phi^{in/out}$ (2.20) and Eq. (2.61), the input–output relation for the bath modes is

$$b_k^{out}(t) = b_k^{in}(t) - i\alpha\kappa(k)\sqrt{\frac{\omega_k}{2\hbar c}} \int_{-\infty}^\infty d\tau e^{-i\omega_k(t-\tau)} X(\tau) \,, \tag{2.65}$$

where we have used the relations between the input and output fields and the left and right movers

$$\begin{aligned} b_{k,in}^{\leftarrow} &= b_k^{in} \,, \quad b_{k,out}^{\leftarrow} = b_k^{out} \,, \\ b_{k,in}^{\rightarrow} &= b_{-k}^{in} \,, \quad b_{k,out}^{\rightarrow} = b_{-k}^{out} \,. \end{aligned} \tag{2.66}$$

For a resonator coupled to the line, we have $X(\tau) = Q_{\mathrm{res}}(\tau)$ and $\alpha = C_\kappa/C$. Introducing the mode-dependent coupling

$$g_k = \frac{1}{2} \frac{C_\kappa}{\sqrt{Cc}} \sqrt{\omega_{\mathrm{r}} \omega_k} \kappa(k) \,, \tag{2.67}$$

the input–output relation becomes

$$b_k^{out}(t) = b_k^{in}(t) - ig_\kappa \int_{-\infty}^{\infty} d\tau e^{-i\omega_k(t-\tau)} \left(a\left(\tau\right) + a^\dagger(\tau) \right) . \tag{2.68}$$

Since we can write the resonator field as $a(t) = e^{-i\omega_r t}\tilde{a}(t)$ with $\tilde{a}(t)$ a slowly varying field, we can perform a rotating wave approximation (RWA) and remove $a^\dagger(\tau)$. This also implies that the integral in Eq. (2.68) contributes only for wave vectors such that $\omega_k \approx \omega_r$. If this range is small enough, we make a flat approximation for g_k

$$g_k = \sqrt{\frac{\kappa}{2\pi}} , \tag{2.69}$$

where κ is a constant. Integrating (2.68) over k leads to the relation

$$b_{out}^{\overleftarrow{\rightarrow}}(t) = b_{in}^{\overleftarrow{\rightarrow}}(t) - i\sqrt{\frac{\kappa}{2}} a(t) , \tag{2.70}$$

where we have introduced the collective input mode propagating to the right/left

$$b_{in/out}^{\overleftarrow{\rightarrow}}(t) = \frac{1}{\sqrt{\pi}} \int_0^\infty dk b_{\pm k}^{in/out}(t) . \tag{2.71}$$

Eq. (2.70) can also be written in terms of the collective input and output mode

$$\begin{aligned} b_{in}(t) &= \frac{1}{\sqrt{2}} \left(b_{in}^{\rightarrow}(t) + b_{in}^{\leftarrow}(t) \right) , \\ b_{out}(t) &= \frac{1}{\sqrt{2}} \left(b_{out}^{\rightarrow}(t) + b_{out}^{\leftarrow}(t) \right) , \end{aligned} \tag{2.72}$$

as

$$b_{out}(t) = b_{in}(t) - i\sqrt{\kappa} a(t) . \tag{2.73}$$

2.3.2 Input-output relations from the Heisenberg equation

Here we show that the solutions of the wave equation and the input-output (IO) relations follow directly from the quantized Hamiltonian via the Heisenberg equation.

After expanding the minimal coupling term in (2.46) and replacing $X = Q_{\rm res}$ with the expressions in Eqs. (2.28),(2.31), the full Hamiltonian of the coupled system reads

$$\mathcal{H} = \mathcal{H}_{\rm sys} + \mathcal{H}_{\rm tml} + \hbar(a + a^\dagger) \int_{-\infty}^{\infty} dk \left(g_k^* b_k + g_k b_k^\dagger \right) , \tag{2.74}$$

where $\mathcal{H}_{\rm sys}$ contains the resonator Hamiltonian and potentially other couplings (such as the coupling between qubit and resonator, see Sec. 2.4). We also remark that the integration in k should be restricted to $[0, \infty)$ for the half-line, since in that case only positive k modes are physical.

The Heisenberg equation for the line bosonic fields reads

$$\dot{b}_k(t) = \frac{i}{\hbar} \left[\mathcal{H}, b_k \right] = -i\omega_k b_k - ig_k(a + a^\dagger) . \tag{2.75}$$

Solving this equation with asymptotic input and output boundary condition at times t_0 and t_1 gives

$$b_k(t) = b_k^{in}(t) - ig_k \int_{t_0}^{t} \mathrm{d}\tau e^{-i\omega_k(t-\tau)}[a(\tau) + a^\dagger(\tau)]\,, \tag{2.76}$$

$$= b_k^{out}(t) + ig_k \int_{t}^{t_1} \mathrm{d}\tau e^{-i\omega_k(t-\tau)}[a(\tau) + a^\dagger(\tau)]\,, \tag{2.77}$$

where the input and output modes evolve according to the free Hamiltonian $\mathcal{H}_{\mathrm{tml}}$. Substituting these expressions into the Fourier decomposition of the transmission-line fields (2.20) reproduces exactly the solutions (2.54-2.58). Combining the two expressions above, we also recover (2.68) in the limit $t_0 \to -\infty$ and $t_1 \to \infty$.

2.3.3 Eliminating the bath Hamiltonian

To obtain an effective description of only cavity modes, we solve the resonator dynamics by tracing out the feedline's modes.

The time evolution of the resonator field follows the Heisenberg equation

$$\dot{a}(t) = \frac{i}{\hbar}\left[\mathcal{H}, a\right] = \frac{i}{\hbar}\left[\mathcal{H}, a\right] - i\int_{-\infty}^{\infty} dk \left(g_k^* b_k + g_k b_k^\dagger\right)\,. \tag{2.78}$$

Substituting $b_k(t)$ from Eq. (2.76) and applying both the RWA and the flat-band approximation (2.69) yields

$$\dot{a}(t) = \frac{i}{\hbar}\left[\mathcal{H}_{\mathrm{sys}}, a\right] - i\sqrt{\kappa} b_{in}(t) - \frac{\kappa}{2}a(t)\,. \tag{2.79}$$

The last term in (2.79) describes the decay rate: it is due to the photons that simply leak into the output mode of the transmission line. This suggests that quantum fluctuations in the line act as a thermal bath that can be treated within an effective description.

Starting from the interaction Hamiltonian

$$\mathcal{H}_{\mathrm{int}} = \hbar(a + a^\dagger)\int_{-\infty}^{\infty} dk \left(g_k^* b_k + g_k b_k^\dagger\right)\,, \tag{2.80}$$

we write the Liouville-Von Neumann equation $\dot{\rho}(t) = -i\left[\mathcal{H}, \rho(t)\right]/\hbar$ in the interacting picture (see Appendix B.3)

$$\dot{\rho}^I(t) = -\frac{i}{\hbar}\left[\mathcal{H}^I_{\mathrm{int}}(t), \rho^I(t)\right]\,. \tag{2.81}$$

Introducing the reduced density matrix of the system $\rho_S^I(t) = \mathrm{Tr}_{\mathrm{tml}}\rho^I(t)$, we can always rewrite the density matrix as the sum of a factorized term plus the system–bath correlations χ^I as

$$\rho^I(t) = \rho_S^I(t) \otimes \rho_{\mathrm{tml}}^I(t) + \chi^I(t)\,, \qquad \text{with } \mathrm{Tr}_{\mathrm{tml}}\chi^I = 0\,. \tag{2.82}$$

One can then trace out the transmission-line fields to obtain

$$\dot{\rho}_S^I(t) = -\frac{i}{\hbar}\left[\left\langle \mathcal{H}^I_{\mathrm{int}}(t)\right\rangle_{\mathrm{tml}}, \rho_S^I(t)\right] - \frac{i}{\hbar}\mathrm{Tr}_{\mathrm{tml}}\left[\delta\mathcal{H}^I_{\mathrm{int}}(t), \chi^I(t)\right]\,, \tag{2.83}$$

where we have split the interacting Hamiltonian into the average $\left\langle \mathcal{H}^I_{\mathrm{int}}(t)\right\rangle_{\mathrm{tml}}$ and the zero mean fluctuations, $\delta\mathcal{H}^I_{\mathrm{int}}(t) = \left\langle \mathcal{H}^I_{\mathrm{int}}(t)\right\rangle_{\mathrm{tml}} - \mathcal{H}^I_{\mathrm{int}}(t)$.

In a typical experiment, the line is populated by an input field and thermal fluctuations. This means that the density matrix is a displaced thermal state

$$\rho^I_{\rm tml}(t) = \mathbf{D}\left[\beta_{in}(t)\right]\rho_{\rm th}\mathbf{D}^\dagger\left[\beta_{in}(t)\right] , \tag{2.84}$$

where we introduced the displacement operator

$$\mathbf{D}\left[\beta_{in}(t)\right] = \exp\left[\int_{-\infty}^{\infty}\int_{-\infty}^{\infty} dk'dt'\left(b^{in}_{k'}(t')\beta^{in}_{k'}(t') + \text{h.c.}\right)\right] , \tag{2.85}$$

such that $\mathbf{D}^\dagger\left[\beta_{in}(t)\right] b^{in}_k(t)\mathbf{D}\left[\beta_{in}(t)\right] = \beta^{in}_k(t) + b^{in}_k(t)$.

The drive Hamiltonian Since the time evolution of the line modes in the interacting picture is given by $b^I_k(t) = b^{in}_k(t)$, we have

$$\left\langle b^I_k(t)\right\rangle_{\rm tml} = \left\langle b^{in}_k(t)\right\rangle_{\rm tml} = \text{Tr}\left\{b^{in}_k(t)\rho^I_{\rm tml}(t)\right\} = \beta^{in}_k(t) , \tag{2.86}$$

and we can identify in the first term of (2.83) the drive Hamiltonian

$$\mathcal{H}_{\rm drive} = \left\langle \mathcal{H}^I_{\rm int}(t)\right\rangle_{\rm tml} = \hbar(a+a^\dagger)\int_{-\infty}^{\infty} dk\left(g^*_k\left\langle b^{in}_k(t)\right\rangle_{\rm tml} + g_k\left\langle b^{in\dagger}_k(t)\right\rangle_{\rm tml}\right) , \tag{2.87}$$

which, considering an input drive

$$\left\langle b^{in}_k(t)\right\rangle = \frac{A_{\rm r}}{2g_k}e^{-i(\omega_{\rm r}t+\varphi)}\delta(k-\omega_r/v) , \tag{2.88}$$

reduces to

$$\mathcal{H}_{\rm drive} = \hbar A_{\rm r}(a+a^\dagger)\cos\left(\omega_{\rm r}t+\varphi\right) . \tag{2.89}$$

Dissipation The second term in (2.83) depends on $\delta\mathcal{H}^I_{\rm int}$, which contains the fluctuations $\delta b^I_k(t) = b^I_k(t) - \langle b^{in}_k(t)\rangle$. From (2.82) and (2.81), the evolution of the system–bath correlations is given by

$$\dot\chi^I(t) = \left[\delta\mathcal{H}^I_{\rm int}(t), \dot\rho^I_S(t)\otimes\rho^I_{\rm tml}(t)\right] + \mathcal{O}(g_k^2) , \tag{2.90}$$

so that its integral form reads

$$\chi^I(t) = \chi^I(t_0) - \frac{i}{\hbar}\int_{t_0}^{t} ds\left[\delta\mathcal{H}^I_{\rm int}(s), \dot\rho^I_S(s)\otimes\rho^I_{\rm tml}(s)\right] + \mathcal{O}(g_k^2) . \tag{2.91}$$

Since t_0 is taken at the remote past where correlations did not yet develop, $\chi^I(t_0) = 0$. Inserting Eq. (2.91) into (2.81) yields

$$\dot\rho^I_S(t) = -\frac{i}{\hbar}\left[\mathcal{H}_{\rm drive}, \rho^I_S(t)\right] - \frac{1}{\hbar^2}\int_0^{t-t_0} ds\left\langle\left[\delta\mathcal{H}^I_{\rm int}(t), \left[\delta\mathcal{H}^I_{\rm int}(t-s), \rho^I_S(t-s)\right]\right]\right\rangle_{\rm tml} . \tag{2.92}$$

Under the Markov approximation we first replace $\rho^I_S(t-s) \to \rho^I_S(t)$. This make the equation local in time. Taking $t_0 = -\infty$ the equation has no more memory about the initial preparation of the resonator and we obtain [65]

$$\dot\rho^I_S(t) = -\frac{i}{\hbar}\left[\mathcal{H}_{\rm drive}, \rho^I_S(t)\right] - \frac{1}{\hbar^2}\int_0^{\infty} ds\left\langle\left[\delta\mathcal{H}_{\rm int}(t), \left[\delta\mathcal{H}^I_{\rm int}(t-s), \rho^I_S(t)\right]\right]\right\rangle_{\rm tml} . \tag{2.93}$$

After applying the RWA we find the master equation

$$\dot{\rho} = \mathcal{L}[\rho]\,, \qquad \mathcal{L}[\rho] = -\frac{i}{\hbar}[\mathcal{H}_{\text{sys}} + \mathcal{H}_{\text{drive}}, \rho] + \kappa \mathcal{D}_a[\rho]\,, \tag{2.94}$$

with the Lindblad dissipator defined as

$$\mathcal{D}_a[\rho] = a\rho a^\dagger - \frac{1}{2}\left\{a^\dagger a, \rho\right\}\,. \tag{2.95}$$

To summarize, the influence of the transmission line on the resonator's equation of motion is fully captured by the drive Hamiltonian (2.89) and the Lindblad dissipator (2.95).

2.4 Hybrid cQED

In this section we consider a prototype of an artificial atom, the charge qubit formed by the charge states of a double quantum dot (DQD) (Sec. 2.4.1), and show how it couples to a resonator (Sec. 2.4.2). This combination of a superconducting resonator with other quantum degrees of freedom, extending the circuit-QED approach, is known as *hybrid circuit quantum electrodynamics* (hybrid cQED) [66]. Other cQED and hybrid cQED platforms are discussed in Chap. 6.

2.4.1 An artificial atom: the charge qubit

An example of artificial atom is a double quantum dot (DQD). Similarly to an atom, where electrons are confined by the attractive potential of the nucleus, in quantum dots the electrons are bound by a quantum well potential. This potential is typically generated by a set of metallic gates which also determine the occupancy of the dots. For sufficiently small dots, it is possible to isolate one level in each dot and tune the voltages such that only a single charge occupies

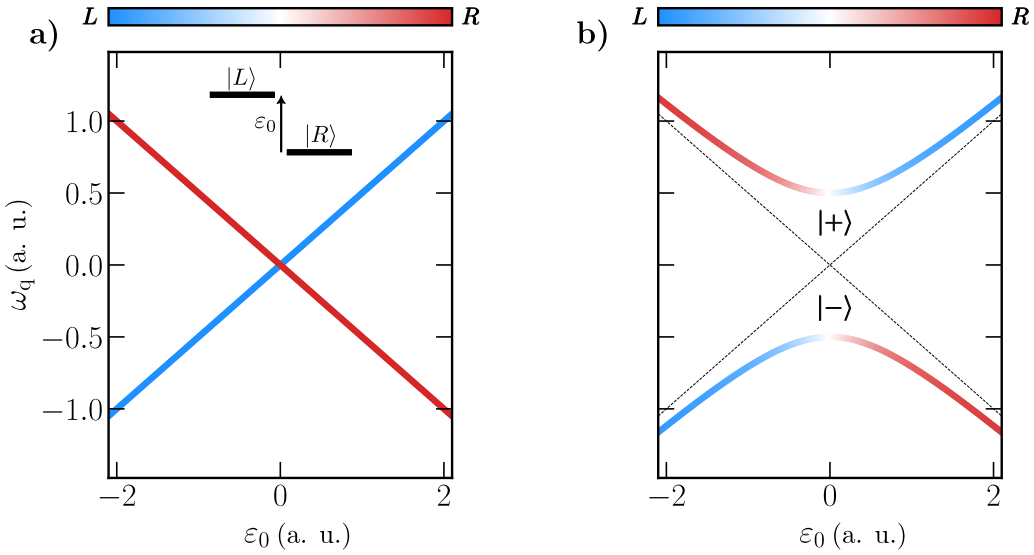

Figure 2.9: Static spectrum of a charge qubit with Larmor frequency at zero detuning ω_{q}. The energy levels ε are plotted in function of the detuning ε_0 considering $t_{\text{c}} = 0$ (a) and $t_{\text{c}} \neq 0$ (b). The colorbar shows the weights of the eigenstates in the $|L\rangle$ and $|R\rangle$ basis. All the axes are in arbitrary units.

either the left or the right dot. In this regime, the charge states of the DQD form a *charge qubit*[4].

Consider the states $|L\rangle$ and $|R\rangle$ localized on the left and right dots and detuned by the energy difference between the left (E_L) and right state (E_R), $\varepsilon_0 = E_L - E_R$ (Fig. (2.9)). Because the interdot barrier is finite, an electron can tunnel between the dots with amplitude t_c. In the basis of the localized states the Hamiltonian then reads

$$\mathcal{H}_{\rm sys}/\hbar = \frac{\varepsilon_0}{2}\tau_z + t_c\tau_x\,, \tag{2.96}$$

with $\tau_z = |L\rangle\langle L| - |R\rangle\langle R|$ and $\tau_x = |L\rangle\langle R| + |R\rangle\langle L|$.

As shown in Fig. (2.9), for vanishing tunneling the level spacing $E_L - E_R$ is exactly ε_0 and the levels cross at $\varepsilon_0 = 0$, which is a degenerate point of the spectrum. For non-zero coupling, the "anticrossing" occurs: the tunneling lifts the degeneracy at the crossing and the Hamiltonian reads

$$\mathcal{H}_{\rm sys} = \frac{\hbar\omega_{\rm q}(\varepsilon_0)}{2}\sigma_z\,, \tag{2.97}$$

with $\sigma_z = |+\rangle\langle +| - |-\rangle\langle -|$ with

$$|+\rangle = \cos\left(\frac{\theta}{2}\right)|L\rangle + \sin\left(\frac{\theta}{2}\right)|R\rangle\,, \qquad |-\rangle = \cos\left(\frac{\theta}{2}\right)|L\rangle - \sin\left(\frac{\theta}{2}\right)|R\rangle\,, \tag{2.98}$$

with $\tan\theta = 2t_c/\varepsilon_0$ and Larmor frequency[5] $\omega_{\rm q}(\varepsilon_0) = \sqrt{\varepsilon_0^2 + 4t_c^2}$. The anticrossing becomes a *sweet spot* for noise. This means that small variations of the detuning, due to voltage fluctuations, do not change the Larmor frequency at first order. Indeed, the Larmor frequency reads which has a stationary point $\partial_{\varepsilon_0}\omega_{\rm q} = 0$ at $\varepsilon_0 = 0$. The *sweet spot* is therefore the optimal working point to excite the atom, since the Larmor frequency there is less sensitive to noise. At this point, the eigenstates are the bonding and antibonding[6] mixture $|+\rangle$ and $|-\rangle$

$$|+\rangle = \frac{1}{\sqrt{2}}(|L\rangle + |R\rangle)\,, \qquad |-\rangle = \frac{1}{\sqrt{2}}(|L\rangle - |R\rangle)\,, \tag{2.99}$$

This is the usual operating point that defines the two levels of the qubit.

2.4.2 Coupling of a double quantum dot to a resonator

In Figure 2.10, we illustrate how a DQD can be coupled to an on-chip resonator. Since the size of the DQD is much smaller than the wavelength of the electromagnetic waves inside the resonator, the interaction can be described within the electric dipole approximation by

$$\mathcal{H}_{\rm int} = -\vec{p}\cdot\vec{E}(x_{\rm DQD})\,, \tag{2.100}$$

where $\vec{p} = -e\vec{r}$ is the electric dipole moment operator, and $\vec{E}(x_{\rm DQD})$ is the electric field at the position $x_{\rm DQD}$ of the DQD. In the single-charge regime, the dipole operator is fully characterized by its matrix elements in the basis of the localized states $|L\rangle, |R\rangle$. Placing the origin at the midpoint of the dots and being d the distance between them, we have

$$\langle L|x|L\rangle = \int dx|L(x)|^2 x \approx -\frac{d}{2}\,, \qquad \langle R|x|R\rangle \approx \frac{d}{2}\,. \tag{2.101}$$

[4]More generally, the term charge qubit denotes any two-level system whose logical states differ primarily in their charge distribution including superconducting island devices such as the Cooper-pair box.

[5]The DQD charge qubit Hamiltonian is equivalent to the Hamiltonian $\hbar\boldsymbol{\tau}\cdot\boldsymbol{\Omega}/2$ of an effective spin-1/2 where the Pauli vector $\boldsymbol{\tau}$ precesses around an effective magnetic field $\boldsymbol{\Omega} = (2t_c, 0, \varepsilon_0)$ with Larmor frequency $\omega_{\rm q} = |\boldsymbol{\Omega}|$.

[6]In chemistry usually $t < 0$, so the symmetric state $|+\rangle$ is actually the ground state, hence the term "bonding".

For the other brakets, we remark that a symmetric well, which implies zero detuning, imposes a parity symmetry. Being Π the parity operator, defined by $\Pi x \Pi = -x$, we have $\langle L|x|R\rangle = \langle R|\,\Pi x \Pi\,|L\rangle = -\langle L|\,x\,|R\rangle^*$, which breaks hermiticity unless $\langle L|x|R\rangle = 0$.

Thus, we can write the dipole moment as

$$\vec{p} = -\frac{ed}{2}\tau_z \vec{x}\,, \tag{2.102}$$

where $\vec{x}$ is a unit vector oriented from L to R.

For the electric field, it is proportional to the resonator voltage at x_{DQD} [68, 69]. From (2.26) in the limit of a single mode resonator, we obtain

$$\vec{E}(x_{\mathrm{DQD}}) \propto E_0 \left(a^\dagger + a\right) \cos\left(\frac{\omega_\mathrm{r}}{v} x_{\mathrm{DQD}}\right) \vec{n}\,, \tag{2.103}$$

where $\vec{n}$ is the normal vector to the central conductor of the CPW.

Finally, the dipole interaction in (2.100) reads

$$\mathcal{H}_{\mathrm{int}} = \hbar g_\perp \left(a + a^\dagger\right) \tau_z\,, \tag{2.104}$$

where the strength of the interaction is given by

$$\hbar g_\perp = \frac{d}{2} e E_0 \cos\left(\frac{\omega_\mathrm{r}}{v} x_{\mathrm{DQD}}\right) \vec{x}\cdot\vec{n}\,. \tag{2.105}$$

This suggests that, in order to maximize the strength of the interaction, the dot should be placed at an antinode of the electric field with the dipole oriented such that the electric field could move the charges inside the DQD.

Finally, in the basis of the qubit eigenstates, the dipole interaction (2.104) contains both a transverse and a static longitudinal component,

$$\mathcal{H}_{\mathrm{int}} = \hbar \frac{\varepsilon_0}{\omega_\mathrm{q}(\varepsilon_0)} g_\perp \left(a + a^\dagger\right) \sigma_z + \hbar \frac{2t_c}{\omega_\mathrm{q}(\varepsilon_0)} g_\perp \left(a + a^\dagger\right) \sigma_x\,, \tag{2.106}$$

with the static longitudinal component vanishing at the sweet spot ($\varepsilon_0 = 0$).

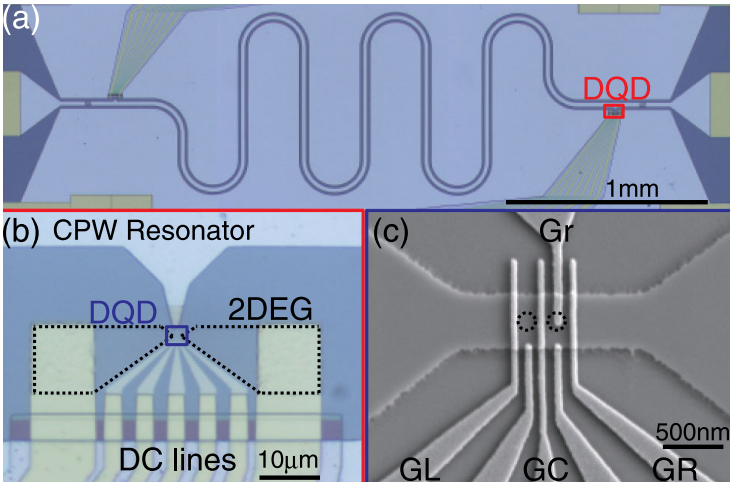

Figure 2.10: A double quantum dot coupled to a resonator in a hybrid cQED setup. (a) Optical microscope image of the coupled DQD-CPW resonator system. The location where the DQD is coupled is marked by the red square, the zoomed version of which is shown in (b). (c) It is a scanning electron microscope image of the DQD, defined by biasing metal gates GL (left), GC (center), and GR (right). The right QD is coupled to the resonator. Figure adapted from [67].

2.5 Chapter 2 in a nutshell

In this chapter, we discussed readout in a cQED platform using feedlines and resonators. With capacitive coupling between the feedline and the resonator, one obtains the standard input-output relation

$$b_{out} = b_{in} - i\sqrt{\kappa}a\,, \tag{2.107}$$

which links the output field to the input field and the intracavity field a (with κ the decay rate due to the coupling). For a geometry with left and right propagating modes and symmetric coupling, this reads

$$\overset{\leftarrow}{b}_{out}(t) = \overset{\leftarrow}{b}_{in}(t) - i\sqrt{\frac{\kappa}{2}}a(t)\,. \tag{2.108}$$

To solve the resonator's equations of motion, it is convenient to get an effective description of the feedline. Tracing out the quantum fluctuation of the line, we have seen that the feedline enters the equations of motion as an effective coherent drive

$$\mathcal{H}_{\text{drive}} = \hbar A_{\text{r}} \cos\left(\omega_{\text{r}} t + \phi\right)\left(a + a^\dagger\right)\,, \tag{2.109}$$

and as a Lindlbad dissipator

$$\mathcal{D}_a[\rho] = a\rho a^\dagger - \frac{1}{2}\left\{a^\dagger a, \rho\right\}\,, \tag{2.110}$$

which captures energy leakage from the resonator into the line. We have learned that a charge qubit can be operated at its sweet spot, where it is more robust to charge noise. When coupled to a resonator to enable readout in this regime, the interaction takes the form

$$\mathcal{H}_{\text{int}} = \hbar g_\perp \left(a + a^\dagger\right)\sigma_x\,. \tag{2.111}$$

These elements will be central to the next chapter, where we introduce readout protocols leveraging this interaction.

Chapter

3 cQED readout protocols in qubits

Contents

3.1 Dispersive readout 32
3.1.1 Dispersive regime 32
3.1.2 Semiclassical approach 34
3.1.3 Review of a classical harmonic oscillator 36
3.2 Field detection and quality of readout 39
3.2.1 Homodyne and heterodyne detection 40
3.2.2 Signal-to-noise ratio 40
3.3 Longitudinal readout 41
3.3.1 Ideal longitudinal coupling 42
3.3.2 Synthetic longitudinal coupling 42
3.4 Analytical integration of the equations of motion 46
3.5 Chapter 3 in a nutshell 48

Improving and speeding-up readout is a key asset for the development of quantum architectures. In the context of circuit quantum electrodynamics (cQED) [50], measurements of the σ_z state of a qubit traditionally rely on dispersive readout [24]. As we have seen in Sec. 2.4, the two levels of an artificial atom exchange virtual excitations with a microwave resonator through the coupling (we set $\hbar = 1$)

$$\mathcal{H}_\perp = g_\perp(a + a^\dagger)\sigma_x \,, \tag{3.1}$$

where $a^{(\dagger)}$ annihilates (creates) photons in the resonator. In the dispersive regime, the transverse coupling 3.1 induce a shift $\chi\sigma_z$ of the cavity resonance frequency, where χ is the dispersive coupling, , enabling quantum non-demolition (QND) measurements. When the resonator gets populated by a drive, as shown in Fig. 3.1a, the dynamics is affected by the dispersive shift and the state of the qubit is revealed. The separation between pointer states increase with the power applied to the resonator grows with time, but it remains independent of the qubit state at short time, as captured by Fig. 3.1a.

Recently, a modulation of the longitudinal interaction [70, 71]

$$\mathcal{H}_\parallel = g_\parallel(t)(a + a^\dagger)\sigma_z \tag{3.2}$$

has emerged as an alternative solution for faster QND readout [29–32], where its strength $g_\parallel$ is the *longitudinal coupling*. As illustrated in Fig. 3.1b, the coupling 3.2 displaces the resonator along qubit-state dependent trajectories that evolve in opposite directions in the phase space. This increases the rate of separation between pointer states and enables faster readout at short times.

While longitudinal coupling is ideal for fast readout, it does not arise naturally from the dipolar interaction between the resonator and the qubit. An identified mechanism to parametrically

engineer the interaction (3.2) is sketched in Fig. 3.1b. Driving the qubit of Larmor frequency $\omega_{\rm q}$ at the resonator frequency $\omega_{\rm r}$ triggers a σ_z-dependent displacement of the resonator.

In this chapter, we develop the standard tools needed to understand both dispersive and longitudinal readout. In Sec. 3.1, we use a Schrieffer-Wolff [72] transformation to derive the dispersive shift and Purcell effect.

Section 3.3 is dedicated to the discussion of longitudinal readout. We show that, while in the adiabatic regime ($\omega_{\rm r} \ll \omega_{\rm q}$), $g_{\parallel}$ connects to the static curvature $\partial^2\omega_q/\partial\varepsilon_0^2$ of the qubit's Larmor frequency [73–77], it connects to the dispersive shift χ in the dispersive regime ($|\omega_{\rm r}-\omega_{\rm q}| \gg g_{\perp}$) [78].

Finally, Sec. 3.4 derives the analytical equation of motion for the cavity field operator.

3.1 Dispersive readout

In this Section we provide an overview of dispersive readout.

As discussed in Sec. 2.4, the dipolar coupling between a charge qubit of frequency $\omega_{\rm q}$ and a microwave resonator of frequency $\omega_{\rm r}$ comprises a transverse interaction of strength $g_{\perp}$ and a static longitudinal interaction, which vanishes at the qubit sweet spot. When qubit and resonator are sufficiently detuned, $|\omega_{\rm q}-\omega_{\rm r}| \gg g_{\perp}$, the system enters the dispersive regime (Sec. 3.1.1). In this limit, the eigenstates of the system are dressed by the transverse interaction, which produces a qubit-dependent shift of the resonator frequency and Purcell effect.

As shown in Fig. 3.1a, dispersive readout is performed exploiting this state-dependent frequency shift by driving the resonator with an external microwave field of amplitude $A_{\rm r}$ (see Sec. 2.3.3). In Sec. 3.1.2, we show that if the qubit is in an eigenstate, the resulting dynamics is well described by a semiclassical theory. Since the effective Hamiltonian reduces to a driven, damped oscillator, Sec. 3.1.3 review its classical equation of motion.

3.1.1 Dispersive regime

In this Section we derive the effective Hamiltonian in the dispersive regime at the operating point of the qubit, the sweet spot. While this might seem to reduce generality, Appendix C.1 shows that the discussion below holds also at finite detuning with a renormalized coupling $g_{\perp}$.

At the sweet spot, the Hamiltonian of the coupled system reads

$$H = \frac{\omega_q}{2}\sigma_z + g_{\perp}\left(a + a^{\dagger}\right)\sigma_x + \omega_r a^{\dagger}a\,. \tag{3.3}$$

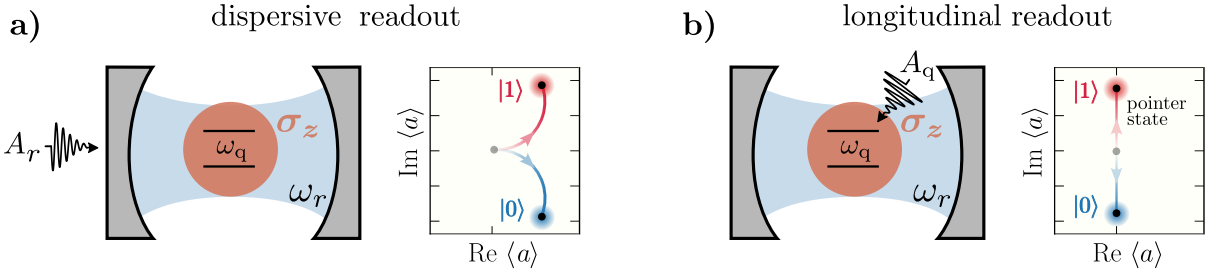

Figure 3.1: A qubit interacts with a resonator with resonant frequency $\omega_{\rm r}$ via a transverse coupling. a) Dispersive readout is achieved by probing the cavity with a signal with amplitude $A_{\rm r}$. b) An effective longitudinal coupling emerges when the qubit is driven by a signal of amplitude $A_{\rm q}$ that is resonant with the cavity. The phase-space trajectories are shown in a frame rotating at the cavity frequency.

When qubit and resonator are sufficiently detuned, $|\omega_\mathrm{q} - \omega_\mathrm{r}| \gg g_\perp$, the system enters the dispersive regime, in which the interaction leads to a qubit-state-dependent frequency shift $\chi\sigma_z$ of the resonator. This shift is obtained by applying the Schrieffer-Wolff transformation (see Appendix C.1)

$$U = e^{i\mathcal{S}}\,, \qquad i\mathcal{S} = \frac{g_\perp}{\omega_\mathrm{q} - \omega_\mathrm{r}}(a\sigma_+ - a^\dagger\sigma_-) + \frac{g_\perp}{\omega_\mathrm{q} + \omega_\mathrm{r}}(a^\dagger\sigma_+ - a\sigma_-)\,, \tag{3.4}$$

to H and expanding up to second order in $g_\perp$, which yields (see Appendix C.1)

$$H_\mathrm{disp} = UHU^\dagger = \frac{\omega_q + \chi}{2}\sigma_z + (\omega_r + \chi\sigma_z)\, a^\dagger a\,, \tag{3.5}$$

where the dispersive shift χ is given by

$$\chi = g_\perp^2\left(\frac{1}{\omega_\mathrm{q} - \omega_\mathrm{r}} + \frac{1}{\omega_\mathrm{q} + \omega_\mathrm{r}}\right) = 2g_\perp^2\frac{\omega_\mathrm{q}}{\omega_\mathrm{q}^2 - \omega_\mathrm{r}^2}\,. \tag{3.6}$$

We remark that this expression contains the Bloch-Siegert shift $\delta\omega_\mathrm{BS} = g_\perp^2\,(\omega_\mathrm{q} + \omega_\mathrm{r})^{-1}$, that is usually neglected if $|\omega_\mathrm{q} + \omega_\mathrm{r}| \gg |\omega_\mathrm{q} - \omega_\mathrm{r}|$ (in the rotating wave approximation).

Critical number of photons n_crit The general SW expansion in Eq. (3.5) is a perturbative series in powers of $\left|[\mathcal{S}, g_\perp\left(a + a^\dagger\right)\sigma_x]\right|$ which must remain small compared to the interaction itself, $\left|[\mathcal{S}, g_\perp\left(a + a^\dagger\right)\sigma_x]\right| \ll \left|g_\perp\left(a + a^\dagger\right)\sigma_x\right|$. This condition reduces to

$$\frac{2g_\perp\sqrt{n}}{\omega_\mathrm{q} - \omega_\mathrm{r}} \ll 1\,,$$

which defines the validity range of the dispersive approximation. Consequently, the critical photon number above which the perturbative expansion breaks down is $n_\mathrm{crit} = (\omega_\mathrm{q} - \omega_\mathrm{r})^2/4g_\perp^2$. Above this limit, higher-order terms in the Schrieffer–Wolff transformation become comparable to those retained, and the simple dispersive picture fails as the system transitions toward the strong hybridization regime.

Purcell effect As the coupling between a feedline and a resonator induces losses in the resonator, the coupling between the resonator and the qubit induces a dissipation in the qubit that takes the name of Purcell effect. We analyze this in the frame defined by the SW transformation, where the density matrix becomes

$$\rho_\mathrm{disp}(t) = U\rho(t)U^\dagger\,,$$

The master equation transforms as

$$\begin{aligned}\partial_t\rho_\mathrm{disp}(t) &= -i\left[UHU^\dagger, \rho_\mathrm{disp}\right] + \kappa U\mathcal{D}_a\left[\rho\right]U^\dagger \\ &= -i\left[H_\mathrm{disp}, \rho_\mathrm{disp}\right] + \kappa\mathcal{D}_{UaU^\dagger}\left[\rho_\mathrm{disp}\right]\,.\end{aligned}$$

To first order in $g_\perp$

$$U\,a\,U^\dagger = a + \frac{g_\perp}{\omega_q - \omega_r}\,\sigma_- - \frac{g_\perp}{\omega_q + \omega_r}\,\sigma_+ + \mathcal{O}\left(g_\perp^2\right)\,, \tag{3.7}$$

Substituting into the dissipator generates an additional qubit decay channel $\mathcal{D}_{\sigma_-}$, mixed "cross" terms oscillating at $\pm(\omega_\mathrm{q}-\omega_\mathrm{r})$ and a counter-rotating channel $\mathcal{D}_{\sigma_+}$. Neglecting fast oscillating cross terms and the counter-rotating contribution, the dissipator separates into independent channels

$$\kappa\mathcal{D}_{UaU^\dagger}\left[\rho_\mathrm{disp}\right] \approx \kappa\mathcal{D}_a\left[\rho_\mathrm{disp}\right] + \gamma\mathcal{D}_{\sigma_-}\left[\rho_\mathrm{disp}\right], \tag{3.8}$$

with the Purcell relaxation rate

$$\gamma = \kappa\left(\frac{g_\perp}{\omega_q-\omega_r}\right)^2, \tag{3.9}$$

which quantifies the qubit decay induced by the resonator.

3.1.2 Semiclassical approach

In this section, we show that when the qubit state is read out by driving the resonator with an external microwave field (Fig. 3.1a), the cavity follows a semiclassical equation of motion.

As discussed in Sec. 2.3.3, the drive introduces a term $A_\mathrm{r}\cos(\omega_\mathrm{r}t+\varphi)(a+a^\dagger)$ in the Hamiltonian, such that, considering the two quadratures of the fields $x=(a+a^*)/\sqrt{2}$ and $p=-i(a-a^*)/\sqrt{2}$, the Hamiltonian describes the dynamics of a driven oscillator

$$H_\mathrm{disp} = \frac{\omega_q+\chi}{2}\sigma_z + (\omega_r+\chi\sigma_z)\,a^\dagger a + \sqrt{2}A_\mathrm{r}\cos(\omega_\mathrm{r}t+\varphi)x \tag{3.10}$$

$$= \frac{\omega_q+\chi}{2}\sigma_z + \frac{1}{2}(\omega_r+\chi\sigma_z)\left(x^2+p^2\right) + \sqrt{2}A_\mathrm{r}\cos(\omega_\mathrm{r}t+\varphi)x\,. \tag{3.11}$$

The rotating frame We first eliminate the explicit time dependence by moving to the frame rotating at the cavity frequency defined by the unitary operator $\mathcal{U}_0(t)=e^{-i\omega_r t a^\dagger a}$. Neglecting the fast oscillating terms (rotating wave approximation), the Hamiltonian reads

$$H'_\mathrm{disp} = \frac{\omega_q+\chi}{2}\sigma_z + \chi a^\dagger a\sigma_z - i\frac{A_\mathrm{r}}{2}(a-a^\dagger)\,. \tag{3.12}$$

In such rotating frame, the density matrix becomes

$$\rho'_\mathrm{disp}(t) = \mathcal{U}_0^\dagger(t)\rho_\mathrm{disp}(t)\mathcal{U}_0(t)\,,$$

such that the master equation transforms as

$$\partial_t\rho'_\mathrm{disp}(t) = -i\left[H'_\mathrm{disp},\rho'_\mathrm{disp}\right] + \kappa\mathcal{D}_{\mathcal{U}^\dagger a\mathcal{U}}\left[\rho'_\mathrm{disp}\right] + \gamma\mathcal{D}_{\sigma_-}\left[\rho'_\mathrm{disp}\right], \tag{3.13}$$

where the rotated dissipator describes the losses of the resonator due to external degrees of freedom coupled to the resonator (see Sec. 2.3.3). Using $\mathcal{U}^\dagger a\mathcal{U} = ae^{-i\omega_\mathrm{r}t}$, we obtain that the dissipator is invariant under the rotation

$$\mathcal{D}_{\mathcal{U}_0^\dagger a\mathcal{U}_0}\left[\rho'_\mathrm{disp}\right] = a\rho'_\mathrm{disp}a^\dagger - \frac{1}{2}\left\{a^\dagger a,\rho'_\mathrm{disp}\right\} = \mathcal{D}_a\left[\rho'_\mathrm{disp}\right]. \tag{3.14}$$

Semiclassical theory To demonstrate that the cavity dynamics is semiclassical, we introduce an Ansatz for the density matrix in the dispersive frame which consists of an incoherent mixture of coherent pointer states $|\alpha'_\sigma(t)\rangle$,

$$\rho'_\mathrm{disp} = \sum_{\sigma=\pm} p_\sigma(t)\,|\sigma\rangle\langle\sigma|\otimes\rho_\sigma(t)\,, \qquad \rho_\sigma(t) = |\alpha'_\sigma(t)\rangle\langle\alpha'_\sigma(t)|\,, \tag{3.15}$$

where $|\sigma = \pm\rangle$ are the eigenstate of σ_z with eigenvalue $\sigma = \pm 1$, and $|\alpha'(t)\rangle = \mathbf{D}(\alpha'(t))\,|0\rangle$ is a coherent state defined through the displacement operator

$$\mathbf{D}(\alpha) = e^{\alpha a^\dagger - \alpha^* a} = e^{\alpha a^\dagger} e^{-\alpha^* a} e^{-\frac{1}{2}\alpha\alpha^*}\,,$$

which satisfies the following properties

$$a\,|\alpha\rangle = \alpha\,|\alpha\rangle\,, \qquad \partial_\alpha\,|\alpha\rangle = \left(a^\dagger - \frac{1}{2}\alpha^*\right)|\alpha\rangle\,, \qquad \partial_{\alpha^*}\,|\alpha\rangle = -\frac{\alpha}{2}\,|\alpha\rangle\,. \tag{3.16}$$

Taking the time derivative of the Ansatz (3.15) gives

$$\partial_t \rho'_{\text{disp}} = \sum_{\sigma=\pm} |\sigma\rangle\langle\sigma| \otimes [p_\sigma(t)\partial_t \rho_\sigma(t) + \rho_\sigma(t)\partial_t p_\sigma(t)]\,, \tag{3.17}$$

and using the identities (3.16), we find

$$\begin{aligned}
\partial_t \rho_\sigma(t) &= |\sigma\rangle\langle\sigma| \otimes \left(\dot\alpha'_\sigma \partial_{\alpha'_\sigma} + \dot\alpha'^*_\sigma \partial_{\alpha'^*}\right)\left(|\alpha'_\sigma(t)\rangle\langle\alpha'_\sigma(t)|\right) \\
&= |\sigma\rangle\langle\sigma| \otimes \left(\dot\alpha'_\sigma \left(a^\dagger - \alpha'^*_\sigma\right)|\alpha'_\sigma(t)\rangle\langle\alpha'_\sigma(t)| + \dot\alpha'^*_\sigma\,|\alpha'_\sigma(t)\rangle\langle\alpha'_\sigma(t)|\,(a - \alpha'_\sigma)\right) \\
&= |\sigma\rangle\langle\sigma| \otimes \left(\dot\alpha'_\sigma a^\dagger\,|\alpha'_\sigma(t)\rangle\langle\alpha'_\sigma(t)| - \dot\alpha_\sigma\,|\alpha'_\sigma(t)\rangle\langle\alpha'_\sigma(t)|\,a^\dagger + \text{h. c.}\right) \\
&= \left[a^\dagger, \rho_\sigma(t)\right]\dot\alpha'_\sigma - [a, \rho_\sigma(t)]\,\dot\alpha'^*_\sigma\,,
\end{aligned} \tag{3.18}$$

We compare the time derivative of the Ansatz with the master equation

$$\partial_t \rho'_{\text{disp}}(t) = \mathcal{L}_{\gamma=0}\left[\rho'_{\text{disp}}\right] + \gamma \mathcal{D}_{\sigma_-}\left[\rho'_{\text{disp}}\right]\,, \tag{3.19}$$

where we have introduced

$$\mathcal{L}_{\gamma=0}\,[\cdot] = -i[H'_{\text{disp}}, \cdot] + \kappa \mathcal{D}_a[\cdot]\,.$$

Substituting the Ansatz in the master equation gives

$$\partial_t \rho'_{\text{disp}} = \sum_{\sigma=\pm} p_\sigma(t)\mathcal{L}_{\gamma=0}\left[|\sigma\rangle\langle\sigma| \otimes \rho_\sigma\right] + \gamma \sum_{\sigma=\pm} p_\sigma(t)\mathcal{D}_{\sigma_-}\left[|\sigma\rangle\langle\sigma|\right]\rho_\sigma\,. \tag{3.20}$$

The first term yields

$$\begin{aligned}
\mathcal{L}_{\gamma=0}[|\sigma\rangle\langle\sigma| \otimes \rho_\sigma] &= -i\left[\frac{\omega_q + \chi}{2}\sigma_z + \chi a^\dagger a \sigma_z - i\frac{A_\text{r}}{2}(a - a^\dagger), \rho_\sigma\right] + \kappa \mathcal{D}_a[\rho_\sigma] \\
&= -i\chi\left[a^\dagger a, \rho_\sigma\right]\sigma - \frac{A_\text{r}}{2}\left[a - a^\dagger, \rho_\sigma\right] + \kappa a \rho_\sigma a^\dagger - \frac{\kappa}{2}\left(a^\dagger a \rho_\sigma + \text{h. c.}\right) \\
&= \left[a^\dagger, \rho_\sigma\right]\left(-i\chi\alpha'_\sigma\sigma + \frac{A_\text{r}}{2} - \frac{\kappa}{2}\alpha'\right) + \text{h. c.}\,,
\end{aligned} \tag{3.21}$$

while the second term yields

$$\gamma \sum_{\sigma=\pm} p_\sigma(t)\mathcal{D}_{\sigma_-}\left[|\sigma\rangle\langle\sigma|\right]\rho_\sigma = \gamma p_+(t)\left[|-\rangle\langle-|\,\rho_- - |+\rangle\langle+|\,\rho_+\right]\,.$$

Comparing these two terms with the derivative of the Ansatz (3.17), we see that the Ansatz satisfies the master equation if and only if

$$\partial_t \alpha'_\sigma(t) = -i\chi\alpha'_\sigma\sigma + \frac{A_\text{r}}{2} - \frac{\kappa}{2}\alpha'_\sigma\,, \tag{3.22}$$

$$\partial_t p_+(t) = -\gamma p_+(t)\,, \tag{3.23}$$

$$\partial_t p_-(t) = \gamma p_+(t)\,, \tag{3.24}$$

Solving the coupled equations for p_+, p_- yields

$$p_+(t) = p_+(0)e^{-\gamma t}\,, \qquad\qquad p_-(t) = 1 - p_+(0)e^{-\gamma t}\,, \tag{3.25}$$

from which we obtain

$$\langle\sigma_z(t)\rangle = p_+(t) - p_-(t) = -1 + \left(\langle\sigma_z(0)\rangle + 1\right) e^{-\gamma t}\,. \tag{3.26}$$

This also implies that the time evolution of $\langle a(t)\rangle = \mathrm{Tr}\left\{\rho'(t)a(t)\right\} = \langle\alpha'(t)\rangle$ is given by

$$\partial_t\alpha'_\sigma(t) = -i\left\langle\sigma\left|\frac{\partial H'_{\mathrm{disp}}(\alpha'_\sigma,\alpha'^*_\sigma)}{\partial\alpha'^*_\sigma}\right|\sigma\right\rangle - \frac{\kappa}{2}\alpha'_\sigma(t)\,, \tag{3.27}$$

where $H'_{\mathrm{disp}}(\alpha'_\sigma,\alpha'^*_\sigma)$ is the normal ordered (all the powers of $a^\dagger$ preceding those of a) dispersive Hamiltonian with the operators a and $a^\dagger$ replaced by the canonical variables α'_σ and α'^*_σ.

3.1.3 Review of a classical harmonic oscillator

To show that Eq. (3.27) is the equation of motion motion for a classical forced and damped harmonic oscillator in a frame rotating at the cavity frequency, we review here key aspects of classical mechanics related to that model. The Hamiltonian of a classical one-dimensional harmonic oscillator of unit mass $m = 1$, subjected to an external periodic driving force, is given by

$$H(x(t),p(t),t) = \frac{1}{2}\left(x^2+p^2\right)\omega_0 + \sqrt{2}A_{\mathrm{r}}\cos(\omega_{\mathrm{r}}t+\varphi)\,x\,, \tag{3.28}$$

where x and p are the normalized canonical position and momentum, ω_0 is the frequency of the oscillator, A_{r} is the amplitude of the driving force, and ω its frequency.

Poisson Brackets The classical equations of motion are derived from the Hamiltonian using Poisson brackets. Indeed for any function $f(x(t),p(t))$ of the canonical variables the classical analogue of the Heisenberg equation of motion is given by

$$\frac{d}{dt}f(x(t),p(t)) = \{f,H\}_{x,p}\,, \tag{3.29}$$

where the Poisson bracket is defined as

$$\{f,g\}_{x,p} = \frac{\partial f}{\partial x}\frac{\partial g}{\partial p} - \frac{\partial f}{\partial p}\frac{\partial g}{\partial x}\,. \tag{3.30}$$

Applying this to x and p, we recover the canonical relations $\{x,p\} = 1$, $\{x,x\} = \{p,p\} = 0$.

Equations of motion Hamilton's equations follow from (3.29) and take the form

$$\dot{x} = \{x,H\} = \frac{\partial H}{\partial p} = \omega_0 p\,, \tag{3.31}$$

$$\dot{p} = \{p,H\} = -\frac{\partial H}{\partial x} = -\omega_0 x - A_{\mathrm{r}}\cos(\omega t+\varphi)\,. \tag{3.32}$$

Combining these equations yields the second-order differential equation

$$\ddot{x} = -\omega_0^2 x - \omega_0\sqrt{2}A_{\mathrm{r}}\cos(\omega_{\mathrm{r}}t+\varphi)\,, \tag{3.33}$$

which describes a linearly forced harmonic oscillator.

To solve the equation of motions it is useful to introduce the complex variables

$$\alpha = \frac{x+ip}{\sqrt{2}}\,, \qquad\qquad \alpha^* = \frac{x-ip}{\sqrt{2}}\,.$$

One can verify that the variables α and $i\alpha^*$ form another pair of canonical variables, as follows from the Poisson bracket

$$\{\alpha,\alpha\}_{x,p} = -i\,.$$

This canonical transformation allows us to rewrite Eq. (3.29) in terms of α and α^* as

$$\frac{d}{dt}f(\alpha(t),\alpha^*(t)) = -i\,\{f,H\}_{\alpha.\alpha^*}\,, \tag{3.34}$$

where the Hamiltonian, expressed in the variables α and α^*, takes the form

$$H(\alpha,\alpha^*,t) = \omega_0\alpha\alpha^* + A_\mathrm{r}\cos(\omega_\mathrm{r}t+\varphi)\,(\alpha+\alpha^*)\,.$$

From Eq. (3.34), the equation of motion of $\alpha(t)$ reads

$$\partial_t\alpha = -i\omega_0\alpha - iA_\mathrm{r}\cos(\omega_\mathrm{r}t+\varphi)\,. \tag{3.35}$$

The solution to Eq. (3.35) is obtained by first considering the homogenous solution $\alpha(t) = \vartheta e^{-i\omega_0 t}$. Employing the method of variation of constants, we write the general solution as

$$\alpha(t) = \vartheta(t)e^{-i\omega_0 t} \qquad \text{with} \qquad \vartheta(t) = \vartheta(0) - iA_\mathrm{r}\int_0^t dt'\cos(\omega_\mathrm{r}t'+\varphi)e^{i\omega_0 t'}\,. \tag{3.36}$$

Evaluating the integral we obtain

$$\vartheta(t) = \vartheta(0) - \frac{A_\mathrm{r}}{2}\left[\frac{e^{i\varphi}\big(e^{i(\omega_0+\omega_\mathrm{r})t}-1\big)}{\omega_0+\omega_\mathrm{r}} + \frac{e^{-i\varphi}\big(e^{i(\omega_0-\omega_\mathrm{r})t}-1\big)}{\omega_0-\omega_\mathrm{r}}\right],$$

which, neglecting the rapidly oscillating terms proportional to $(\omega_0+\omega_\mathrm{r})^{-1}$ (rotating wave approximation), simplifies to

$$\vartheta(t) = \vartheta(0) - e^{-i\varphi}\frac{A_\mathrm{r}}{2}\frac{1}{(\omega_0-\omega_\mathrm{r})}\left(e^{i(\omega_0-\omega_\mathrm{r})t}-1\right). \tag{3.37}$$

The complete solution can then be written as

$$\alpha(t) = \alpha'(t)e^{-i\omega_\mathrm{r}t}\,, \qquad \alpha'(t) = \alpha'(0)e^{-i(\omega_0-\omega_\mathrm{r})t} - e^{-i\varphi}\frac{A_\mathrm{r}}{2}\frac{1}{(\omega_0-\omega_\mathrm{r})}(1-e^{-i(\omega_0-\omega_\mathrm{r})t})\,, \tag{3.38}$$

where $\alpha'(t)$ is a slowly varying field in the near-resonant regime $\omega_0 \sim \omega_\mathrm{r}$.

Rotating frame The evolution of $\alpha'(t)$ describes the motion of the spring in a frame rotating at frequency ω_r, defined via the canonical transformation

$$\begin{pmatrix}\alpha\\ i\alpha^*\end{pmatrix} = \begin{pmatrix}e^{-i\omega_\mathrm{r}t} & 0\\ 0 & e^{i\omega_\mathrm{r}t}\end{pmatrix}\begin{pmatrix}\alpha'\\ i\alpha'^*\end{pmatrix}, \tag{3.39}$$

which corresponds, for canonical variables x and p, to

$$\begin{pmatrix} x \\ p \end{pmatrix} = \mathcal{R}(\omega_{\rm r} t) \begin{pmatrix} x' \\ p' \end{pmatrix} , \qquad \mathcal{R}(\omega_{\rm r} t) = \begin{pmatrix} \cos(\omega_{\rm r} t) & \sin(\omega_{\rm r} t) \\ -\sin(\omega_{\rm r} t) & \cos(\omega_{\rm r} t) \end{pmatrix} . \tag{3.40}$$

This transformation can be interpreted either as an active rotation of the entire phase space, or as passive change of coordinates describing the same trajectory in a rotating reference frame (see Appendix B.1 for the discussion in quantum mechanics). It is generated by the type-II generating function [57] $F_2(\alpha, \alpha'^*, t)$

$$F_2(\alpha, \alpha'^*, t) = i\alpha'^* \alpha e^{i\omega_{\rm r} t} , \tag{3.41}$$

which satisfies

$$\frac{\partial F_2}{\partial \alpha} = i\alpha^* , \qquad \frac{\partial F_2}{\partial \left(i\alpha'^*\right)} = \alpha' , \tag{3.42}$$

In the rotating frame, the dynamics are governed by the effective Hamiltonian which reads, within the rotating wave approximation (RWA)

$$H'_{\rm cl} = H + \frac{\partial F_2}{\partial t} = (\omega_0 - \omega_{\rm r})\, \alpha'^* \alpha' + \frac{A_{\rm r}}{2} (\alpha' e^{i\varphi} + \alpha'^* e^{-i\varphi}) . \tag{3.43}$$

From Eq. (3.34), the equation of motion in the rotating frame is

$$\partial_t \alpha' = -i \left\{ \alpha', H'_{\rm cl} \right\}_{\alpha', \alpha'^*} = -i \frac{\partial H'_{\rm cl}}{\partial \alpha'^*} .$$

If $\omega_0 = \omega_{\rm r} + \chi\sigma$, we have $H'_{\rm cl} = \left\langle \sigma | H'_{\rm disp}(\alpha', \alpha'^*) | \sigma \right\rangle$, this is the semiclassical equation of motion (3.27) without dissipation. We are now left to demonstrate that the dissipative term also arises from a classical dissipation.

Dissipation To account for the energy losses of the oscillator, we consider an additional damping term $-\kappa p$ in Eq. (3.32). The equation of motion then takes the form

$$\dot{p} = \sqrt{2} A_{\rm r} \cos(\omega_{\rm r} t + \varphi) - (\omega_r + \chi\sigma_z)\, x - \kappa p ,$$

which corresponds to a forced damped harmonic oscillator. This modifies Eq. (3.35) as

$$\frac{d\alpha(t)}{dt} = -i\omega_0 \alpha - i A_{\rm r} \cos(\omega_{\rm r} t + \varphi) - \frac{\kappa}{2} (\alpha - \alpha^*) , \tag{3.44}$$

which, in terms of the slow-varying field $\alpha'(t)$, becomes

$$\frac{d\alpha'(t)}{dt} = -i\,(\omega_0 - \omega_{\rm r})\, \alpha' - i \frac{A_{\rm r}}{2} e^{-i\varphi} - \frac{\kappa}{2} \alpha' , \tag{3.45}$$

which is exactly Eq. (3.27) if $\omega_0 = \omega_{\rm r} + \chi\sigma$. Hence, our classical model exhibits the same equation of motion as the semiclassical theory, which in turn reproduces the dynamics of the quantum master equation, as discussed in the previous Section.

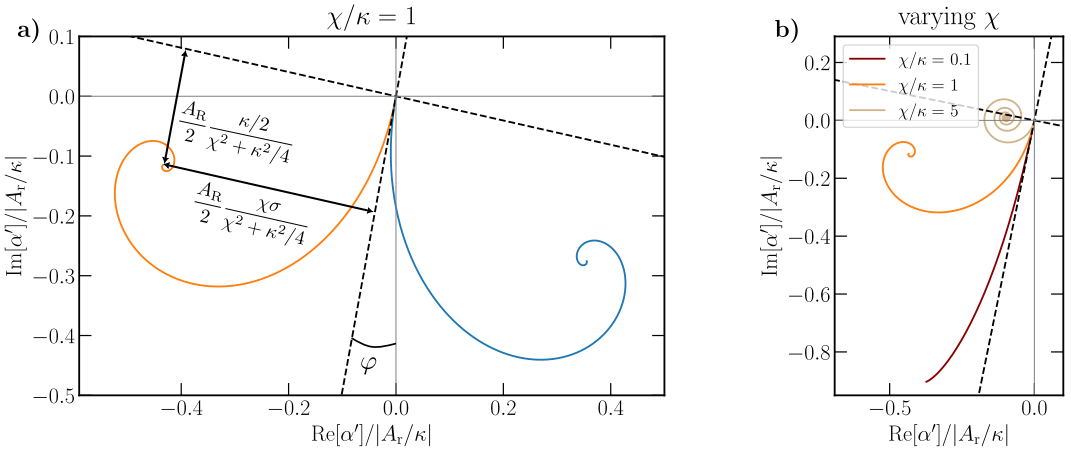

Figure 3.2: Dispersive readout. Time evolution of the cavity pointer states $\alpha'(t)$ as in Eq. (3.46) with $\varphi = 0.2$ and from $t = 0$ to $\kappa t = 10$. The dashed lines represents the real and imaginary axis rotated by an angle $-\varphi$. In a) the solution $\varphi = 0.2$ is obtained rotating the solution for $\varphi = 0$ clockwise by an angle φ. In b) the time evolution of $\alpha'(t)$ for different values of χ. As χ decreases, the steady state value approaches the (rotated) imaginary axis.

Dynamics in the phase space Within the RWA, the solution to this equation modifies (3.38) and reads

$$\alpha'_\sigma(t) = \alpha'_\sigma(0)e^{-i\chi\sigma t-\frac{\kappa}{2}t} - e^{-i\varphi}\frac{A_r}{2}\frac{1}{\chi\sigma - i\kappa/2}(1 - e^{-i\chi\sigma t-\frac{\kappa}{2}t}), \tag{3.46}$$

where we reintroduced the subscript σ to emphasize that α'_σ are the cavity pointer states. The corresponding dynamics in the phase space for different values of the detuning $\chi = \omega_0 - \omega_r$ is illustrated in Fig. 3.2b. As shown in Fig. 3.2, while in the steady state the pointer states approach

$$\mathrm{Re}\,\alpha'_\sigma(t) = \frac{A_r}{2}\frac{\kappa/2}{\chi^2+\kappa^2/4}e^{-i\varphi}, \qquad \mathrm{Im}\,\alpha'_\sigma(t) = \frac{A_r}{2}\frac{\chi\sigma}{\chi^2+\kappa^2/4}e^{-i\varphi}, \tag{3.47}$$

and are well separated, for short time the dynamics is qubit-independent

$$\alpha'_\sigma(t) = \frac{A_r}{2}\frac{1}{i\chi\sigma}(1 - e^{-i\chi\sigma t}) \xrightarrow[t\to 0]{} \frac{A_r}{2}t, \tag{3.48}$$

which is one of the main limitations of dispersive readout. It is worth remarking that the transformation $b' = \alpha' e^{i\varphi}$ maps the solution with arbitrary phase to the case $\varphi = 0$. Hence, the trajectory for a finite φ can be obtained by rotating the $\varphi = 0$ solution by an angle $-\varphi$ in the phase space, by a clockwise rotation of angle φ.

Conventionally, for dispersive readout this phase is set at $\varphi = -\pi/2$.

3.2 Field detection and quality of readout

In this section we discuss the homodyne and heterodyne methods for the detection of b_{out} (Sec. 3.2.1) and the signal-to-noise ratio, a figure of merit that measures the quality of the readout (Sec. 3.2.2).

3.2.1 Homodyne and heterodyne detection

Given a signal $s(t)$, its two quadratures are defined as

$$I(t) = \sqrt{2}\mathrm{Re}s(t) = \frac{s(t) + s^*(t)}{\sqrt{2}}\,, \qquad Q(t) = \sqrt{2}\mathrm{Im}s(t) = \frac{s(t) - s^*(t)}{\sqrt{2}i}\,. \tag{3.49}$$

which define the so-called IQ plane. To measure the two quadratures of $b_{out}(t)$ ($b^{\rightarrow}_{out}(t)$ for an infinite line), we use a beam-splitter (BS) to mix the signal with the local oscillator $\alpha_{LO}(t) = |\alpha_{LO}|\exp\left(-i\left(\omega_{LO}t + \phi\right)\right)$, as shown in Fig. 3.3. If T and R are the transmission and reflection coefficients of the BS, the two signals entering the BS become

$$b_+ = Tb_{out} + R\alpha_{LO}\,, \qquad b_- = Rb_{out} + T\alpha_{LO}\,. \tag{3.50}$$

Considering a balanced beam-splitter, $T = i/\sqrt{2}$ and $R = 1/\sqrt{2}$, we have

$$b_\pm = \frac{1}{\sqrt{2}}\left(b_{out} \pm \alpha_{LO}\right)\,. \tag{3.51}$$

The signals are then measured by a photo-detector and the net photo-current is

$$i \propto \left\langle b_+^\dagger b_+ - b_-^\dagger b_- \right\rangle = \alpha_{LO}^* \left\langle b_{out}\right\rangle + \alpha_{LO}\left\langle b_{out}^\dagger\right\rangle\,. \tag{3.52}$$

Since $b_{out}(t)$ is $b_{out}(t) = b'_{out}(t)e^{-i\omega_{\mathrm{r}}t}$, where $b'_{out}(t)$ is a slowly oscillating field, given $\Delta\omega = \omega_{LO} - \omega_{\mathrm{r}}$, the net photo-current reads

$$i \propto |\alpha_{LO}|\left(\left\langle b'_{out}(t)e^{i\Delta\omega t + i\phi} - b'^\dagger_{out}(t)e^{-i\Delta\omega t - i\phi}\right\rangle\right)\,. \tag{3.53}$$

By selecting a local frequency ω_{LO} small enough to facilitate the reasonable digitization of the signal, it is possible to extract both quadratures of the field. This detection technique is called *heterodyne detection* and allows the detection of both quadratures at the same time. We remark that the choice $\omega_{LO} = 0$ corresponds to *homodyne detection*. Taking $\phi = 0$ allows the detection of the in-phase quadrature I while $\phi = \pi/2$ leads to the orthogonal quadrature Q. Although this choice seems easier to implement, it permits the extraction of only one quadrature at a time.

3.2.2 Signal-to-noise ratio

This Section follows closely Ref. [79].

As we have seen, the measurement signal generally consists of an in-phase component (I) and an in-quadrature component (Q) of the output signal. Since the output field is related to the resonator field, this let us have access through Eq. (2.73) to the IQ quadratures of $\sqrt{\kappa}a$

$$V_{I,|i\rangle}(t) = V_0\left[\sqrt{2\kappa}\,\mathrm{Re}\Big(\alpha_{|i\rangle}(t)\Big) + n_I(t)\right]\,, \tag{3.54}$$

$$V_{Q,|i\rangle}(t) = V_0\left[\sqrt{2\kappa}\,\mathrm{Im}\Big(\alpha_{|i\rangle}(t)\Big) + n_Q(t)\right]\,, \tag{3.55}$$

where V_0 is an irrelevant gain factor and n_{IQ}, n_Q are independent Gaussian white noise terms with unit variance, $\langle n_j(t)\, n_k(t')\rangle = \delta_{jk}\,\delta(t - t')$. The resonator field $\alpha_{|i\rangle}$ is the expectation value of a when the qubit is in the eigenstate $|i\rangle$ and is called a *pointer state*.

For state discrimination, the two quadratures are each multiplied with weight functions, then summed and integrated over the measurement window of duration T

$$V_{\mathrm{int},|i\rangle} = \int_0^T \left(w_I V_{I,|i\rangle}(t) + w_Q V_{Q,|i\rangle}(t)\right) dt. \tag{3.56}$$

We define the signal S and the noise N as

$$S = \left| \left\langle V_{\text{int},|1\rangle} - V_{\text{int},|0\rangle} \right\rangle \right| , \qquad N^2 = \left\langle V^2_{\text{int},|i\rangle} \right\rangle - \left\langle V_{\text{int},|i\rangle} \right\rangle^2 . \tag{3.57}$$

Using the optimal weight functions

$$w_{I/Q} = \left\langle V_{I/Q,|1\rangle} - V_{I/Q,|0\rangle} \right\rangle , \tag{3.58}$$

we obtain the optimal signal and noise

$$S_{\text{opt}} = 2\kappa\, V_0^2 \int_0^T \left| \alpha_{|+\rangle}(t) - \alpha_{|-\rangle}(t) \right|^2 dt , \tag{3.59}$$

$$\begin{aligned} N^2_{\text{opt}} &= V_0^2 \left\langle \left(\int_0^T \left(w_I n_I + w_Q n_Q \right) dt \right)^2 \right\rangle \\ &= 2\kappa\, V_0^4 \int_0^T \left| \alpha_{|+\rangle}(t) - \alpha_{|-\rangle}(t) \right|^2 dt , \end{aligned} \tag{3.60}$$

such that the signal-to-noise ratio (SNR)

$$\text{SNR}_{\text{opt}}(T) = \frac{S_{\text{opt}}}{N_{\text{opt}}} = \sqrt{2\kappa \int_0^T \left| \alpha_{|+\rangle}(t) - \alpha_{|-\rangle}(t) \right|^2 dt} , \tag{3.61}$$

is maximized. The SNR is an important figure of merit which measures the quality of the readout. We will use it to compare the efficiency of dispersive and longitudinal readout.

3.3 Longitudinal readout

In this section we discuss longitudinal readout. In Sec. 3.3.1 we present ideal longitudinal readout, as first proposed in Ref. [29]. In Sec. 3.3.2 we discuss the protocol to synthetize a longitudinal coupling described in Fig. 3.1b.

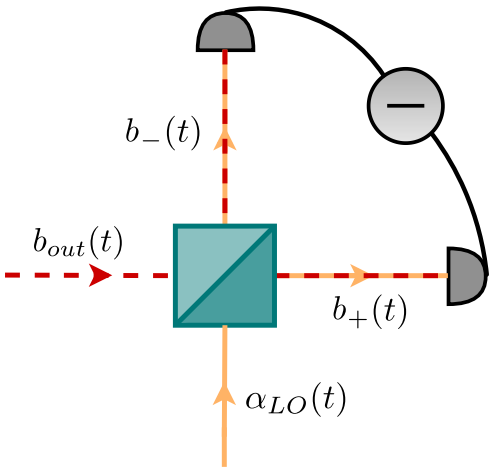

Figure 3.3: Setup for the detection of the field b_{out}. Both b_{out} and an auxialiary signal α_{LO} enter a beam-splitter. This gives rise to the signals b_+ and b_- which generates the photocurrent i_+ and i_-. The net photocurrent $i_+ - i_-$ is used to reveal the two quadratures of b_{out}.

3.3.1 Ideal longitudinal coupling

An alternative to conventional dispersive readout in circuit QED is the use of a longitudinal interaction of the form [29]

$$H_{\text{long}}^{\text{ideal}} = \frac{\omega_{\text{q}}}{2}\sigma_z + g_{\parallel}(t)(a + a^\dagger)\sigma_z + \omega_r a^\dagger a\,. \tag{3.62}$$

Unlike the most common transverse coupling, which relies on qubit-state-dependent shifts of the resonator frequency, longitudinal coupling directly induces a qubit-state-dependent drive on the resonator. When the coupling strength $g_{\parallel}(t)$ is modulated at the frequency of the resonator frequency, $g_{\parallel}(t) = g_{\parallel}^{\text{stat}} + 2g_{\parallel}\cos(\omega_{\text{r}}t)$, the cavity field evolves into qubit-state-dependent coherent states. This enables fast and high-fidelity readout, as the measurement signal rapidly becomes distinguishable depending on the qubit state. The method is inherently quantum non-demolition (QND), since σ_z commutes with the qubit Hamiltonian.

To obtain the dynamics of the cavity, it is sufficient to remark that the Hamiltonian can be rewritten as

$$H = \frac{\omega_{\text{q}}}{2}\sigma_z + \sqrt{2}g_{\parallel}(t)x\sigma_z + \frac{1}{2}\omega_r(x^2 + p^2)\,, \tag{3.63}$$

The dynamics is again the one of an harmonic oscillator and given by Eq. (3.36) with $A_{\text{r}}\cos(\omega_{\text{r}}t + \varphi) \to g_{\parallel}^{\text{stat}} + 2g_{\parallel}\cos(\omega_{\text{r}}t)$ and $\omega_0 = \omega_{\text{r}}$. This substitution yields ($\sigma = \pm 1$ for the qubit eigenstate $|\pm\rangle$)

$$\alpha(t) = \vartheta(t)e^{-i\omega_0 t} \qquad \text{with} \qquad \vartheta(t) = \vartheta(0) + \sigma\int_0^t dt' g_{\parallel}(t)e^{i\omega_0 t'}\,. \tag{3.64}$$

Evaluating the integral we obtain

$$\vartheta(t) = \vartheta(0) - ig_{\parallel}^{\text{stat}}\frac{e^{i\omega_0 t} - 1}{\omega_0}\sigma - ig_{\parallel}\left[\frac{e^{i\varphi}\left(e^{i(\omega_0+\omega_{\text{r}})t} - 1\right)}{\omega_0 + \omega_{\text{r}}} + \frac{e^{-i\varphi}\left(e^{i(\omega_0-\omega_{\text{r}})t} - 1\right)}{\omega_0 - \omega_{\text{r}}}\right]\sigma\,,$$

which, neglecting fast oscillating terms, is Eq. (3.38) with $A_{\text{r}} = 2g_{\parallel}\sigma$ and $\chi = 0$. An important consequence of this is that, at short times, Eq. (3.46) now reads

$$\alpha'(t) = -i\frac{g_{\parallel}\sigma}{\kappa/2}(1 - e^{-\frac{\kappa}{2}t}) \xrightarrow[t\to 0]{} -ig_{\parallel}\sigma t\,, \tag{3.65}$$

showcasing a 180° splitting of the trajectories at short times, as shown in Fig. 3.4a. As a result, the readout is faster with at least a factor 10 gain in the SNR at $t \to 0$ (see Fig. 3.4b).

3.3.2 Synthetic longitudinal coupling

In this Section we show how it is possible to engineer the effective longitudinal interaction of Eq. (3.2). This *synthetic* interaction can be realized by driving the qubit at the resonator frequency ω_{r}, as shown in Fig. 3.1b. In the low-frequency (adiabatic) limit, this realizes the parametric modulation discussed in the previous Section and ties directly to the qubit's static curvature. In the dispersive regime, it can be viewed as a renormalization of the cavity field which reveals the connection between the synthetic longitudinal coupling and the dispersive shift. If these two interpretation seem now disconnected, Chapter (5) shows how they unify under a Floquet theory.

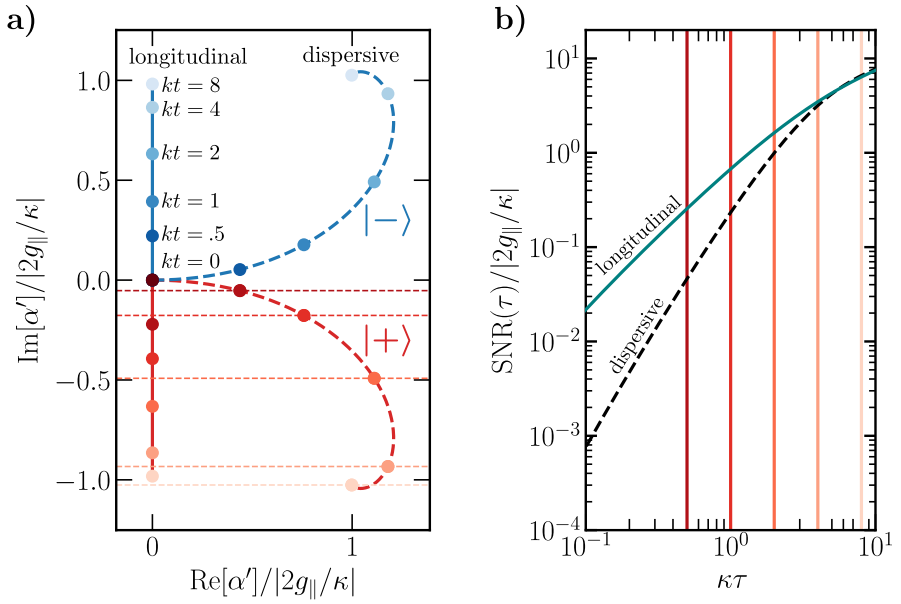

Figure 3.4: a) Evolution of the cavity field a for longitudinal (full lines) and dispersive coupling (dashed lines). Blue and red lines indicate the state in which the qubit has been prepared. The circles illustrate the position of the pointer states at characteristic times until steady state. b) The signal-to-noise ratio (SNR) measures the rate of the pointer state separation for the cavity field as a function of time. The time dependence is obtained using a cavity decay rate $\kappa = 0.1$ and $\chi = 0.05$ (values in unit of the amplitude of the probe at the resonator). $g_\parallel$ is adjusted to match the dispersive steady state. Note that conventionally dispersive readout is obtained with an input signal with phase $\varphi = -\pi/2$.

Parametric modulation of the detuning Considering the full Hamiltonian of the system with the qubit Hamiltonian $\mathcal{H}_{\mathrm{sys}}$, the dipolar coupling $\mathcal{H}_{\mathrm{int}}$, and the resonator $\mathcal{H}_{\mathrm{res}}$,

$$H = \frac{\omega_{\mathrm{q}}(\varepsilon_0)}{2}\sigma_z + g_\perp \frac{\varepsilon_0}{\omega_{\mathrm{q}}(\varepsilon_0)}\left(a + a^\dagger\right)\sigma_z + g_\perp \frac{2t_c}{\omega_{\mathrm{q}}(\varepsilon_0)}\left(a + a^\dagger\right)\sigma_x + \omega_r a^\dagger a\,, \tag{3.66}$$

we apply a drive to the qubit at the resonator frequency ω_{r}, which results as a parametric modulation of the detuning $\varepsilon_0(t) = \varepsilon_0 + \delta\varepsilon_0$, with $\delta\varepsilon_0 = 2A_{\mathrm{q}}\cos(\omega_{\mathrm{r}}t)$. In the limit $\omega_{\mathrm{r}} \ll \omega_{\mathrm{q}}$, the time dependence of the basis can be neglected and the Hamiltonian reduces to Eq. (3.66) with $\varepsilon_0 \to \varepsilon_0(t)$. Using the Taylor expansions

$$\frac{\varepsilon_0(t)}{\omega_{\mathrm{q}}(\varepsilon_0(t))} = \left.\frac{\partial\omega_{\mathrm{q}}}{\partial\varepsilon_0}\right|_{\varepsilon_0(t)} \approx \left.\frac{\partial\omega_{\mathrm{q}}}{\partial\varepsilon_0}\right|_{\varepsilon_0} + \left.\frac{\partial^2\omega_{\mathrm{q}}}{\partial\varepsilon_0^2}\right|_{\varepsilon_0}\delta\varepsilon_0(t) + \mathcal{O}\left(\delta\varepsilon_0(t)^2\right)\,, \tag{3.67}$$

$$\frac{2t_c}{\omega_{\mathrm{q}}(\varepsilon_0(t))} \approx \frac{2t_c}{\omega_{\mathrm{q}}(\varepsilon_0)} + \mathcal{O}\left(\delta\varepsilon_0(t)\right)\,, \tag{3.68}$$

the Hamiltonian becomes

$$H = \frac{\omega_{\mathrm{q}}(\varepsilon_0)}{2}\sigma_z + g_\parallel^{\mathrm{stat}}\left(a + a^\dagger\right)\sigma_z + 2g_\parallel\cos(\omega_{\mathrm{r}}t)\left(a + a^\dagger\right)\sigma_z + \frac{2t_c}{\omega_{\mathrm{q}}}g_\perp\left(a + a^\dagger\right)\sigma_x + \omega_r a^\dagger a\,, \tag{3.69}$$

with

$$g_\parallel^{\mathrm{stat}} = g_\perp\frac{\varepsilon_0}{\omega_{\mathrm{q}}(\varepsilon_0)}\,, \tag{3.70}$$

$$g_\parallel = 2g_\perp A_{\mathrm{q}}\left.\frac{\partial^2\omega_{\mathrm{q}}}{\partial\varepsilon_0^2}\right|_{\varepsilon_0} = \frac{g_\perp}{\omega_{\mathrm{q}}(\varepsilon_0)}\left(\frac{2t_c}{\omega_{\mathrm{q}}(\varepsilon_0)}\right)^2 A_{\mathrm{q}}\,. \tag{3.71}$$

To handle the residual transverse term, we apply a Schrieffer–Wolff transformation as in Sec. (3.1) with $g_\perp \to g_\perp(2t_c/\omega_{\rm q}(\varepsilon_0))$. This yields

$$H = \frac{\omega_{\rm q}\left(\varepsilon_0\right)+\chi}{2}\sigma_z + g_\parallel(t)\left(a+a^\dagger\right)\sigma_z + \left(\omega_{\rm r}+\chi\sigma_z\right)a^\dagger a\,, \tag{3.72}$$

with

$$\chi = \frac{2g_\perp^2}{\omega_{\rm q}(\varepsilon_0)}\left(\frac{2t_c}{\omega_{\rm q}(\varepsilon_0)}\right)^2 = 2g_\perp\frac{g_\parallel}{A_{\rm q}}\,. \tag{3.73}$$

In the rotating frame we neglect $g_\parallel^{\rm stat}$ and the effective Hamiltonian is then

$$H'_{\rm long} = \frac{\omega_{\rm q}\left(\varepsilon_0\right)+\chi}{2}\sigma_z + g_\parallel\left(a+a^\dagger\right)\sigma_z + \chi a^\dagger a\sigma_z\,. \tag{3.74}$$

Hence, in the adiabatic limit $\omega_{\rm r}\ll\omega_{\rm q}$, the effective Hamiltonian contains both $g_\parallel$ and χ which are proportional to the static curvature of the qubit's Larmor frequency $\partial^2\omega_{\rm q}/\partial\varepsilon_0^2$. Since the static curvature probes the response of the qubit to charge noise (see Sec. 2.4.1) it takes also the name of *quantum capacitance* [75]. The strength of the longitudinal coupling is maximal at the sweet spot $\varepsilon_0=0$, where $\omega_{\rm q}=2t_c$. In this case the expressions for $g_\parallel$ and χ simplify to

$$g_\parallel = 2g_\perp A_{\rm q}\left.\frac{\partial^2\omega_{\rm q}}{\partial\varepsilon_0^2}\right|_{\varepsilon_0} = \frac{g_\perp}{\omega_{\rm q}}A_{\rm q}\,, \qquad\qquad \chi = \frac{2g_\perp^2}{\omega_{\rm q}}\,. \tag{3.75}$$

Relation with the quantum capacitance An alternative approach [73, 80], valid specifically in the adiabatic or ultra-dispersive regime $\omega_{\rm r}\ll\omega_{\rm q}$ consists in projecting the Hamiltonian onto coherent states. Both the cavity and the drive produce a time dependent detuning

$$\varepsilon_0(t) = \varepsilon_0 + \delta(t)\,, \qquad \text{with} \qquad \delta(t) = 2g_\perp\left(\alpha+\alpha^*\right) + 2A_{\rm q}\cos(\omega_{\rm r}t)\,. \tag{3.76}$$

In the limit $\omega_{\rm r}\ll\omega_{\rm q}$, one can diagonalize the qubit sector neglecting the non adiabatic corrections arising from the time dependence of the transformation that diagonalize the Hamiltonian (i.e. terms involving $\partial_t U$). The resulting effective Hamiltonian becomes

$$H'(\alpha,\alpha^*) = \frac{\omega_{\rm q}(\varepsilon_0(t))}{2}\sigma_z\,, \tag{3.77}$$

where the dressed qubit energy can be expanded into a Taylor series as

$$\omega_{\rm q}(\varepsilon_0(t)) = \omega_{\rm q}\left(\varepsilon_0\right) + \left.\frac{\partial\omega_{\rm q}}{\partial\varepsilon_0}\right|_{\varepsilon_0}\delta(t) + \frac{1}{2}\left.\frac{\partial^2\omega_{\rm q}}{\partial\varepsilon_0^2}\right|_{\varepsilon_0}\delta(t)^2 + \mathcal{O}(\delta(t)^3)\,. \tag{3.78}$$

The effective Hamiltonian (3.77) becomes

$$H'_{\rm long}(\alpha,\alpha^*) = \frac{\omega_{\rm q}}{2}\sigma_z + g_\parallel^{\rm stat}(\alpha+\alpha^*)\sigma_z + 2g_\parallel\cos\left(\omega_{\rm r}t\right)(\alpha+\alpha^*)\sigma_z + \chi\alpha^*\alpha\sigma_z\,, \tag{3.79}$$

where $g_\parallel^{\rm stat}$, $g_\parallel$ and χ are given by Eqs. (3.70),(3.71) and (3.73).

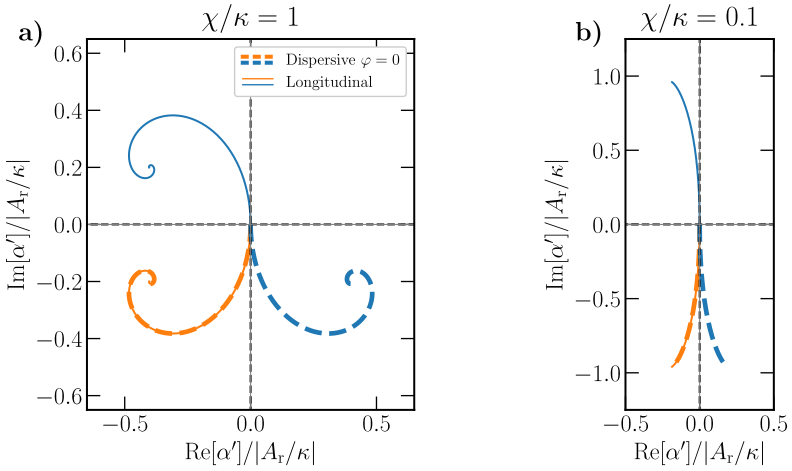

Figure 3.5: Longitudinal and dispersive readout at $\varphi = 0$. The time evolution of the cavity pointer states $\alpha'(t)$ are computed as in Eq. (3.46) with $A_\mathrm{r} = 2g_\parallel\sigma$ for longitudinal readout. Orange (blue) trajectory corresponds to $\sigma = \pm 1$. Note that conventional dispersive readout is obtained with $\varphi = -\pi/2$.

Dispersive regime At zero detuning ($\varepsilon_0 = 0$), applying the rotating wave approximation (RWA) to Eq. (3.66), and neglecting terms oscillating at frequencies $(\omega_\mathrm{q} + \omega_\mathrm{r})$ and $(2\omega_\mathrm{r})$, we obtain the effective Hamiltonian

$$H' = \frac{\omega_\mathrm{q} - \omega_\mathrm{r}}{2}\sigma_z + g_\perp(a\sigma_+ + a^\dagger\sigma_-)\sigma_x + \frac{A_\mathrm{q}}{2}\sigma_x + \omega_r a^\dagger a\,. \tag{3.80}$$

Introducing the displaced operator $b = a + A_\mathrm{q}/2g_\perp$, this becomes

$$H' = \frac{\omega_\mathrm{q} - \omega_\mathrm{r}}{2}\sigma_z + g_\perp(b\sigma_+ + b^\dagger\sigma_-)\,, \tag{3.81}$$

which can be diagonalized using (3.4) for the fields b and $b^\dagger$ and neglecting terms proportional to $(\omega_\mathrm{q} + \omega_\mathrm{r})^{-1}$. We obtain a dispersive Hamiltonian in the fields b, $b^\dagger$

$$H'_\mathrm{long} = \frac{\omega_\mathrm{q} - \omega_\mathrm{r} + \chi}{2}\sigma_z + \chi b^\dagger b\sigma_z\,, \tag{3.82}$$

with dispersive shift $\chi = g_\perp^2/(\omega_\mathrm{q} - \omega_\mathrm{r})$. Rewriting H'_long in terms of the original fields a, $a^\dagger$, we obtain

$$H'_\mathrm{long} = \frac{\omega_\mathrm{q} - \omega_\mathrm{r} + \chi}{2}\sigma_z + A_\mathrm{q}\frac{\chi}{2g_\perp}\left(a + a^\dagger\right)\sigma_z + \chi a^\dagger a\sigma_z\,, \tag{3.83}$$

which clearly exhibits an effective longitudinal coupling which grows linearly with A_q

$$g_\parallel = A_\mathrm{q}\frac{\chi}{2g_\perp}\,. \tag{3.84}$$

Hence, the protocol in Fig. 3.1b produces both a longitudinal coupling *parametric* in the drive strength A_q and a dispersive shift as for dispersive readout. Because of this additional dispersive shift, we cannot take $\chi = 0$ in (3.10) and the trajectories depicted in Fig. 3.4a bend at $t > 0$, as shown in Fig. 3.5b.

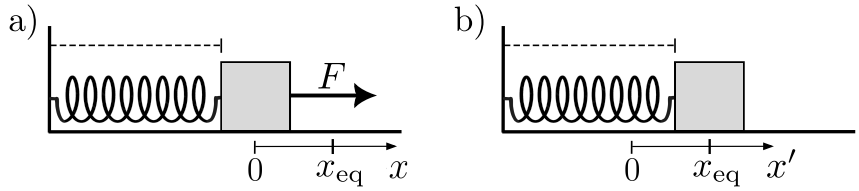

Figure 3.6: a) The force F applied to an harmonic oscillator shifts its equilibrium position to $x_{\rm eq}$. b) The same dynamics can be reproduced by a free harmonic oscillator whose coordinate is redefined as $x'(t) = x(t) + x_{\rm eq}$, and which starts from the initial condition $x'(0) = x_{\rm eq}$.

The equivalence between H' expressed as a dispersive Hamiltonian for the fields b, $b^\dagger$ and as a longitudinal Hamiltonian for the fields a, $a^\dagger$ reflects a fundamental physical insight: applying a force F to an harmonic oscillator shifts its equilibrium position to $x_{\rm eq}$. This is equivalent to displacing the coordinate axis of a free oscillator by $-x_{\rm eq}$, as shown in Fig. (3.6).

3.4 Analytical integration of the equations of motion

So far, we have seen that when the qubit is prepared in an incoherent mixture of eigenstates of σ_z, the resonator evolves according to classical equations of motion. Here, we lift this assumption and treat the general case in which the qubit is in an arbitrary state. We also allow coherent drives on both the qubit and the resonator at a common frequency $\omega_{\rm d} \neq \omega_{\rm r}$ (see Chap. 6) and we derive the equation of motion for the cavity field $a(t)$ in a rotating frame at $\omega_{\rm d}$. Hence, the Hamiltonian of our system is

$$H = \left(\frac{\omega_{\rm q} + \chi}{2}\right)\sigma_z + g_{\parallel}\left(a + a^\dagger\right)\sigma_z + \left(\chi\sigma_z + \delta\right)\, a^\dagger a \, + \frac{A_{\rm r}}{2}(a e^{i\varphi} + a^\dagger e^{-i\varphi})\,, \tag{3.85}$$

with $\delta = \omega_{\rm d} - \omega_{\rm r}$. Accounting for both the losses of the resonator and for Purcell effect, the equation of motion of any observable $\mathcal{O}$ reads

$$\langle \partial_t \mathcal{O}(t)\rangle = {\rm Tr}\{(\partial_t \rho)\,\mathcal{O}\} = i\,\langle [H, \mathcal{O}]\rangle + \kappa\left\langle \mathcal{D}_a^\dagger[\mathcal{O}]\right\rangle + \gamma\left\langle \mathcal{D}_{\sigma_-}^\dagger[\mathcal{O}]\right\rangle\,, \tag{3.86}$$

where we have introduced consider the adjoint Lindblad dissipator $\mathcal{D}_X^\dagger$, which acts on observables in the Heisenberg picture and is defined by duality with respect to the inner product [65]

$$\langle \mathcal{O},\, \mathcal{D}_X[\rho]\rangle = {\rm Tr}\Big\{\mathcal{O}^\dagger \mathcal{D}_X[\rho]\Big\} = {\rm Tr}\Big\{\left(\mathcal{D}_X^\dagger[\mathcal{O}]\right)^\dagger \rho\Big\} = \Big\langle \mathcal{D}_X^\dagger[\mathcal{O}],\, \rho\Big\rangle\,. \tag{3.87}$$

From its definition, it has the form

$$\mathcal{D}_X^\dagger[\mathcal{O}] = X^\dagger \mathcal{O} X - \tfrac{1}{2}\left\{X^\dagger X,\, \mathcal{O}\right\}\,. \tag{3.88}$$

Equation (3.86) naturally generalizes the Heisenberg picture for dissipative system. In this generalized Heisenberg picture, the operator $\mathcal{O}(t)$ evolves as

$$\partial_t \mathcal{O}(t) = i\,[H, \mathcal{O}] + \kappa\,\mathcal{D}_a^\dagger[\mathcal{O}] + \gamma\,\mathcal{D}_{\sigma_-}^\dagger[\mathcal{O}]\,. \tag{3.89}$$

For the cavity field operator $a(t)$, this read

$$\partial_t a = -i\chi a\sigma_z - \left(\frac{\kappa}{2} + i\delta\right) a - i g_{\parallel}\sigma_z - i\frac{A_{\rm r}}{2}e^{-i\varphi}\,, \tag{3.90}$$

while the dynamics of σ_z is immediately obtained from

$$\partial_t \sigma_z = -\gamma\,(1+\sigma_z) \quad \Longrightarrow \quad \sigma_z\,(t) = -1 + (\sigma_z\,(0)+1)\,e^{-\gamma t}\,. \tag{3.91}$$

Since in the general case $\langle a\sigma_z\rangle \neq \langle a\rangle\,\langle\sigma_z\rangle$, to solve the dynamics of the cavity field a, we also need the equation of motion of $a\sigma_z$

$$\partial_t\,(a\sigma_z) = -(i\chi+\gamma)a - \left(\frac{\kappa}{2}+\gamma+i\delta\right)a\sigma_z - ig_{\parallel} - i\frac{A_{\rm r}}{2}e^{-i\varphi}\sigma_z\,. \tag{3.92}$$

To solve the system of differential equations given by Eqs. (3.90-3.92), we introduce the normal modes

$$\varsigma = a - \frac{i\chi}{\gamma+i\chi}a\sigma_z\,, \qquad\qquad \xi = a + a\sigma_z\,. \tag{3.93}$$

The system can now be decoupled and reads

$$\begin{aligned}
\partial_t\varsigma = &-\left[i\,(\delta-\chi)+\frac{\kappa}{2}\right]\varsigma - i\left[g_{\parallel} - \frac{i\chi}{\gamma+i\chi}\frac{A_{\rm r}}{2}e^{-i\varphi}\right](\sigma_z+1)\\
&+ i\frac{\gamma+2i\chi}{\gamma+i\chi}\left(g_{\parallel}-\frac{A_{\rm r}}{2}e^{-i\varphi}\right),\\
\partial_t\xi = &-\left[i\,(\delta+\chi)+\frac{\kappa}{2}+\gamma\right]\xi - i\left[g_{\parallel}+\frac{A_{\rm r}}{2}e^{-i\varphi}\right](\sigma_z+1)\,.
\end{aligned} \tag{3.94}$$

Considering an empty cavity at $t=0$, the solutions of (3.94) are

$$\begin{aligned}
\varsigma\,(t) = -i\Bigg[&\left(\frac{A_{\rm r}}{2}e^{-i\varphi}-g_{\parallel}\right)\left(\frac{\gamma+2i\chi}{\gamma+i\chi}\right)\frac{1-e^{-\frac{\kappa}{2}t-i(\delta-\chi)t}}{i(\delta-\chi)+\kappa/2}\\
&+(\sigma_z\,(0)+1)\left(g_{\parallel}-\frac{i\chi}{\gamma+i\chi}\frac{A_{\rm r}}{2}e^{-i\varphi}\right)\frac{e^{-\gamma t}-e^{-\frac{\kappa}{2}t-i(\delta-\chi)t}}{i(\delta-\chi)+\kappa/2-\gamma}\Bigg],
\end{aligned} \tag{3.95}$$

$$\xi\,(t) = -i\,(\sigma_z\,(0)+1)\left(\frac{A_{\rm r}}{2}e^{-i\varphi}+g_{\parallel}\right)\frac{1-e^{-\frac{\kappa}{2}t-i(\delta+\chi)t}}{i(\delta+\chi)+\kappa/2}e^{-\gamma t}\,, \tag{3.96}$$

and the evolution of $\langle a(t)\rangle$ is obtained through

$$\langle a(t)\rangle = \frac{1}{\gamma+2i\chi}\big[\,(\gamma+i\chi)\,\langle\varsigma\,(t)\rangle + i\chi\,\langle\xi\,(t)\rangle\,\big]\,. \tag{3.97}$$

Below, we discuss Eq. (3.97) in the limit $\delta=\gamma=0$.

Dispersive readout – The evolution of the cavity field expectation value $\langle a(t)\rangle$ is given by Eq. (3.97) with $g_{\parallel}=0$ and $\varphi=-\pi/2$, namely

$$\langle a(t)\rangle_{\rm disp.} = \frac{A_{\rm r}}{4}\sum_{\sigma=\pm1}\sigma\left[(\langle\sigma_z(0)\rangle+\sigma)\frac{1-e^{-\frac{\kappa}{2}t-i\sigma\chi t}}{i\sigma\chi+\frac{\kappa}{2}}\right]. \tag{3.98}$$

In the stationary $t\to\infty$ limit, assuming $\langle\sigma_z(0)\rangle\simeq\sigma$, one finds that $\langle a(t=\infty)\rangle_{\rm disp.} = A_{\rm r}/2(i\sigma\chi+\kappa/2)$, while, at short times, the expansion of the exponential gives $\langle a(t\to0)\rangle_{\rm disp.}\approx A_{\rm r}t/2$, that is qubit state independent.

Longitudinal readout – For the longitudinal driving protocol we consider $A_{\rm r}=0$ and $\varphi=0$ in Eq. (3.97). We obtain

$$\langle a(t)\rangle_{\rm long.} = -\frac{ig_{\parallel}}{2}\sum_{\sigma=\pm1}\left[(\langle\sigma_z(0)\rangle+\sigma)\frac{1-e^{-\frac{\kappa}{2}t-i\sigma\chi t}}{i\sigma\chi+\frac{\kappa}{2}}\right], \tag{3.99}$$

which, if $\chi \ll \kappa$, can be further simplified to

$$\langle a(t)\rangle_{\text{long.}} = -ig_{\parallel}\langle\sigma_z(0)\rangle\left(\frac{1-e^{-\frac{\kappa}{2}t}}{\kappa/2}\right). \tag{3.100}$$

This evolution describes the 180° splitting of the trajectories sketched in Fig. 3.1b, since at short times $\langle a(t\to 0)\rangle_{\text{long.}} = -ig_{\parallel}\langle\sigma_z\rangle t$.

3.5 Chapter 3 in a nutshell

In this chapter we have examined both dispersive and longitudinal readout. Using a Schrieffer–Wolff transformation, we have shown that in the dispersive regime the transverse (dipolar) qubit-resonator interaction produces a qubit-state-dependent shift of the cavity frequency $\chi\sigma_z$, where χ is the dispersive shift. When the resonator is driven, this frequency shift enables discrimination of the qubit state. However, the measurement is effectively insensitive to the qubit at very short integration times.

We have then turned to longitudinal readout. In the ideal limit it yields a perfect 180° separation separation of the pointer states and can operate faster than dispersive readout. Realizing this advantage in practice requires engineering a longitudinal coupling driving the qubit at the cavity frequency, which results in a synthetic longitudinal coupling parametric in the drive strength. In the dispersive regime the strength of the longitudinal coupling scales with χ. In the adiabatic (ultra-dispersive) regime it also connects to the curvature of the static spectrum (the quantum capacitance).

Two main questions naturally arise: applying this same protocol, is the longitudinal coupling always parametric in the drive strength? Is there a more general way to derive χ and $g_{\parallel}$ which connects the dispersive expression with the curvature of the Larmor frequency of the qubit? While the first question founds a negative answer in the next Chapter, the unified Floquet theory developed in Chap. 5 provides a connection between χ, $g_{\parallel}$ and the AC Stark shift that goes beyond the parametric regime, explaining its breakdown at strong drives.

Chapter

4 Experimental realization of longitudinal coupling in a charge qubit

Contents

4.1 The device 49
4.1.1 Experimental setup 50
4.1.2 The model 50
4.2 Transmission measurement of dispersive and longitudinal readout . 51
4.3 Qubit state displacement 53
4.4 Breakdown of the parametric regime 55
4.4.1 Parametric dependence of the longitudinal interaction 55
4.5 Chapter 4 in a nutshell 55

The fast and efficient measurement of an electron or a hole is a key challenge to devise scalable architectures. As discussed in Chapter 3, a longitudinal interaction enables faster-than-dispersive readout. Recent works demonstrated longitudinal readout in superconducting circuits [78, 81] and reported signatures of longitudinal coupling in semiconductor qubits [80, 82, 83]. However, longitudinal and dispersive couplings may be difficult to discriminate due to crosstalks causing photon leakage into the resonator. A drive to the qubit may partially leak in the resonator, and the measured signal can then reflect a dispersive shift rather than a longitudinal state-dependent displacement.

In this Chapter, we propose two clear signatures that distinguish a longitudinal signal from a dispersive one, even when full coherent control of the qubit is unavailable, and we demonstrate the breakdown of the parametric regime.

In Sec. 4.1, we present the experimental setup and its model. In Sec. 4.2, we demonstrate the existence of longitudinal coupling via transmission measurements of the device in a triple-quantum-dot configuration. In Sec. 4.3, we use a protocol to discriminate longitudinal and dispersive readout using a thermal state in a two-dot configuration. In Sect. 4.4, we show the agreement of the longitudinal coupling strength with the predictions of Chap. 5 in the parametric regime, and the breakdown of such regime at strong drives.

The experimental work presented in this Chapter was carried out by the experimental team at CEA Grenoble. We provided theoretical modeling of the system (Sec. 4.1) and the proposal in Sec. 4.3 to distinguish between longitudinal and dispersive readout using a thermal state.

4.1 The device

In this Section we present the experimental setup (Sec. 4.1.1) and we apply the theory developed in the previous Chapter to describe longitudinal and dispersive readout (Sec. 4.1.2).

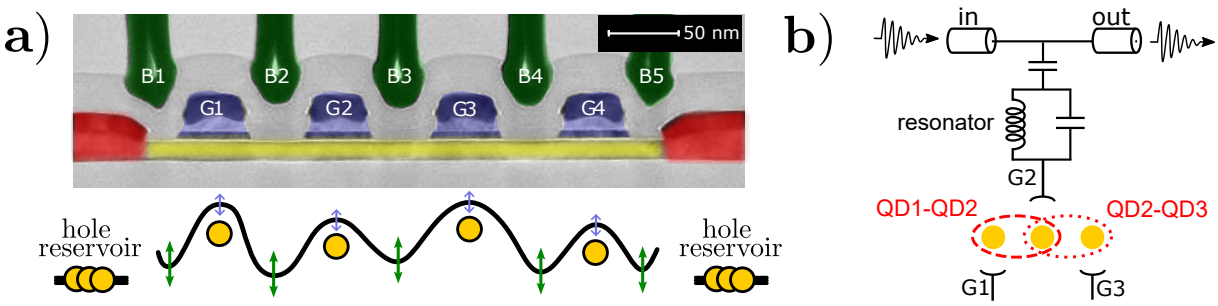

Figure 4.1: Experimental setup. a) False-colored transmission electron micrograph of the device. Yellow: Silicon nanowire. Red: Boron-doped leads, acting as reservoirs for holes. Blue: four parallel gates are used to shape the quantum well potentials to confine quantum dots. Green: five parallel gates modify the potential barrier between the dots therefore tuning the tunneling coupling between them. b) Circuit model of the system. A resonator is coupled at gate G2 and capacitively coupled to a transmission line. Three dots are schematically represented below gates G1, G2 and G3 and form the two charge qubits QD1-QD2 and QD2-QD3.

4.1.1 Experimental setup

The experimental setup is shown in Figure 4.1. It consists of a metal-oxide-semiconductor (MOS) device obtained from a silicon-on-insulator nanowire with a 50×11 nm^2 rectangular cross-section. The nanowire is covered by a first layer of 4 parallel plunger gates (G1 to G4) with a pitch of 80 nm, that create a potential landscape confining holes in quantum dots. A second layer of 5 barrier gates (B1 to B5) sets the heights of the potential barriers between adjacent dots, tuning the tunnel couplings between the dots [84]. Electrical control of the plunger and barrier gates determines the charge configuration in the dots.

A resonator of frequency $\omega_r/2\pi = 526$ MHz and decay rate $\kappa/2\pi = 13.9$ MHz is capacitively coupled to gate G2 with strength $g_\perp/2\pi = 25.0$ MHz and to a transmission line for readout. The RF signal passing through the feed-line is demodulated via homodyne detection (see Sec. 3.2).

4.1.2 The model

As discussed in Sec. 2.4.1, a single charge trapped inside a double quantum dot has two localized states $|L\rangle$ and $|R\rangle$. The Hamiltonian describing this two-level system is given by $\mathcal{H}_{\rm sys} = \varepsilon_0\tau_z/2 + t_c\tau_x$ (we set $\hbar = 1$), where ε_0 is the energy detuning between the two dots, and t_c is the tunnel coupling. The double QD acts as an electric dipole that interacts with the oscillating electric field of the microwave resonator, described by the Hamiltonian $\mathcal{H}_{\rm res} = \omega_r a^\dagger a$, where $a^{(\dagger)}$ are bosonic annihilation (creation) operators. In the qubit eigenbasis the system Hamiltonian $\mathcal{H}_{\rm sys}$ is diagonal

$$\mathcal{H}_{\rm sys} = \frac{\omega_{\rm q}(\varepsilon_0)}{2}\sigma_z\,, \qquad \text{with} \qquad \omega_{\rm q}(\varepsilon_0) = \sqrt{\varepsilon_0^2 + 4t_c^2}\,, \tag{4.1}$$

while the photon-dipole interaction takes the form (see Sec. 2.4.2)

$$\mathcal{H}_{\rm int} = g_\perp \frac{\varepsilon_0}{\omega_{\rm q}(\varepsilon_0)}\left(a + a^\dagger\right)\sigma_z + \frac{2t_c}{\omega_{\rm q}(\varepsilon_0)} g_\perp \left(a + a^\dagger\right)\sigma_x\,, \tag{4.2}$$

where $g_\perp$ is the charge-photon coupling.

Longitudinal readout As discussed in Sec. 3.3.2, driving the qubit at the resonator frequency modulates the detuning as $\varepsilon_0 \to \varepsilon_0 + 2A_q \cos\omega_r t$, which generates a parametric longitudinal coupling. The resulting effective Hamiltonian is

$$\mathcal{H} = \frac{\omega_{\rm q}(\varepsilon_0)+\chi}{2}\sigma_z + (\omega_{\rm r}+\chi\sigma_z)\, a^\dagger a + g_\parallel(t)(a+a^\dagger)\sigma_z\,, \tag{4.3}$$

with a parametric longitudinal coupling $g_\parallel(t) = g_\parallel^{\rm stat} + 2g_\parallel\cos(\omega_{\rm r}t)$, where $g_\parallel^{\rm stat}$, $g_\parallel$ and χ given by Eqs. (3.70,3.71,3.73). Explicitely,

$$g_\parallel^{\rm stat} = g_\perp\frac{\varepsilon_0}{\omega_{\rm q}(\varepsilon_0)}\,, \qquad g_\parallel = \frac{g_\perp}{\omega_{\rm q}(\varepsilon_0)}\left(\frac{2t_c}{\omega_{\rm q}(\varepsilon_0)}\right)^2 A_{\rm q}\,, \qquad \chi = \frac{2g_\perp^2}{\omega_{\rm q}(\varepsilon_0)}\left(\frac{2t_c}{\omega_{\rm q}(\varepsilon_0)}\right)^2. \tag{4.4}$$

Solving the Heisenberg equations of motion in the rotating frame at $\omega_{\rm r}$ (see Eq. (3.99)), yields the steady-state cavity field

$$\langle a\rangle_\parallel = -g_\parallel\frac{\chi + i\frac{\kappa}{2}\langle\sigma_z\rangle}{\chi^2+\frac{\kappa^2}{4}}\,. \tag{4.5}$$

Dispersive readout Dispersive readout is obtained by driving the cavity (rather than the qubit) at the resonator frequency. This is realized by applying an input signal on the feedline

$$\langle b_{in}^{\rightarrow}(t)\rangle = \sqrt{\frac{2}{\kappa}}\frac{A_{\rm r}}{2}e^{-i(\omega_{\rm r}t+\varphi)}\,, \tag{4.6}$$

which translates into a contribution $A_{\rm r}\cos(\omega_{\rm r}t+\varphi)\left(a+a^\dagger\right)$ in the Hamiltonian (see Sec. 2.3.3). In this case, the steady-state cavity field in the rotating frame at $\omega_{\rm r}$ is (see Eq. (3.98))

$$\langle a\rangle_{\rm disp} = -\frac{A_{\rm r}}{2}\frac{\chi\langle\sigma_z\rangle + i\frac{\kappa}{2}}{\chi^2+\frac{\kappa^2}{4}}e^{-i\varphi}\,. \tag{4.7}$$

In the next Section, we use the steady-state expressions (4.5-4.7) to distinguish longitudinal and dispersive readout in a triple-quantum-dot configuration.

4.2 Transmission measurement of dispersive and longitudinal readout

To showcase the difference between dispersive and longitudinal readout mechanisms, we consider the triple QD (QD1, QD2 and QD3 in Fig. 4.1a) formed by hole accumulation below G1, G2 and G3. Since the resonator is coupled to G2, it addresses both the interdot dipoles QD1-QD2 and QD2-QD3.

For dispersive readout, the transmission coefficient as function of the detuning between the quantum wells reveals all the sweet spots between the dots, where the hole delocalizes between adjacent dots (the interdot transitions). For longitudinal readout, selective driving of individual plunger gates targets a chosen charge dipole, so the transmitted signal isolates the corresponding interdot transition.

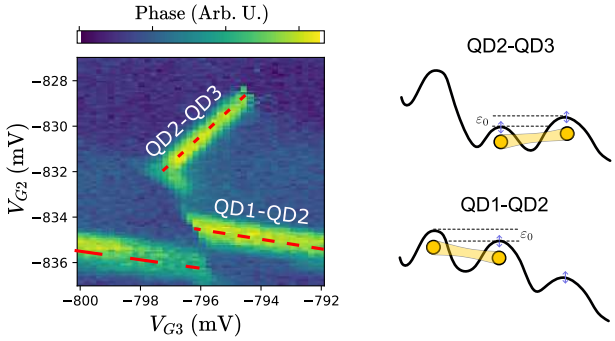

Figure 4.2: Phase of the signal transmitted at $\omega_r/2\pi = 526$ MHz through the transmission line as a function of the voltages on G2 and G3. The red-dotted (resp. dashed) line corresponds to interdot transitions between QD2 and QD3 (resp. QD1 and QD2). Interdot transitions occur when two dots are aligned and the hole delocalizes between them.

Dispersive readout in transmission As shown in Fig. 4.1b, we realize dispersive readout via an input-output measurement on the feedline. At time t_0, an input tone $b_{in}^{\rightarrow}(t)$ is injected at one end of the feedline, and at a later time t_1 the transmitted output signal $b_{out}^{\rightarrow}(t)$ is recovered at the other end. As discussed in Sec. 2.3.1, the input and output signals are related by

$$\langle b_{out}^{\rightarrow}(t)\rangle = \langle b_{in}^{\rightarrow}(t)\rangle - i\sqrt{\frac{\kappa}{2}}\,\langle a(t)\rangle\ . \tag{4.8}$$

Moving to the rotating frame and substituting the steady-state cavity field (4.7) into the input-output relation, yields the complex transmission

$$T(\omega_r) \equiv \frac{\langle b_{out}^{\rightarrow}\rangle}{A_r} = \sqrt{\frac{1}{2\kappa}}\left(\chi\frac{\chi + i\frac{\kappa}{2}\langle\sigma_z\rangle}{\chi^2+\frac{\kappa^2}{4}}\right)\,, \tag{4.9}$$

Hence, the transmission amplitude and phase are

$$|T(\omega_r)| = \sqrt{\frac{1}{2\kappa}}\frac{|\chi|}{\sqrt{\chi^2+\kappa^2/4}}\,, \qquad \angle T(\omega_r) = \arctan\left(\frac{\kappa/2}{\chi}\langle\sigma_z\rangle\right)\,. \tag{4.10}$$

Sweeping the gate voltages G1-G3 controls the interwell detuning. When all the wells are far detuned, $\omega_q(\varepsilon_0) \gg 2t_c$, and Eq. (4.4) yields $\chi \approx 0$. As two wells are aligned, the associated charge qubit sits at its sweet spot and χ attains its maximum. The phase response in Fig. (4.2)b highlights this behavior. As χ increases from $\chi = 0$ to larger values, the phase shifts from $\angle T(\omega_r) = -\pi/2$ toward $\angle T(\omega_r) = 0$.

Longitudinal readout in transmission Let us now turn to the problem of probing longitudinal coupling. In this case, no input signal is injected in the feedline and the transmitted signal originates only from the leakage of the cavity, populated by the longitudinal interaction. The output signal is therefore

$$b_{out}^{\rightarrow}(t) = -i\sqrt{\frac{\kappa}{2}}a(t)\,. \tag{4.11}$$

The transmission coefficient is given by

$$T(\omega_r) \equiv \frac{b_{out}^{\rightarrow}(t)}{A_q} = i\sqrt{\frac{\kappa}{2}}\frac{g_\parallel}{A_q}\frac{\chi + i\kappa\,\langle\sigma_z\rangle/2}{\chi^2+\kappa^2/4}\,,$$

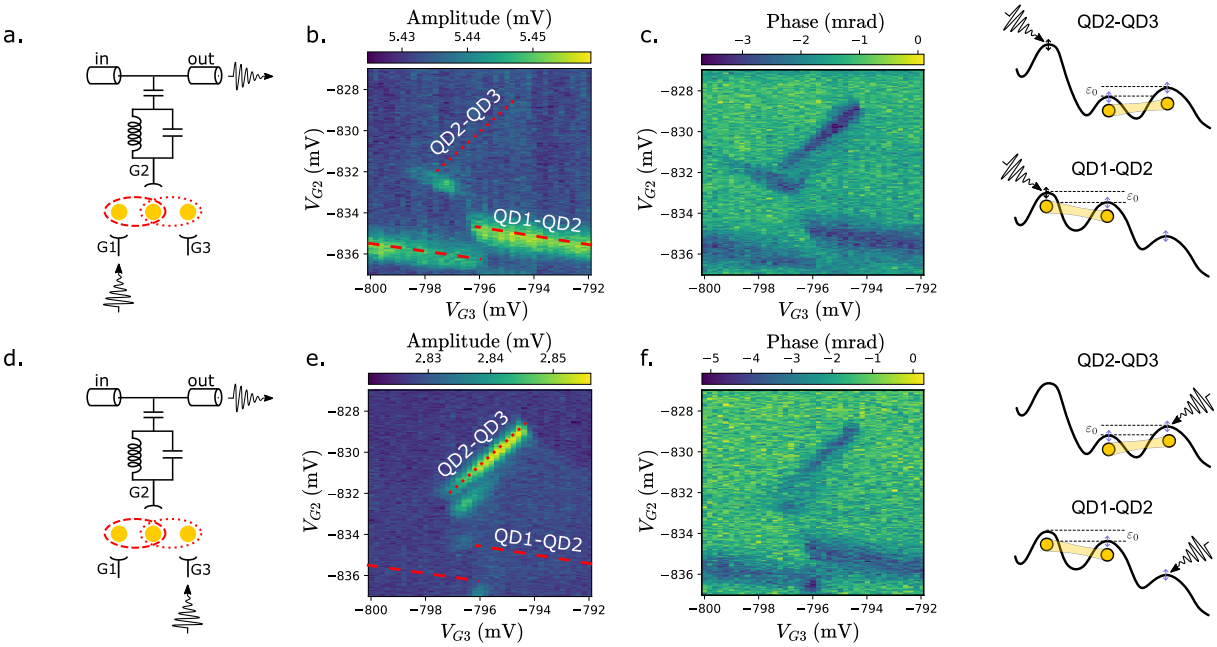

Figure 4.3: Longitudinal measurement by driving on the gates. a) (resp. d)) The readout tone is applied on gate G1 (resp. G3). b) (resp. e)) Amplitude of the signal measured at the output of the transmission line, demodulated at frequency $\omega_{\rm r}$, with the drive on gate G1 (resp. G3). c) (resp. f)) Phase shift of the transmitted signals. Interdot transitions occur when two dots are aligned and the hole delocalizes between them.

with amplitude and phase given by

$$|T(\omega_{\rm r})| = \sqrt{\frac{\kappa}{2}}\frac{|g_{\parallel}|}{\sqrt{\chi^2+\kappa^2/4}}\,, \qquad \angle T(\omega_{\rm r}) = \frac{\pi}{2} + \arctan\left(\frac{\kappa/2}{\chi}\langle\sigma_z\rangle\right)\,. \tag{4.12}$$

In Figure 4.3 we analyze the amplitude response to show the existence of a longitudinal interaction by selectively driving QD1/QD2 or the QD2/QD3 charge transition. This is achieved by applying a RF tone at frequency $\omega_r/2\pi$ either on G1 or on G3, as schematically shown in Fig. 4.3a and 4.3d. The amplitude measurements exhibit noticeable differences. When driving G1 (G3), only the charge transition QD1/QD2 (QD2/QD3) is visible, as shown in Fig. 4.3b (Fig. 4.3e). The presence of only specific signals in Fig. 4.3b,e, associated with well identified interdot transitions, is rather consistent with the presence of the longitudinal coupling.

The stability diagrams in phase are, however, incompatible with (4.12), since they exhibit a phase signal at the interdot transition of both QD1/QD2 and QD2/QD3, regardless of the qubit port which is driven. This is a clear indication of a residual crosstalk between G1 (G3) and the resonator, which drives dispersive readout and causes the discontinuity in the phase signal. To deal with this cross-talk, a compensation tone is applied to the resonator [81].

4.3 Qubit state displacement

In this Section we restrict our attention to the prototypical case of a charge qubit formed by a single hole delocalized in the double quantum dot under gates G2 and G3.

Dispersive readout is obtained by applying a drive at the resonator of strength $A_{\rm r}$ and phase φ. The steady state expression is obtained from Eq. (3.98). Longitudinal readout is obtained by

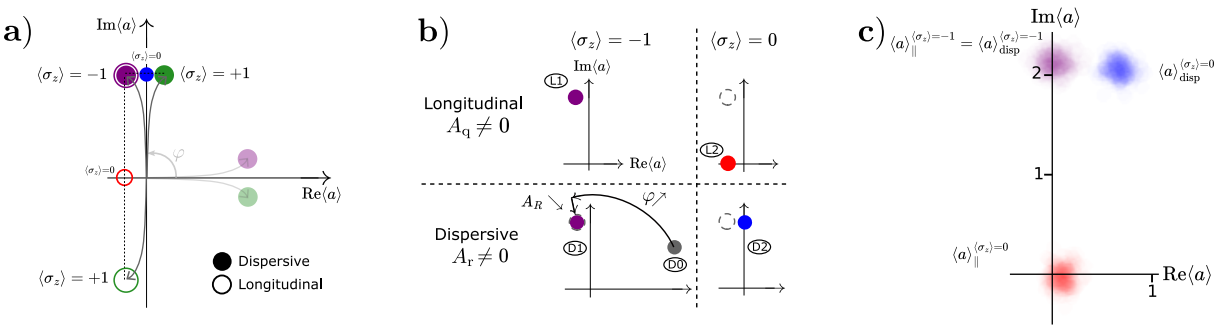

Figure 4.4: Conditional displacement of the pointer state. a) Cavity field steady state for longitudinal and dispersive readout. The amplitude and phase of the input signal for dispersive readout can be adjusted such that the steady state for both protocols coincide for $\langle\sigma_z\rangle = -1$. Conventional dispersive readout (faded) is obtained with $\varphi = \pi/2$. b) Details of the experimental protocol for probing the conditional displacement. c) Pointer states measured for two different qubit states and two drive mechanisms. Notice that the origin of the phase space is shifted due to a cancellation tone applied to compensate cross-talks. Here $\omega_q/2\pi = 4.1$ GHz and $A_q = 10\ \mu eV$.

applying a drive at the qubit of strength A_q. To highlight the difference between longitudinal and dispersive readout, we operate on the phase and amplitudes of the drives $A_{q,r}$ in such a way that the signal sits on the same point in the phase space when $\langle\sigma_z\rangle = -1$ for both driving protocols (purple data points in Figure 4.4a). An easy way to distinguish longitudinal and dispersive readout would be to drive the qubit to its excited state and inspect the steady state in this case, as shown in Fig. 4.4b. However, the relaxation time of this qubit is too short to let us coherently drive the excited state. Hence, by applying a continuous drive of frequency $\omega_q/2\pi$ we obtain an incoherent mixture $\langle\sigma_z\rangle \sim 0$. The following protocol describes how we used the $\langle\sigma_z\rangle \sim 0$ state to discriminate longitudinal and dispersive readout, as shown in Fig. 4.4b.

L1: We prepare the qubit in its ground state, and activate the longitudinal interaction by a modulation $A_q \cos\omega_r t$. One measures a resonator state $\langle a\rangle_{\parallel,\langle\sigma_z\rangle=-1}$.

L2: We drive the qubit to an incoherent mixture of ground and excited states, and the resonator is then displaced to a state $\langle a\rangle_{\parallel,\langle\sigma_z\rangle=0}$.

D0: We prepare now the qubit in its ground state, and activate only the dispersive interaction, by populating the resonator with an external drive $A_r \cos(\omega_r t + \varphi)$ on the resonator (Note that $A_q = 0$).

D1: We prepare the resonator in the same state than during L1 by tuning A_r and φ in such a way that the resonator steady state reads $\langle a\rangle_{\text{disp},\langle\sigma_z\rangle=-1} = \langle a\rangle_{\parallel,\langle\sigma_z\rangle=-1}$.

D2: We drive again the qubit to an incoherent mixture, and the resonator reads $\langle a\rangle_{\text{disp},\langle\sigma_z\rangle=0}$.

Figure 4.4c shows the steady state pointer states in phase space measured for the two qubit states (ground or mixed) for both readout schemes (dispersive and parametric longitudinal). Dispersive and longitudinal readout schemes exhibit a radically different behavior. Dispersive readout leads to a displacement of the pointer state as expected from Fig. 4.4a (blue signal). Parametric longitudinal readout moves the pointer state back to $(\text{Re}\langle a\rangle, \text{Im}\langle a\rangle) \sim 0$ (red signal). These outcomes are consistent with Eqs. (4.5) and (4.7).

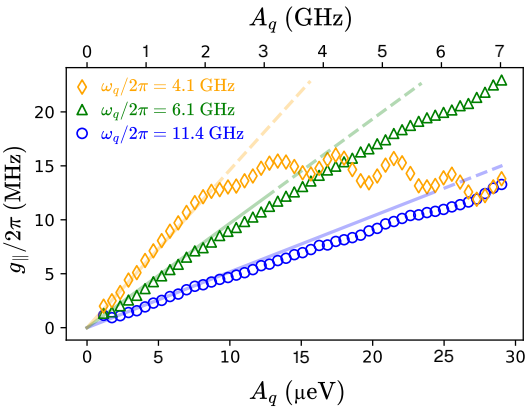

Figure 4.5: Extracted longitudinal coupling strength $g_\parallel$ as a function of the drive amplitude A_q for three different qubit energies at zero detuning. The model (4.13) is represented in solid lines up to $A_\mathrm{q} = \omega_\mathrm{q}/2$, without any additional fitting parameters. The model's lines become dashed for $A_\mathrm{q} > \omega_\mathrm{q}/2$. Note that the x-axis has been duplicated in frequency units above the graph.

4.4 Breakdown of the parametric regime

Following the demonstration of longitudinal readout, we now turn to a quantitative study of the coupling strength.

4.4.1 Parametric dependence of the longitudinal interaction

To measure the strength of the longitudinal coupling, we compute first the steady state of the cavity from Eq. (3.99). This way, assuming the charge qubit to be in its ground state, the longitudinal coupling reads

$$g_\parallel = |\langle a \rangle_\parallel| \sqrt{\chi^2 + \kappa^2/4}\,, \tag{4.13}$$

where $|\langle a \rangle_\parallel|$ can be deduced from the measurement of the output-field.

We modify the tunnel rate between the two dots to change the charge qubit energy at zero detuning from $\omega_q/2\pi = 4.1$ GHz to $\omega_q/2\pi = 11.4$ GHz. For each different Larmor frequency, the dispersive shift $\chi(\omega_q)$ is measured by spectroscopy measurements obtained both varying the drive frequency and the detuning [47]. In practice, we find that $\chi \ll \kappa$ for all ω_q values, implying that χ plays a minor role in the investigated experimental regime.

Equipped with χ, we measure $g_\parallel$ from Eq. (4.13). The results for the three qubit frequencies are shown in Fig. 4.5 together with the corresponding linear-in-A_q dependence expected from Eq. (3.73). The remarkable agreement obtained with no fitting parameter confirms the validity of the measurement protocol and demonstrates the realization of parametric longitudinal driving. We notice that the slope of the $g_\parallel(A_\mathrm{q})$ linear dependence is, to a good approximation, inversely proportional to the qubit frequency up to $A_\mathrm{q} \sim \omega_\mathrm{q}/2$, followed by a tendency to saturation due to the breakdown of the weak-drive approximation $A_\mathrm{q} < \omega_\mathrm{q}/2$.

4.5 Chapter 4 in a nutshell

In this Chapter, we demonstrated the existence of longitudinal coupling in a charge qubit coupled to a microwave resonator. By selectively driving different charge qubits in a triple quantum dot array, we addressed specific interdot transitions, demonstrating the existence of a longitudinal interaction. Focusing on a single charge qubit, we showed how thermal state can be leveraged

to show the difference between longitudinal and dispersive readout mechanisms. These results in charge qubits form a practical foundation for realizing longitudinal coupling of spin qubits to microwave cavities through spin orbit interaction (see Chap. 6). Building on this foundation, we found that the extracted coupling agrees with theory at weak drive, while at strong drive the system leaves the parametric regime. This observation leads directly to the next Chapter, where a unified Floquet theory of readout explains the origin of this breakdown.

Chapter

5 Unifying Floquet Theory of readout

Contents

5.1 Floquet theorem 58
5.2 Spatial periodic potentials 61
5.2.1 Bloch's theorem as a consequence of the Floquet theorem 61
5.2.2 The band spectrum 63
5.3 Time periodic Hamiltonians 64
5.4 cQED readout protocols using Floquet theory 67
5.4.1 Semiclassical approach : the quantum Rabi model 67
5.4.2 Beyond the semiclassical approach 71
5.4.3 Purcell effect 76
5.5 Limiting cases 77
5.6 Dispersive readout 78
5.7 Discussion of longitudinal readout 78
5.7.1 Change of sign across resonance 79
5.7.2 Deviations from parametric longitudinal coupling at strong drives . . . 79
5.8 Chapter 5 in a nutshell 80

As discussed in Chapter 3, driving a qubit of Larmor frequency $\omega_{\rm q}$ at the resonator frequency $\omega_{\rm r}$ gives rise to an effective longitudinal interaction, leading to a σ_z-dependent displacement of the resonator field. In Section 3.3.2, we have seen that while $g_{\parallel}$ connects to the dispersive shift χ in the dispersive regime, in the adiabatic limit ($\omega_{\rm r} \ll \omega_{\rm q}$) it becomes proportional to the static curvature of the Larmor frequency of the qubit $\partial^2\omega_{\rm q}/\partial\varepsilon_0^2$. We concluded the Chapter by raising two central questions: is the longitudinal coupling always parametric in the drive strength? Is there a unified derivation of χ and $g_{\parallel}$ that recovers the dispersive and adiabatic limits? These sharpen our guiding question introduced at the beginning of the manuscript

Is there a universal mechanism to implement a longitudinal interaction? (5.1)

In this Chapter we adress it by developing a unified Floquet theory that establishes a universal connection between the AC Stark shift, longitudinal and dispersive coupling in cQED. Within this framework, we show that the longitudinal coupling $g_{\parallel}$ is a generic mechanism which is controlled by the *slope* of the drive-induced AC Stark shift of the qubit, whereas its second derivative (curvature) mainly sets the dispersive shift χ.

We set $\hbar = 1$. The starting point is to rewrite the Hamiltonian of the longitudinal protocol at zero detuning[1]

$$H = \frac{\omega_{\rm q}}{2}\sigma_z + g_{\perp}\left(a + a^{\dagger}\right)\sigma_x + A_{\rm q}\cos(\omega_{\rm r}t)\sigma_x + \omega_r a^{\dagger}a\,, \tag{5.2}$$

[1]This is not a less of generality as already discussed in Sec. 3.3.2.

in the frame rotating at the resonator frequency,

$$\mathcal{H}' = \frac{\omega_\mathrm{q}}{2}\sigma_z + \frac{1}{2}\left(\mathcal{A}e^{-i\omega_\mathrm{r}t} + \mathcal{A}^\dagger e^{i\omega_\mathrm{r}t}\right)\sigma_x\,, \qquad \text{with} \qquad \mathcal{A} = A_\mathrm{q} + 2g_\perp a\,. \tag{5.3}$$

In this form, the resonator renormalizes the drive and the Hamiltonian exposes the time periodicity of the Hamiltonian required for a Floquet treatment.

In Sec. (5.1), we review the mathematical background of Floquet theorem [85], which applies to any linear differential equation whose coefficient matrices depend on a variable t and are periodic in this variable. Before addressing our time-periodic system of interest, we briefly show in Sec. (5.2) how Bloch's theorem can be seen as a consequence of Floquet theorem in the case of spatial periodicity. In Sec. (5.3), this allows us to build analogies between the features of Floquet theory in time-periodic systems [86–90] and Bloch's band theory.

Section 5.4 develops the unified Floquet theory of readout, relating longitudinal and dispersive couplings to the drive-induced AC Stark shift. In Sec. 5.5 we recover the coupling expressions discussed in Chap. 3 as limiting cases of our theory, and in Sec. 5.6 we revisit dispersive readout within this framework. We then analyze the implications of this theory for readout in Sec. 5.7, explaining the degradation of the readout at particular frequency in the strong drive regime.

5.1 Floquet theorem

In this Section we explore the mathematical background of Floquet's theorem [85]. Any physical implications are discussed in the next Section with the applications of the theory to space and time-periodic systems. Here t denotes a generic variable (not necessarily time).

Floquet theorem applies to any linear differential equation

$$\dot{\vec{\psi}} = A(t)\vec{\psi}\,, \tag{5.4}$$

where $A(t+T) = A(t)$ is a $n \times n$ periodic matrix with period T. Such systems are invariant under a discrete t-translation up to the period T. The differential equation in (5.4) admits n linearly independent solutions [91] that can be organized as columns of an $n \times n$ matrix $\Psi(t) = \left[\vec{\psi}_1 \quad \vec{\psi}_2 \quad \dots \quad \vec{\psi}_n\right]$, which is itself a solution of

$$\dot{\Psi}(t) = A(t)\Psi(t)\,. \tag{5.5}$$

The evolution between two instants t_0 and t is described by the propagator $P(t, t_0)$, defined via

$$\Psi(t) = P(t, t_0)\Psi(t_0)\,. \tag{5.6}$$

However, given a fundamental solution $\Psi(t)$, the matrix $\Psi'(t) = \Psi(t)\Psi(t_0)^{-1}$ also satisfies (5.5) with $\Psi'(t_0) = \mathbf{1}$. Hence, we may assume without loss of generality $\Psi(t_0) = \mathbf{1}$.

Floquet's theorem [85] states that, if $P_0 = P(t_0 + T, t_0)$ is the initial time stroboscopic propagator, then $\Psi(t)$ can always be decomposed as

$$\Psi(t) = L(t, t_0)e^{\frac{\ln P_0}{T}(t-t_0)}\,, \tag{5.7}$$

where $L(t, t_0) = P(t, t_0)\, e^{-\frac{\ln P_0}{T}(t-t_0)} = L(t+T, t_0)$ is a periodic matrix of period T, responsible for the 'micromotion' of the solution (see Fig. 5.1).

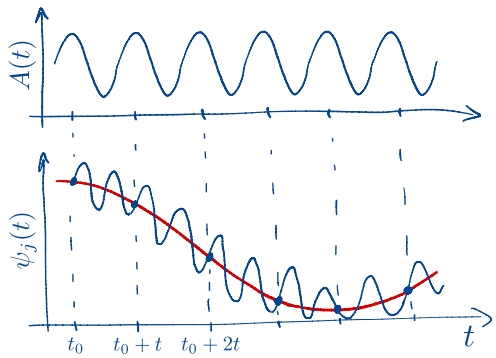

Figure 5.1: The action of $A(t)$ on the evolution of $\psi_j(t)$ in one dimension. The dynamics (blue line) is given by the propagator $P(t,t_0) = L(t,t_0)\, e^{\frac{\ln P_0}{T}(t-t_0)}$ and is composed by a slow dynamics (red line), captured by the stroboscopic operator P_0, and a slow dynamics. The slow dynamics (micromotion) is described by $L(t_0,t)$ and vanishes at $t_0 + nT$ (blue points), where $L(t_0 + nT, t_0) = \mathbf{1}$. Figure adapted from Ref. [92].

Proof of the Floquet theorem

To prove (5.7), we first observe that

$$L(t,t_0) = \Psi(t) e^{-\frac{\ln P_0}{T}(t-t_0)} = P(t,t_0)\, e^{-\frac{\ln P_0}{T}(t-t_0)} \tag{5.8}$$

trivially satisfies Eq. (5.7), provided that P_0 is non-singular. The core of the proof then reduces to: (i) showing that P_0 is invertible and (ii) proving that L is a periodic matrix of period T.
First, observe that the propagator satisfies the same differential equation as (5.5),

$$\dot{P}(t,t_0) = A(t) P(t,t_0)\,, \tag{5.9}$$

and as a solution to a linear differential equation with an invertible initial condition $P(t_0,t_0) = \mathbf{1}$, it is a nonsingular matrix for all t.
For (ii), we use the composition property of the propagator, which is easily verifiable

$$P(t_2,t_0) = P(t_2,t_1) P(t_1,t_0)\,, \tag{5.10}$$

for any $t_0 \le t_1 \le t_2$. Since $P(t+T, t_0+T)$ and $P(t,t_0)$ both solve (5.9) with the same initial condition, we also have

$$P(t+T, t_0+T) = P(t,t_0)\,. \tag{5.11}$$

Using (5.10) and (5.11), we obtain from Eq. (5.6)

$$\Psi(t+T) = \Psi(t) P_0\,. \tag{5.12}$$

Plugging this into the expression for $L(t,t_0)$, we find $L(t+T,t_0) = \Psi(t+T) P_0^{-1} e^{-\frac{\ln P_0}{T}(t-t_0)} = L(t,t_0)$, which proves (ii) and concludes our proof of the Floquet theorem.

The Floquet modes The matrix $L(t, t_0)$ defines the propagation of the eigenvectors of P_0, known as the *Floquet modes*. Indeed, if P_0 is diagonalizable, there exist n Floquet modes $\vec{u}_j(t_0)$, eigenvectors of P_0 with eigenvalues μ_j,

$$P_0\vec{u}_j(t_0) = \mu_j\vec{u}_j(t_0)\,. \tag{5.13}$$

Defining $\vec{u}_j(t) = L(t, t_0)\vec{u}_j(t_0)$, we immediately see that $\vec{u}_j$ is T-periodic

$$\vec{u}_j(t+T) = \vec{u}_j(t)\,, \tag{5.14}$$

and that it is the eigenvector of the stroboscopic propagator $P(t+T, t)$ with the same eigenvalue μ_j

$$\begin{aligned} P(t+T,t)\vec{u}_j(t) &= P(t+T,t_0)P(t_0,t)L(t,t_0)\vec{u}_j(t_0) \\ &= P(t+T,t_0)\, e^{-\frac{\ln P_0}{T}(t-t_0)}\vec{u}_j(t_0) \\ &= L(t,t_0)P_0\vec{u}_j(t_0) \\ &= \mu_j\vec{u}_j(t)\,. \end{aligned} \tag{5.15}$$

By definition, Floquet modes are t-periodic functions with period T and can be used to construct the solutions of $\dot{\vec{\psi}} = A(t)\vec{\psi}$. The general solution $\vec{\psi}_j(t) = \Psi(t)\vec{u}_j(t_0)$ with initial condition $\vec{\psi}_j(t_0) = \vec{u}_j(t_0)$ can be decomposed as

$$\vec{\psi}_j(t) = \Psi(t)\vec{u}_j(t_0) = L(t,t_0)e^{\frac{\ln P_0}{T}(t-t_0)}\vec{u}_j(t_0) = e^{\frac{\ln \mu_j}{T}(t-t_0)}\vec{u}_j(t)\,. \tag{5.16}$$

Plugging this solution into the original problem $\dot{\vec{\psi}} = A(t)\vec{\psi}$, we obtain that the Floquet modes can be found from the differential equation

$$\dot{\vec{u}}_j(t) = \left(A(t) - \frac{\ln \mu_j}{T}\right)\vec{u}_j(t)\,. \tag{5.17}$$

Lyapunov transformation The matrix L has another important property. It defines the so-called Floquet-Lyapunov transformation [85]

$$\Psi(t) = L(t, t_0)\Phi(t)\,, \tag{5.18}$$

with $\Phi(t) = e^{\frac{\ln P_0}{T}(t-t_0)}$. This transformation maps the original t-dependent problem $\dot{\Psi}(t) = A(t)\Psi(t)$ into the system of equations with t-independent coefficients

$$\dot{\Phi}(t) = Q\Phi(t)\,, \tag{5.19}$$

where Q is t-independent and reads

$$Q = L^{-1}AL - L^{-1}\frac{dL}{dt} = \frac{\ln P_0}{T}\,. \tag{5.20}$$

Projecting onto $\vec{u}_j(t_0)$, the Lyapunov transformation (5.18) becomes a change of variables

$$\vec{\psi}_j(t) = L(t, t_0)\vec{\phi}_j(t)\,, \tag{5.21}$$

where $\vec{\phi}_j(t) = e^{\frac{\ln \mu_j}{T}(t-t_0)}\vec{u}_j(t_0)$ satisfies the time-independent equation

$$\dot{\vec{\phi}}_j(t) = Q\vec{\phi}_j(t)\,, \tag{5.22}$$

We have seen that the propagator of the Floquet modes defines a change of variables that transforms the original t-dependent system into a t-independent one.

5.2 Spatial periodic potentials

For systems with periodic potentials, the periodicity lies in the spatial coordinate x. This Section is structured as follows. In Sec. 5.2.1 that Bloch's theorem [93] can be seen as a consequence of the Floquet theorem. Section 5.2.2 discusses the band spectrum with an example that provides useful insights for the Floquet spectrum discussed in Sec. 5.4.1.

5.2.1 Bloch's theorem as a consequence of the Floquet theorem

Consider an electron with mass m in a one-dimensional crystal with lattice constant a, described by the time-independent Schrödinger equation

$$H\psi(x) = E\psi(x)\,, \qquad H = -\frac{\partial_x^2}{2m} + V(x)\,, \tag{5.23}$$

with the a-periodic potential $V(x+a) = V(x)$. To connect this problem with Floquet theory, we rewrite the Schrödinger equation as a first-order system

$$\partial_x\vec{\psi} = A(x)\vec{\psi}\,, \qquad \vec{\psi} = \begin{pmatrix}\psi(x)\\ \partial_x\psi(x)\end{pmatrix}\,, \qquad A(x) = \begin{pmatrix}0 & 1\\ 2m(V(x)-E) & 0\end{pmatrix}\,, \tag{5.24}$$

Since $A(x+a) = A(x)$, Floquet theorem applies in the variable x. Before invoking it, we recall Bloch's theorem.

Bloch's theorem The translation operator T_y is defined by its action on position eigenstates, $T_y\,|x\rangle = |x+y\rangle$. In the position representation it acts on any wavefunction as

$$T_y\phi(x) \equiv \langle x|\,T_y\,|\phi\rangle = \phi(x-y) = \sum_n (-y)^n \partial_x^n \phi(x)\,. \tag{5.25}$$

Since the momentum operator in the position representation is $\mathrm{p}_x = -i\partial_x$, we can write $T_y = e^{-i\mathrm{p}y}$. Since the Hamiltonian is periodic in the lattice constant a, the translation by one lattice period T_a commutes with H. Thus, H and T_a share a common set of eigenfunctions $\psi_k(x)$, labeled by the so-called crystal momentum k, defined modulo the reciprocal lattice vector $k_a = 2\pi/a$. These eigenfunctions satisfy

$$\psi_k(x+a) = e^{ika}\psi_k(x)\,, \tag{5.26}$$

which is the statement of Bloch's theorem. Introducing the Bloch modes $u_k(x) = e^{-ikx}\psi_k(x)$, we find that it is periodic,

$$u_k(x) = u_k(x+a)\,, \tag{5.27}$$

and the eigenstate can thus be written as

$$\psi_k(x) = e^{ikx}u_k(x)\,. \tag{5.28}$$

Connection with the Floquet theorem At this point, the analogy with Floquet theorem is apparent. However, two important precautions must be noted

- One is tempted to identify the Bloch modes u_k with the Floquet modes defined in the previous Section. However, the solution to Eq. (5.24) are $\vec{\psi}_k = \begin{pmatrix}\psi_k(x) & \partial_x\psi_k(x)\end{pmatrix}^T$ so the Floquet modes are in reality $\vec{u}_k = \begin{pmatrix}u_k(x) & \partial_x u_k(x)\end{pmatrix}^T$.

- One might be inclined to identify the stroboscopic Floquet propagator with the translation operator T_a. However, T_a applies to any wavefunction, whereas the Floquet propagator applies only to the solutions of the linear system (5.24). Denoting by $P(x+a,x)$ the stroboscopic propagator of the system, we have that, while it acts like T_a on the solutions ψ_k,

$$P(x+a,x)\psi_k(x) = \psi_k(x+a) = T_a\psi_k(x)\,, \tag{5.29}$$

its action on the Bloch mode is

$$P(x+a,x)u_k(x) = e^{-ikx}\psi_k(x+a) = e^{-ika}u_k(x)\,, \tag{5.30}$$

whereas T_a acts also on plane waves, $T_a u_k(x) = T_a\left[e^{-ikx}\psi_k(x)\right] = e^{-ik(x+a)}\psi_k(x+a) = u_k(x+a)$.

Apart from these technical distinctions, the analogy holds since $P(x+a)$ acts like T_a on ψ_k.

Plugging the Floquet modes $\vec{u}_k$ into the Schrödinger (5.24), $\partial_x\vec{\psi} = A(x)\vec{\psi}$, we obtain

$$\left[\begin{pmatrix} 0 & 1 \\ 2m(V(x)-E) & 0 \end{pmatrix} - \partial_x\right]\begin{pmatrix} u_k(x) \\ iku_k(x)+\partial_x u_k(x)\end{pmatrix} = ik\begin{pmatrix} u_k(x) \\ iku_k(x)+\partial_x u_k(x)\end{pmatrix}\,, \tag{5.31}$$

Rearranging the terms in the second row yields the differential equation for the Bloch modes

$$\frac{1}{2m}\left(-i\frac{\partial}{\partial x}+k\right)^2 u_k(x) + V(x)u_k(x) = E_k u_k(x)\,. \tag{5.32}$$

At first glance, this decomposition simply shifts the problem of finding $\psi_k(x)$ to that of determining another unknown function $u_k(x)$. However, the key advantage lies in the periodicity of $u_k(x)$. This allows us to express $u_k(x)$ as the Fourier series $u_k(x) = \sum_p u_{k,p}e^{-ipk_a x}$, where $p\in\mathbb{Z}$. Similarly, the periodic potential can be expanded as

$$V(x) = \sum_n V^{(n)}e^{-ik_a nx}\,. \tag{5.33}$$

Substituting these expansions into the Schrödinger equation yields

$$\sum_m V^{(m)}u_{k,p-m} + \frac{(k-k_a p)^2}{2m}u_{k,p} = E_k u_{k,p}\,, \tag{5.34}$$

which takes the form of an infinite-dimensional linear system indexed by the Fourier mode p

$$\begin{pmatrix} \cdots & \cdots & \cdots & \cdots & \cdots \\ \cdots & V^{(0)}+\frac{(k+k_a)^2}{2m} & V^{(-1)} & \cdots & \cdots \\ \cdots & V^{(1)} & V^{(0)}+\frac{k^2}{2m} & V^{(-1)} & \cdots \\ \cdots & \cdots & V^{(1)} & V^{(0)}+\frac{(k-k_a)^2}{2m} & \cdots \\ \cdots & \cdots & \cdots & \cdots & \cdots \end{pmatrix}\begin{pmatrix} \vdots \\ u_{k,-1} \\ u_{k,0} \\ u_{k,1} \\ \vdots \end{pmatrix} = E_k\begin{pmatrix} \vdots \\ u_{k,-1} \\ u_{k,0} \\ u_{k,1} \\ \vdots \end{pmatrix}\,. \tag{5.35}$$

We have thus reduced the original differential equation to an eigenvalue problem, though now defined in an infinite-dimensional space.

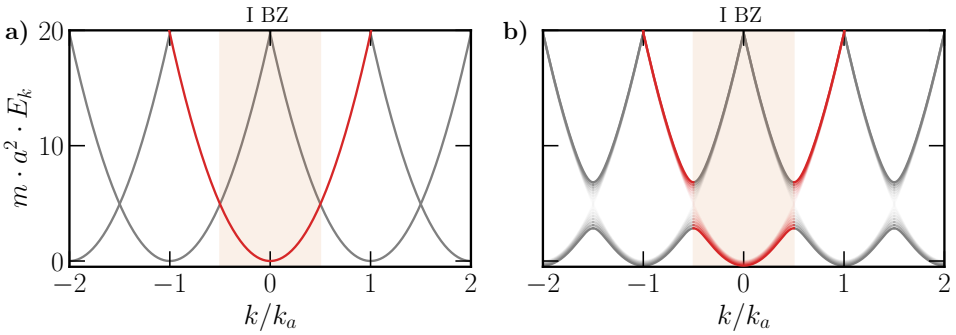

Figure 5.2: Band structure for an electron in a periodic potential. The highlighted orange region is the First Brillouin Zone. a) When $V_0 = 0$, the spectrum consists of replicas of parabolas shifted by integer multiples of k_a. b) The potential V_0 removes the degeneracy and opens a gap at $k = nk_a/2$, with n integer. Increasing opacity indicates increasing potential till $V_0 = 2/ma^2$.

5.2.2 The band spectrum

To find the eigenvectors of (5.35), we consider the family of functions $\psi_k^{(n)}(x)$ defined by

$$\psi_k^{(n)}(x) = \psi_{k+nk_a}(x)\,. \tag{5.36}$$

Each of these functions satisfies the Bloch's theorem, since

$$\psi_k^{(n)}(x) = e^{ikx} e^{ink_a x} u_{k+nk_a}(x) = e^{ikx} u_k^{(n)}(x)\,, \tag{5.37}$$

where $u_k^{(n)}(x) = e^{ink_a x} u_{k+nk_a}(x)$ is still spatially periodic. Moreover, $\psi_k^{(n)}(x)$ obeys the same Schrödinger equation as $\psi_{k+nk_a}(x)$. Therefore, their energies coincide, $E_k^{(n)} = E_{k+nk_a}$. This means that if we decompose $u_k^{(n)}(x)$ into a Fourier series, $u_k^{(n)}(x) = \sum_p e^{-ipk_a x} u_{k,p}^{(n)}$, the components

$$u_{k,p}^{(n)} = u_{k+nk_a,p+n}\,, \tag{5.38}$$

are also solutions of (5.35), with energy $E_k^{(n)} = E_{k+nk_a}$. We have thus shown that for each k, there exists an infinite set of eigenvalues $E_k^{(n)}$, labeled by the index n, which is commonly referred to as the *band index*.

As an example, we consider the case of a periodic potential given by

$$V(x) = V_0 \cos(k_a x)\,, \tag{5.39}$$

such that Eq. (5.35) reads

$$\begin{pmatrix} \ddots & \ddots & & & \\ \ddots & \frac{(k+k_a)^2}{2m} & \frac{V_0}{2} & & \\ & \frac{V_0}{2} & \frac{k^2}{2m} & \frac{V_0}{2} & \\ & & \frac{V_0}{2} & \frac{(k-k_a)^2}{2m} & \ddots \\ & & & \ddots & \ddots \end{pmatrix} \begin{pmatrix} \vdots \\ u_{k,-1} \\ u_{k,0} \\ u_{k,1} \\ \vdots \end{pmatrix} = E_k \begin{pmatrix} \vdots \\ u_{k,-1} \\ u_{k,0} \\ u_{k,1} \\ \vdots \end{pmatrix}\,. \tag{5.40}$$

In the absence of potential, $V_0 = 0$, the spectrum consists of a series of parabolic dispersion curves, replicated at momenta shifted by integer multiples of k_a, with degeneracy points at

	Spatial periodicity	Time periodicity
General Floquet Theorem	$\vec{\psi}_k(x) = e^{ikx}\vec{u}_k(x)$	$\lvert\psi_j(t)\rangle = e^{-i\varepsilon_j t}\lvert u_j(t)\rangle$
Stroboscopic propagator $P(t+T,t)$	$P(x+a,x)$	$\mathcal{U}(t+T,t)$
Eigenvalues of P, μ_j	e^{ika}	$e^{-i\varepsilon_j T}$
Floquet modes	$\begin{pmatrix} u_k(x) & \partial_x u_k(x)\end{pmatrix}^T$	$\lvert u_j(t)\rangle$
Fourier decomposition	$u_k^{(n)}(x) = \sum_p e^{-ipk_a x} u_{k,p}^{(n)}$	$\left\lvert u_j^{(n)}(t)\right\rangle = \sum_p e^{-ip\omega t}\left\lvert u_{j,p}^{(n)}\right\rangle$
Replica structure of the eigenvalues	$E_k^{(n)} = E_{k+nk_a}$	$\varepsilon_j^{(n)} = \varepsilon_j + n\omega$
Replica structure of the eigenvectors	$u_{k,p}^{(n)} = u_{k+nk_a,p+n}$	$\left\lvert u_{j,p}^{(n)}\right\rangle = \lvert u_{j,p+n}\rangle$

Table 5.1: Summary table of the analogy between Bloch theory and Floquet theory.

$k = nk_a/2$, see Fig. (5.2)a. Turning on the periodic potential couples adjacent replicas and lifts these degeneracies, opening energy gaps at the crossings, as illustrated in Fig. (5.2)b. The spectrum remains periodic in reciprocal space, so one may either (i) restrict k to the first Brillouin zone $[-k_a/2, k_a/2]$ (see Fig. (5.2)) and view distinct bands separated by gaps, or (ii) work with a single replica in the unfolded picture.

5.3 Time periodic Hamiltonians

In this Section we apply the Floquet theorem to study a periodic time-dependent Hamiltonian $H(t+T) = H(t)$. The discussion closely follows that of Sec. (5.1). The Schrödinger equation

$$i\partial_t \psi(t) = H(t)\psi(t) \tag{5.41}$$

takes the form (5.5), with $A(t) = -iH(t)$. According to Eq. (5.16), the solutions can be written as

$$\lvert\psi_j(t)\rangle = e^{-i\varepsilon_j t}\lvert u_j(t)\rangle \ , \tag{5.42}$$

where $\lvert u_j(t+T)\rangle = \lvert u_j(t)\rangle$ are the Floquet modes and ε_j are the so-called *quasi-energies*. The Floquet modes are eigenvectors of the stroboscopi propagator $\mathcal{U}(t+T,t)$ with eigenvalue $\mu_j = e^{-i\varepsilon_j T}$. Plugging Eq. (5.42) into Eq. (5.41), we obtain that the Floquet modes satisfies

$$\left(H(t) - i\frac{d}{dt}\right)\lvert u_j(t)\rangle = \varepsilon_j \lvert u_j(t)\rangle \ . \tag{5.43}$$

The analogies between this description and what discussed in the previous Section are summarized in Table 5.1. As in Sec. (5.2), we expand each Floquet mode in a Fourier series $\lvert u_j(t)\rangle = \sum_{p=-\infty}^{\infty} e^{-ip\omega t}\lvert u_{j,p}\rangle$, where $\omega = 2\pi/T$ and $p \in \mathbb{Z}$. Similarly, we decompose the Hamiltonian in Fourier components

$$H(t) = \sum_n H^{(n)} e^{-i\omega n t}\,, \qquad \text{with} \qquad H^{(n)} = \frac{1}{T}\int_0^T dt e^{in\omega t} H(t)\,, \tag{5.44}$$

Substituting these expressions into Eq. (5.43) yields

$$\sum_n H^{(n)}\lvert u_{j,p-n}\rangle - p\,\omega\lvert u_{j,p}\rangle = \varepsilon_j\lvert u_{j,p}\rangle \ , \tag{5.45}$$

a linear system that can be written in matrix form (analogue of (5.35))

$$\begin{pmatrix} \dots & \dots & \dots & \dots & \dots \\ \dots & H^{(0)}+\omega & H^{(-1)} & \dots & \dots \\ \dots & H^{(1)} & H^{(0)} & H^{(-1)} & \dots \\ \dots & \dots & H^{(1)} & H^{(0)}-\omega & \dots \\ \dots & \dots & \dots & \dots & \dots \end{pmatrix} \begin{pmatrix} \vdots \\ |u_{j,-1}\rangle \\ |u_{j,0}\rangle \\ |u_{j,+1}\rangle \\ \vdots \end{pmatrix} = \varepsilon_j \begin{pmatrix} \vdots \\ |u_{j,-1}\rangle \\ |u_{j,0}\rangle \\ |u_{j,+1}\rangle \\ \vdots \end{pmatrix} , \tag{5.46}$$

As in the case of the periodic potential in space, this eigenvalue problem admits an infinite family of solutions. If $|u_j(t)\rangle$ in Eq. (5.43) solves the time-dependent Schrödinger equation with the quasi-energy ε_j, then also $\left|u_j^{(n)}(t)\right\rangle = e^{in\omega t}\,|u_j(t)\rangle$ with $\varepsilon_j^{(n)} = \varepsilon_j + n\omega$ does. This is immediately demonstrated by the equality

$$|\psi_j\,(t)\rangle = e^{-i\varepsilon_j t}\,|u_j\,(t)\rangle = e^{-i\varepsilon_j^{(n)} t}\left|u_j^{(n)}\,(t)\right\rangle = \left|\psi_j^{(n)}\,(t)\right\rangle , \tag{5.47}$$

which implies, by making the Fourier decomposition $\left|u_j^{(n)}(t)\right\rangle = \sum_p e^{-ip\omega t}\left|u_{j,p}^{(n)}\right\rangle$, that

$$\left|u_{j,p}^{(n)}\right\rangle = |u_{j,p+n}\rangle\ . \tag{5.48}$$

Once again, the spectrum is periodic and one may restrict quasi-energies to a single Floquet zone $[-\omega/2, \omega/2]$ or work with a single replica in the unfolded picture.

The Sambe space The matrix differential equations (5.35) and (5.46) suggest the introduction of an auxiliary infinite dimensional Hilbert space, the so-called *Sambe* space [87], spanned by the canonical basis

$$\dots \qquad |-1) = \begin{pmatrix} \vdots \\ 0 \\ 0 \\ 1 \\ \vdots \end{pmatrix} , \qquad |0) = \begin{pmatrix} \vdots \\ 0 \\ 1 \\ 0 \\ \vdots \end{pmatrix} , \qquad |1) = \begin{pmatrix} \vdots \\ 1 \\ 0 \\ 0 \\ \vdots \end{pmatrix} , \qquad \dots . \tag{5.49}$$

Using this formalism, the system in (5.46) becomes the eigenvalue problem for the so-called *Floquet Hamiltonian*[2]

$$\mathcal{H}_{\mathcal{F}} = \mathbf{p}\,\omega_{\mathrm{r}} + \sum_n H^{(n)} f_-^n\,. \tag{5.50}$$

where $\mathbf{p} = \sum_p p\,|p)\,(p|$ is the replica number operator and

$$f_- = \sum_p |p-1)(p|\,, \qquad\qquad f_-^{-1} = f_+ = \sum_p |p+1)(p|\,, \tag{5.51}$$

are the jump operators, with $f_-^0 = \mathbb{1}$ by convention. This implies that if the reference vector in the Sambe space

$$|\,u_j, 0\rangle\rangle \equiv \sum_p |p) \otimes |u_{j,-p}\rangle \tag{5.52}$$

[2]Notice that our definition of Floquet Hamiltonian is different from the one in Ref. [92].

is a solution of (5.46), then

$$|\,u_j,n\rangle\rangle \equiv \begin{pmatrix} \vdots \\ \left|u^{(n)}_{j,-1}\right\rangle \\ \left|u^{(n)}_{j,0}\right\rangle \\ \left|u^{(n)}_{j,+1}\right\rangle \\ \vdots \end{pmatrix} = f_+^n\,|\,u_j,0\rangle\rangle = \sum_p |p)\otimes|u_{j,n-p}\rangle = \begin{pmatrix} \vdots \\ |u_{j,n-1}\rangle \\ |u_{j,n}\rangle \\ |u_{j,n+1}\rangle \\ \vdots \end{pmatrix} \tag{5.53}$$

is also a solution of (5.46) with the shifted quasi-energy $\varepsilon_j^{(n)} = \varepsilon_j + n\omega$. The eigenvalue problem in (5.46) therefore reads

$$\mathcal{H}_{\mathcal{F}}\,|\,u_j,n\rangle\rangle = \varepsilon_j^{(n)}\,|\,u_j,n\rangle\rangle\ . \tag{5.54}$$

To stress the consistency of this notation, observe that the vectors $|u_j,n\rangle\rangle$ are orthonormal

$$\delta_{jk}\delta_{nm} = \langle\langle u_j,n|u_k,m\rangle\rangle = \sum_p \left\langle u^{(0)}_{j,n+p}|u^{(0)}_{k,m+p}\right\rangle = \sum_p \langle u_{j,p}|u_{k,p+m-n}\rangle\ , \tag{5.55}$$

from which we deduce that the modes $|u_j(t)\rangle$ are orthonormal at any instant t

$$\begin{aligned}\langle u_j(t)|u_k(t)\rangle &= \sum_{pq} e^{i(p-q)\omega_{\rm r}t}\left\langle u^{(0)}_{j,p}|u^{(0)}_{k,q}\right\rangle \\ &= \sum_p \left\langle u^{(0)}_{j,p}|u^{(0)}_{k,p}\right\rangle + \sum_{d\neq 0} e^{id\omega_{\rm r}t}\sum_p \left\langle u^{(0)}_{j,p}|u^{(0)}_{k,p+d}\right\rangle = \delta_{jk}\,,\end{aligned} \tag{5.56}$$

Floquet-Lyapunov transformation The Floquet mode propagator reads in this case $L(t) = \sum_j |u_j(t)\rangle\langle u_j(0)|$ and defines the Floquet-Lyapunov transformation (5.21),

$$|\psi(t)\rangle = L(t)\,|\phi(t)\rangle\ , \tag{5.57}$$

which defines a rotated frame where the dynamics of $|\phi(t)\rangle = e^{-i\varepsilon_j t}\,|u_j(0)\rangle$ is time-indipendent. Indeed, the Hamiltonian in the rotating frame reads

$$H_{\rm FL} = L^\dagger H(t) L + i\left(\partial_t L^\dagger\right)L = \sum_j \varepsilon_j\,|u_j(0)\rangle\langle u_j(0)|\ , \tag{5.58}$$

which is the time-independent equation (5.22). This same Hamiltonian can also be obtained projecting the Floquet Hamiltonian on the reference replica

$$H_{\rm FL} = \sum_j |u_j(0)\rangle\,\langle\langle u_j,0|\mathcal{H}_{\mathcal{F}}|u_j,0\rangle\rangle\,\langle u_j(0)|\ . \tag{5.59}$$

Notice that an additional transformation $U = \sum_j |j\rangle\langle u_j(0)|$ can be used to bring the Hamiltonian diagonal in the qubit basis. Indeed, the dynamics for the rotated state

$$\left|\bar\phi_j(t)\right\rangle = U\,|\phi_j(t)\rangle = e^{-i\varepsilon_j t}\,|j\rangle\ , \tag{5.60}$$

is given by

$$\mathcal{H}'_{\rm FL} = \varepsilon\sigma_z\,, \qquad \text{with} \qquad \varepsilon = \frac{\varepsilon_+ - \varepsilon_-}{2}\,. \tag{5.61}$$

5.4 cQED readout protocols using Floquet theory

In this Section we provide a simple illustration of Floquet theory on a two-level system which allows us to answer the guiding question (1.4)

Is there a generic mechanism to implement a longitudinal interaction? (5.62)

This Section is structured as follows

- In Section 5.4.1 we treat the problem semiclassically reducing to the quantum Rabi model discussed in Sec. 5.4.1, and obtaining the longitudinal and dispersive coupling by a Taylor expansion of the AC Stark shift around the drive point.
- In Sec. 5.4.2 we go beyond the semiclassical approach by performing a Schrieffer-Wolff transformation on the Floquet Hamiltonian. We recover the same expressions as in the semiclassical limit, plus a Lamb shift contribution to the qubit energy.

Finally, in Sec. 5.4.3, we treat the Purcell effect in our framework.

5.4.1 Semiclassical approach : the quantum Rabi model

In this Section we use the Floquet theory developed in the previous Section to derive the longitudinal and dispersive coupling from the drive-induced AC Stark shift of the qubit in the semiclassical limit $a \to \alpha$ (Sec. 3.1.2). First, we derive the drive-induced AC Stark shift of the qubit Larmor frequency in the quantum Rabi model, which is our model of interest 5.3 in the semiclassical approximation. Then, we obtain the longitudinal and dispersive coupling with a Taylor expansion of the AC Stark shift around the drive point.

The drive-induced AC Stark shift In this Section we derive the drive-induced AC-Stark shift in the quantum Rabi model, which is our system of interest in the semiclassical limit $a \to \alpha$. Its Hamiltonian reads (see Eq. (5.3))

$$\mathcal{H}' = \frac{\omega_{\mathrm{q}}}{2}\sigma_z + \frac{1}{2}\left(\mathcal{A}e^{-i\omega_{\mathrm{r}}t} + \mathcal{A}^* e^{i\omega_{\mathrm{r}}t}\right)\sigma_x \,. \tag{5.63}$$

To solve the quasi-energy spectrum, we consider the Floquet Hamiltonian

$$\mathcal{H}_{\mathcal{F}} = \mathbf{p}\,\omega_{\mathrm{r}} + \frac{\omega_{\mathrm{q}}}{2}\sigma_z + \frac{1}{2}\left(\mathcal{A}\, f_- + \mathcal{A}^*\, f_+\right)\sigma_x \,, \tag{5.64}$$

in the canonical basis $\{|\pm\rangle \otimes |p)\}$ of the Sambe space

$$\mathcal{H}_{\mathcal{F}} = \begin{pmatrix} \cdots & & & & & & \\ & \omega_{\mathrm{r}} + \frac{\omega_{\mathrm{q}}}{2} & 0 & 0 & \frac{\mathcal{A}^*}{2} & 0 & 0 & \\ & 0 & \omega_{\mathrm{r}} - \frac{\omega_{\mathrm{q}}}{2} & \frac{\mathcal{A}^*}{2} & 0 & 0 & 0 & \\ & 0 & \frac{\mathcal{A}}{2} & \frac{\omega_{\mathrm{q}}}{2} & 0 & 0 & \frac{\mathcal{A}^*}{2} & \\ & \frac{\mathcal{A}}{2} & 0 & 0 & -\frac{\omega_{\mathrm{q}}}{2} & \frac{\mathcal{A}^*}{2} & 0 & \\ & 0 & 0 & 0 & \frac{\mathcal{A}}{2} & -\omega_{\mathrm{r}} + \frac{\omega_{\mathrm{q}}}{2} & 0 & \\ & 0 & 0 & \frac{\mathcal{A}}{2} & 0 & 0 & -\omega_{\mathrm{r}} - \frac{\omega_{\mathrm{q}}}{2} & \\ & & & & & & & \cdots \end{pmatrix}, \tag{5.65}$$

and we solve its eigenvalue problem. From Eq. (5.65) we see that the renormalized drive $\mathcal{A}$ couples only adjacent replicas. Numerically, one can truncate the Floquet Hamiltonian up to

N_{rep} replicas and diagonalize the Hamiltonian. Convergence is ensured by increasing N_{rep} till the quasi-energies of interest change by less than a chosen tolerance. The problem yields N_{rep} eigenvectors

$$|u_j, n\rangle\rangle \equiv \begin{pmatrix} \vdots \\ \left|u^{(n)}_{j,-1}\right\rangle \\ \left|u^{(n)}_{j,0}\right\rangle \\ \left|u^{(n)}_{j,+1}\right\rangle \\ \vdots \end{pmatrix}, \tag{5.66}$$

with quasi-energy $\varepsilon^{(n)}_j = \varepsilon_j + n\omega_{\text{r}}$. Since the spectrum is periodic, one may restrict quasi-energies to a single Floquet zone $[-\omega_{\text{r}}/2, \omega_{\text{r}}/2]$ or work with a single replica in the unfolded picture. In this manuscript, we choose to work with a reference replica in the unfolded picture, since we developed a tracking scheme to follow the qubit states in the spectrum. At $\mathcal{A} = 0$ we fix the reference replica by choosing $\varepsilon_{\pm} = \pm\omega_{\text{q}}/2$ such that $\left|u^{(0)}_{j,0}\right\rangle$ is an eigenstate of σ_z, i.e. $\left|u^{(0)}_{j,0}\right\rangle = |\pm\rangle$, while all the other coefficients are zero, i.e. $\left|u^{(n)}_{j,0}\right\rangle = 0$ for $n \neq 0$. Hence,

$$|u_j, 0\rangle\rangle = \begin{pmatrix} \vdots \\ 0 \\ |\pm\rangle \\ 0 \\ \vdots \end{pmatrix}, \tag{5.67}$$

and from Eq. (5.48), this uniquely defines all the $|u_j, n\rangle\rangle$. To track each state as $\mathcal{A}$ increases, we make small increments $\mathcal{A} \to \mathcal{A} + \delta\mathcal{A}$ starting from $\mathcal{A} = 0$ and recompute the spectrum of (5.65)

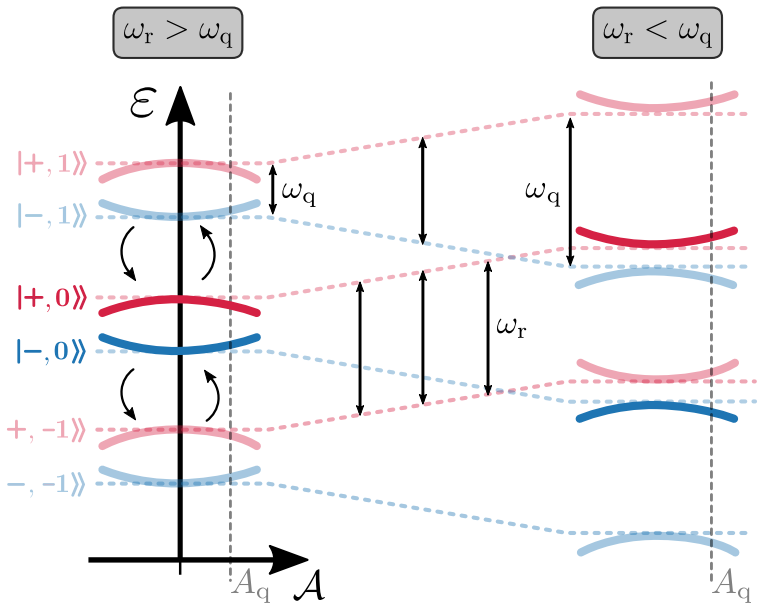

Figure 5.3: Schematic sketch of the Floquet spectrum. At zero drive $\mathcal{A} = 0$, the spectrum consists of the replicated qubit energies $\pm\omega_{\text{q}}/2 + n\omega_{\text{r}}$ (dashed red and blue lines). As $\mathcal{A}$ increases, level repulsion between $|\pm\rangle$ state in one replica and $|\mp\rangle$ state in the closest bends the spectrum. Sweeping ω_{q} from below to above ω_{q}, the relative position of the replica changes and the concavity of the spectrum changes sign.

at each step. Among the eigenvectors thus obtained, we identify $\left|u_j^{(n)}(\mathcal{A}+\delta\mathcal{A})\right\rangle\!\rangle$ as the one that maximizes the overlap $\left|\left\langle\!\left\langle u_j^{(n)}(\mathcal{A})\ \middle|\ u_j^{(n)}(\mathcal{A}+\delta\mathcal{A})\right\rangle\!\right\rangle\right|^2$.

Once the eigenvectors are known, we build the operator $\mathcal{U}^\dagger = \sum_{jn} |u_j, n\rangle\!\rangle \langle j|(n|$ whose columns are the coordinates of the eigenvectors in the canonical basis of the Sambe space and we obtain the diagonal Hamiltonian

$$\mathcal{D} = \mathcal{U}\mathcal{H}_{\mathcal{F}}\mathcal{U}^\dagger = \mathbf{p}\,\omega_{\mathrm{r}} + \varepsilon(\omega_{\mathrm{q}}, \omega_{\mathrm{r}}, |\mathcal{A}|)\,\sigma_z\,, \tag{5.68}$$

whose spectrum is sketched in Fig. 5.3. For $\mathcal{A} = 0$, the spectrum consists of the replicated qubit energies $\pm\omega_{\mathrm{q}}/2 + n\omega_{\mathrm{r}}$. As $\mathcal{A}$ increases, the drive term couples every $|\pm\rangle$ state of one replica to the $|\mp\rangle$ state of the closest one [94–98]. Similarly to a charge qubit detuning, $|\mathcal{A}|$ controls the repulsion between replicas, leading to a modification of the Larmor frequency known as *AC Stark shift*. When $\omega_{\mathrm{r}} > \omega_{\mathrm{q}}$, the $n = 1$ replica lies above the $n = 0$ and level repulsion bends the the $n = 0$ replica downward. When $\omega_{\mathrm{r}} < \omega_{\mathrm{q}}$, the ordering reverses, and level repulsion bends the $n = 0$ upward.

Figure 5.4 shows a numerical computation of the Floquet spectrum for stronger drive strength. For $\omega_{\mathrm{q}} > \omega_{\mathrm{r}}$, increasing $\mathcal{A}$ further brings $|-, 0\rangle\!\rangle$ into near-resonance with $|+, -3\rangle\!\rangle$, leading to the opening of a gap at the avoided crossing. This anticrossing originates from higher-order processes mediated by the third-order term $\mathcal{A}^3 f_-^3 \sigma_+$.

On the other hand, the spectrum in the diabatic regime $\omega_{\mathrm{q}} < \omega_{\mathrm{r}}$ does not suffer from these high order couplings, but it is rather dominated by the couplings between adjacent replicas, which flatten the spectrum at a much higher drive. This follows from the ordering of replicas in the diabatic regime: the replicas are well separated, whereas the qubit states within a replica lie close together. Any influence from a distant replica would require the quasi-energies of the $n = 0$ replica to pass through the $n = 1$ branch first, which is prevented by level repulsion. In other words, each replica remains confined to a "Floquet zone". For $n = 0$, this confinement

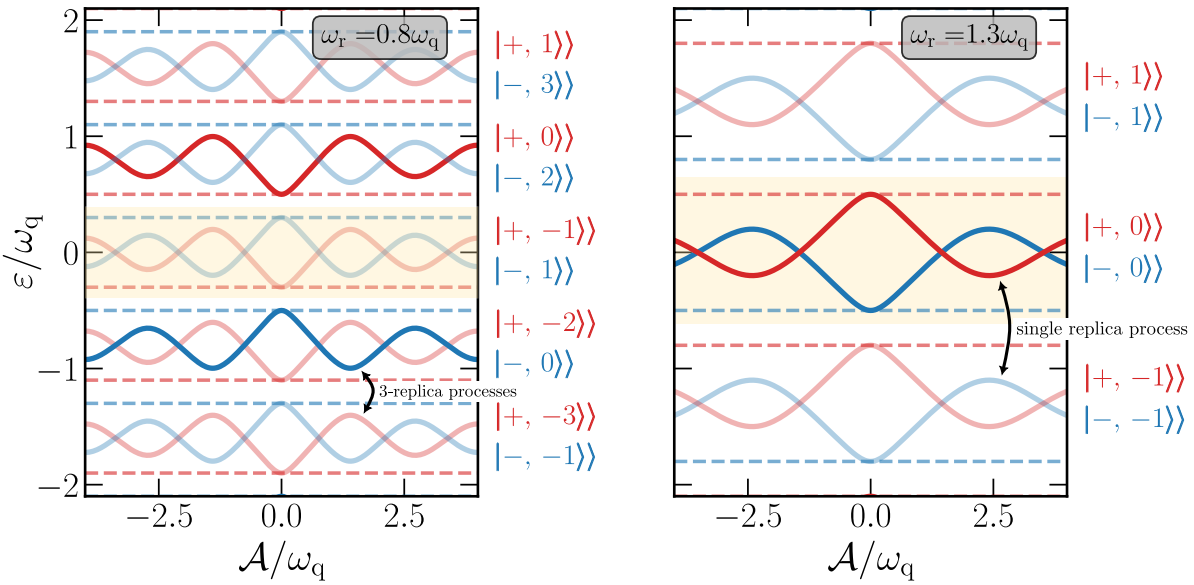

Figure 5.4: Floquet spectrum numerically computed as a function of the drive $\mathcal{A}$, that we chose to be real. On the right side of each plot, we connect each quasi-energy $\varepsilon_j^{(n)}$. We consider the case $\omega_{\mathrm{r}} < \omega_{\mathrm{q}}$ (left panel) and $\omega_{\mathrm{r}} > \omega_{\mathrm{q}}$ (right panel). Couplings with high order replicas affect only the spectrum for $\omega_{\mathrm{r}} < \omega_{\mathrm{q}}$. The highlighted orange region is the First Floquet Zone.

keeps the quasi-energy within $[-\omega_r/2, \omega_r/2]$ which is the *First Floquet Zone* (see also Fig. 5.5). The situation is different for $\omega_r < \omega_q$, where others replica ($n \neq 0$) fold into the First Floquet Zone in between the two branches ($|\pm\rangle$) of the $n = 0$ replica. Hence, the $n = 0$ replica interact with higher-order replicas. For fixed ω_r, increasing ω_q enlarges the separation between the $|\pm\rangle$ branches of $n = 0$ and more distant replica can fold in the First Floquet Zone in between them.

In Figure 5.5 we present an overview of the spectrum that summarize the preceding discussion. Panels (a) and (b) are analogues of the band plots in in Fig. 5.2. In 5.5a, for $\mathcal{A} = 0$, the spectrum consists of replicas shifted by quasienergies in multiples of the drive frequency. Crossings occur at $\varepsilon_j = n\omega_r/2$ open into avoided crossings when $\mathcal{A} \neq 0$. As the drive strength increases, the quasi-energy of the state $|+, 0\rangle\rangle$ bends and approaches $|-, 3\rangle\rangle$ in the regime $\omega_q > \omega_r$ (see Fig. 5.5c), while in the opposite regime it crosses $|-, 0\rangle\rangle$ without repulsion, since these levels are not coupled (see Fig. 5.5d).

Taylor expansion of the AC Stark shift Since we are interested in the dynamics at $\mathcal{A} = A_q + 2g_\perp\alpha$, we perform a Taylor expansion of the quasi-energy ε close to $\mathcal{A} = A_q$. Up to second order in $g_\perp\alpha$ the expansion yields

$$\varepsilon(\omega_q, \omega_r, |\mathcal{A}|) = \varepsilon(|A_q|) + 2g_\perp\alpha \left.\frac{\partial\varepsilon}{\partial\mathcal{A}}\right|_{A_q} + 2g_\perp\alpha^* \left.\frac{\partial\varepsilon}{\partial\mathcal{A}^*}\right|_{A_q} + 2g_\perp^2 \left[\alpha^2 \frac{\partial^2\varepsilon}{\partial\mathcal{A}^2} + 2|\alpha|^2 \frac{\partial^2\varepsilon}{\partial\mathcal{A}\partial\mathcal{A}^*} + \alpha^{*2} \frac{\partial^2\varepsilon}{\partial\mathcal{A}^{*2}}\right]_{A_q}, \tag{5.69}$$

such that using the Floquet-Lyapunov transformation (5.57) and neglecting the Kerr terms $\propto \alpha^2$, α^{*2}, the diagonal Hamiltonian reads

$$\mathcal{D} = \mathbf{p}\,\omega_r + \varepsilon(|A_q|)\sigma_z + 2g_\perp\alpha \left.\frac{\partial\varepsilon}{\partial\mathcal{A}}\right|_{A_q} \sigma_z + 2g_\perp\alpha^* \left.\frac{\partial\varepsilon}{\partial\mathcal{A}^*}\right|_{A_q} \sigma_z + 2g_\perp^2\alpha^2 \left.\frac{\partial^2\varepsilon}{\partial\mathcal{A}^2}\right|_{A_q} \sigma_z\,, \tag{5.70}$$

A more compact form is derived by expressing the derivatives along the real and imaginary part of $\mathcal{A}$, namely

$$\frac{\partial}{\partial\mathcal{A}} = \frac{1}{2}\left(\frac{\partial}{\partial \mathrm{Re}\mathcal{A}} - i\frac{\partial}{\partial \mathrm{Im}\mathcal{A}}\right), \qquad \frac{\partial}{\partial\mathcal{A}^*} = \frac{1}{2}\left(\frac{\partial}{\partial \mathrm{Re}\mathcal{A}} + i\frac{\partial}{\partial \mathrm{Im}\mathcal{A}}\right). \tag{5.71}$$

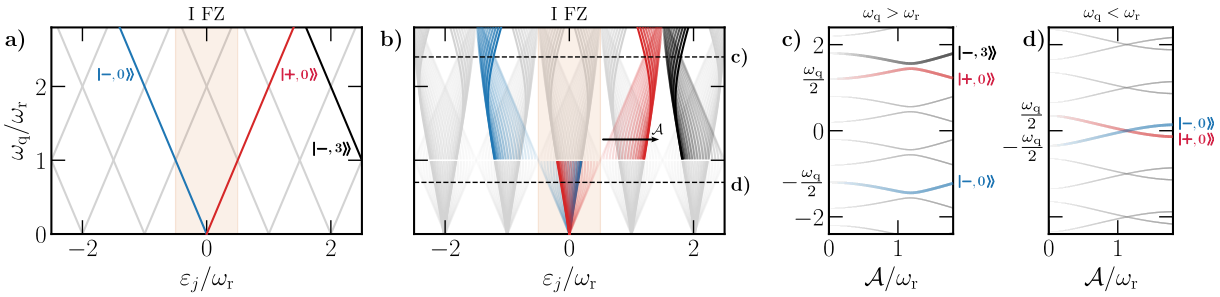

Figure 5.5: Floquet spectrum for the quantum Rabi model. The highlighted orange region is the First Floquet Zone. a) Floquet spectrum in the limit $\mathcal{A} = 0$. b) When $\mathcal{A} \neq 0$, the opacity of the lines increase with the drive strength and different replicas with different σ_z character cause the quasi-energies to bend. c-d) Detail of the AC Stark shift of the qubit energy as a function of the drive strength for $\omega_q > \omega_r$ (c) and $\omega_q < \omega_r$ (d). In c), couplings with higher order replicas flatten the quasi-energy spectrum at strong drive.

Since the derivatives in the expansion are evaluated on the real axis $\mathcal{A} = A_{\rm q}$, the first derivative on the imaginary part vanishes

$$\left.\frac{\partial\varepsilon}{\partial \mathrm{Im}\mathcal{A}}\right|_{A_{\rm q}} = 0\,. \tag{5.72}$$

As a result, we find that up to second order in $g_\perp\alpha$, the expansion in Eq. (5.69) close to $\mathcal{A} = A_{\rm q}$ gives

$$\mathcal{H}'_{\rm FL} = \left[\varepsilon(|A_{\rm q}|) + g_\parallel(\alpha+\alpha^*) + \chi|\alpha|^2\right]\sigma_z\,, \tag{5.73}$$

where the first-order term gives rise to a synthetic longitudinal coupling, and the second-order term gives a dispersive shift:

$$2g_\perp\alpha\left.\frac{\partial\varepsilon}{\partial\mathcal{A}}\right|_{A_{\rm q}} + 2g_\perp\alpha^*\left.\frac{\partial\varepsilon}{\partial\mathcal{A}^*}\right|_{A_{\rm q}} = g_\parallel(\alpha+\alpha^*)\,, \qquad 4g_\perp^2|\alpha|^2\left.\frac{\partial^2\varepsilon}{\partial\mathcal{A}\partial\mathcal{A}^*}\right|_{A_{\rm q}} = \chi|\alpha|^2\,, \tag{5.74}$$

with

$$g_\parallel = g_\perp\left.\frac{\partial\varepsilon}{\partial\mathrm{Re}\mathcal{A}}\right|_{A_{\rm q}}, \qquad \chi = g_\perp^2\left[\frac{\partial^2\varepsilon}{\partial|\mathcal{A}|^2} + \frac{1}{|\mathcal{A}|}\frac{\partial\varepsilon}{\partial|\mathcal{A}|}\right]_{A_{\rm q}}. \tag{5.75}$$

These equations establish a relation between the AC Stark shift, controlled by the driving amplitude $A_{\rm q}$, the longitudinal coupling $g_\parallel$ and the dispersive shift χ. The longitudinal coupling $g_\parallel$ is proportional to the *slope* of the Floquet quasi-energies, while the dispersive coupling χ includes a contribution from their *curvature* with respect to the drive strength. Equation (5.75) generalizes the expectation that both $g_\parallel$ and χ are governed by the curvature of the static spectrum $\partial^2\varepsilon/\partial|\mathcal{A}|^2|_{A_{\rm q},\omega_{\rm r}\to 0}$, as discussed previously in Sec. 3.3.2 [29, 30, 73–77, 99, 100].

5.4.2 Beyond the semiclassical approach

In this Section we go beyond the semiclassical approach $a \to \alpha$. We perform a Schrieffer-Wolff transformation obtaining the same expression (5.75) obtained in the semiclassical limit, plus a Lamb shift contribution to the qubit energy which corrects (5.75).Our goal here is to show that the expression (5.75) holds even beyond the semiclassical limit. To do so, we compare the Floquet Hamiltonian in the semiclassical limit,

$$\mathcal{H}_{\mathcal{F}} = \mathbf{p}\,\omega_{\rm r} + \frac{\omega_{\rm q}}{2}\sigma_z + \frac{1}{2}\left(\mathcal{A}\,f_- + \mathcal{A}^*\,f_+\right)\sigma_x\,, \tag{5.76}$$

and

$$\bar{\mathcal{H}}_{\mathcal{F}} = \mathbf{p}\,\omega_{\rm r} + \frac{\omega_{\rm q}}{2}\sigma_z + \frac{1}{2}\left(\mathcal{A}\,f_- + \mathcal{A}^\dagger\,f_+\right)\sigma_x\,, \tag{5.77}$$

which is the Floquet Hamiltonian associated with (5.3) without assuming the cavity in a coherent state. To keep notations as simple as possible, we have introduced the bar to distinguish $\bar{\mathcal{H}}_{\mathcal{F}}$ from $\mathcal{H}_{\mathcal{F}}$, where $\mathcal{A}$ will be considered as an operator or as a complex number respectively and without ambiguity.

To expose the relations in (5.75), which connect the derivatives of the Floquet spectrum to $g_\parallel$ and χ, it is useful to make explicit the presence of derivatives in $\bar{\mathcal{H}}_F$, namely

$$\bar{\mathcal{H}}_{\mathcal{F}} = \mathcal{H}_{\mathcal{F}}|_{\mathcal{A}=A_{\rm q}} + 2g_\perp a\left.\frac{\partial\mathcal{H}_{\mathcal{F}}}{\partial\mathcal{A}}\right|_{\mathcal{A}=A_{\rm q}} + 2g_\perp a^\dagger\left.\frac{\partial\mathcal{H}_{\mathcal{F}}}{\partial\mathcal{A}^*}\right|_{\mathcal{A}=A_{\rm q}}. \tag{5.78}$$

To make the derivatives of the Floquet spectrum appear, $\mathcal{H}_\mathcal{F}$ has to be diagonalized (see Sec. 5.4.1 for the diagonalization of the quantum Rabi model) and cast in the diagonal form

$$\mathcal{D} = \mathcal{U}\mathcal{H}_\mathcal{F}\mathcal{U}^\dagger = \mathbf{p}s\,\omega_\mathrm{r} + \varepsilon(\omega_\mathrm{q}, \omega_\mathrm{r}, |\mathcal{A}|)\,\sigma_z\,, \tag{5.79}$$

We then apply to the full quantum Hamiltonian $\bar{\mathcal{H}}_\mathcal{F}$ the unitary transformation $\mathcal{U}$ that diagonalizes the semiclassical $\mathcal{H}_\mathcal{F}$. The idea is that, if the semiclassical approximation does not hold, any correction to (5.75) should come from $\mathcal{U}\left(\bar{\mathcal{H}}_\mathcal{F} - \mathcal{H}_\mathcal{F}\right)\mathcal{U}^\dagger$.

To compute the terms in the rotated Hamiltonian $\mathcal{U}\bar{\mathcal{H}}_\mathcal{F}\mathcal{U}^\dagger = \bar{\mathcal{H}}'_\mathcal{F}$, we make use of the identity

$$\frac{\partial\mathcal{D}}{\partial\mathcal{A}} = [\gamma_1, \mathcal{D}] + \mathcal{U}\frac{\partial\mathcal{H}_\mathcal{F}}{\partial\mathcal{A}}\mathcal{U}^\dagger\,, \qquad \text{where} \qquad \gamma_1 = \mathcal{U}\,\frac{\partial\mathcal{U}^\dagger}{\partial\mathcal{A}}\bigg|_{\mathcal{A}=A_\mathrm{q}}\,. \tag{5.80}$$

The rotated Hamiltonian splits in three terms $\bar{\mathcal{H}}'_\mathcal{F} = \mathcal{D} + \mathcal{H}_1 + \mathcal{H}_2$ where

$$\mathcal{D} = \mathcal{U}\mathcal{H}_\mathcal{F}\mathcal{U}^\dagger = \mathbf{p}\,\omega_\mathrm{r} + \varepsilon(\omega_\mathrm{q}, \omega_\mathrm{r}, |\mathcal{A}|)\sigma_z\,, \tag{5.81}$$

$$\mathcal{H}_1 = 2g_\perp\left(a\,\frac{\partial\mathcal{D}}{\partial\mathcal{A}}\bigg| + a^\dagger\,\frac{\partial\mathcal{D}}{\partial\mathcal{A}^*}\bigg|\right)\,, \tag{5.82}$$

$$\mathcal{H}_2 = -2g_\perp[\gamma_1, \mathcal{D}]a + \mathrm{h.c.}\,, \tag{5.83}$$

where the shorthand notation $|_{\mathcal{A}=A_\mathrm{q}} \to |$ has been introduced to compactify the expressions and where h.c. stands for Hermitian conjugate. The contribution $\mathcal{D}$ is diagonal in the replica, qubit and Fock basis of the cavity, $\mathcal{H}_1$ is off-diagonal only in the Fock basis and $\mathcal{H}_2$ is off-diagonal in all the bases.

The longitudinal contribution At this stage, one can immediately show that $\mathcal{H}_1$ extends the result of Eq. (5.74), without assuming the cavity to be in a coherent state

$$\mathcal{H}_1 = g_\parallel(a + a^\dagger)\sigma_z\,, \qquad g_\parallel = g_\perp\,\frac{\partial\varepsilon}{\partial\mathrm{Re}\mathcal{A}}\bigg|_{A_\mathrm{q}}\,. \tag{5.84}$$

The dispersive contribution The off-diagonal term $\mathcal{H}_2$ in Eq. (5.81) is the one leading to the dispersive contribution. To perform the equivalent of the Taylor expansion in $g_\perp\alpha$ of the Floquet spectrum, we perform a Schrieffer-Wolff [72] transformation to $\bar{\mathcal{H}}'_\mathcal{F}$ up to second order in $g_\perp$. To do so, we introduce the effective Hamiltonian, as discussed in Appendix C

$$\bar{\mathcal{H}}''_\mathcal{F} = e^{i\mathcal{S}}\bar{\mathcal{H}}'_\mathcal{F}e^{-i\mathcal{S}} \simeq \mathcal{D} + \mathcal{H}_1 + \mathcal{H}_2 + i[\mathcal{S}, \mathcal{D}] + i[\mathcal{S}, \mathcal{H}_1 + \mathcal{H}_2] - \frac{1}{2}[\mathcal{S}, [\mathcal{S}, \mathcal{D}]] + \dots \tag{5.85}$$

Since the first order of $\mathcal{S}$ is derived by imposing the elimination of $\mathcal{H}_2$ through

$$i\left[\mathcal{S}^{(1)}, \mathcal{D}\right] = -\mathcal{H}_2\,, \tag{5.86}$$

one possible choice is clearly

$$i\mathcal{S}^{(1)} = 2g_\perp(\gamma_1 a + \gamma_2 a^\dagger)\,, \qquad \text{with}\,\gamma_2 = -\gamma_1^\dagger = -\mathcal{U}\,\frac{\partial\mathcal{U}^\dagger}{\partial\mathcal{A}^*}\bigg|_{\mathcal{A}=A_\mathrm{q}}\,. \tag{5.87}$$

However, as it can be seen from (5.86), $\mathcal{S}^{(1)}$ is defined up to elements that commute with $\mathcal{D}$. Introducing the projector $P_{\vec{q}_j} = |j\rangle |q\rangle (q| \langle j|$ onto the subspace $\vec{q}_j = (q, j)$, where q indexes the replica state and $j = \pm$ the qubit state, we introduce the short-hand notation

$$*X* = \sum_{\vec{q}_j} P_{\vec{q}_j} X P_{\vec{q}_j} \,, \tag{5.88}$$

which extracts the block-diagonal part of the operator X in the $\vec{q}_j$ sector basis. Using this, we choose $\mathcal{S}^{(1)}$ to contain only off-diagonal terms between the $\vec{q}$-sectors

$$i\mathcal{S}^{(1)} = 2g_\perp(\bar{\gamma}_1 a + \bar{\gamma}_2 a^\dagger) \,, \qquad \text{with} \qquad \bar{\gamma}_i = \gamma_i - *\gamma_i * \,. \tag{5.89}$$

Plugging Eq. (5.86) into Eq. (5.85), one sees that the second-order corrections generated by $\mathcal{S}$ read

$$\begin{aligned} \mathrm{II} = i\left[\mathcal{S}^{(1)}, \mathcal{H}_1\right] + \frac{i}{2}[\mathcal{S}^{(1)}, \mathcal{H}_2] = 4g_\perp^2 \Bigg(\left[\gamma_1, \frac{\partial \mathcal{D}}{\partial \mathcal{A}}\right] a^2 + \left[\gamma_2 a^\dagger, \frac{\partial \mathcal{D}}{\partial \mathcal{A}} a\right] \\ - \frac{1}{2}\left[\gamma_1, [\gamma_1, \mathcal{D}]\right] a^2 - \frac{1}{2}\left[\gamma_2 a^\dagger, [\gamma_1, \mathcal{D}]\, a\right] + \text{h.c.}\Bigg) \,. \end{aligned} \tag{5.90}$$

Among these, only the terms that are diagonal in both the qubit and replica space contribute to the effective Hamiltonian, while the other terms are eliminated by higher-order terms in $\mathcal{S}$, as discussed in Appendix C. The diagonal terms are captured by

$$*\mathrm{II}* = -2g_\perp^2 \left(* \left[\bar{\gamma}_1, [\bar{\gamma}_1, \mathcal{D}]\right] * a^2 + * \left[\bar{\gamma}_2 a^\dagger, [\bar{\gamma}_1, \mathcal{D}]\, a\right] * \right) + \text{h.c.} \,, \tag{5.91}$$

In this framework, our aim is to make apparent in (5.91) the presence of the second derivatives of the spectrum in the dispersive term as in (5.75) derived in the semiclassical limit. Thus, we first establish the connection between such derivatives and the $\gamma_{1,2}$ operator factors introduced in Eq. (5.89). From Eq. (5.80), we have

$$\begin{aligned} \frac{\partial^2 \mathcal{D}}{\partial \mathcal{A}^2} &= \frac{\partial}{\partial \mathcal{A}}\left[\gamma_1, \mathcal{D}\right] + \left[\gamma_1, \mathcal{U}\frac{\partial \mathcal{H}_\mathcal{F}}{\partial \mathcal{A}}\mathcal{U}^\dagger\right] \,, \\ \frac{\partial^2 \mathcal{D}}{\partial \mathcal{A}\partial \mathcal{A}^*} &= \frac{\partial}{\partial \mathcal{A}^*}\left[\gamma_1, \mathcal{D}\right] + \left[\gamma_2, \mathcal{U}\frac{\partial \mathcal{H}_\mathcal{F}}{\partial \mathcal{A}}\mathcal{U}^\dagger\right] \,. \end{aligned} \tag{5.92}$$

Now, since $*\gamma_1*$ is diagonal in the qubit and replica space, it commutes with $\mathcal{D}$ and its derivatives. Applying the operator $* \cdot *$ to both sides of (5.92) gives

$$\begin{aligned} \frac{\partial^2 \mathcal{D}}{\partial \mathcal{A}^2} &= * \left[\gamma_1, \frac{\partial \mathcal{D}}{\partial \mathcal{A}} - \left[\gamma_1, \mathcal{D}\right]\right] * = - * \left[\gamma_1, [\gamma_1, \mathcal{D}]\right] * \\ \frac{\partial^2 \mathcal{D}}{\partial \mathcal{A}\partial \mathcal{A}^*} &= * \left[\gamma_2, \frac{\partial \mathcal{D}}{\partial \mathcal{A}} - \left[\gamma_1, \mathcal{D}\right]\right] * = - * \left[\gamma_2, [\gamma_1, \mathcal{D}]\right] * \,. \end{aligned} \tag{5.93}$$

In addition, since $\bar{\gamma}_i$ is the purely off-diagonal part of γ_i, one finds

$$* \left[\gamma_i, [\gamma_j, \mathcal{D}]\right] * = * \left[\bar{\gamma}_i + *\gamma_i *, [\bar{\gamma}_j + *\gamma_j *, \mathcal{D}]\right] * = * \left[\bar{\gamma}_i, [\bar{\gamma}_j, \mathcal{D}]\right] * \,. \tag{5.94}$$

These expressions provide the relations between the second order derivatives of $\mathcal{D}$ and Eq. (5.91). Using the identities $[AB, C] = A[B, C] + [B, C]A$ and $AB = \{B, A\}/2 - [B, A]/2$, we evaluate

the second order contributions to the effective Hamiltonian

$$\begin{aligned}
-2g_\perp^2 * [\bar{\gamma}_1, [\bar{\gamma}_1, \mathcal{D}]] * a^2 &= 2g_\perp^2 \frac{\partial^2 \mathcal{D}}{\partial \mathcal{A}^2} a^2 \,, \\
-2g_\perp^2 * \left[\bar{\gamma}_2 a^\dagger, [\bar{\gamma}_1, \mathcal{D}]\, a\right] * &= 2g_\perp^2 \frac{\partial^2 \mathcal{D}}{\partial \mathcal{A} \partial \mathcal{A}^*} a a^\dagger + 2g_\perp^2 * \tilde{\gamma}_2 \, [\tilde{\gamma}_1, \mathcal{D}] * \\
&= 2g_\perp^2 \frac{\partial^2 \mathcal{D}}{\partial \mathcal{A} \partial \mathcal{A}^*} \left(a a^\dagger - \frac{1}{2}\right) + g_\perp^2 * \{\tilde{\gamma}_2, [\tilde{\gamma}_1, \mathcal{D}]\} * \,.
\end{aligned} \tag{5.95}$$

Reorganizing the terms in Eq. (5.91) with (5.95) we arrive at the form

$$*\mathrm{II}* = \chi \left(a^\dagger a + \frac{1}{2}\right) \sigma_z + 2g_\perp^2 \frac{\partial^2 \varepsilon}{\partial \mathcal{A}^2} a^2 \sigma_z + 2g_\perp^2 \frac{\partial^2 \varepsilon}{\partial \mathcal{A}^{*2}} a^{\dagger 2} \sigma_z + \mathcal{V} \,, \tag{5.96}$$

where the dispersive shift matches exactly the semiclassical expression (5.75)

$$\chi = 4g_\perp^2 \left.\frac{\partial^2 \mathcal{D}}{\partial \mathcal{A} \partial \mathcal{A}^*}\right|_{A_\mathrm{q}} = 4g_\perp^2 \left.\frac{\partial^2 \varepsilon}{\partial \mathcal{A} \partial \mathcal{A}^*}\right|_{A_\mathrm{q}} = g_\perp^2 \left[\frac{\partial^2 \varepsilon}{\partial |\mathcal{A}|^2} + \frac{1}{|\mathcal{A}|} \frac{\partial \varepsilon}{\partial |\mathcal{A}|}\right]_{A_\mathrm{q}} . \tag{5.97}$$

The remaining term

$$\mathcal{V} = g_\perp^2 * \{\bar{\gamma}_2, [\bar{\gamma}_1, \mathcal{D}]\} * + \mathrm{h.c.}\,. \tag{5.98}$$

will be shown below to be proportional to the identity operator in both the qubit and the replica space.

To examine $\mathcal{V}$, we inspect the general structure of the operators $\gamma_{1,2}$. The general form of γ_1 reads

$$\gamma_1 = -\sum_{jj'\alpha} \Gamma^\alpha_{jj'} f^\alpha_+ \left|j\right\rangle \left\langle j'\right| \,, \qquad \text{with}\, \Gamma^\alpha_{00} = (-1)^{\alpha+1} \Gamma^\alpha_{11} \,, \tag{5.99}$$

such that

$$\begin{aligned}
* \{\gamma_2, [\gamma_1, \mathcal{D}]\} * &= -\sum_{jj'\alpha} \Gamma^\alpha_{jj'} \Gamma^{\alpha *}_{jj'} \left(\left|j'\right\rangle \left\langle j'\right| + \left|j\right\rangle \left\langle j\right|\right) \left(\varepsilon_{j'} - \varepsilon_j - \alpha \omega_\mathrm{r}\right) \\
&= \omega_\mathrm{r} \sum_\alpha \alpha \left(2|\Gamma^\alpha_{00}|^2 + |\Gamma^\alpha_{10}|^2 + |\Gamma^\alpha_{01}|^2\right) \mathbf{1} + (\varepsilon_1 - \varepsilon_0) \sum_\alpha \left(|\Gamma^\alpha_{10}|^2 - |\Gamma^\alpha_{01}|^2\right) \mathbf{1}
\end{aligned} \tag{5.100}$$

which, together with $* \{\bar{\gamma}_2, [\bar{\gamma}_1, \mathcal{D}]\} * = * \{\gamma_2, [\gamma_1, \mathcal{D}]\} *$, shows that $\mathcal{V}$ contains only terms proportional to the identity.

Proof of (5.99)

We start writing explicitly the operator $\mathcal{U}^\dagger$, whose columns are the eigenvectors of $\mathcal{H}_\mathcal{F}$

$$\mathcal{U}^\dagger = \sum_{jn} \left|\, u_j, n\right\rangle\!\rangle \left\langle j\right| \left(n\right| = \sum_{jn} f^n_+ \left|u_{j,-n}\right\rangle \left\langle j\right| \,. \tag{5.101}$$

With this, the operator γ_1 takes the form

$$\gamma_1 = -\mathcal{U} \frac{\partial \mathcal{U}^\dagger}{\partial \mathcal{A}} = -\sum_{jj'\alpha} \Gamma^\alpha_{jj'} f^\alpha_+ \left|j\right\rangle \left\langle j'\right| \,, \quad \text{with} \quad \Gamma^\alpha_{jj'} = \sum_n \left\langle u_{j,n}\right| \frac{\partial}{\partial \mathcal{A}} \left|u_{j',n-\alpha}\right\rangle \,. \tag{5.102}$$

The symmetry of the Hamiltonian implies the relation$\Gamma^{\alpha}_{00} = (-1)^{\alpha+1}\Gamma^{\alpha}_{11}$. This property stems from an anti-unitary symmetry in the extended Floquet space, encoded in the transformation

$$\Theta = \sum_n (-1)^n |-n)(n|\sigma_x \mathcal{K}\,, \tag{5.103}$$

where $\mathcal{K}$ is the complex conjugate operator[a] . This symmetry satisfies

$$\Theta \mathcal{H}_{\mathcal{F}} \Theta^{\dagger} = -\mathcal{H}_{\mathcal{F}}\,,$$

and allows to construct the an eigenstate with energy $-\varepsilon_j$ from an eigenstate at ε_j. Indeed

$$\mathcal{H}_{\mathcal{F}} \Theta |u_j, 0\rangle\rangle = -\varepsilon_j \Theta |u_j, 0\rangle\rangle\,, \tag{5.104}$$

which, since $\varepsilon_{1-j} = -\varepsilon_j$, implies

$$|u_{1-j}, 0\rangle\rangle = \Theta |u_j, 0\rangle\rangle\,.$$

This leads to the identity

$$|u_{1-j,-n}\rangle = (-1)^n \sigma_x \mathcal{K}\, |u_{j,n}\rangle\ ,$$

or, in components

$$u_{j,n,\sigma} = (-1)^n u^*_{1-j,-n,1-\sigma}\,. \tag{5.105}$$

Using this identity, we now compute the matrix elements $\Gamma^{\alpha}_{jj'}$

$$\begin{aligned}
\Gamma^{\alpha}_{jj'} &= \sum_n \langle u_{j,n}|\, \partial_{\mathcal{A}}\, |u_{j',n-\alpha}\rangle \\
&= (-1)^{\alpha} \sum_n \langle \mathcal{K} u_{1-j,-n}|\, \partial_{\mathcal{A}}\, |\mathcal{K} u_{1-j',-n+\alpha}\rangle \\
&= (-1)^{\alpha} \sum_n \left(\partial_{\mathcal{A}} \langle u_{1-j',n}|\right) |u_{1-j,n+\alpha}\rangle \\
&= (-1)^{\alpha+1} \sum_n \langle u_{1-j',n}|\, \partial_{\mathcal{A}}\, |u_{1-j,n-\alpha}\rangle \\
&= (-1)^{\alpha+1} \Gamma^{\alpha}_{1-j',1-j}
\end{aligned}$$

finding the relation $\Gamma^{\alpha}_{00} = (-1)^{\alpha+1}\Gamma^{\alpha}_{11}$.

[a]The complex conjugate operator is anti-linear. This means that $\mathcal{K} c\,|\psi\rangle = c^* \mathcal{K}\,|\psi\rangle$. Note that the adjoint for an antilinear operator is defined through $\langle\phi|\mathcal{K}\psi\rangle = \left\langle \mathcal{K}^{\dagger}\phi|\psi\right\rangle^*$. Considering $|\psi\rangle = \sum_i \psi_i\,|i\rangle$ and $|\phi\rangle = \sum_i \phi_i\,|i\rangle$ we have $\langle \mathcal{K}\psi|\mathcal{K}\phi\rangle = \sum_i \psi_i \phi_i^* = \langle\psi|\phi\rangle^* = \langle\phi|\psi\rangle$ which implies $\mathcal{K}^{\dagger} = \mathcal{K}$.

Through a Schrieffer-Wolff transformation in the Sambe space, we have derived the effective Hamiltonian (5.85) up to order $g_{\perp}^2$

$$\bar{\mathcal{H}}''_{\mathcal{F}} = \mathcal{D} + g_{\parallel}(a + a^{\dagger})\sigma_z + \chi\left(a^{\dagger}a + \frac{1}{2}\right)\sigma_z + 2g_{\perp}^2 \frac{\partial^2 \varepsilon}{\partial \mathcal{A}^2} a^2 \sigma_z + 2g_{\perp}^2 \frac{\partial^2 \varepsilon}{\partial \mathcal{A}^{*2}} a^{\dagger 2} \sigma_z\,, \tag{5.106}$$

where we can recognize a Lamb shift correction $\chi/2$ of the qubit quasi-energy. Neglecting Kerr

terms, this is

$$\bar{\mathcal{H}}''_{\mathcal{F}} = \mathcal{D} + g_{\parallel}(a + a^{\dagger})\sigma_z + \chi\left(a^{\dagger}a + \frac{1}{2}\right)\sigma_z\,, \tag{5.107}$$

As shown by Eqs. (5.84) and (5.97), the longitudinal and dispersive couplings, $g_{\parallel}$ and χ, coincide with the semiclassical expression (5.75) given in Sec. (5.4.1)

$$g_{\parallel} = g_{\perp}\,\frac{\partial\varepsilon}{\partial \mathrm{Re}\mathcal{A}}\Big|_{A_{\mathrm{q}}}\,, \qquad\qquad \chi = g_{\perp}^2\left[\frac{\partial^2\varepsilon}{\partial|\mathcal{A}|^2} + \frac{1}{|\mathcal{A}|}\frac{\partial\varepsilon}{\partial|\mathcal{A}|}\right]_{A_{\mathrm{q}}}\,. \tag{5.108}$$

Hence, we have demonstrated that, up to a Lamb shift correction of the qubit quasi-energy, the expressions (5.75) found in the semiclassical limit hold.

5.4.3 Purcell effect

In this Section we give an alternative derivation of the Purcell effect within our formalism, which is equivalent to standard approaches [24] (see Sec. 3.1.1). To estimate the relaxation rate induced by the Purcell effect, we consider first the fact that photons in the cavity decay at rate κ. This decay is described by a Lindblad equation, which describes the evolution of the density matrix ρ of the system

$$\frac{\partial\rho}{\partial t} = -i[\mathcal{H},\rho] + \kappa\mathcal{D}_a[\rho]\,, \qquad\qquad \mathcal{D}_a\left[\rho\right] = a\rho a^{\dagger} - \frac{1}{2}\left\{a^{\dagger}a,\rho\right\}\,. \tag{5.109}$$

In the rotated frame defined by the combination of the Schrieffer-Wolff transformation $e^{i\mathcal{S}}$ and $\mathcal{U}$, the density matrix reads

$$\bar{\rho}(t) = \mathcal{U}^{\dagger}e^{-i\mathcal{S}}\rho(t)e^{i\mathcal{S}}\mathcal{U}\,, \tag{5.110}$$

which satisfies the master equation

$$\dot{\bar{\rho}} = \mathcal{L}\left[\bar{\rho}\right]\,, \qquad \text{with} \qquad \mathcal{L}\left[\bar{\rho}\right] = -i\left[\bar{\mathcal{H}}''_{\mathcal{F}},\bar{\rho}\right] + \mathcal{D}_{e^{i\mathcal{S}}ae^{-i\mathcal{S}}}\left[\bar{\rho}\right]\,. \tag{5.111}$$

The Purcell effect arises from the expansion of $e^{i\mathcal{S}}ae^{-i\mathcal{S}}$ at first order in $g_{\perp}$, where

$$i\mathcal{S}^{(1)} = 2g_{\perp}(\bar{\gamma}_1 a + \bar{\gamma}_2 a^{\dagger})\,, \qquad \text{with} \qquad \bar{\gamma}_i = \gamma_i - *\gamma_i *\,. \tag{5.112}$$

In practice, $i\mathcal{S}^{(1)}$ up to linear order in $g_{\perp}$ is given by γ_1 up to zero-th order in $\mathcal{A}$. Since $\gamma_1 = -\mathcal{U}\partial\mathcal{U}^{\dagger}/\partial\mathcal{A}$, we use the perturbative expression of $\mathcal{U}$ obtained in Appendix C.2 up to linear order in $\mathcal{A}$. We have

$$\mathcal{U} = \mathbf{1} + \frac{i}{2}\left(\frac{\mathcal{A}}{\omega_{\mathrm{q}}-\omega_{\mathrm{r}}}f_- + \frac{\mathcal{A}^*}{\omega_{\mathrm{q}}+\omega_{\mathrm{r}}}f_+\right)\sigma_+ - \frac{1}{2}\left(\frac{\mathcal{A}}{\omega_{\mathrm{q}}+\omega_{\mathrm{r}}}f_- + \frac{\mathcal{A}^*}{\omega_{\mathrm{q}}-\omega_{\mathrm{r}}}f_+\right)\sigma_-\,. \tag{5.113}$$

From this expression, we obtain

$$\gamma_1 = -\mathcal{U}\frac{\partial\mathcal{U}^{\dagger}}{\partial\mathcal{A}} = \frac{1}{2}\frac{1}{\omega_{\mathrm{q}}-\omega_{\mathrm{r}}}f_-\sigma_+ - \frac{1}{2}\frac{1}{\omega_{\mathrm{q}}+\omega_{\mathrm{r}}}f_-\sigma_-\,. \tag{5.114}$$

To leading order in $g_{\perp}$, we have

$$e^{i\mathcal{S}}ae^{-i\mathcal{S}} \simeq a + 2g_{\perp}\gamma_1^{\dagger} = a + \frac{g_{\perp}}{\omega_{\mathrm{q}}-\omega_{\mathrm{r}}}f_+\sigma_- - \frac{g_{\perp}}{\omega_{\mathrm{q}}+\omega_{\mathrm{r}}}f_+\sigma_+\,. \tag{5.115}$$

Neglecting sub-dominant cross-dissipative and counter-rotating terms, we obtain

$$\mathcal{D}_{e^{i\mathcal{S}}ae^{-i\mathcal{S}}}\left[\cdot\right] \approx \mathcal{D}_a\left[\cdot\right] + \gamma\mathcal{D}_{\sigma_-}\left[\cdot\right], \tag{5.116}$$

which describes an effective decay for the qubit at rate

$$\gamma = \frac{\kappa g_\perp^2}{(\omega_\mathrm{q}-\omega_\mathrm{r})^2}, \tag{5.117}$$

representing the manifestation of the Purcell effect.

5.5 Limiting cases

Considering the small drive limit $A_\mathrm{q} \to 0$, but for arbitrary ω_r, we find the direct connection between the longitudinal $g_\parallel^{(0)}$ and the dispersive coupling $\chi^{(0)}$ already discussed in Sec. 3.3.2. We perform a power series expansion of the quasi-energy

$$\varepsilon(|\mathcal{A}|) = \frac{\varepsilon_+ - \varepsilon_-}{2} = \sum_{n=0}^{\infty} q_n |\mathcal{A}|^{2n}, \tag{5.118}$$

where q_n are real coefficients. To leading order in A_q, one thus obtains that the second term in the expression of χ from Eq. (5.75) coincides with the curvature of the quasi-energies:

$$\lim_{|\mathcal{A}|\to 0} \frac{1}{|\mathcal{A}|}\frac{\partial\varepsilon}{\partial|\mathcal{A}|} = \lim_{|\mathcal{A}|\to 0} \frac{\partial^2\varepsilon}{\partial|\mathcal{A}|^2}. \tag{5.119}$$

We denote χ in this limit by $\chi^{(0)}$:

$$\chi^{(0)} = g_\perp^2 \lim_{|\mathcal{A}|\to 0}\left(\frac{\partial^2\varepsilon}{\partial|\mathcal{A}|^2} + \frac{1}{|\mathcal{A}|}\frac{\partial\varepsilon}{\partial|\mathcal{A}|}\right) = 2g_\perp^2 \lim_{|\mathcal{A}|\to 0}\frac{\partial^2\varepsilon}{\partial|\mathcal{A}|^2}. \tag{5.120}$$

Similarly, for the longitudinal coupling, we find to leading order in A_q

$$g_\parallel^{(0)} = g_\perp \left.\frac{\partial\varepsilon}{\partial \mathrm{Re}\mathcal{A}}\right|_{A_\mathrm{q}} = g_\perp A_\mathrm{q} \left.\frac{1}{|\mathcal{A}|}\frac{\partial\varepsilon}{\partial|\mathcal{A}|}\right|_{A_\mathrm{q}} = \frac{\chi^{(0)}}{2g_\perp}A_\mathrm{q}, \tag{5.121}$$

which is the same expression already found in Sec. 3.3.2. Equation (5.121) showcases the parametric dependence of the longitudinal coupling $g_\parallel$ on the drive A_q. The expression for q_1 can be found using a perturbative expansion of the eigen-energies in power series of $|\mathcal{A}|^2$, where the perturbation is $\mathcal{V} = (\mathcal{A}f_- + \mathcal{A}f_+)/2$

$$\varepsilon_\pm = \pm\frac{\omega_\mathrm{q}}{2} + \sum_k \frac{|\langle\langle \pm,0|\mathcal{V}|\mp,k\rangle\rangle|^2}{\pm\frac{\omega_\mathrm{q}}{2} - \left(\mp\frac{\omega_\mathrm{q}}{2} + k\omega_\mathrm{r}\right)} + \mathcal{O}\left(|\mathcal{A}|^4\right) \qquad \Longrightarrow \qquad q_1 = \frac{1}{2}\frac{\omega_\mathrm{q}}{(\omega_\mathrm{q}^2-\omega_\mathrm{r}^2)}. \tag{5.122}$$

For $\chi^{(0)}$, we obtain

$$\lim_{|\mathcal{A}|\to 0}\frac{\partial^2\varepsilon}{\partial|\mathcal{A}|^2} = \frac{\omega_\mathrm{q}}{(\omega_\mathrm{q}^2-\omega_\mathrm{r}^2)} \qquad \Longrightarrow \qquad \chi^{(0)} = 4g_\perp^2\frac{\omega_\mathrm{q}}{(\omega_\mathrm{q}^2-\omega_\mathrm{r}^2)}. \tag{5.123}$$

In the adiabatic limit $\omega_\mathrm{r} \to 0$, longitudinal and dispersive coupling reduce to

$$\lim_{\omega_\mathrm{r}\to 0} g_\parallel^{(0)} = \frac{g_\perp A_\mathrm{q}}{\omega_\mathrm{q}}, \qquad\qquad \lim_{\omega_\mathrm{r}\to 0}\chi^{(0)} = \frac{2g_\perp^2}{\omega_\mathrm{q}}, \tag{5.124}$$

which are exactly the curvature couplings in Eqs. (3.70-3.71).

We have thus demonstrated that Eq. (5.75) reproduces $g_\parallel, \chi$ in the dispersive and adiabatic regime.

5.6 Dispersive readout

For completeness, we show in this Section how the dispersive protocol, discussed in Sec. 3.1, is already embedded in the formalism just developed. For dispersive readout, we do not drive the qubit ($A_q = 0$) but rather drive the resonator with strength A_r, frequency ω_r, and phase-shifted by a conventional phase $\varphi = -\pi/2$. The Hamiltonian has the form

$$\mathcal{H} = \frac{\omega_q}{2}\sigma_z + g_\perp(a + a^\dagger)\sigma_x + \omega_r a^\dagger a + A_r \cos\left(\omega_r t - \frac{\pi}{2}\right)(a + a^\dagger)\,. \tag{5.125}$$

In the rotating frame defined by $\mathcal{U}_0(t) = e^{-i\omega_r t a^\dagger a}$, the rotated Hamiltonian $\mathcal{H}' = \mathcal{U}_0^\dagger \mathcal{H} \mathcal{U}_0 + i(\partial_t \mathcal{U}_0^\dagger)\mathcal{U}_0$ reads

$$\mathcal{H}' = \frac{\omega_q}{2}\sigma_z + \frac{1}{2}\left(\mathcal{A}e^{-i\omega_r t} + \mathcal{A}^\dagger e^{i\omega_r t}\right)\sigma_x - i\frac{A_r}{2}\left(a - a^\dagger\right)\,, \tag{5.126}$$

with $\mathcal{A} = 2g_\perp\alpha$ and where we have neglected the fast terms rotating at $\pm 2\omega_r t$. Following the same procedure used in Section 5.4.2, one finds the extended version of Eq. (5.106), namely

$$\bar{\mathcal{H}}''_{\mathcal{F}} = \mathbf{n}\omega_r + \varepsilon(\omega_q, \omega_d, |\mathcal{A}|)\sigma_z + \chi\left(a^\dagger a + \frac{1}{2}\right)\sigma_z - i\frac{A_r}{2}\left(a - a^\dagger\right)\,, \tag{5.127}$$

which is the Floquet Hamiltonian associated to the dispersive Hamiltonian (3.12).

5.7 Discussion of longitudinal readout

In this Section we discuss the implications of the expression for $g_\parallel$ and χ found in Eq. (5.75)

$$g_\parallel = g_\perp \left.\frac{\partial\varepsilon}{\partial \mathrm{Re}\mathcal{A}}\right|_{A_q}\,, \qquad \chi = g_\perp^2 \left[\frac{\partial^2\varepsilon}{\partial|\mathcal{A}|^2} + \frac{1}{|\mathcal{A}|}\frac{\partial\varepsilon}{\partial|\mathcal{A}|}\right]_{A_q}\,. \tag{5.128}$$

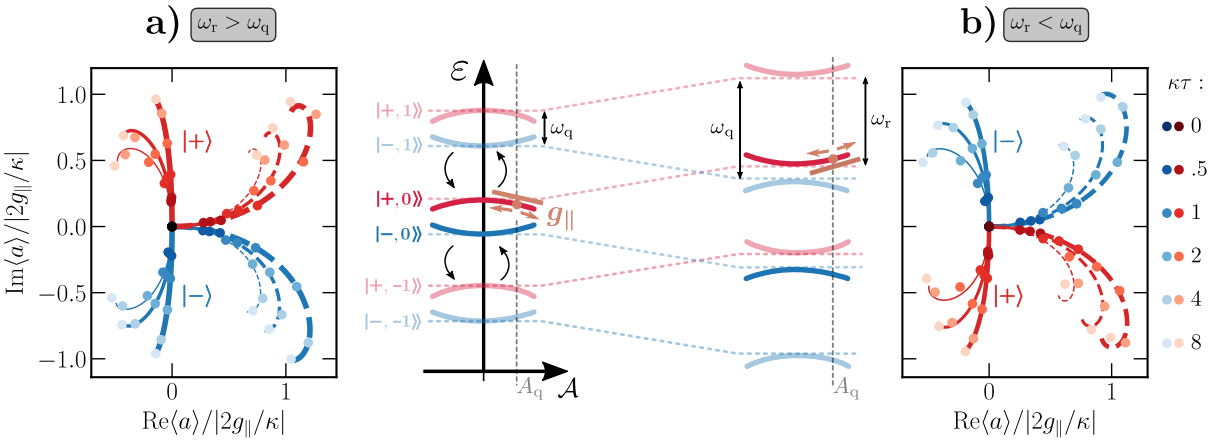

Figure 5.6: Sketch of Floquet spectrum for $\omega_r \gtrless \omega_q$ and trajectories of $\langle a(t)\rangle$ for longitudinal (solid) and dispersive readout (dashed), with $g_\perp/\omega_q = 10^{-2}$ and $\kappa/\omega_q = 2\cdot 10^{-3}$. a) Longitudinal trajectories are obtained for $A_q/\omega_q = 0.05$ and $\omega_r/\omega_q = 1.1, 1.15, 1.5$ (thin to thick). For dispersive readout, we set $\omega_r/\omega_q = 1.1$ to enforce the condition $|\chi^{(0)}| = \kappa/2$. b) Longitudinal trajectories are obtained for $A_q/\omega_q = 0.05$ and $\omega_r/\omega_q = 0.9, 0.8, 0.3$ (thin to thick). For dispersive readout, we set $\omega_r/\omega_q = 1.1$, to enforce the condition $|\chi^{(0)}| = \kappa/2$. In both panels, the cavity drive A_r is tuned so that the dispersive SNR matches the longitudinal SNR in the long-time limit $t \to \infty$ (see Fig. 3.4). The dashed lines in the Floquet spectrum indicate the quasi-energy levels for $\mathcal{A} = 0$. When $\mathcal{A} \neq 0$, the coupling between adjacent replicas causes the spectrum to bend.

This Section contains numerical simulations[3] that are not based on an effective description to verify the validity of our theory. Our theory predicts that the evolution of the cavity field follows from an effective longitudinal interaction. We compute these evolutions using the analytical expressions (3.97) where the coupling constants $g_\parallel$ and χ are computed by taking numerical derivatives of the Floquet spectrum. For all these (semi-)analytic evolutions, the spectrum is computed with at most $N_{\text{rep}} = 80$ replicas.

5.7.1 Change of sign across resonance

The expressions for $g_\parallel^{(0)}, \chi^{(0)}$ (5.120-(5.121)) obtained up to leading order in A_{q} exhibit a sign change across the resonance, $\omega_{\text{r}} \gtrless \omega_{\text{q}}$. Our theory provides a geometric interpretation of this behavior. As already discussed in Sec. 5.4.1, level repulsion bends the the $n = 0$ replica downward or upward according to $\omega_{\text{q}} \gtrless \omega_{\text{r}}$ (see in Fig. 5.6). Hence, both the slope and the curvature of the quasi-energies reverse sign when $\omega_{\text{r}} \gtrless \omega_{\text{q}}$. This mirrors the phase-space trajectories across the real axis and yields the sign change of $g_\parallel^{(0)}$ and $\chi^{(0)}$ across the resonance.

Figure 5.6 shows also the good agreement between the analytical time evolution and the exact numerics, and indicates that the purest longitudinal splitting is achieved by suppressing χ increasing the qubit-cavity detuning, see Eq. (5.121). The same expression predicts that $g_\parallel$ scales with χ and therefore vanishes as $\chi \to 0$. One can compensate this suppression by increasing A_{q} but, as shown below, large A_{q} drives the system beyond the parametric regime, introduces additional resonances, and can severely degrade the signal-to-noise ratio (SNR).

5.7.2 Deviations from parametric longitudinal coupling at strong drives

In this Section we explore the strong drive regime. We show that strong drives break the parametric regime of the longitudinal coupling.

As we have discussed in Sec. 3.3.2, the synthetic longitudinal coupling obtained driving the qubit at the resonator frequency is proportional to the drive strength A_{q} at small drives. Hence, the longitudinal coupling is parametric in the drive. We found that the parametric regime breaks down at strong drives. Figure 5.7a illustrates this by inspecting the signal-to-noise ratio (see Sec. 3.2.2) $\text{SNR}^2(t) = 2\kappa \int_0^t d\tau \, |\langle a(\tau)\rangle_+ - \langle a(\tau)\rangle_-|^2$ at short times, where $\langle a(t)\rangle_\pm \approx \mp i g_\parallel t$ (see Eq. (3.100)). While the linear dependence on A_{q} of the SNR at small drives reflects the parametric regime of $g_\parallel$, the saturation and drop at strong drive results from the flattening of the Floquet spectrum. Since this is more pronounced in the $\omega_{\text{r}} < \omega_{\text{q}}$ regime, due to the presence of higher-order replicas, the diabatic regime proves more robust at comparable drive strengths.

This situation is most evident in Fig. 5.7b, where the sudden drops for specific values of ω_{r} are entirely mirrored by the corresponding suppression of $g_\parallel$ in Fig. 5.7c, which explicitly reveals the limited range of validity of the parametric regime $g_\parallel^{(0)}$. These drops arise from anticrossings between distant replicas (Fig. 5.7d), which flatten the Floquet spectrum and, according to Eq. (5.75), suppress $g_\parallel$.

In Figure 5.8a we show that an SNR suppression also appears in the diabatic regime, but only at substantially larger drive strength. Rather than arising from couplings to distant replicas, this effect is due entirely to coupling between adjacent replicas (Fig. 5.8b) and corresponds to

[3]The numerical simulations were performed with QuTiP [101] simulating the evolution of $\langle a(t)\rangle$ with the Louvillian $\mathcal{L}[\cdot] = -i[H, \cdot] + \kappa \mathcal{D}_a[\cdot]$ with the *parent* Hamiltonian (5.2) and the initial condition $\rho_0 = |\pm\rangle\langle\pm|$, where $|\pm\rangle$ are the excited and ground state of the qubit. All the codes for generating data can be found at https://github.com/aleeschessari/Unifying-Floquet-Theory. For all the numerical simulations we consider at most 30 levels in the resonator.

the resonance condition $\omega_q' = \omega_r$, where $\omega_q' = \varepsilon_+(|\mathcal{A}|) - \varepsilon_-(|\mathcal{A}|)$. At weak drive, $\omega_q' \approx \omega_q$ and this resonance is the zero-detuning resonance $\omega_q = \omega_r$. At strong drive, the AC Stark shift moves away ω_q' from ω_q, so the resonance shifts to higher ω_r, as shown in Fig. 5.8a. In this sense, the signal in the diabatic regime is more robust towards degradation due to strong drive. Figure 5.8b confirms that this resonance involves adjacent replicas only, as already discussed.

5.8 Chapter 5 in a nutshell

In this Chapter we answered the main question posed in Chapter (1)

Is there a universal mechanism to implement a longitudinal interaction? (5.129)

We developed a unified Floquet theory of longitudinal and dispersive readout, and used it in two complementary ways.

First, using a semiclassical approach for intuition, we showed that $g_\parallel$ and χ follow from the first- and second-order variations of the Floquet quasi-energies

$$g_\parallel = g_\perp \left.\frac{\partial\varepsilon}{\partial \mathrm{Re}\mathcal{A}}\right|_{A_q}, \qquad \chi = g_\perp^2 \left[\frac{\partial^2\varepsilon}{\partial|\mathcal{A}|^2} + \frac{1}{|\mathcal{A}|}\frac{\partial\varepsilon}{\partial|\mathcal{A}|}\right]_{A_q}. \tag{5.130}$$

Then, we performed a Schrieffer–Wolff transformation in the Sambe space and showed that these expressions remain valid beyond our semiclassical approach.

These results reduce, in the appropriate limits, to the formulas derived in Chapter (3), and they also clarify their limitations:

- The longitudinal coupling is not, in general, set by the curvature of the static spectrum; generically it is controlled by the first-order variation of the Floquet spectrum (whose quasi-energies define the AC Stark shift of the qubit Larmor frequency).

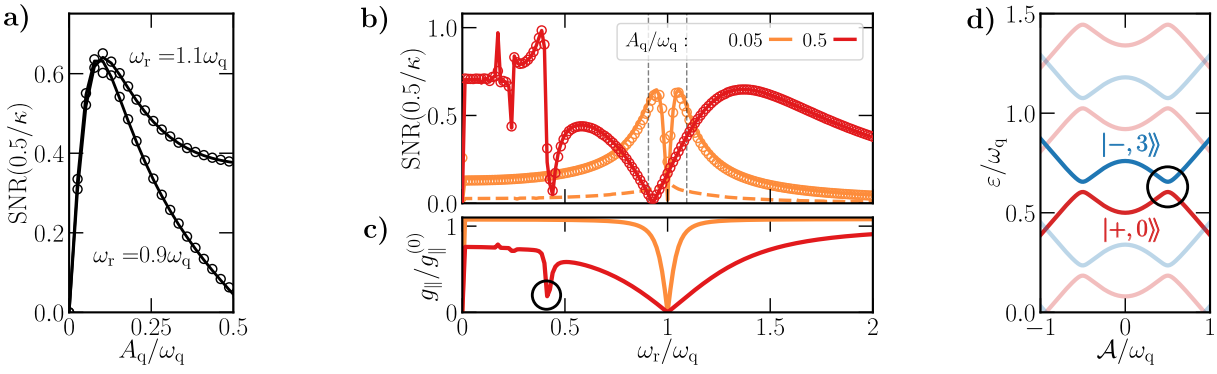

Figure 5.7: Deviations of the longitudinal coupling from the parametric regime. The dots correspond to numerical simulations, while solid lines are evolution obtained through Eq. (3.97) with $g_\parallel$,χ extracted from numerical evaluation of the Floquet spectrum. a) Parametric increase and suppression of the SNR at time $t = 0.5/\kappa$ as a function of A_q for $\omega_r/\omega_q = 0.9, 1.1$ (vertical dashed lines in panel (b)). b) SNR for different values of ω_r/ω_q and drive strength A_q. The vertical dashed line corresponds to the optimal dispersive case matching the longitudinal SNR for $A_q/\omega_q = 0.05$. d) Deviations from unity of $g_\parallel/g_\parallel^{(0)}$ as a function of ω_r/ω_q, where $g_\parallel^{(0)}$ is the longitudinal coupling in the small drive limit (Eq. (5.121)). e) Floquet spectrum as a function of the drive $\mathcal{A}$ (assumed to be real) for $\omega_r/\omega_q = 0.42$. The circle highlights avoided crossings between distant replicas at $A_q \simeq 0.5$, which are responsible for the suppression of $g_\parallel$ in panel (d).

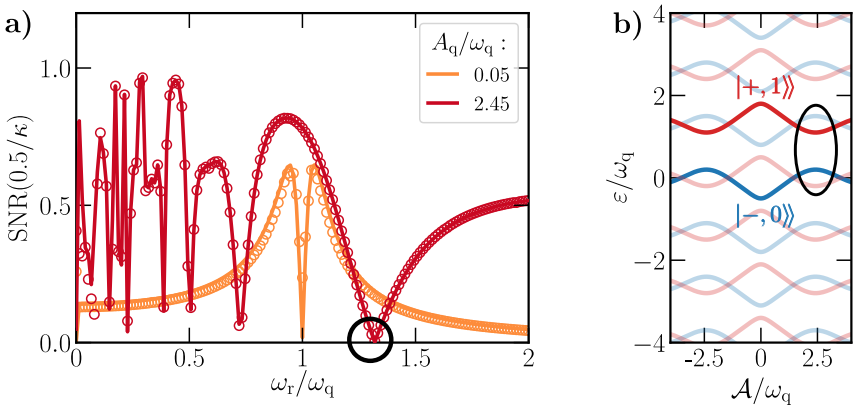

Figure 5.8: Signal-to-noise ratio suppression at strong drive. a) In the diabatic regime the suppression is only due to the usual resonance condition $\omega_q' = \omega_r$, where the qubit energy has been renormalized by the drive. Dots correspond to numerical simulations, while solid line are evolution obtained through Eq. (3.97) with $g_\parallel$,χ extracted from numerical evaluation of the Floquet spectrum. The circle highlights deterioration of the SNR at $\omega_r = 1.3\omega_q$ (diabatic regime). b) Floquet spectrum for $\omega_r = 1.3\omega_q$ shows that the deterioration of the SNR at $A_q/\omega_q = 2.45$ is due solely to coupling between adjacent replicas.

- The sign change across resonance in $g_\parallel$ and χ, obtained in the dispersive regime has a geometric interpretation as it is related to the relative positions of the replicas in the Floquet spectrum.

Finally, our theory has predictive power in a new regime prior theories could not reach, the strong-drive regime. We have seen that $g_\parallel$ is not always parametric in A_q since it is suppressed as the quasi-energy spectrum flattens at strong drive. If in the regime $\omega_r < \omega_q$ this occurs for specific values of ω_r, at the anticrossings between distant replicas, in the diabatic limit ($\omega_r > \omega_q$) the suppression occurs only when the usual resonance condition $\omega_q' = \omega_r$ holds. As a sizeable shift of the qubit frequency towards higher frequencies requires very large drive amplitudes, the diabatic regime is more robust against strong drive. Since the synthetic longitudinal coupling is obtained through a perturbative expansion in $g_\perp$, longitudinal readout is also limited by a critical number of photons n_{crit}.

Chapter

6 Applications to realistic multi-level systems

Contents

6.1 Extension of Floquet Theory to multi-level systems 82
6.2 Spin qubits 86
6.2.1 The model 88
6.2.2 The Floquet spectrum 91
6.2.3 Longitudinal readout of flopping-mode qubits 93
6.3 Superconducting qubits 94
6.3.1 The Josephson junction 94
6.3.2 The Transmon qubit 95
6.3.2.1 From the Cooper pair box to the transmon regime 96
6.3.2.2 Floquet spectrum 98
6.3.2.3 Longitudinal readout of a transmon qubit 100
6.3.3 The Fluxonium qubit 100
6.3.3.1 The model 101
6.3.3.2 The Floquet spectrum 102
6.3.3.3 Longitudinal readout for a fluxonium qubit 102
6.4 Polarizability contributions 103
6.5 Chapter 6 in a nutshell 104

The study of realistic systems requires to go beyond the idealized two-level scenario. In this chapter we show that the theory developed in Chapter 5 is relevant for actual devices, as the results readily extend to realistic spin and superconducting cQED architectures. Indeed, a straightforward generalization of Eqs. (5.75-5.106) to m-levels still holds.

In Section 6.1, we show that each qubit level couples independently to the cavity with its own longitudinal $g_{\parallel,j}$ and dispersive χ_j coupling. They are both given by Eq. (5.75) with the substitution $\varepsilon \to \varepsilon_j$. Since in general $\varepsilon_1(|\mathcal{A}|) \neq -\varepsilon_0(|\mathcal{A}|)$, projecting on the two level subspace, the mapping onto Eq. (5.107) leads to an effective longitudinal coupling renormalized by an additional σ_z-independent term.

This generalization applies to a variety of different platforms from spin-qubits to superconducting qubits (Sec. 6.3).

Finally, in Section 6.4, we show how the theory could be further generalized to account for polarizability contributions.

6.1 Extension of Floquet Theory to multi-level systems

In this section we give a generalization of the Floquet approach of Section 5.4.1 to multi-level systems. We consider systems described by a general Hamiltonian $\mathcal{H}_{\rm sys}[Q]$. The Hamiltonian

depends on a generic parameter Q (detuning, number of Cooper pairs induced on the superconducting island by the gate voltage, ...). A classical drive and the resonator modulate this parameter, $Q \to Q_0 + \delta Q$, with $\delta Q = A_\mathrm{q}\cos(\omega_\mathrm{d} t) + g_\perp(a + a^\dagger)$. The coupling between system and resonator $g_\perp$ depends on the coupling scheme whereas A_q is the strength of the drive. We consider the drive at a general frequency ω_d which, for the moment, we set to be equal to the resonator frequency: $\omega_\mathrm{d} = \omega_\mathrm{r}$.

This framework is intentionally general. It allows us to treat a wide range of platforms, from spin to superconducting qubits, and it lends itself to straightforward generalization to other coupling schemes.

Expanding the Hamiltonian to linear order in δQ (terms in δQ^2 are called the polarizability contributions and are treated in Sec. 6.4) we obtain

$$\mathcal{H} = \mathcal{H}_\mathrm{sys}[Q_0] + \left.\frac{\partial \mathcal{H}_\mathrm{sys}}{\partial Q}\right|_{Q_0} \delta Q + \omega_\mathrm{r} a^\dagger a \,. \tag{6.1}$$

Following the same procedures detailed in Sections 5.3, we build the Floquet Hamiltonian

$$\mathcal{H}_\mathcal{F} = \mathbf{n}\omega_\mathrm{d} + \mathcal{H}_\mathrm{sys}[Q_0] \otimes \mathbf{1}_\mathcal{F} + \frac{1}{2}\left(\mathcal{A} f_- + \mathcal{A}^\dagger f_+\right) \left.\frac{\partial \mathcal{H}_\mathrm{sys}}{\partial Q}\right|_{Q_0} , \tag{6.2}$$

where the Floquet replicas are shifted by integer multiples of the drive frequency ω_d and $\mathbf{1}_\mathcal{F}$ is the identity operator acting on the Floquet (Sambe) space. Projecting the Hamiltonian onto a basis of coherent states $|\alpha\rangle$, and expressing it in the qubit $\{|j\rangle\}$ and Floquet basis $\{|p)\}$, the Hamiltonian takes the block matrix form

$$\mathcal{H}_\mathcal{F} = \begin{pmatrix} \ddots & \ddots & & & \\ \ddots & \omega_\mathrm{d}\mathbf{1} + \mathcal{H}_\mathrm{sys} & \frac{\mathcal{A}^*}{2}\left.\frac{\partial \mathcal{H}_\mathrm{sys}}{\partial Q}\right|_{Q_0} & 0 & \\ & \frac{\mathcal{A}}{2}\left.\frac{\partial \mathcal{H}_\mathrm{sys}}{\partial Q}\right|_{Q_0} & \mathcal{H}_\mathrm{sys} & \frac{\mathcal{A}^*}{2}\left.\frac{\partial \mathcal{H}_\mathrm{sys}}{\partial Q}\right|_{Q_0} & \\ & 0 & \frac{\mathcal{A}}{2}\left.\frac{\partial \mathcal{H}_\mathrm{sys}}{\partial Q}\right|_{Q_0} & -\omega_\mathrm{d}\mathbf{1} + \mathcal{H}_\mathrm{sys} & \ddots \\ & & & \ddots & \ddots \end{pmatrix} , \tag{6.3}$$

where $\mathbf{1}$ is the identity acting on the Hilbert space on which the system Hamiltonian $\mathcal{H}_\mathrm{sys}$ acts. The Floquet Hamiltonian can be diagonalized leading to the quasi-energies ε_j. Projecting onto the zero-th replica, we obtain the effective Hamiltonian in the rotating frame, as discussed in Sec. 5.3. The Taylor expansion of the quasi-energies around $\mathcal{A} = A_\mathrm{q}$ yields

$$\mathcal{H}'_\mathcal{F} = \sum_{j=1}^{m} \left[\varepsilon_j(\omega_\mathrm{q}, \omega_\mathrm{d}, |A_\mathrm{q}|) + \frac{1}{2}\chi_j\right] \mathcal{P}_j + g_{\parallel,j}(a + a^\dagger)\mathcal{P}_j + \chi_j a^\dagger a \mathcal{P}_j \,, \tag{6.4}$$

where we have introduced the projectors over the j-th level $\mathcal{P}_j = |j\rangle\langle j|$. Notice the presence of the term $\chi_j \mathcal{P}_j/2$, which accounts for quantum effects in the cavity. These terms arise from the Schrieffer-Wolff transformation discussed in Section 5.4.2, which we assumed can be generalized to this case. Each Floquet mode couples longitudinally and dispersively to the cavity independently. The expressions of $g_{\parallel,j}$ and χ_j are given by

$$g_{\parallel,j} = g_\perp \left.\frac{\partial \varepsilon_j}{\partial \mathrm{Re}\mathcal{A}}\right|_{\mathcal{A}=A_\mathrm{q}} , \qquad \chi_j = g_\perp^2 \left[\frac{\partial^2 \varepsilon_j}{\partial |\mathcal{A}|^2} + \frac{1}{|\mathcal{A}|}\frac{\partial \varepsilon_j}{\partial |\mathcal{A}|}\right]_{\mathcal{A}=A_\mathrm{q}} . \tag{6.5}$$

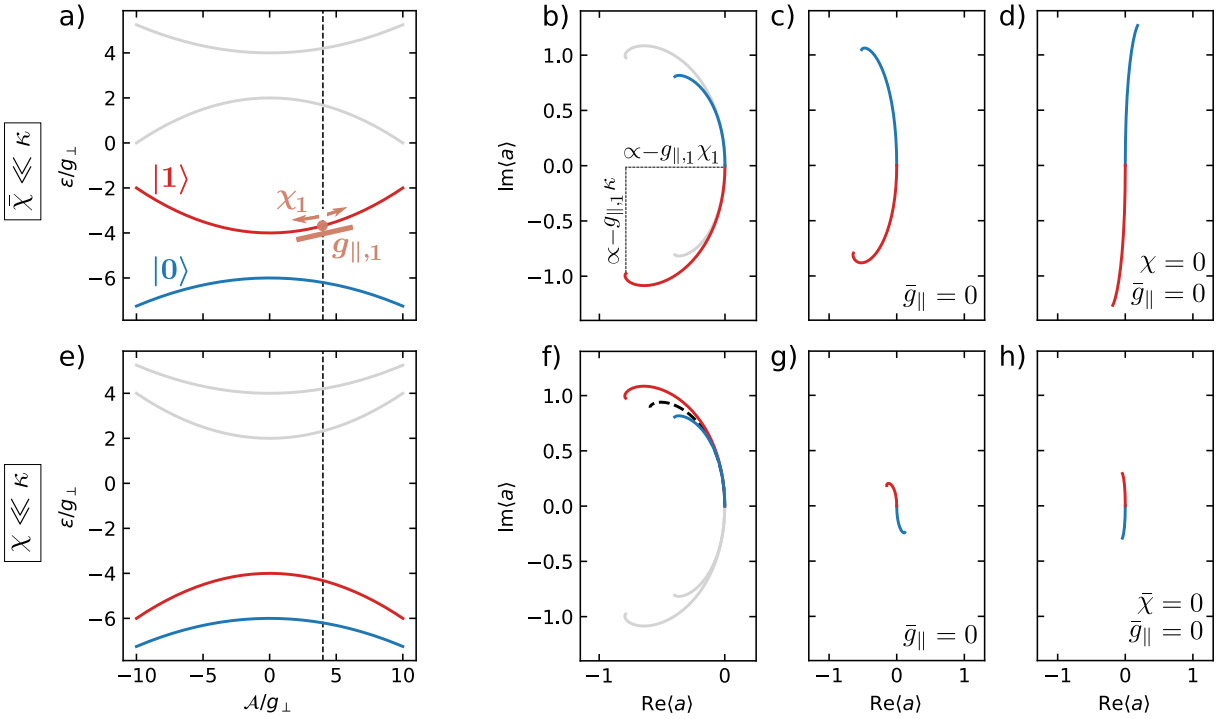

Figure 6.1: Floquet spectrum and readout of a multi-level system for $\bar{\chi} \ll \kappa$ (a-d) and $\chi \ll \kappa$ (e-h). The Floquet spectrum in function of a real $\mathcal{A}$ is used to determine the couplings $\chi_0/g_\perp = -0.05$, $\chi_1/g_\perp = 0.08$ (a) and $\chi_0/g_\perp = -0.05$, $\chi_1/g_\perp = -0.08$ (e) at the drive point at $A_\mathrm{q}/g_\perp = 0,4$ (dashed vertical line). The longitudinal coupling is related to the first derivative of the spectrum and for a quadratic spectrum is related to the value of χ_j through $g_{\parallel,j} = A_\mathrm{q}\chi_j/2g_\perp$. In b), f) the time evolution of $\langle a(t)\rangle$ for a qubit prepared in $|0\rangle$ (blue trajectory) or $|1\rangle$ (red trajectory) reaches a steady state whose real (imaginary) part is determined by $-g_{\parallel,1}\chi_1$ ($-g_{\parallel,1}\kappa$). In f) $\bar{g}_\parallel$ is responsible for the dynamics of the "center of mass" $(\langle a(t)\rangle_1 + \langle a(t)\rangle_0)/2$ (dashed black line). In (c), (g) the same evolution is plotted considering $\bar{g}_\parallel = 0$ to isolate the effects of χ (c) or $\bar{\chi}$ (g) on the dynamics. An almost perfect 180° is obtained considering $\chi = \bar{g}_\parallel = 0$ (d) or $\bar{\chi} = \bar{g}_\parallel = 0$ (h). The steady state in (b-d) and (f-h) are obtained considering time evolution till $t = 10/\kappa$ with $\kappa = 0.2/g_\perp$.

To gain insight into the influence of $g_{\parallel,j}$ and χ_j in shaping the cavity response, we consider the Heisenberg equation of motion for the cavity field $\langle a(t)\rangle$. Assuming the qubit is initialized in $|j\rangle$, we have

$$\partial_t \langle a(t)\rangle = -ig_{\parallel,j} - i\chi_j \langle a(t)\rangle - \frac{\kappa}{2}\langle a(t)\rangle \,. \tag{6.6}$$

The solution to this linear differential equation is given by

$$\langle a(t)\rangle = \frac{-ig_{\parallel,j}}{i\chi_j + \kappa/2}\left(1 - e^{-i\chi_j t - \frac{\kappa}{2}t}\right) . \tag{6.7}$$

As shown in Fig. 6.1b, for each level the real part of the steady-state amplitude is proportional to $-g_{\parallel,j}\chi_j$, while the imaginary part scales as $-g_{\parallel,j}\kappa$.

Projection onto a two level system A projection of Eq. (6.4) onto the manifold spanned by $|0\rangle$ and $|1\rangle$ leads to

$$\mathcal{H}_\mathcal{F} = \left(\varepsilon(A_\mathrm{q}) + \frac{\chi}{2}\right)\sigma_z + g_\parallel(a + a^\dagger)\sigma_z + \chi a^\dagger a\sigma_z + \bar{g}_\parallel(a + a^\dagger) + \bar{\chi}a^\dagger a \,, \tag{6.8}$$

where we have mapped the system onto a qubit Hamiltonian whose energy is given by

$$\varepsilon(A_{\mathrm{q}}) = \frac{1}{2}\left[\varepsilon_1(A_{\mathrm{q}}) - \varepsilon_0(A_{\mathrm{q}})\right] , \tag{6.9}$$

and with the resulting couplings

$$g_{\parallel} = \frac{1}{2}\left(g_{\parallel,1} - g_{\parallel,0}\right) , \quad \bar{g}_{\parallel} = \frac{1}{2}\left(g_{\parallel,1} + g_{\parallel,0}\right) , \quad \chi = \frac{1}{2}(\chi_1 - \chi_0) , \quad \bar{\chi} = \frac{1}{2}(\chi_1 + \chi_0) . \tag{6.10}$$

The terms proportional to $\bar{\chi}$ and $\bar{g}_{\parallel}$ in Eq. (6.8) do not couple the qubit and the resonator, thus giving rise to a qubit-independent dynamics. The influence of these terms becomes more apparent by inspecting Eq. (3.85). Indeed, the Hamiltonian (6.8) is exactly (3.85) with the substitutions $\delta \to \bar{\chi}$, $A_{\mathrm{r}}/2 \to \bar{g}_{\parallel}$ and $\varphi \to 0$. Hence, the dynamics of the cavity is still given by Eqs. (3.95-3.97).

Compensation tone Although the contributions from $\bar{\chi}$ and $\bar{g}_{\parallel}$ are always present when considering realistic systems outside of an idealized charge qubit, the equivalence between (6.8) and (3.85) through the substitutions $\delta \to \bar{\chi}$, $A_{\mathrm{r}}/2 \to \bar{g}_{\parallel}$ and $\varphi \to 0$ indicates that by applying a compensation tone to the cavity with amplitude $A_{\mathrm{r}} = -2\bar{g}_{\parallel}$ and frequency $\omega_{\mathrm{d}} = \omega_{\mathrm{r}}$, one can compensate the term proportional to $\bar{g}_{\parallel}$ in the Hamiltonian. We show the influence of this term and the effects of its removal in following limiting cases :

- Quasi-energies with opposite curvature: $\bar{\chi} \ll \kappa$. In this regime, the cavity dynamics is given by

$$\langle a(t)\rangle_{\text{long.}} = -\frac{i}{2}\sum_{\sigma=\pm 1}\left[(g_{\parallel} + \sigma\bar{g}_{\parallel})(\langle\sigma_z(0)\rangle + \sigma)\frac{1 - e^{-\frac{\kappa}{2}t - i\sigma\chi t}}{i\sigma\chi + \frac{\kappa}{2}}\right] , \tag{6.11}$$

  and the system's behavior closely resembles that of the ideal two level system studied in Chapter 5 with the effect of $\bar{g}_{\parallel}$ limited to a renormalization of the longitudinal coupling $g_{\parallel}$, as illustrated in Fig. 6.1b. Compensating $\bar{g}_{\parallel}$ reproduces the longitudinal splitting (Fig. 6.1c) of the two-level system discussed in the previous Chapter, see Fig. 5.6.

- Quasi-energies with similar curvature: $\chi \ll \kappa$, the evolution of the cavity expectation value reads

$$\langle a(t)\rangle_{\text{long.}} = -i\left(\bar{g}_{\parallel} + g_{\parallel}\langle\sigma_z(0)\rangle\right)\frac{1 - e^{-\frac{\kappa}{2}t - i\bar{\chi}t}}{i\bar{\chi} + \kappa/2} . \tag{6.12}$$

  As shown in Fig. 6.1f, $\bar{g}_{\parallel}$ governs the dynamics of the "center of mass" of the pointer states of $|0\rangle$ and $|1\rangle$

$$\frac{1}{2}\left(\langle a(t)\rangle_1 + \langle a(t)\rangle_0\right) = -i\bar{g}_{\parallel}\left(\frac{1 - e^{-\frac{\kappa}{2}t - i\bar{\chi}t}}{i\bar{\chi} + \kappa/2}\right) , \tag{6.13}$$

  where $\langle a(t)\rangle_j$ is the expectation value of the field when the qubit is initialized in the $|j\rangle$ state. When this dynamics is subtracted, the effects of $\bar{\chi}$ becomes apparent: a change in the qubit state results in a change of sign of both the real and imaginary part of the cavity expectation value, as shown in Fig. 6.1g.

Furthermore, by tuning ω_{d} such that[1] $\delta = \omega_{\mathrm{d}} - \omega_{\mathrm{r}} = \bar{\chi}$, one may also compensate the term proportional to $\bar{\chi}$.

In the following Sections, we use the generalized Floquet theory developed here to study longitudinal readout for spin and superconducting qubits.

[1]The condition $\omega_{\mathrm{d}} - \omega_{\mathrm{r}} = \bar{\chi}$ is a self-consistency equation for ω_{d}, since $\bar{\chi}$ is computed from $\varepsilon_j(\omega_{\mathrm{q}}, \omega_{\mathrm{d}}, |A_{\mathrm{q}}|)$.

6.2 Spin qubits

In this Section we give a brief introduction of spin-qubits, present the Hamiltonian for a typical cQED implementation (Sec. 6.2.1), describe the Floquet spectrum (Sec. 6.2.2), and discuss how to perform longitudinal readout (Sec. 6.2.3).

Spin qubits are actively studied as promising platforms for scalable quantum information processing as the spin degree of freedom of an electron or a hole naturally provides a two-level system that is relatively insensitive to electric field noise. The small size, long coherence times, and available industrial infrastructure provide a highly competitive candidate for scalable solid-state quantum information processing [103].

In particular, quantum dot (QD) spin qubits can be fabricated using standard CMOS processes or quantum-dot nanostructures, offering the potential to exploit existing semiconductor manufacturing techniques for the creation of dense, scalable qubit arrays (see Fig. 6.2). As shown in Fig. 6.3a, a carrier is trapped in a semiconductor material thanks to the interplay between electrical and structural confinements. Structural confinement typically arises from the finite thickness of the host material, while metallic gate electrodes introduce both vertical and in-plane electric fields, ultimately trapping the carrier in a localized potential well. The electrons or holes are fed to the QDs by *reservoirs*, which are device areas with an excess of carriers. The proper alignment of the QD levels and the chemical potential of the reservoirs provides a tight control over the number of charges in the QD. An external magnetic field lifts the degeneracy between the spin states $|\uparrow\rangle$ and $|\downarrow\rangle$ of the trapped carrier and defines the Larmor frequency $\omega_q = g\mu_B B$, where g is its g-factor and μ_B is the Bohr magneton. This Zeeman splitting defines a quantum two-level system, where the information is encoded in the spin state of the trapped particle. With typical Larmor frequencies in the order of few GHzs, temperatures well below 1 K are required to discriminate the two energy levels and avoid thermal population.

The intrinsic size of quantum dots, on the order of ~ 100 nm, makes them ideally suited for integration into dense architectures that could be mass-produced using microelectronics industry processes [21]. Still, this compact scale also introduces significant engineering challenges, particularly with respect to the individual addressing and control of each qubit. Since electron spins

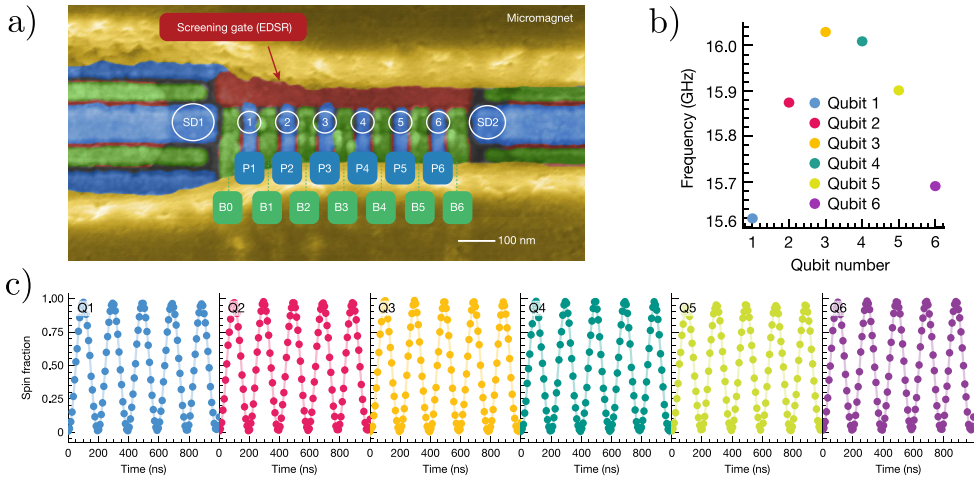

Figure 6.2: Coherent control of an array of spin qubits. a) Each colour represents a different metallization layer. Plunger (P, blue) and barrier (B, green) gates are used to define quantum dots in the channel between the screening gates (red) and sensing dots (SD1 and SD2) on the side. Two cobalt micromagnets (yellow) are placed on top of the gatestack. b) Qubit frequency for each of the six qubits. c) Rabi oscillations for every qubit, taken sequentially. Figure adapted from Ref. [102]

naturally couple to magnetic fields, coherent transitions between the $|\uparrow\rangle$ and $|\downarrow\rangle$ states can only be driven, in principle, only by an oscillating magnetic field. This approach, known as electron spin resonance (ESR), was first demonstrated in silicon-based qubits [107]. While ESR is effective for single-qubit control, the implementation of localized oscillating magnetic fields across large-scale qubit arrays poses substantial technical difficulties. To overcome these limitations, an alternative and more scalable approach is to rely on Electric Dipole Spin Resonance (EDSR), which leverages electric fields instead of magnetic fields to drive spin transitions. EDSR offers better prospects for scalability, as electric fields can be locally applied to individual qubits via gate electrodes. However, since electric fields couple to charge rather than spin, an intermediate mechanism is required to mediate the interaction between the electric field and the spin state. Spin-orbit coupling (SOC) provides this necessary link. Spin-orbit coupling (SOC) also plays a crucial role in enabling coupling between spin qubits and superconducting microwave cavities, underpinning the foundation of hybrid circuit quantum electrodynamics (cQED) architectures. Indeed, direct coupling between a single spin magnetic dipole and the magnetic field of the cavity results in a spin-cavity coupling rate which is too weak to be useful.

Strong spin-orbit coupling had been found for electrons in InAs nanowires, where the large g-factor [108–110] enables coupling of a single electron spin to a microwave cavity (see Fig. 6.3c) [25]. Unfortunately, the coherence time for electron spins in InAs is limited by the abundance of nuclear spins, which couple to the electron spins via the hyperfine interaction and enhancing their relaxation rate. Better coherence times can be achieved in Silicon, but the intrinsic SOC is too weak, and an artificial SOC has to be engineered [104, 105, 111, 112]. In Fig. 6.3a-b, this is achieved placing Cobalt micromagnets near the quantum dots. Micromagnets produce a local gradient in the static magnetic field such that, when an electron oscillates between the two dots, it experiences an oscillating magnetic field, providing the necessary (indirect) spin-charge hybridization.

Although micromagnets have been successfully used to control electron spins in hybrid cQED platforms, they require additional magnetic control lines that are not very scalable. On the other hand, leveraging valence band states to host spin qubits offers significant advantages due to the intrinsic properties of hole states. Unlike conduction-band electrons, which experience weak spin-orbit coupling (SOC) due to their predominantly s-like orbital character, holes in the

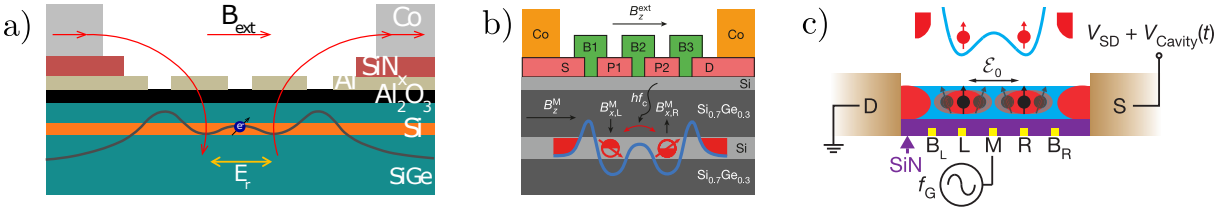

Figure 6.3: Spin qubits in different configurations. a) A single electron moves in the double dot potential landscape (greyline) in response to the resonator electric field, E_r [104, 105]. b) The blue line indicates the electrostatic confinement potential which delocalizes a single electron between the two dots (indicated as half-filled circles). The quantization axis of the electron spin (red arrow) changes between the dots [106]. In a)-b) micromagnets create an a magnetic field gradient providing a spin-charge hybridization. c) The left and right barrier gates (BL and BR), left and rightplunger gates (L and R), and middle gate (M) are biased to create a double-well potential within the nanowire. The drain contact of the nanowire, D, is grounded, and the source contact, S, is connected to an antinode of the resonator, oscillating at a voltage $V_\mathrm{cavity}(t)$. An a.c. voltage at a frequency f_G is applied to gate M to generate an oscillating electric field, $\mathcal{E}_0$. Due to the presence of a strong spin–orbitinteraction, the displacement of the electron induces transitions between the spin-states [25].

valence band originate from p-like orbitals and thus exhibit inherently stronger SOC. CMOS-compatible Hole spin qubits in Silicon have been realized for the first time in Grenoble [20] in 2016. More recently, they showed good coherence times [28] and strong spin-photon coupling (Fig. 6.4) [26], making this platform a suitable candidate to explore longitudinal readout.

6.2.1 The model

We consider the general setup sketched in Fig. 6.4c, which represents a general configuration in which a double quantum dot traps a single charge and is coupled to a superconducting cavity. The Hamiltonian describing the qubit reads [25, 26, 104, 105, 111–120]

$$\mathcal{H}_{\text{sys}}\left[\frac{\varepsilon_0}{2}\right] = \underbrace{\frac{\Delta}{2}\sigma_z}_{\substack{\text{Zeeman}\\ \text{splitting}}} + \underbrace{\frac{\varepsilon_0}{2}\tau_z}_{\substack{\text{Dot}\\ \text{detuning}}} + \underbrace{t_{\text{sc}}\,\tau_x}_{\substack{\text{Spin-conserving}\\ \text{tunneling}}} - \underbrace{t_{\text{sf}}\,\tau_y\sigma_y}_{\substack{\text{Spin-flip}\\ \text{tunneling}}}, \tag{6.14}$$

where the Pauli operator $\sigma_z = |\uparrow\rangle\langle\uparrow| - |\downarrow\rangle\langle\downarrow|$ acts on the spin degrees of freedom ($|\uparrow,\downarrow\rangle$) whereas $\tau_z = |L\rangle\langle L| - |R\rangle\langle R|$ acts on the spatial ($|L,R\rangle$) degrees of freedom. In the absence of magnetic field, the tunneling between between the left ($|L\rangle$) and right ($|R\rangle$) dots, which are detuned by the energy ε_0, is purely spin-conserving with amplitude t_{c}. A static magnetic field induces a Zeeman splitting $\Delta > 0$ between the $|\uparrow,\downarrow\rangle$ spin states, and a finite SOC. This gives rise to two distinct tunneling processes : a spin-conserving tunneling with amplitude t_{sc} and a spin-flipping tunneling with amplitude t_{sf}.

These two amplitudes are related to the zero-field tunneling strength t_c via the relations $t_{\text{sc}} = t_{\text{c}}\cos\eta$ and $t_{\text{sf}} = t_{\text{c}}\sin\eta$, where η is an effective SOC angle. This angle depends on the SOC strength, the orientation and strength of the magnetic field, and the device geometry [26].

The spectrum of the Hamiltonian The Hamiltonian (6.14) has a symmetry generated by $\Gamma = \tau_y\sigma_x$, which anticommutes with the Hamiltonian, $\Gamma\mathcal{H}_{\text{sys}}\Gamma^{-1} = -\mathcal{H}_{\text{sys}}$. Hence, each of the two lowest energy qubit eigenstates $|0\rangle$ and $|1\rangle$ has a high energy partner $\left|\bar{j}\right\rangle = \Gamma\,|j\rangle$ with energy $E_{\bar{j}} = -E_j$, where the notation $\left|\bar{j}\right\rangle$ emphasizes the chiral symmetry. We can therefore write the

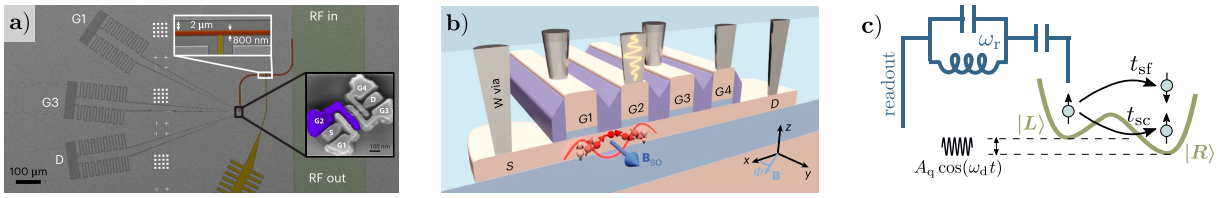

Figure 6.4: Hybrid cQED platform for readout of a hole spin qubit in Silicon. a) False-colour top-view scanning electron micrograph of a representative circuit. The resonator (red) is galvanically connected to the gate electrode G2. b) Schematic cross section of the DQD device. The gates (G), the source (S) and the drain (D) of the nanowire transistor are connected with vertical vias to the NbN circuitry located at the surface of the device. The double quantum well is located below the gates G1 and G2. The effect of the SO interaction is illustrated by a hole whose spin rotates coherently while tunneling from one dot to the other in the presence of an effective spin-orbit field B_{SO} (blue arrow). The orange wave-packet on the via connecting G2 pictures the photon in the microwave cavity. The external magnetic field B is applied in-plane with an angle φ to the nanowire axis. c) Schema of a general hybrid cQED setup where a particle is confined in a double potential well formed by two tunnel-coupled quantum dots. The left dot is coupled to the resonator while the right dot is controlled via an electrical signal with amplitude A_{q} and frequency ω_{d}. Panels a) and b) are adapted from Ref. [26].

	t_c/Δ	η	t_{sc}/Δ	t_{sf}/Δ	ω_q/Δ	$g_\perp/\Delta$	κ/Δ
charge regime	2	$2\pi/10$	0.4	0.29	0.64	-	-
spin regime	0.6	$2\pi/7$	1	1.3	0.6	$2\cdot10^{-2}$	$2\cdot10^{-3}$

Table 6.1: Parameters of the spin qubit in Figure 6.5 and 6.7. Values of $g_\perp$ and κ are extracted from Ref. [26].

Hamiltonian in the basis of the two doublets $|0\rangle$, $|1\rangle$ and $|\bar{0}\rangle$, $|\bar{1}\rangle$ as

$$\mathcal{H}_{sys}\left[\frac{\varepsilon_0}{2}\right] = \frac{\omega_q(\varepsilon_0)}{2}\tau_z + \frac{\bar{\omega}_q(\varepsilon_0)}{2}\tau_z',$$

where we have introduced the Pauli-Z operators in the eigenbasis of the system

$$\tau_z' = |1\rangle\langle 1| - |0\rangle\langle 0|, \qquad \bar{\tau}_z' = |\bar{1}\rangle\langle\bar{1}| - |\bar{0}\rangle\langle\bar{0}|, \tag{6.15}$$

and the Larmor frequency of the doublets

$$\omega_q(\varepsilon_0) = E_1(\varepsilon_0) - E_0(\varepsilon_0), \qquad \bar{\omega}_q = E_{\bar{1}}(\varepsilon_0) - E_{\bar{0}}(\varepsilon_0). \tag{6.16}$$

The spectrum of the Hamiltonian in function of the detuning ε_0 is shown in Fig. 6.5. When $t_{sc/sf} = 0$, the eigenstates are localized in space and spin. Switching on t_{sc} hybridizes the $|L\rangle$ and $|R\rangle$ states, while t_{sf} causes anticrossings between charge qubit states with different spin component.

Analytical evaluation of the spectrum at the sweet spot Below, we focus the discussion at $\varepsilon_0 = 0$, since this is the charge noise sweet spot.

The tunneling t_{sc} splits the antibonding state $|+\rangle = (|L\rangle + |R\rangle)/\sqrt{2}$ and the bonding state $|-\rangle = (|L\rangle - |R\rangle)/\sqrt{2}$. To analyze the impact of spin-flip tunneling t_{sf} on $|\pm\rangle$, we consider the basis

$$\mathcal{B} = \{|+,\uparrow\rangle, |-,\uparrow\rangle, |+,\downarrow\rangle, |-,\downarrow\rangle\}. \tag{6.17}$$

In this basis the Hamiltonian is the matrix

$$\begin{pmatrix} t_{sc}+\frac{\Delta}{2} & & & -t_{sf} \\ & -t_{sc}+\frac{\Delta}{2} & t_{sf} & \\ & t_{sf} & t_{sc}-\frac{\Delta}{2} & \\ -t_{sf} & & & -t_{sc}-\frac{\Delta}{2} \end{pmatrix}. \tag{6.18}$$

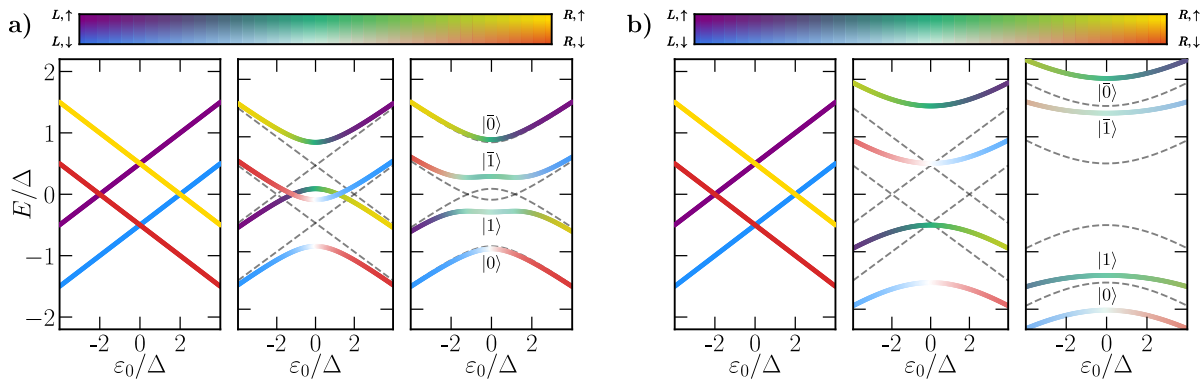

Figure 6.5: Static spectrum of the charge regime $2t_{sc} < \Delta$ (a) and of the flopping mode regime $2t_{sc} > \Delta$ (b). In (a) and (b) the panels show the spectrum for i) $t_{sc} = t_{sf} = 0$, ii) $t_{sf} = 0$ and iii) t_{sc}, $t_{sf} \neq 0$ (from left to right). The figures are generated using the parameters of the qubit detailed in Table 6.1.

Without loss of generalities we consider in this discussion the case $t_{\rm sc} > 0$.

The matrix (6.18) is block-diagonal and can be separated in two independent 2×2 blocks, which can be treated separately. The first block is spanned by $|+,\uparrow\rangle, |-,\downarrow\rangle$ and reads

$$\begin{pmatrix} t_{\rm sc} + \frac{\Delta}{2} & -t_{\rm sf} \\ -t_{\rm sf} & -t_{\rm sc} - \frac{\Delta}{2} \end{pmatrix} . \tag{6.19}$$

The eigenenergies are

$$E_{\bar{0},0} = \pm \frac{1}{2} \sqrt{4t_{\rm sf}^2 + (2t_{\rm sc} + \Delta)^2} , \tag{6.20}$$

and corresponds to the highest ($E_{\bar{0}}$) and lowest (E_0) energy eigenstates of the system, namely

$$\begin{aligned} |\bar{0}\rangle &= \cos\frac{\theta}{2} |+,\uparrow\rangle - \sin\frac{\theta}{2} |-,\downarrow\rangle , \\ |0\rangle &= \sin\frac{\theta}{2} |+,\uparrow\rangle + \cos\frac{\theta}{2} |-,\downarrow\rangle , \end{aligned} \tag{6.21}$$

with the mixing angle defined by

$$\tan\theta = \frac{2t_{\rm sf}}{2t_{\rm sc} + \Delta} . \tag{6.22}$$

As shown in Fig. 6.6, we have $\sin\theta/2 \approx 1$ and the effects of $t_{\rm sf}$ on this block are minimal, as the unperturbed states $|-,\downarrow\rangle$ and $|+,\uparrow\rangle$ are well separated in energy. As a result, the eigenstates remain close to their unperturbed forms: $|0\rangle \approx |-,\downarrow\rangle$ and $|\bar{1}\rangle \approx |+,\uparrow\rangle$.

The second block, spanned by $|-,\uparrow\rangle$ and $|+,\downarrow\rangle$, is given by

$$\begin{pmatrix} -t_{\rm sc} + \frac{\Delta}{2} & t_{\rm sf} \\ t_{\rm sf} & t_{\rm sc} - \frac{\Delta}{2} \end{pmatrix} . \tag{6.23}$$

Its eigenenergies are

$$E_{\bar{1},1} = \pm \frac{1}{2} \sqrt{4t_{\rm sf}^2 + (2t_{\rm sc} - \Delta)^2} , \tag{6.24}$$

and the corresponding eigenstates are

$$\begin{aligned} |\bar{1}\rangle &= \cos\frac{\phi}{2} |+,\downarrow\rangle + \sin\frac{\phi}{2} |-,\uparrow\rangle , \\ |1\rangle &= \sin\frac{\phi}{2} |+,\downarrow\rangle - \cos\frac{\phi}{2} |-,\uparrow\rangle , \end{aligned} \tag{6.25}$$

with the mixing angle defined by

$$\tan\phi = \frac{2t_{\rm sf}}{2t_{\rm sc} - \Delta} . \tag{6.26}$$

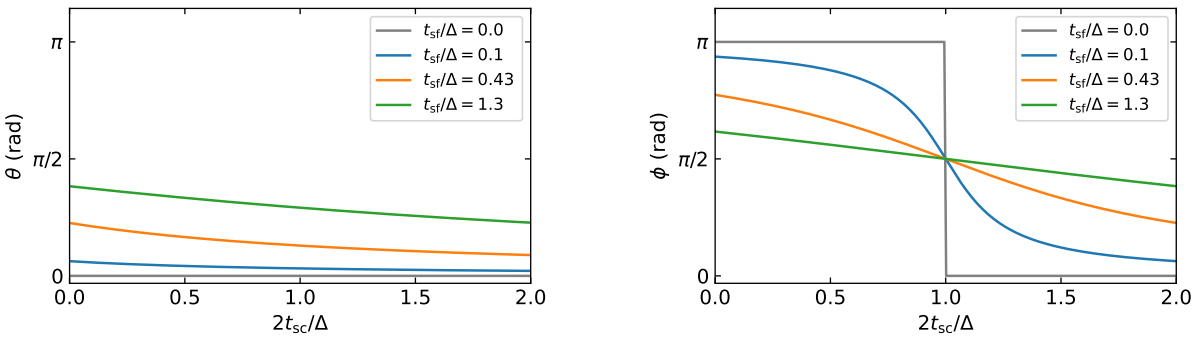

Figure 6.6: Angles ϕ and θ computed through Eqs. (6.22)-(6.26) in function of $2t_{\rm sc}/\Delta$.

Charge ($2t_{\rm sc} < \Delta$) and spin ($2t_{\rm sc} > \Delta$) regimes Two distinct regimes can be identified. In both cases the logical qubit is formed by the two lowest levels, with Larmor frequency $\omega_{\rm q} = E_1 - E_0$. When $2t_{\rm sc} < \Delta$, the magnetic field is so strong that the Zeeman splitting dominates, and the spin sectors are well-separated. In this regime we have $\sin\phi/2 \approx 1$ (see Fig. 6.6) and the two lowest eigenstates that define the logical qubit are $|0\rangle = |-,\downarrow\rangle$ and $|1\rangle = |+,\downarrow\rangle$. The $|0\rangle \to |1\rangle$ transition is almost purely a charge excitation, making the qubit more sensitive to charge noise. This is the *charge regime*, since within each spin sector the system reduces to the charge qubit discussed in Section 4.1.

In the spin (or *flopping mode* [121]) regime with $2t_{\rm sc} > \Delta$, one has $\cos\phi/2 \approx 1$ (see Fig. 6.6), and the logical states of the qubit are $|0\rangle = |-,\downarrow\rangle$ and $|1\rangle = |-,\uparrow\rangle$. The key advantage of this regime lies in the nature of the $|0\rangle \to |1\rangle$ transition, which corresponds to an almost pure spin flip, with any change in the charge configuration controlled by $t_{\rm sf}$. As a result, the qubit's Larmor frequency becomes largely insensitive to low frequency modulation of the detuning (charge noise), since the charge configuration remains unchanged during the transition.

6.2.2 The Floquet spectrum

In this Section we analyze the Floquet spectrum of the system. The parameter Q in this case is the detuning, $Q = \varepsilon_0/2$, and the drive realizes a parametric modulation of the detuning $\varepsilon_0(t) = \varepsilon_0 + 2A_{\rm q}\cos(\omega_{\rm d}t)$. As in Secs. 2.4 and 3.3.2, we write the dipole operator τ_z in the eigenbasis of the system. Although the theory is not restricted to $\varepsilon_0 = 0$, we focus on this operating point since it is the charge noise sweet spot. In this case, the eigenstates of the system are the ones computed in the previous Section, and τ_z can be expressed in such basis by introducing the *intra-doublets* (τ') and *inter-doublets* (σ') operators (see Appendix (B.1.2.1))

$$\tau'_x = |0\rangle\langle 1| + |1\rangle\langle 0| \qquad \bar{\tau}'_x = |\bar{0}\rangle\langle\bar{1}| + |\bar{1}\rangle\langle\bar{0}| \,, \tag{6.27}$$

$$\sigma'_x = |0\rangle\langle\bar{1}| + |\bar{1}\rangle\langle 0| \,, \qquad \bar{\sigma}'_x = |\bar{0}\rangle\langle 1| + |1\rangle\langle\bar{0}| \,. \tag{6.28}$$

With these notations,

$$\tau_z = \sin\left(\frac{\phi-\theta}{2}\right)(\tau'_x + \bar{\tau}'_x) + \cos\left(\frac{\phi-\theta}{2}\right)(\sigma'_x - \bar{\sigma}'_x) \,. \tag{6.29}$$

The first term, proportional to $\sin\left(\frac{\phi-\theta}{2}\right)$, couples the doublets $|0\rangle, |1\rangle$ and $|\bar{0}\rangle, |\bar{1}\rangle$. The second term, proportional to $\cos\left(\frac{\phi-\theta}{2}\right)$, controls the coupling between the distant states $|0\rangle$, $|\bar{1}\rangle$ and $|1\rangle$, $|\bar{0}\rangle$. As discussed below, the relative strength of these terms governs the level repulsion in the Sambe space, and therefore shapes the Floquet spectrum.

We start our discussion considering the Floquet Hamiltonian. Since the parameter Q is here the detuning, $Q = \varepsilon_0/2$, we have $\frac{\partial\mathcal{H}_{\rm sys}}{\partial Q}\Big|_{Q_0} = \tau_z$ and the Floquet Hamiltonian (6.3) reads

$$\mathcal{H}_{\mathcal{F}} = \mathbf{n}\omega_{\rm d} + \mathcal{H}_{\rm sys}[\varepsilon_0 = 0] \otimes \mathbf{1}_{\mathcal{F}} + \frac{1}{2}\left(\mathcal{A}f_- + \mathcal{A}^* f_+\right)\tau_z \,, \tag{6.30}$$

where

$$\mathcal{H}_{\rm sys}[\varepsilon_0 = 0] = \frac{\omega_{\rm q}}{2}\tau'_z + \frac{\omega_{\rm q}}{2}\bar{\tau}'_z \,. \tag{6.31}$$

To understand the effects of the drive in the quasi-energy spectrum, we treat the drive as a perturbation, $\mathcal{V} = (\mathcal{A}f_- + \mathcal{A}^* f_+)\,\tau_z/2$. Using the expression (6.29) for the dipole, the perturbation reads

$$\mathcal{V} = \frac{1}{2}\left(\mathcal{A}f_- + \mathcal{A}^* f_+\right)\left[\sin\left(\frac{\phi-\theta}{2}\right)(\tau'_x + \bar{\tau}'_x) + \cos\left(\frac{\phi-\theta}{2}\right)(\sigma'_x - \bar{\sigma}'_x)\right] . \tag{6.32}$$

Since $\mathcal{V}$ couples only adjacent replicas, to lowest order in the complex drive amplitude $\mathcal{A}$, the Floquet spectrum can be understood from the perturbative expression

$$\varepsilon_j = E_j + \sum_{k,\pm} \frac{|\langle\langle j,0|\mathcal{V}|k,\pm 1\rangle\rangle|^2}{E_j - (E_k \pm \omega_\mathrm{d})}\,. \tag{6.33}$$

At this order, the shape of the spectrum in the zero-th replica varies for $\Delta \gtrless 2t_\mathrm{sc}$, as shown in Fig. 6.7.

Charge regime ($\Delta > 2t_\mathrm{sc}$) Here $\sin\left(\frac{\phi-\theta}{2}\right) > \cos\left(\frac{\phi-\theta}{2}\right)$, so the dominant coupling are intra-doublet, $|0\rangle \longleftrightarrow |1\rangle$ and $|\bar{0}\rangle \longleftrightarrow |\bar{1}\rangle$. The Floquet spectrum is similar to the one of the charge qubit discussed in Sec. 4.1, where SOC is responsible for the weaker inter-doublets couplings $|0\rangle \longleftrightarrow |\bar{1}\rangle$ and $|\bar{0}\rangle \longleftrightarrow |1\rangle$.

- In the regime $\omega_\mathrm{d} < \omega_\mathrm{q}$, the state $|\bar{1},-1\rangle\rangle$ lies above $|0,0\rangle\rangle$ and hence enhance the curvature of ε_0, accordingly to Eq. (6.33). Conversely, $|\bar{0},-1\rangle\rangle$ above $|1,0\rangle\rangle$ flattens ε_1.
- In the diabatic regime ($\omega_\mathrm{d} > \omega_\mathrm{q}$) the situation is reversed. Now $|\bar{1},-1\rangle\rangle$ lies below $|0,0\rangle\rangle$ and flattens ε_0, while $|\bar{0},-1\rangle\rangle$ increases the curvature of ε_1.

Overall, this regime remains close to a pure charge qubit.

Flopping mode regime ($\Delta < 2t_\mathrm{sc}$) Now $\sin\left(\frac{\phi-\theta}{2}\right) < \cos\left(\frac{\phi-\theta}{2}\right)$. In this regime the dominant couplings are $|0,0\rangle\rangle \longleftrightarrow |\bar{1},-1\rangle\rangle$ and $|1,0\rangle\rangle \longleftrightarrow |\bar{0},-1\rangle\rangle$. Hence, the drive mainly induces a spin-flip processes accompanied by the exchange of a drive photon. In particular, the farthest state $|\bar{0},-1\rangle\rangle$ does not merely flatten the quasi-energy ε_1; it largely sets his curvature, whereas

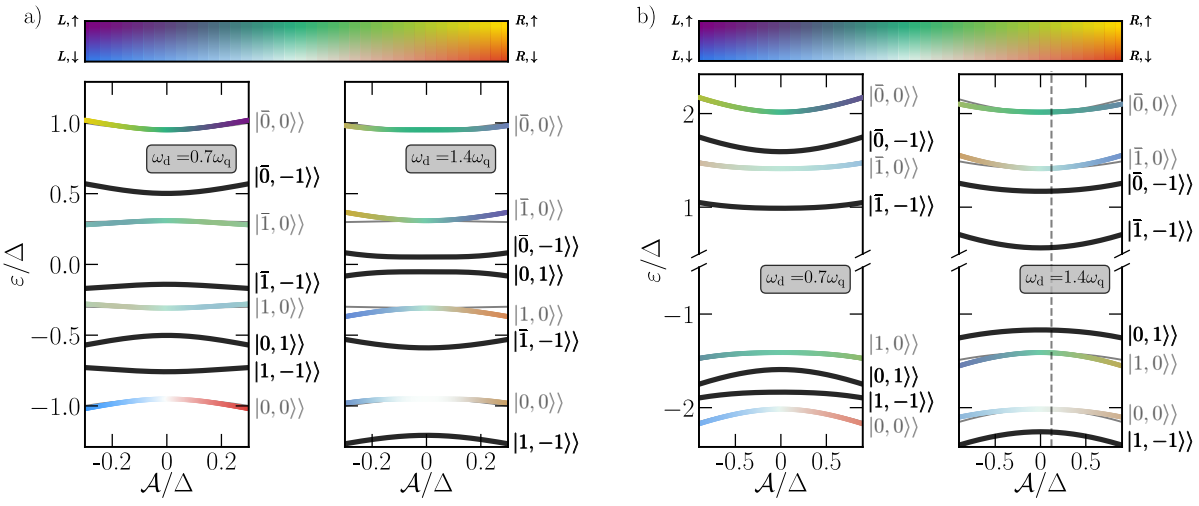

Figure 6.7: Floquet spectrum of the charge regime $\Delta > 2t_\mathrm{sc}$ (a) and of the flopping mode regime $\Delta < 2t_\mathrm{sc}$ (b) with respect to a real $\mathcal{A}$. For the Floquet modes lying in replica zero, colors represent the projection weight onto the qubit basis states. Grey lines show the limit $\omega_\mathrm{d} \ll \omega_\mathrm{q}$. Floquet spectra are computed considering enough replicas in the Floquet Hamiltonian to assure convergence. Only the replicas relevant for understanding the quasi-energy behaviour of the logical qubit are shown, with the solid black lines corresponding to replicas ± 1. The figures are generated using the parameters of the qubit detailed in Table 6.1.

the weaker coupling to $|0,1\rangle\rangle$ provides only a small additional flattening in the adiabatic limit. Similar consideration holds for ε_0 in the diabatic regime.

Comparison of the Floquet spectrum to the quasi-static limit $\omega_\mathrm{d} \ll \omega_\mathrm{q}$ reveals a key advantage of our approach. By tuning ω_d we can drastically change the behavior of the Floquet quasi-energies, and hence the value of $g_\parallel$ and χ, while keeping the same robustness of the flopping mode regime towards low-frequency noise.

6.2.3 Longitudinal readout of flopping-mode qubits

In this Section we discuss longitudinal readout for the flopping mode regime. This regime is particularly attractive because the qubit transition is almost a pure spin flip, which makes it more robust against low-frequency charge noise.

Figure 6.8a shows the conditional displacement of the cavity pointer state. The analytical trajectories are obtained from the effective model with $g_\parallel$, $\bar{g}_\parallel$, χ and $\bar{\chi}$ by numerically differentiating the Floquet spectrum (Fig. 6.7) at the drive point $\mathcal{A} = A_\mathrm{q}$. We observe that the quasi-energies of the first doublet $\{|0\rangle, |1\rangle\}$ have similar curvatures. For realistic cavity decay rate (see Table 6.1) this places the system in the regime $\chi \ll \kappa$ as in Fig. 6.1f, and the pointer-state dynamics follows the behavior illustrated in Fig. 6.1e. As in that case, the dynamics for a qubit prepared in $|j\rangle$ is controlled by $g_{\parallel,j}$ and χ_j, which depend on the first and second derivative of the Floquet spectrum of ε_j according to Eq. (6.5). In particular, the behavior in the logical qubit is dominated by $\bar{g}_\parallel = \left(g_{\parallel,1} + g_{\parallel,0}\right)/2$ and $\bar{\chi} = \left(\chi_1 + \chi_0\right)/2$. Because $g_{\parallel,0}$ and $g_{\parallel,1}$ have the same sign, the pointer states for $|0\rangle$ and $|1\rangle$ translate in the same direction but they still split longitudinally according to the slope difference $g_\parallel = \left(g_{\parallel,1} - g_{\parallel,0}\right)/2$.

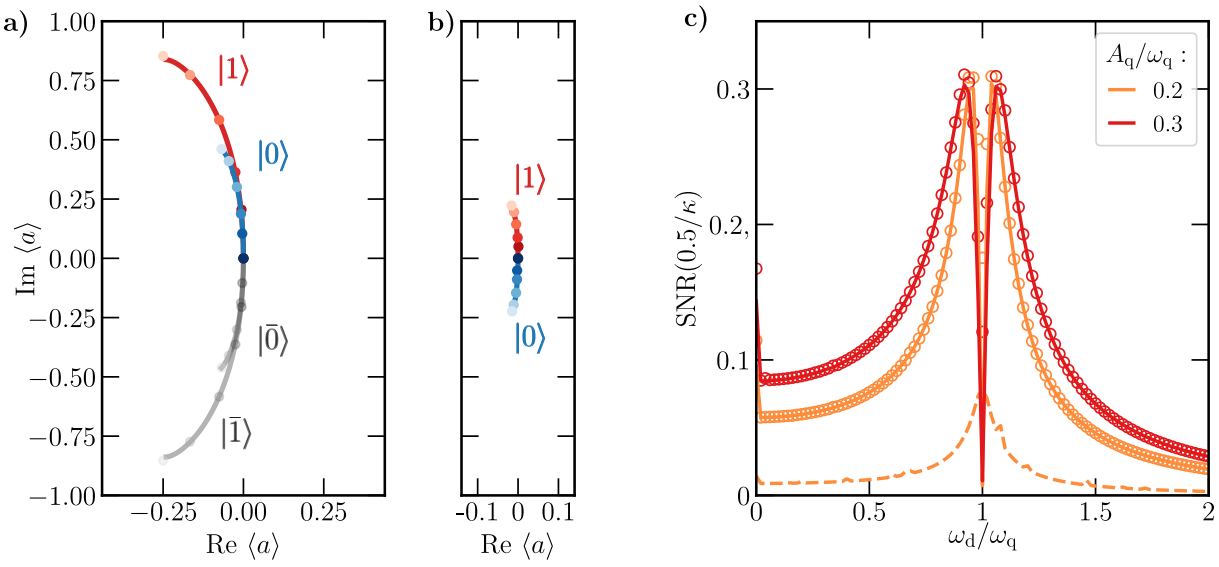

Figure 6.8: Longitudinal readout of spin qubits. The numerics (dots) are obtained considering till 30 levels in the resonator to assure convergence. Solid lines corresponds to analytic results obtained computing $g_\parallel$, $\bar{g}_\parallel$, χ and $\bar{\chi}$ from the Floquet spectrum. a) Longitudinal splitting of the resonator pointer states depending on the initial state of the system for $\omega_\mathrm{d}/\omega_\mathrm{q} = 1.4$, $\omega_\mathrm{r} = \omega_\mathrm{d}$ and $A_\mathrm{q}/\omega_\mathrm{q} = 0.2$ (value corresponding to the dashed vertical lines in Fig. (6.7)b). In b) The dynamics given by $\bar{g}_\parallel$ is compensated by an additional drive on the cavity. To compensate the effects of $\bar{A}_q$ we consider a cavity with $\omega_\mathrm{r} = \omega_\mathrm{d} - \bar{\chi}$. Dots correspond to numerical simulations, as in Fig. 5.7a. c) SNR as in Fig. 5.7c. Model parameters detailed in Table 6.1.

Figure 6.8b shows that an additional compensation tone on the cavity with amplitude $A_r = -2\bar{g}_{\|}$ leads to the cancellation of the dynamics of the "center of mass" of the pointer states of $|0\rangle$ and $|1\rangle$, given by $\bar{g}_{\|}$. Together with the choice $\omega_d - \omega_r = \bar{\chi}$ this restores an almost pure longitudinal dynamics as in Fig. 6.1h.

In Fig. 6.8c the inspection of the SNR at $t = 0.5/\kappa$, shows a factor 5 gain between longitudinal and dispersive readout.

We remark that the analytic evolution agrees with high accuracy with numerical simulations obtained in QuTiP [101] considering the parent Hamiltonian $\mathcal{H}_{\rm sys}[\varepsilon_0(t)/2]$ and a cavity decay rate κ.

6.3 Superconducting qubits

As we have seen, spin qubits are constructed from microscopic degrees of freedom. While this leads to good coherence times due to their natural isolation from the environment, it also makes coupling them to other systems challenging. On the other hand, superconducting qubits are built from collective electrodynamic modes of macroscopic electrical elements and are nowadays implemented in chips of hundred of qubits [17, 18, 122]. The key advantage is that these qubits couple easily to microwave resonators, enabling efficient control and readout. Furthermore, their strong interaction with electromagnetic fields makes it straightforward to couple multiple qubits together using simple linear circuit elements such as capacitors, inductors, or transmission lines. However, the implementation of a logical qubit relies on isolating two energy levels that can be coherently controlled and individually addressed in frequency. This requires intrinsic anharmonicity in the circuit, which is provided by the Josephson junction. Without such nonlinearity, circuits like LC oscillators would have equally spaced energy levels, making selective qubit control impossible.

In this Section we discuss longitudinal readout for the transmon and the fluxonium qubit. We begin with a brief overview of the Josephson junction in Sec. 6.3.1, which is a key element in both devices. We then explore longitudinal readout in the transmon (Sec. 6.3.2) and in the fluxonium (Sec. 6.3.3).

6.3.1 The Josephson junction

As shown in Fig. 6.9a, a Josephson junction consists of two superconducting electrodes separated by a thin insulating layer through which Cooper pairs can tunnel without resistance. At low

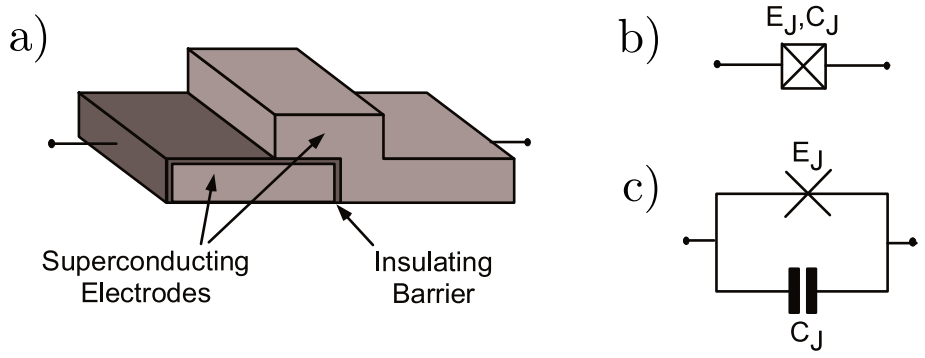

Figure 6.9: a) Sketch of a Josephson junction. b) Electrical symbol. c) Decomposition into a capacitor and a pure Josephson element. Figure taken from [123].

temperatures, voltages and frequencies, the Josephson tunnel junction behaves as a pure nonlinear inductance (Josephson element) in parallel with the capacitance corresponding to the parallel plate capacitor formed by the two overlapping films of the junction (Fig. 6.9c) [124].

To understand the physical laws governing this element, we consider a finite voltage between the electrodes. The phase[2] difference ϕ between the BCS ground state of the electrodes is related to the current flowing in the junction by the first Josephson relation

$$I = I_c \sin(\phi) \,, \tag{6.34}$$

and to the voltage by the second Josephson relation

$$\frac{\partial \phi}{\partial t} = \frac{V}{\varphi_0} \,, \tag{6.35}$$

where I_c is the critical current and $\varphi_0 = \hbar/2e$ is the so-called reduced flux quantum. Considering now the generalized flux $\Phi(t) = \int_{-\infty}^{t} V(\tau) d\tau$, the second Josephson relation gives us the relation $\Phi = \varphi_0 \phi$. This flux plays the same role as the magnetic flux for an inductive element, but it is not associated to a magnetic field: the energy is stored in the phase difference between the two sides of the junction. Since the Josephson junction allows Cooper pairs to pass through the insulating layer, its Hamiltonian is the tunneling Hamiltonian

$$H = -\frac{E_J}{2} \sum_{n \in \mathbb{Z}} |n\rangle \langle n+1| + |n+1\rangle \langle n| \,, \tag{6.36}$$

where $|n\rangle$ is a charge state with n Cooper pairs in one of the electrodes and the Josephson energy E_J is the characteristic energy of the junction.

To write the Hamiltonian (6.36) in the phase representation, we recall that the flux and the charge $q = -2en$ are conjugated variables, satisfying $[\Phi, q] = i\hbar$. This implies the canonical commutation relation $[n, \phi] = i$ between n and ϕ. In the phase basis, this allows us to represent the number operator as $n = -i\frac{d}{d\phi}$ such that the charge translation operator can be written as $T_{n_0} = e^{in_0\phi}$. Making use of $|n+1\rangle = T_1 |n\rangle$, we can then rewrite the Hamiltonian (6.36) as

$$H = -E_J \cos(\phi) \,, \tag{6.37}$$

which is a nonlinear function of the phase ϕ. This nonlinearity is the key feature that allows Josephson junctions to act as the nonlinear element required to define anharmonic energy levels in superconducting qubits.

Finally, in the phase representation we can relate the Josephson energy E_J to the critical current I_c. Indeed, from the Heisenberg equation of motion we have

$$\frac{\partial q}{\partial t} = -\frac{2e}{\hbar} i [H, n] = \frac{2e}{\hbar} \frac{\partial H}{\partial \phi} = \frac{2e}{\hbar} E_J \sin(\phi) \,,$$

and therefore, comparing the latter with the first Josephson relation (6.34), $2eE_J/\hbar = I_c$.

6.3.2 The Transmon qubit

To build a superconducting qubit, we connect a Josephson junction to a capacitor C_g. One junction electrode at least will form an isolated superconducting "island", a node whose charge, can vary only by electron tunneling.

[2] Note that the phase is defined modulo 2π. Hence, any phase state satisfies $|\phi + 2\pi\rangle = |\phi\rangle$, and any wavefunction is 2π periodic: $\psi(\phi) = \langle\phi|\psi\rangle = \langle\phi + 2\pi|\psi\rangle = \psi(\phi + 2\pi)$.

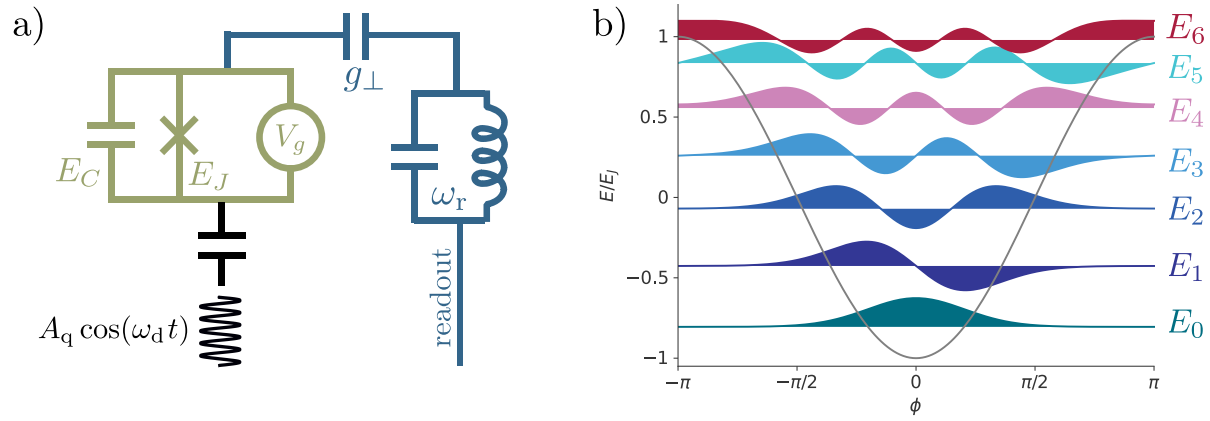

Figure 6.10: a) Circuit representation of a transmon (green) coupled to a resonator (blue) through the coupling $g_\perp$. An extra capacitor lets a classical drive fluctuate the number of Cooper pairs in the island. b) First six energies and wavefunctions of a transmon with $E_J/E_c = 50$.

A schematic of the circuit is shown in Fig. 6.10a. The total electrostatic energy of the island is $4E_C(n - n_g)^2$, where $E_C = e^2/2\,(C_g + C_J)$ is the charging energy of the capacitor and $n_g \approx C_g V_g/2e$ is the charge induced on the island by the gate voltage V_g, normalized to units of Cooper pairs.

6.3.2.1 From the Cooper pair box to the transmon regime

The full Hamiltonian of the system is

$$\mathcal{H}_{\text{sys}} = 4E_C(n - n_g)^2 - E_J \cos\phi\,. \tag{6.38}$$

In the phase representation, the number operator acts as $n = -i\frac{d}{d\phi}$, so the Hamiltonian becomes

$$\mathcal{H}_{\text{sys}} = 4E_C\left(-i\frac{d}{d\phi} - n_g\right)^2 - E_J \cos\phi\,. \tag{6.39}$$

In this form, the charging energy behaves like kinetic energy, while the Josephson term creates a nonlinear periodic potential. As shown in Fig. 6.10b, the spectrum contains both bound states with energy within the potential landscape and delocalized states.

Periodicity of the spectrum as a function of n_g

Comparison between $\mathcal{H}_{\text{sys}}$ and Eq. (5.32) shows that n_g plays the role of the crystal momentum k and suggests that the periodicity of the spectrum in n_g can be explained using the Floquet Theorem (Sec. 5.1) since $\mathcal{H}_{\text{sys}}$ has a 2π-periodic potential. However, the application of Floquet Theorem is not straightforward and one needs first to bring the eigenvalue problem into the form (5.4). To do so, we transform the Hamiltonian under the charge translation operator T_{-n_g} to cancel the n_g term in (6.38). We are then left with

$$\mathcal{H}'_{\text{sys}} = T_{-n_g}\mathcal{H}_{\text{sys}}T^\dagger_{-n_g} = -4E_C\frac{d^2}{d\phi^2} - E_J\cos\phi\,,$$

which is the equivalent of the Hamiltonian in (5.23). If $\psi(\phi)$ are eigenstate of $\mathcal{H}_{\text{sys}}$ with boundary condition $\psi(\phi+2\pi) = \psi(\phi)$ then the eigenvectors of $\mathcal{H}'_{\text{sys}}$ are obtained applying

T_{-n_g} to $\psi(\phi)$. This yields to the wavefunctions $u(\phi) = e^{-in_g\phi}\psi(\phi)$ which satisfies the boundary condition $u(\phi+2\pi) = e^{-i2\pi n_g}u(\phi)$. It follows immediately that the eigenvalues of the one-period propagator in phase, $\mathcal{T}_{2\pi} = e^{i2\pi n}$, are $\mu_{n_g} = e^{-in_g 2\pi}$. Thus n_g plays the role of the quasi-momentum k in Bloch theory, and the spectrum is 1-periodic in n_g.

Two crucial quantities determine how well this system works as a qubit : the anharmonicity and the charge dispersion of the energy levels. A sufficiently large anharmonicity ensures that transitions between energy levels can be individually controlled. The charge dispersion describes the variation of the energy levels with respect to environmental offset charge and gate voltages, and determines the sensitivity to charge noise: the smaller the charge dispersion, the less the qubit frequency will change in response to gate charge fluctuations.

As shown in Fig. 6.11, both properties depend on the ratio E_J/E_C . For small ratios, the charge states are almost eigenstates, making the system very sensitive to charge fluctuations. This was the first regime explored, and the device operating in this regime was known as the Cooper pair box. As E_J/E_C increases, the cosine potential becomes deeper, the wavefunctions localize in phase, and the energy levels become much less sensitive to n_g.

The transmon exploits a remarkable fact: the charge dispersion reduces exponentially in E_J/E_C, while the anharmonicity only decreases algebraically with a slow power law in E_J/E_C [125]. This separation of scaling behaviors makes it possible to significantly reduce sensitivity to charge noise without sacrificing control over the qubit. We define the transmon regime as the parameter range where $E_J/E_C > 10$. Other designs of qubits, such as the fluxonium [126], demonstrated even better results [127], but the transmon is still widely used because of its performances that are good enough for a wide range of experiments and its relatively easy fabrication.

From a historical perspective, it is worth noting that the first superconducting qubit, the Cooper pair box, was not operating in the transmon regime even if it was clear that increasing E_J would solve the problem of charge noise [128]. The issue at the time was the inability to readout the qubit state if the ratio was too large. The key breakthrough with the idea of coupling the qubit to a microwave cavity [24], leading to the dispersive readout scheme discussed in Chap. 5.4, which truly allowed the development of the transmon.

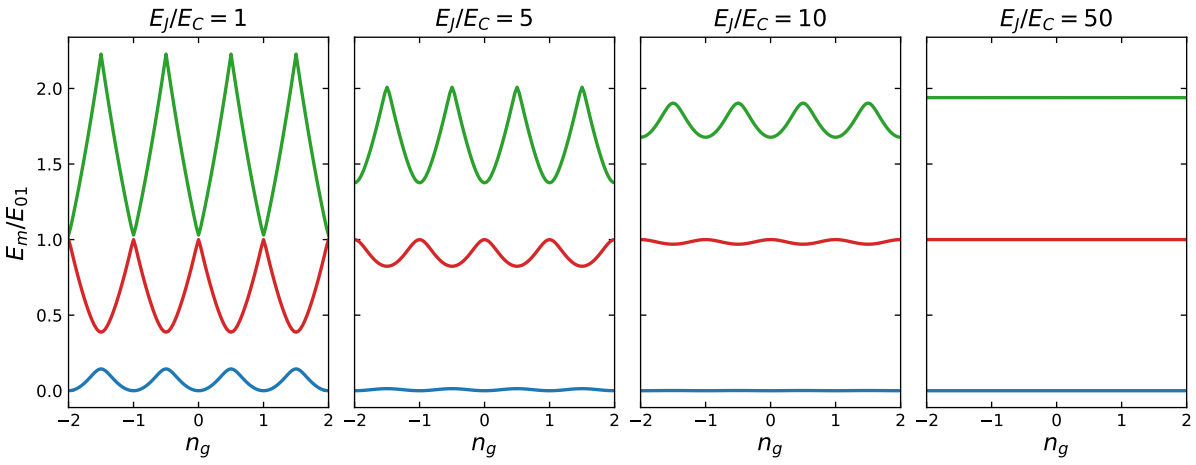

Figure 6.11: First three eigenvalues E_m of the Hamiltonian (6.38) as a function of the offset charge n_g for different ratios E_J/E_C . Energies are given in units of the transition energy $E_{01} = E_1 - E_0$, evaluated $n_g = 0$. The zero point of energy is chosen as the bottom of the $m = 0$ level.

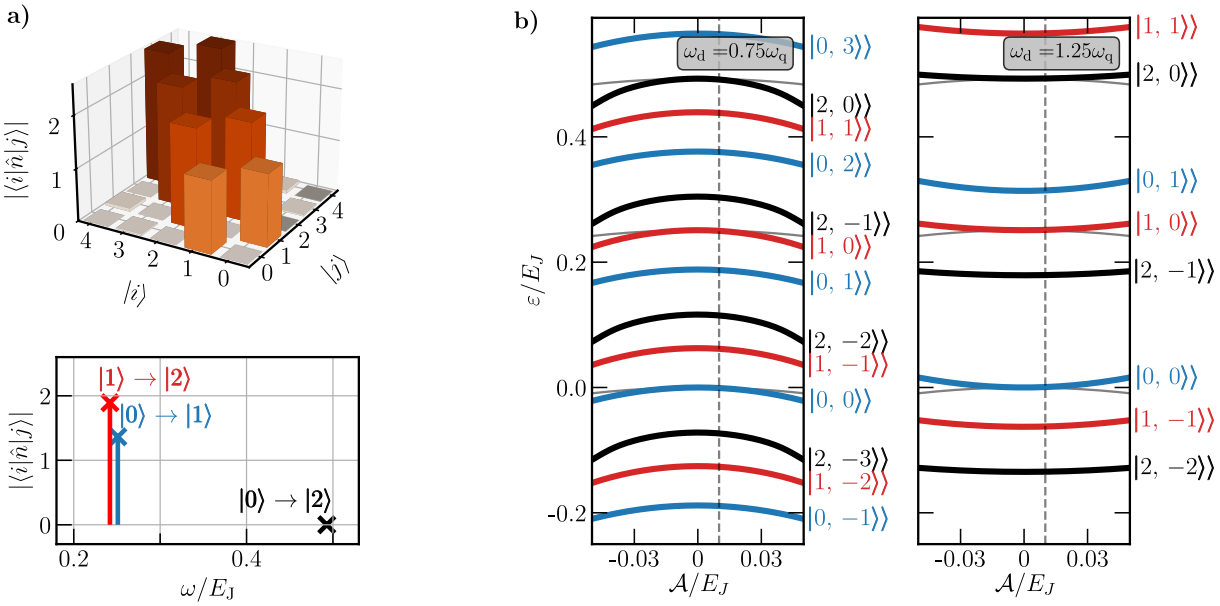

Figure 6.12: a) Matrix elements of the charge operator n for the transmon obtained with Scqubits [129, 130]. b) Floquet spectrum for a drive frequency $\omega_d \gtrless \omega_q$. Grey lines represent the spectrum in the limit $\omega_d \ll \omega_q$. The Floquet spectrum is computed with $N_{rep} = 31$ and considering 20 states in the transmon to ensure convergence as a function of the number of states and replicas. The figures are generated using the parameters of the qubit detailed in Table 6.2.

6.3.2.2 Floquet spectrum

In this section we analyze the Floquet spectrum of the transmon, which is obtained from the Floquet Hamiltonian 6.3, where the parameter Q corresponds here to a charge accumulation of Cooper pairs, $Q = n_g$. Hence, the Floquet Hamiltonian reads

$$\mathcal{H}_{\mathcal{F}} = \mathbf{n}\omega_d + \mathcal{H}_{sys}[n_g = 0] \otimes \mathbf{1}_{\mathcal{F}} + \frac{1}{2}(-8E_C)(\mathcal{A}f_- + \mathcal{A}^* f_+)\, n\,. \tag{6.40}$$

In order to simplify notations, we absorb the factor $-8E_C$ into $\mathcal{A}$, which is equivalent to the choice $Q = -8E_C n_g$.

We compute numerically the matrix elements of the charge operator n (see Fig. 6.12a), in Fig. 6.12b we compute numerically the Floquet spectrum diagonalizing the Floquet Hamiltonian $\mathcal{H}_{\mathcal{F}}$. To understand the spectrum, we write the Floquet Hamiltonian $\mathcal{H}_{\mathcal{F}}$ in the eigenbasis $\mathcal{B}' = \{|0\rangle \dots |j\rangle \dots\}$ of $\mathcal{H}_{sys}[n_g = 0]$. To do so, we compute the matrix elements of the charge operator in the eigenbasis $n_{ij} = \langle i|n|j\rangle$. Figure 6.12a shows that the charge operator only couples adjacent state, as given also by asymptotic expressions, valid in the regime $E_J/E_C \gg 1$ [125]

$$\langle j+1|n|j\rangle \approx i\sqrt{\frac{j+1}{2}}\left(\frac{E_J}{8E_C}\right)^{1/4}, \quad \langle j+k|n|j\rangle \approx 0\,. \tag{6.41}$$

The weak anharmonicity and the value of the charge matrix elements make it difficult to develop an intuition for the behavior of the quasi-energies. To understand the Floquet spectrum shown

E_C/E_J	ω_q/E_J	κ/E_J	$g_\perp/E_J$
$8.4 \cdot 10^{-3}$	0.25	$6.4 \cdot 10^{-5}$	$3 \cdot 10^{-3}$

Table 6.2: Parameters of the transmon in Figure 6.12 and 6.13 [78].

in Fig. 6.12b, we examine the Floquet Hamiltonian $\mathcal{H}_{\mathcal{F}}$ in the basis $\mathcal{B}'$

$$\mathcal{H}_{\mathcal{F}} = \begin{pmatrix} \ddots & & & & & & & & & \\ & E_2+\omega_d & 0 & 0 & 0 & \frac{\mathcal{A}^*}{2}n_{12}^* & 0 & 0 & 0 & 0 \\ & 0 & E_1+\omega_d & 0 & \frac{\mathcal{A}^*}{2}n_{12} & 0 & \frac{\mathcal{A}^*}{2}n_{01}^* & 0 & 0 & 0 \\ & 0 & 0 & E_0+\omega_d & 0 & \frac{\mathcal{A}^*}{2}n_{01} & 0 & 0 & 0 & 0 \\ & 0 & \frac{\mathcal{A}}{2}n_{12}^* & 0 & E_2 & 0 & 0 & 0 & \frac{\mathcal{A}^*}{2}n_{12}^* & 0 \\ & \frac{\mathcal{A}}{2}n_{12} & 0 & \frac{\mathcal{A}}{2}n_{01}^* & 0 & E_1 & 0 & \frac{\mathcal{A}^*}{2}n_{12} & 0 & \frac{\mathcal{A}^*}{2}n_{01}^* \\ & 0 & \frac{\mathcal{A}}{2}n_{01} & 0 & 0 & 0 & E_0 & 0 & \frac{\mathcal{A}^*}{2}n_{01} & 0 \\ & 0 & 0 & 0 & 0 & \frac{\mathcal{A}}{2}n_{12}^* & 0 & E_2-\omega_d & 0 & 0 \\ & 0 & 0 & 0 & \frac{\mathcal{A}}{2}n_{12} & 0 & \frac{\mathcal{A}}{2}n_{01}^* & 0 & E_1-\omega_d & 0 \\ & 0 & 0 & 0 & 0 & \frac{\mathcal{A}}{2}n_{01} & 0 & 0 & 0 & E_0-\omega_d \\ & & & & & & & & & \ddots \end{pmatrix}, \tag{6.42}$$

and we consider a perturbative expansion in $\mathcal{A}$ of the quasi-energies. We use the asymptotic expressions, valid in the regime $E_J/E_C \gg 1$ [125]

$$E_j \simeq -E_J + \sqrt{8E_JE_C}\left(j+\frac{1}{2}\right) - \frac{E_C}{12}(6j^2+6j+3)\,, \tag{6.43}$$

which correspond to the unperturbed quasi-energies at $n_g = 0$. Second order perturbation theory in $\mathcal{A}$ for the Floquet Hamiltonian gives the expressions, which explain the spectrum in Fig. 6.12b,

$$\begin{aligned} \varepsilon_0 &= E_0 - |n_{01}|^2\frac{|\mathcal{A}|^2}{2}\left(\frac{1}{\omega_q-\omega_d}+\frac{1}{\omega_q+\omega_d}\right), \\ \varepsilon_1 &= E_1 + |n_{01}|^2\frac{|\mathcal{A}|^2}{2}\left(\frac{1}{\omega_q-\omega_d}+\frac{1}{\omega_q+\omega_d}-2\frac{1}{\omega_q-E_C-\omega_d}-2\frac{1}{\omega_q-E_C+\omega_d}\right), \end{aligned} \tag{6.44}$$

where we have used that $|n_{12}|^2 = 2|n_{01}|^2$. In the next Section, we use the latter asymptotic expressions to compute $g_{\parallel}$ and discuss the evolution of the pointer states.

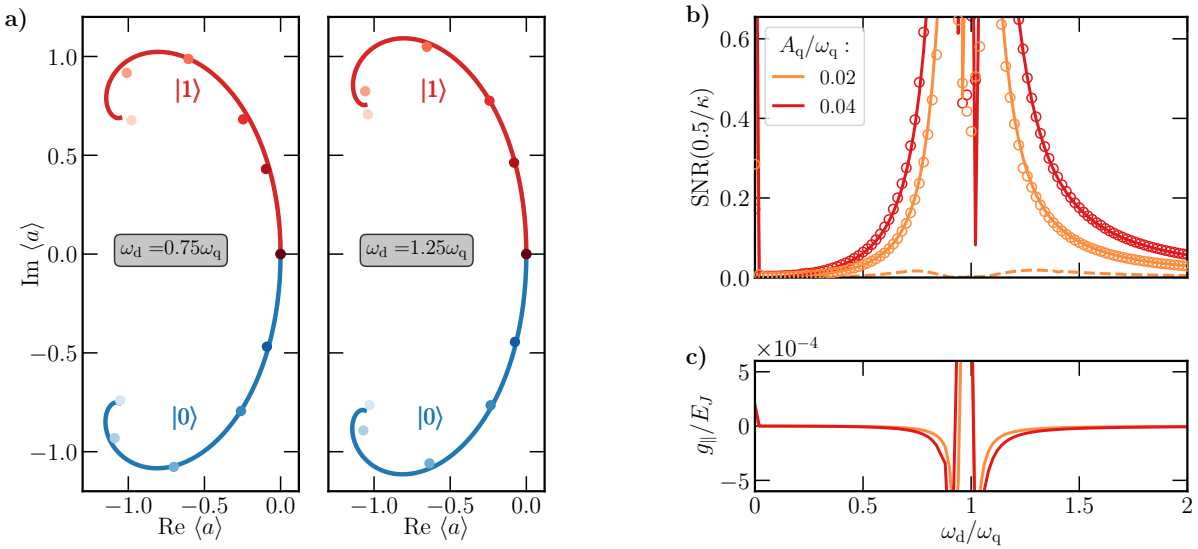

Figure 6.13: a) Evolution of the cavity pointer states for $\omega_d \gtrless \omega_q$ with a compensation tone. The frequency of the cavity is set to $\omega_r = \omega_d - \bar{\chi}$ to compensate the effects of $\bar{\chi}$. b) $g_{\parallel}$ in function of the cavity frequency for different value of A_q. The figures are generated using the parameters of the qubit detailed in Table 6.2.

6.3.2.3 Longitudinal readout of a transmon qubit

In this Section we discuss longitudinal readout for the transmon qubit.

Differently from the spin-qubit discussed in Section 6.2, the weak anharmonicity of the transmon makes the longitudinal coupling always negative far from the resonance condition $\omega_q = \omega_d$. This makes the evolution of the pointer state similar in the adiabatic and diabatic regime.

To show this explicitly, we use the perturbative expression for the quasi-energies in Eq. (6.44). We can compute $g_\parallel$ through Eq. (6.10). One finds

$$g_\parallel^{(0)} = g_\perp A_q |n_{01}|^2 \frac{1}{2}\left(\frac{1}{\omega_q - \omega_d} + \frac{1}{\omega_q + \omega_d} - \frac{1}{(\omega_q - E_C) - \omega_d} - \frac{1}{(\omega_q - E_C) + \omega_d}\right), \tag{6.45}$$

with $\omega_q = E_1 - E_0$.

In the small drive limit $A_q \to 0$, and neglecting the counter-rotating terms $\propto (\omega_q + \omega_d)^{-1}$, $(\omega_q - E_C + \omega_d)^{-1}$, we can compute $\chi^{(0)}$ through Eq. (5.121). This reproduces the expression for the dispersive coupling known in the literature [50]

$$\chi^{(0)} \approx -g_\perp^2 |n_{01}|^2 \frac{E_C}{(\omega_q - \omega_d)(\omega_q - \omega_d - E_C)}. \tag{6.46}$$

The expressions (6.45) and (6.46) show that both the longitudinal and the dispersive coupling, for $E_J < |\omega_q - \omega_d|$, are negative (see Fig. (6.13)c).

The SNR signals shown in Fig. (6.13)b display a factor 5 gain at short times when longitudinal readout is compared to dispersive readout. However, the weak anharmonicity of the transmon leads to additional resonances, spoiling readout for $\omega_d \sim \omega_q$.

6.3.3 The Fluxonium qubit

As we have seen, we can reduce the sensitivity to charge noise by increasing the ratio E_J/E_C. However, this comes at the cost of reducing anharmonicity, which is essential for distinguishing qubit transitions. A complementary strategy is the fluxonium qubit: a small Josephson junction shunted by both a capacitance and a very large superinductance (typically a series array of Josephson junctions). The superinductance strongly connects the island to ground, such that

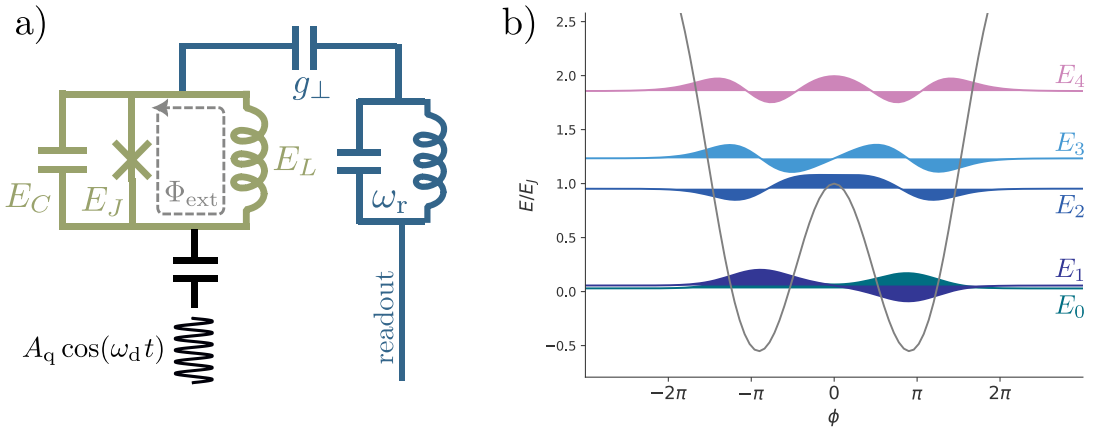

Figure 6.14: a) Circuit representation of a fluxonium (green) coupled to a resonator (blue) through the coupling $g_\perp$. b) First four energies and wavefunctions of a fluxonium with the parameters of Table 6.3.

charge imbalances on the island can be relaxed through the inductor. Yet, its energy levels manifest the anharmonic structure associated with single Cooper pair effects, a useful component for solid state quantum computation [126]. The device exhibits a strongly anharmonic energy spectrum, enabling fast and high-fidelity gate operations while suppressing leakage to higher energy levels. Due to its large effective inductive energy and operation at low transition frequencies (often below 1 GHz), the fluxonium is inherently less sensitive to charge and flux noise, particularly when biased at flux "sweet spots". Recent experimental advances have demonstrated coherence times exceeding one millisecond and two-qubit gate fidelities above 99.7 %, positioning fluxonium as a strong candidate for fault-tolerant superconducting quantum computing. However, its enhanced performance comes at the cost of increased circuit complexity and requires high-quality superinductive elements.

6.3.3.1 The model

In this section we analyze the fluxonium Hamiltonian [126]

$$\mathcal{H}_{\text{sys}} = 4E_C n^2 - E_J \cos\left(\phi - 2\pi\frac{\Phi_{\text{ext}}}{\Phi_0}\right) + \frac{1}{2}E_L\phi^2 \,. \tag{6.47}$$

The large shunt inductance L adds a parabolic confinement (proportional to E_L), making the phase landscape richer (see Fig. 6.14) . Since $E_L \propto 1/L$, achieving large L keeps E_L small, so the Josephson non-linear term remains nonperturbative and the spectrum stays strongly anharmonic. However, even a small E_L keeps the phase bounded. If L is not large, the cosine becomes a weak perturbation of a deep harmonic well. This makes the qubit look like a linear harmonic oscillator, with equally spaced levels.

An external magnetic flux Φ_{ext} displaces the minima of the potential. This is used to bring the device into a flux *sweet spot*, where the qubit is less susceptible to flux noise.

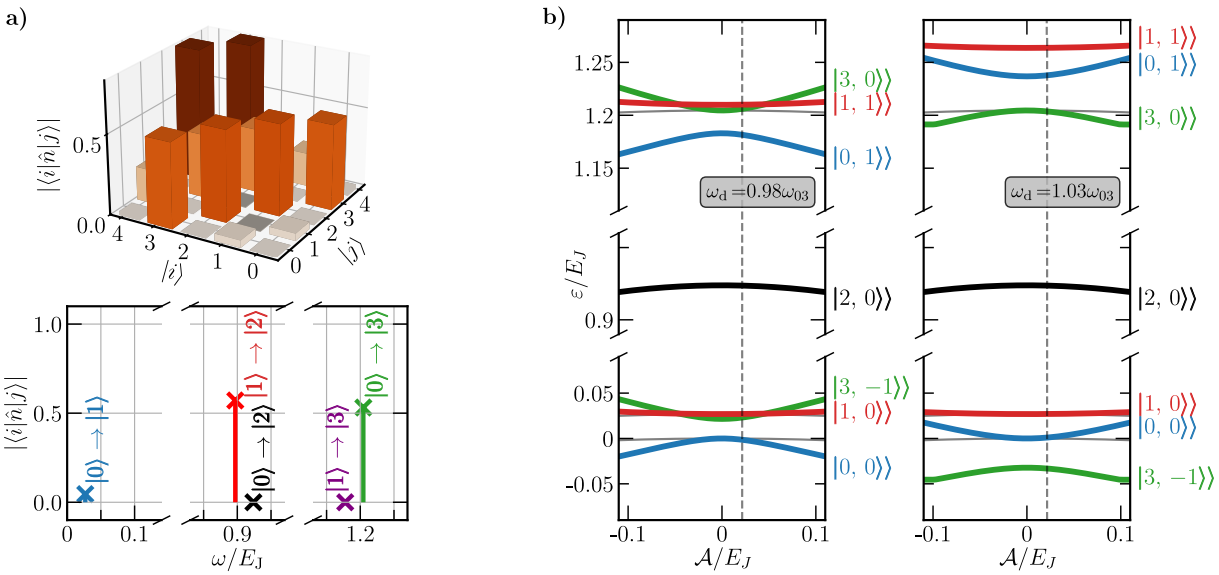

Figure 6.15: a) Matrix elements of the charge operator n for the fluxonium obtained with Scqubits [129, 130]. b) Floquet spectrum for $\omega_d \gtrless \omega_{03}$. Grey lines represent the spectrum in the limit $\omega_d \ll \omega_{03}$. The Floquet spectrum is computed with $N_{\text{rep}} = 31$ and considering 20 states in the fluxonium to ensure convergence in function of the number of states and replicas. The figures are generated using the parameters detailed in Table 6.3.

E_C/E_J	E_L/E_J	Φ_{ext}/Φ_0	ω_{03}/E_J	$g_\perp/E_J$	κ/E_J
0.2	0.1	0.5	1.2	0.01	$1 \cdot 10^{-3}$

Table 6.3: Parameters of the fluxonium in Figure 6.15 and 6.16. Parameters adapted from Ref. [131].

6.3.3.2 The Floquet spectrum

To understand the Floquet spectrum, we proceed as in Sec. 6.3.2.2 defining $Q = -8E_C n_g$. We then diagonalize numerically the system Hamiltonian and compute the matrix elements of the charge operator in the system eigenbasis (see Fig. 6.15a).

The behavior of the quasi-energies in the Floquet spectrum shown in Fig. 6.15b is almost entirely determined by the coupling between the fluxonium levels $|0\rangle$ and $|3\rangle$ (see Fig. 6.15a) that determines the curvature of the quasi-energy ε_0 associated to $|0,0\rangle\rangle$. On the other hand, $|2,-1\rangle\rangle$ is too energetically distant from $|1,0\rangle\rangle$ and ε_1 stays almost flat.

6.3.3.3 Longitudinal readout for a fluxonium qubit

As in Sec. 6.2.3, here we discuss longitudinal readout for the fluxonium qubit.

As shown in Fig. 6.16c, due to the more important anharmonicity in the fluxonium, we observe a change of sign in the $g_\parallel$ at $\omega_{\text{d}} \simeq \omega_{\text{q}}$. This is reflected in the pointer state evolutions in Fig. 6.16a, where the application of a compensation tone to the resonator eliminates the $\bar{g}_\parallel$ and $\bar{\chi}$ terms and restores longitudinal dynamics only depending on $g_\parallel$ and χ. The levels of the fluxonium display less curvature, which thus showcases a purest longitudinal cavity-splitting.

The SNRs in Fig. 6.16c show a factor 5 gain at short times when compared to dispersive readout.

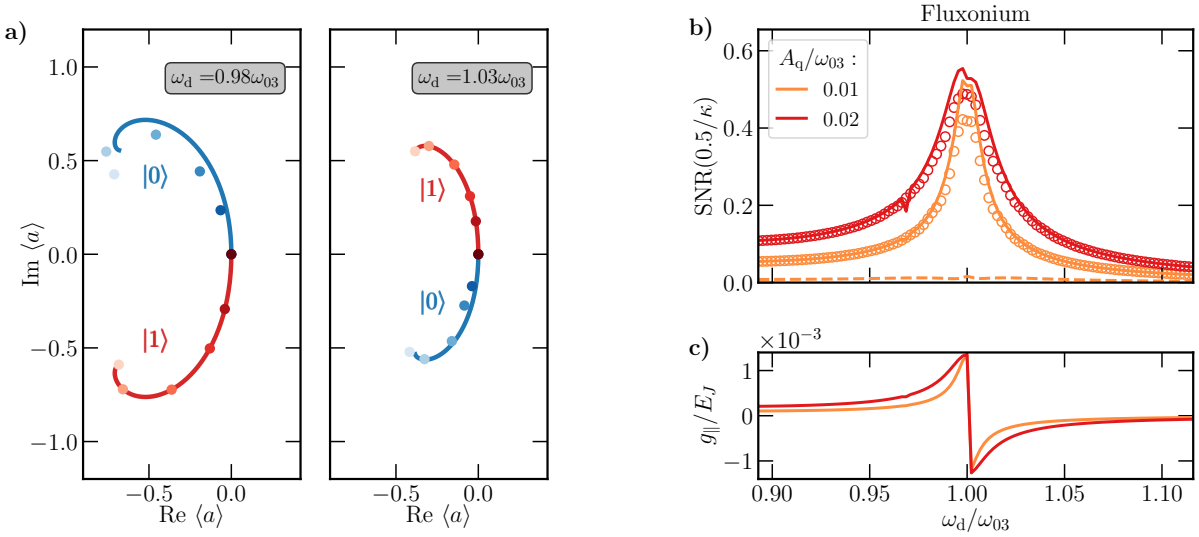

Figure 6.16: a) Evolution of the cavity pointer states for $\omega_{\text{d}} \gtrless \omega_{03}$. The frequency of the cavity is set to $\omega_{\text{r}} = \omega_{\text{d}} - \bar{\chi}$ to compensate the effects of $\bar{\chi}$. b) $g_\parallel$ in function of the cavity frequency for different value of A_{q}. The figures are generated using the parameters detailed in Table 6.3.

6.4 Polarizability contributions

In this section we consider a possible extension of the theory to account for second order terms in the expansion (6.1). Performing the Taylor expansion to second order in δQ, yields

$$\mathcal{H} = \mathcal{H}_{\rm sys}[Q_0] + \left.\frac{\partial \mathcal{H}_{\rm sys}}{\partial Q}\right|_{Q_0} \delta Q + \frac{1}{2}\left.\frac{\partial^2 \mathcal{H}_{\rm sys}}{\partial Q^2}\right|_{Q_0} \delta Q^2 + \omega_{\rm r} a^\dagger a\,, \tag{6.48}$$

with $\delta Q = A_{\rm q}\cos(\omega_{\rm d} t) + g_\perp(a + a^\dagger)$. The Floquet Hamiltonian reads

$$\begin{aligned}\mathcal{H}_\mathcal{F} = \mathcal{H}_{\rm sys}[Q_0]\otimes \mathbb{1}_\mathcal{F} + \frac{1}{2}\left(\mathcal{A} f_- + \mathcal{A}^\dagger f_+\right)\left.\frac{\partial \mathcal{H}_{\rm sys}}{\partial Q}\right|_{Q_0} \\ + \frac{1}{8}\left(\mathcal{A}^2 f_-^2 + {\mathcal{A}^\dagger}^2 f_+^2\right)\left.\frac{\partial^2 \mathcal{H}_{\rm sys}}{\partial Q^2}\right|_{Q_0} + \frac{1}{2}(\mathcal{A}\mathcal{A}^\dagger + \mathcal{A}^\dagger\mathcal{A})\left.\frac{\partial^2 \mathcal{H}_{\rm sys}}{\partial Q^2}\right|_{Q_0}.\end{aligned} \tag{6.49}$$

The terms proportional to $\frac{\partial^2 \mathcal{H}_{\rm sys}}{\partial Q^2}$ modify the Floquet spectrum, giving rise to the so-called polarizability contributions [75, 77].

As an example, we compute the polarizability contribution for the transmon. Inserting $\left.\frac{\partial^2 \mathcal{H}_{\rm sys}}{\partial Q^2}\right|_{n_g=0} = 1/(8E_C)$ into Eq. (6.48) we obtain

$$\begin{aligned}\mathcal{H} = \sum_j E_j \left|j\right\rangle\left\langle j\right| + g_\perp(a + a^\dagger)n + A_{\rm q}\cos(\omega_{\rm d} t)n \\ + \frac{(A_{\rm q}\cos(\omega_{\rm d} t) + g_\perp(a + a^\dagger))^2}{16E_C} + \omega_{\rm r} a^\dagger a\,,\end{aligned} \tag{6.50}$$

and the corresponding Floquet Hamiltonian (6.49) becomes $\mathcal{H}_\mathcal{F} = \mathcal{H}'_\mathcal{F} + \frac{|\mathcal{A}|^2}{8E_C}\mathbf{1}$, with

$$\mathcal{H}'_\mathcal{F} = \begin{pmatrix} \ddots & & & & & & & & & \\ & E_2+\omega_{\rm d} & 0 & 0 & 0 & \frac{\mathcal{A}^*}{2}n_{12}^* & 0 & \frac{\mathcal{A}^{*2}}{64E_C} & 0 & 0 \\ & 0 & E_1+\omega_{\rm d} & 0 & \frac{\mathcal{A}^*}{2}n_{12} & 0 & \frac{\mathcal{A}^*}{2}n_{01}^* & 0 & \frac{\mathcal{A}^{*2}}{64E_C} & 0 \\ & 0 & 0 & E_0+\omega_{\rm d} & 0 & \frac{\mathcal{A}^*}{2}n_{01} & 0 & 0 & 0 & \frac{\mathcal{A}^{*2}}{64E_C} \\ & 0 & \frac{\mathcal{A}}{2}n_{12}^* & 0 & E_2 & 0 & 0 & 0 & \frac{\mathcal{A}^*}{2}n_{12}^* & 0 \\ & \frac{\mathcal{A}}{2}n_{12} & 0 & \frac{\mathcal{A}}{2}n_{01}^* & 0 & E_1 & 0 & \frac{\mathcal{A}^*}{2}n_{12} & 0 & \frac{\mathcal{A}^*}{2}n_{01}^* \\ & 0 & \frac{\mathcal{A}}{2}n_{01} & 0 & 0 & 0 & E_0 & 0 & \frac{\mathcal{A}^*}{2}n_{01} & 0 \\ & \frac{\mathcal{A}^2}{64E_C} & 0 & 0 & 0 & \frac{\mathcal{A}}{2}n_{12}^* & 0 & E_2-\omega_{\rm d} & 0 & 0 \\ & 0 & \frac{\mathcal{A}^2}{64E_C} & 0 & \frac{\mathcal{A}}{2}n_{12} & 0 & \frac{\mathcal{A}}{2}n_{01}^* & 0 & E_1-\omega_{\rm d} & 0 \\ & 0 & 0 & \frac{\mathcal{A}^2}{64E_C} & 0 & \frac{\mathcal{A}}{2}n_{01} & 0 & 0 & 0 & E_0-\omega_{\rm d} \\ & & & & & & & & & \ddots \end{pmatrix}. \tag{6.51}$$

Up to second order in $\mathcal{A}$, the quasi-energies are

$$\begin{aligned}\varepsilon_0 &= E_0 - |n_{01}|^2\frac{|\mathcal{A}|^2}{2}\left(\frac{1}{\omega_{\rm q}-\omega_{\rm d}} + \frac{1}{\omega_{\rm q}+\omega_{\rm d}}\right) + \frac{|\mathcal{A}|^2}{8E_C}\,, \\ \varepsilon_1 &= E_1 + |n_{01}|^2\frac{|\mathcal{A}|^2}{2}\left(\frac{1}{\omega_{\rm q}-\omega_{\rm d}} + \frac{1}{\omega_{\rm q}+\omega_{\rm d}} - \frac{2}{\omega_{\rm q}-E_C-\omega_{\rm d}} - \frac{2}{\omega_{\rm q}-E_C+\omega_{\rm d}}\right) + \frac{|\mathcal{A}|^2}{8E_C}\,,\end{aligned} \tag{6.52}$$

such that, in the transmon limit, the polarizability contributions do not enter the $g_\parallel$ and χ, but only modify $\bar{g}_\parallel$ and $\bar{\chi}$ [75, 77], terms that do not alter much the dynamics and can be compensated.

6.5 Chapter 6 in a nutshell

In this Chapter, we extended the Floquet framework of Chapter 5 to realistic multi-level devices and discussed longitudinal readout in spin and superconducting cQED platforms. Starting from a very general case where the Hamiltonian is expanded with respect to a generic parameter Q containing both the drive and the cavity fluctuations, we have shown that a straightforward generalization of our Floquet framework still holds. Each Floquet mode couples to the resonator with its own longitudinal coupling $g_{\parallel,j}$ and dispersive shift χ_j proportional to the first and second order variations of the associated quasi-energy. When the multi-level Hamiltonian is mapped onto a two-level subspace, the only additional terms are qubit-independent renormalizations $\bar{g}_{\parallel}$ and $\bar{\chi}$. These can be canceled by applying a compensation tone on the cavity, which restores purely longitudinal dynamics. Finally, we have shown that the theory can be extended to include polarizability effects that arise from higher-order terms in the expansion.

Chapter

7 Many-Body Admittance Spectroscopy

Contents

7.1 Experimental protocol for MADS 106
7.1.1 The model 107
7.1.2 Input-output relations 107
7.2 MADS for spinless fermions in 1D 110
7.2.1 Non-interacting fermions 111
7.2.2 Interacting gapless regime 115
7.3 Chapter 7 in a nutshell 121

The properties of quantum matter are closely tied to the low-energy excitation spectrum, which typically encodes its response to weak external perturbations. The argument essentially revolves around the fluctuation-dissipation theorem, which relates the linear response function to the spectrum of spontaneous fluctuations [132]. Low-dimensional materials have long served as a broad and fruitful playground for theory, thanks to the variety of analytical and numerical methods available. In these materials, neutron scattering probes fluctuations of the magnetic moments and provides experimental access to the dynamical structure factor (DSF, see Fig. 7.1) [133, 134], which is related to the S^z spin-spin correlation functions [135–137]. Analogously, in solid state devices, the DSF $S(q,\omega)$ probes the propagation of density fluctuations with wavenumber q and energy ω. These correlation functions are the Fourier transform of two-time and two-site correlation functions $\langle n_l(t)n_m\rangle$ of the density operator n at different times and positions [138].

Computing the DSF generally requires the many-body eigenstates of the unperturbed system, which are difficult to derive. In this sense, quantum simulators not only realize a form of "synthetic" quantum matter but pave the way to new methods to perform the spectroscopy of low-energy excitations. This has been the case for Bose-Einstein condensates [139–141] and Fermi gases of cold atoms [142–145], where the density correlation function can be obtained by Bragg scattering far-detuned laser light off atomic ensembles or by angle-resolved photoemission spectroscopy [146–148]. Alternative readout techniques have also been recently proposed to study the DSF in Rydberg atoms [149, 150], in one dimensional array of bosonic atoms [151] and in universal quantum computers [152].

In this Chapter we move beyond single-qubit measurement, discussed in Chaps. 3-6, to study a hybrid cQED platform for many-body readout in quantum simulators. In particular, we propose in Sec. 7.1 Many-Body Admittance Spectroscopy (MADS) as an alternative method to access the dynamical structure factor in solid state quantum simulators. Unlike cold atoms or ion platforms, solid state quantum simulators such as quantum dot arrays inherently exhibit a broader variety of interactions, such as spin-orbit coupling [153], , thereby enabling the simulation of a wider class of phenomena. The high tunability of these platforms [153] has already

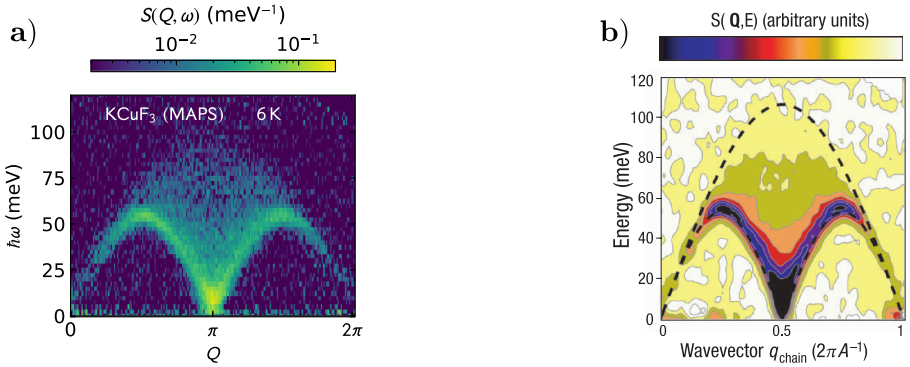

Figure 7.1: Inelastic neutron scattering data for $KCuF_3$. The DSF $S(q, \omega)$ is measured at $T = 6$ K. Figure adapted from Refs. [133, 134].

enabled the exploration of the phase diagram of the Fermi-Hubbard model, including the transition from Coulomb blockade to collective Coulomb blockade [36] and the emergence of Nagaoka ferromagnetism [46]. Traditional readout techniques rely on the charge stability diagrams and on spin-to-charge conversion [36]. On the other hand, with MADS we offer a weak-measurement approach in which the system is coupled to a network of transmission lines and the transmission coefficient is measured across various combinations of input-output ports.

The DSF is defined as

$$S(q,\omega) = \frac{1}{N}\sum_{lm} e^{-iq(l-m)} \int dt e^{i\omega t} \langle n_l(t) n_m(0)\rangle \ . \tag{7.1}$$

At zero temperature, it can be obtained from the admittance $\chi_{lm}(t) = -i\theta(t)\langle[n_l(t), n_m]\rangle$ through (see Appendix E.2.1) [138]

$$S(q,\omega>0) = -2\mathrm{Im}\left[\chi(q,\omega)\right] , \qquad \text{with} \qquad \chi(q,\omega) = \frac{1}{N}\sum_{lm} e^{-iq(l-m)}\chi_{lm}(\omega)\,. \tag{7.2}$$

In Section 7.2, we specifically focus on a one-dimensional spinless chain of N quantum dots, taken as a prototypical one dimensional quantum simulator. In one dimensional systems, the Jordan-Wigner transformation maps longitudinal spin correlators to density correlators. Hence, one dimensional quantum simulators can be exploited as an alternative to neutron scattering experiments to probe the exotic physics of the Heisenberg model [154]. In this case the DSF does not admit a closed analytic form in the interacting regime. Semi-analytical predictions rely on Bethe Ansatz methods [155–160] and, in the thermodynamic limit, on non linear Luttinger liquid theory [161, 162]. Using numerical methods such as exact diagonalization [163] and density matrix renormalization group (DMRG) [164], we compute the DSF for finite size systems, comparing the result with the expected behavior in the thermodynamic limit and showcasing how MADS can be used to probe the DSF $S(q, \omega)$.

7.1 Experimental protocol for MADS

This section introduces Many Body Admittance Spectroscopy (MADS), a readout protocol that links experimentally accessible transmission data to the dynamical structure factor of a chain of quantum dots. Starting from the description of the Hamiltonian of the hybrid cQED platform (Sec. 7.1.1), we derive the input-output relations in an experimentally relevant situation that considers spatially extended couplings and cross-talks (Sec. 7.1.2).

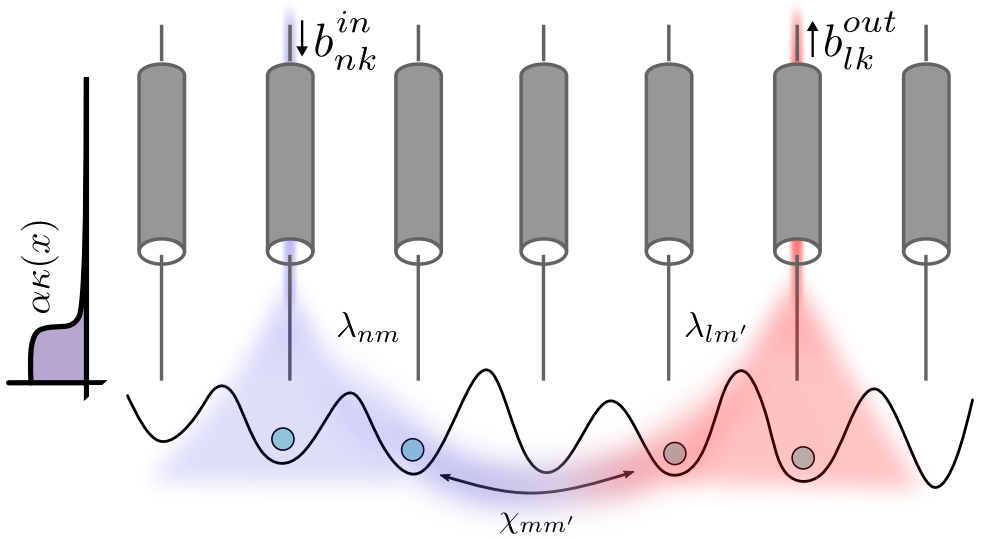

Figure 7.2: MADS readout protocol of a quantum simulator. A potential landscape confines particles in a lattice configuration. Each site can host a charge that is coupled to a transmission line through a spatially extended coupler envelope $\alpha\kappa(x)$. An input mode b_{nk}^{in} is sent along the n-th line exciting the charge in dot m via the cross-talk λ_{nm}. If the density-density correlator $\chi_{mm'}$ is finite, the charge fluctuations propagate to dot m', exciting the output mode b_{lk}^{out} .

7.1.1 The model

Figure 7.2 illustrates the experimental setup to perform MADS in a solid-state quantum simulator. We imagine that each site could be coupled to a quantum optical "bus", a transmission line, via the spatially extended coupling $\alpha\kappa(x)$, with $\kappa(x)$ normalized to unity in the domain $[0,\infty)$ of the feedline. As discussed in 2.3.1, the Hamiltonian describing this experimental setup reads (we take $\hbar = 1$)

$$\mathcal{H} = \mathcal{H}_0 + \frac{e\alpha}{c}\sum_{lm}\lambda_{lm}\int_0^\infty dx\kappa(x)Q_l(x)n_m\,, \qquad \mathcal{H}_0 = \mathcal{H}_{\rm sys} + \sum_l\int_0^\infty \omega_k b_{lk}^\dagger b_{lk}\,, \tag{7.3}$$

where we have separated the coupling terms from the isolated Hamiltonian $\mathcal{H}_0$. The isolated Hamiltonian $\mathcal{H}_0$ governs the evolution of transmission line modes b_{lk} and the quantum simulator. The cross term λ_{lm} quantifies the cross-coupling between the charge density Q_l in line l and the charge en_m on site m.

7.1.2 Input-output relations

We now derive the input–output (IO) relations linking the line fields and the density-density correlators in the system.

Input-output relations from the equation of motion Starting from the Fourier expansion in (2.62)

$$Q_l(x,t) = \sqrt{\frac{c}{\pi}}\int_0^\infty \sqrt{\omega_k}dk\left(b_{kl}(t) + b_{kl}^\dagger(t)\right)\cos(kx)\,, \tag{7.4}$$

the equations of motion for the b_{lk} read

$$\dot{b}_{lk} = i[H, b_{lk}] = -i\omega_k b_{lk} - ie\alpha\kappa(k)\sqrt{\frac{\omega_k}{2c}}\sum_m \lambda_{lm}n_m\,. \tag{7.5}$$

As already discussed in Sec. 2.3.1, solving this equation gives

$$\begin{aligned} b_{lk}(t) &= b_{lk}^{in}(t) - ie\alpha\kappa(k)\sqrt{\frac{\omega_k}{2c}}\sum_m \lambda_{lm}\int_{t_0}^{t} d\tau e^{-i\omega_k(t-\tau)} n_m(\tau) \\ &= b_{lk}^{out}(t) + ie\alpha\kappa(k)\sqrt{\frac{\omega_k}{2c}}\sum_m \lambda_{lm}\int_{t}^{t_1} d\tau e^{-i\omega_k(t-\tau)} n_m(\tau)\,, \end{aligned} \tag{7.6}$$

where the input and output modes are the free evolutions of the line modes from an initial condition t_0 in the remote past, and t_1 in the distant future

$$b_{lk}^{in}(t) = b_{lk}(t_0)e^{-i\omega_k(t-t_0)}\,, \quad b_{lk}^{out}(t) = b_{lk}(t_1)e^{-i\omega_k(t-t_1)}\,. \tag{7.7}$$

They are linked by the input-output relation

$$b_{lk}^{out}(t) = b_{lk}^{in}(t) - ie\alpha\kappa(k)\sqrt{\frac{\omega_k}{2c}}\sum_m \lambda_{lm}\int_{t_0}^{t_1} d\tau e^{-i\omega_k(t-\tau)} n_m(\tau)\,. \tag{7.8}$$

To express the IO relation in terms of measurable voltages, we decompose the charge density right and left moving envelopes

$$\overset{in}{Q}{}_n^{out}(x,t) = \overset{in}{Q}{}_n^{out}\left(t - \frac{x}{v}\right) + \overset{in}{Q}{}_n^{out}\left(t + \frac{x}{v}\right)\,,$$

where

$$\overset{in}{Q}{}_l^{out}(t) = \frac{1}{2}\sqrt{\frac{c}{\pi}}\int_0^\infty \sqrt{\omega_k}dk\left(b_{lk}^{out}(t) + b_{lk}^{out\,\dagger}(t)\right)\,. \tag{7.9}$$

Since the input and output modes evolve freely, their voltages are simply $\overset{in}{V}{}_l^{out}(t) = \overset{in}{Q}{}_l^{out}(t)/c$. Integrating Eq. (7.8) then yields

$$V_l^{out}(t) = V_l^{in}(t) - ie\frac{\alpha}{2c}\sum_m \lambda_{lm}\int_0^\infty dk\frac{\kappa(k)}{\sqrt{2\pi}}\omega_k\left(e^{-i\omega_k t}n_m(\omega_k) - e^{i\omega_k t}n_m(-\omega_k)\right)\,. \tag{7.10}$$

With the convention $V_l(\omega) = \int_{-\infty}^{\infty} dt V_l(t)e^{i\omega t}$, the IO relation in frequency domain reads, for any $\omega > 0$,

$$V_l^{out}(\omega) = V_l^{in}(\omega) - ie\frac{\alpha}{2c}\sum_m \lambda_{lm}\int_0^\infty dk\sqrt{2\pi}\kappa(k)\omega_k n_m(\omega_k)\delta(\omega-\omega_k)\,. \tag{7.11}$$

To simplify the δ-function in the integral, it is convenient to define $\tilde{\kappa}(x/v) = \kappa(x)$, so that its Fourier transform is

$$\tilde{\kappa}\,(\omega) = \frac{2}{v}\int_0^\infty dx\tilde{\kappa}\left(\frac{x}{v}\right)\cos\left(\omega\frac{x}{v}\right) = \frac{1}{v}\sqrt{2\pi}\kappa(k)\,. \tag{7.12}$$

With this shorthand notation, we obtain the voltage IO relation, which links the input and output voltages with the spectral properties of the system

$$V_l^{out}(\omega) = \sum_n V_n^{in}(\omega)\delta_{ln} - ie\omega\tilde{\kappa}\,(\omega)\,\frac{\alpha}{2c}\sum_m \lambda_{lm}n_m(\omega)\,. \tag{7.13}$$

Here $n_m(\omega)$ captures the system response to the input voltage. This response can be computed to leading order using the Kubo linear response formula.

Kubo linear response formula We now use the Kubo formula (see Appendix D.3) to obtain the linear response of the dot occupations to a weak drive applied from $t_0 = -\infty$. We obtain

$$\langle n_m(\tau)\rangle = \langle n_m\rangle_{\mathcal{H}_0} + \frac{e\alpha}{2c}\sum_{nm'}\lambda_{nm'}(\chi_{mm'} \star \mathcal{Q}_n)(\tau)\,, \tag{7.14}$$

where $(f \star g)(\tau) = \int_{-\infty}^{\infty} dt' f(\tau - t')g(t')$ denotes convolution, and $\mathcal{Q}_n(t')$ is the spatially filtered input charge

$$\mathcal{Q}_n(x,t') = \int_0^\infty dx\kappa(x)\langle Q_n^{in}(x,t')\rangle = v\left(\langle Q_n^{in}\rangle \star \tilde{\kappa}\right)(t')\,.$$

In the frequency domain, since the equilibrium term $\langle n_m\rangle_{\mathcal{H}_0}$ contributes only at $\omega = 0$, we obtain for any $\omega > 0$

$$\langle n_m(\omega)\rangle = \frac{e\alpha v}{2}\sum_{nm'}\lambda_{nm'}\chi_{mm'}(\omega)\tilde{\kappa}\left(\omega\right)\langle V_n^{in}(\omega)\rangle\,, \tag{7.15}$$

with $\chi_{lm}(\omega) = \int_{-\infty}^{\infty} dt e^{i\omega t}\chi_{lm}(t)$ the Fourier transform of the admittance.

Substituting this result into the voltage IO relation (7.13) yields

$$\left\langle V_l^{out}(\omega)\right\rangle = \left\langle V_l^{in}(\omega)\right\rangle - i\mathcal{Z}\Gamma(\omega)\sum_{nmm'}\lambda_{lm}\chi_{mm'}(\omega)\lambda_{nm'}\langle V_n^{in}(\omega)\rangle\,. \tag{7.16}$$

In words, the output on line l results from the reflected signal and the system's response, driven by all inputs and filtered by the effective density of states of the line $\Gamma(\omega) = \alpha^2 v^2\omega\tilde{\kappa}^2\left(\omega\right)/4$. Here we have restored the Planck's constant $\hbar$ and introduced the reduced line impedance

$$\mathcal{Z} = Z\frac{e^2}{\hbar} = 2\pi\frac{Z}{R_K}\,, \tag{7.17}$$

with $Z = \sqrt{l/c}$ the impedance of the transmission line and R_K the von Klitzing constant (the "quantum of resistance"). For a typical transmission line with impedance $Z = 50\ \Omega$, we have $\mathcal{Z} \approx 0.01$. Collecting terms, the IO relation can be written compactly in matrix form as

$$\left\langle \mathbf{V^{out}}(\omega)\right\rangle = \left\langle \mathbf{V^{in}}(\omega)\right\rangle - i\mathcal{Z}\Gamma(\omega)\boldsymbol{\lambda}\boldsymbol{\chi}(\omega)\boldsymbol{\lambda}^{\boldsymbol{T}}\left\langle \mathbf{V^{in}}(\omega)\right\rangle\,. \tag{7.18}$$

In words, this expression states that the output voltages are equal to the input voltages minus the signal re-radiated by the system, where the re-radiated part depends on the line impedance, the line's effective density of states at that frequency, the system's internal linear response, and the geometry of the couplings between the simulator and the lines.

The transmission matrix In practice, we exploit Eq. (7.18) through the protocol shown in Fig. 7.2. We drive the n-th line and record the output from all the lines. This gives the entire n-th column of the transmission matrix via $T_{ln}(\omega) = V_l^{out}(\omega)/V_n^{in}(\omega)$. Cycling over all the input lines, we build the full transmission matrix, which relates to the admittance $\chi_{lm}(\omega)$ as

$$\mathbf{T}(\omega) = \mathbf{1} - i\mathcal{Z}\Gamma(\omega)\boldsymbol{\lambda}\boldsymbol{\chi}(\omega)\boldsymbol{\lambda}^{\boldsymbol{T}}\,. \tag{7.19}$$

To connect with the dynamical structure factor (DSF) defined in (7.2), we move to momentum space by considering

$$T(q,\omega) = \frac{1}{N}\sum_{ln}T_{ln}(\omega)e^{-iq(l-n)}\,, \qquad \lambda_m(q) = \frac{1}{\sqrt{N}}\sum_l\lambda_{lm}e^{-iql}\,. \tag{7.20}$$

With these, Eq. (7.19) becomes

$$T(q,\omega) = 1 - i\mathcal{Z}\Gamma(\omega) \sum_{mm'} \lambda_m(q)\chi_{mm'}(\omega)\lambda^*_{m'}(q)\,. \tag{7.21}$$

Here we can see that the density of states of the line is responsible for the resolution in the frequency domain, while the couplings λ_{lm} filter the signal in momentum space.

Realistic experimentally relevant scenario As a concrete experimentally relevant choice we take $\kappa(x)$ as the one-sided Lorentzian envelope with half-width at half–maximum $(2\omega_c/v)^{-1}$

$$\kappa(x) = \frac{4}{\pi}\frac{\omega_c/v}{1+4x^2\,(\omega_c/v)^2}\theta(x)\,, \qquad \tilde{\kappa}\,(\omega) = \frac{2}{v}e^{-\frac{\omega}{2\omega_c}}\,. \tag{7.22}$$

With this choice the effective density of states is $\Gamma(\omega) = \alpha^2\omega e^{-\frac{\omega}{\omega_c}}$, exhibiting a high energy cutoff set by ω_c. For the cross-talk matrix, we consider an exponential decay $\lambda_{lm} = e^{-\xi|l-m|}$ with decay length $1/\xi$. This yields

$$\lambda_m(q) = \frac{e^{-iqm}}{\sqrt{N}}\left[\frac{1-e^{-2\xi}}{1-2e^{-\xi}\cos q + e^{-2\xi}} - \frac{\left(e^{iq-\xi}\right)^{d_L+1}}{1-e^{iq-\xi}} - \frac{\left(e^{-iq-\xi}\right)^{d_R+1}}{1-e^{-iq-\xi}}\right], \tag{7.23}$$

where the last two terms are edge corrections with $d_L = m-1$ and $d_R = N-m$ the distances from the left and right edge, respectively.

To gain further insight we consider now periodic boundary conditions (PBC). Translational invariance allows us to define $\lambda(q) = \sum_l \lambda_{lm}e^{-iq(l-m)} = \sqrt{N}e^{iqm}\lambda_m(q)$ and directly relate it to the DSF. Taking the real part, Eq. (7.21) becomes

$$\mathrm{Re}T(q,\omega) = 1 - \frac{\mathcal{Z}}{2}\Gamma(\omega)|\lambda(q)|^2 S(q,\omega)\,, \tag{7.24}$$

with $q = 2\pi n/N$ and $n = 1,\ldots,N$.

In the next section, we compute $S(q,\omega)$ and show that it can be directly measured by $T(q,\omega)$ in a realistic experimentally relevant scenario.

7.2 MADS for spinless fermions in 1D

In this Section we apply MADS for a spinless one dimensional chain of N quantum dots. This system realizes the one dimensional spin-less Fermi-Hubbard model, which maps to the Heisenberg spin chain via the Jordan-Wigner transformation, and thus provides an alternative to neutron scattering for probing the DSF (see Fig. 7.1).

The experimental cQED platform to realize MADS in this system is shown in Fig. 7.3. To each site i, we associate fermionic creation and annihilation operators $c_i^\dagger$, c_i. The system is characterized by a tunneling rate t between neighboring dots and a nearest neighbor Coulomb interaction U. The Hamiltonian reads

$$\mathcal{H}_{\mathrm{sys}} = -t\sum_i \left(c_{i+1}^\dagger c_i + \mathrm{h.c.}\right) + U\sum_i n_i n_{i+1} + \mu N\,, \tag{7.25}$$

where we have introduced the occupation number operator $n_i = c_i^\dagger c_i$ and the total occupation $N = \sum_i n_i$. The Hamiltonian conserves particle number, which is set by the chemical potential μ.

In this Section we compute the DSF in the non-interacting case (Sec. 7.2.1) and discuss the features of the interacting regime, showing how the transmission coefficient can be used to extract the DSF (Sec. 7.2.2).

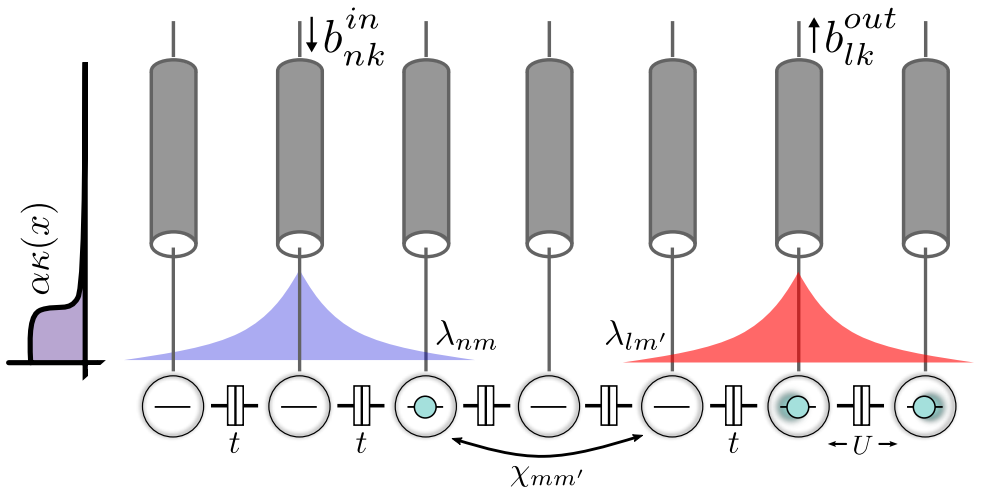

Figure 7.3: MADS readout of the dynamical structure factor in a chain of quantum dots. Particles (light blue circles) hop between neighboring dots via the tunnel coupling t and experience a nearest-neighbor Coulomb interaction U. Each dot is coupled to a transmission line through a spatially extended coupler envelope $\alpha\kappa(x)$. An input mode b^{in}_{nk} is sent along the n-th line exciting the charge in dot m via the cross-talk λ_{nm}. If the density-density correlator $\chi_{mm'}$ is finite, the charge fluctuations propagates to dot m', exciting the output mode b^{out}_{lk} .

7.2.1 Non-interacting fermions

In this Section we compute the DSF in the non interacting regime for a periodic and open chain.

Periodic boundary conditions (PBC) For non-interacting fermions, Eq. (7.25) reduces to a free tight-binding Hamiltonian. The single-particle eigenstates are the crystal momentum eigenstates [93]

$$|k\rangle = \frac{1}{\sqrt{N}} \sum_n e^{ikl} |l\rangle \,, \qquad k = \frac{2\pi}{N} n \,, \qquad n = 1, \dots, N \,. \tag{7.26}$$

where $\{|l\rangle\}$ are states[1] localized at lattice sites n. We can use these eigenstates to perform the change of basis on the fermionic creation/annihilation operators (see Appendix E.1)

$$c_k = \sum_n \langle k|l\rangle \, c_l = \frac{1}{\sqrt{N}} \sum_n e^{-ikn} c_n \,. \tag{7.27}$$

In this momentum basis, the Hamiltonian becomes $\mathcal{H}_{\text{sys}} = \sum_k \epsilon(k) c^\dagger_k c_k$ and the assembly of free fermions is fully described by the dispersion law $\epsilon(k) = -2t \cos k + \mu$. The ground state has all the levels with $\epsilon(k) \leq 0$ occupied. For $\mu < 2t$ all levels are occupied, for $\mu > 2t$ they are all vacant, whereas for intermediate μ two Fermi points $k = \pm k_F$ exist, separating occupied and vacant levels. This is the regime with a ground state which is a simple Slater determinant of the single-particle wave functions of each fermion. The case of $\mu = 0$ corresponds to the half-filling condition in which $k_F = \pi/2$ and the total occupation is equal to half the number of available sites. Unlike free fermions in the continuum, the spectrum here is bounded, as shown in Fig. 7.4a. This is no surprise since the model is equivalent to free fermions in a periodic potential. Couplings between replicas of the free-fermion dispersion open gaps at the first Brillouin zone boundary, so the dispersion within one band is necessarily bounded (see Sec. 5.2).

[1] These are the Wannier functions expressed in ket notation, $\langle x|n\rangle = w_{n,R}(x)$ (See Eq. (7.28)) [165].

Relation between the tight-binding Hamiltonian and free fermions in a periodic potentials

The Wannier functions for the band n are the Fourier transform in the lattice-space R of the state $\psi_k^{(n)}$

$$w_{n,R}(x) = \frac{1}{\sqrt{N}} \sum_k e^{-ikR} \psi_k^{(n)}(x) \,, \tag{7.28}$$

and form a complete basis set of the Hilbert space. By lattice translation symmetry the Hamiltonian matrix elements in this basis read

$$\mu = \langle w_{n,0} \,|H|\, w_{n,0} \rangle \,, \qquad\qquad t_\Delta = -\langle w_{n,\Delta} \,|H|\, w_{n,0} \rangle \,. \tag{7.29}$$

Now, if we consider only one band and c_R annihilates an electron in $|w_{n,R}\rangle$, the Hamiltonian can be rewritten as

$$H = \mu \sum_R c_R^\dagger c_R - \sum_{R,\Delta>0} t_\delta \left(c_{R+\Delta}^\dagger c_R + c_R^\dagger c_{R+\Delta} \right) \,. \tag{7.30}$$

Considering the case of the periodic potential discussed in Sec. 5.2, for sufficiently deep potential well naturally reduces to the tight-binding Hamiltonian (7.25). In this regime, the Wannier functions of an isolated band are exponentially localized around the lattice sites, so overlaps between distant centers are negligible and the dominant tunneling is between nearest neighbors, $t_\Delta \approx t\delta_{\Delta 1}$. Hence, the spectrum follows from the single-band projection of the dispersion shown in Fig. 5.2, where the periodic potential opens gaps between different replicas of the non-interacting free fermion dispersion.

In momentum space, the density operator reads $n_q = \sum_{k_i} c_{k_i}^\dagger c_{k_i+q}$ and the density-density correlation functions are obtained by excited states $|k_i + q\rangle = c_{k_i+q}^\dagger c_{k_i} |GS\rangle$ with only one particle-hole excitation carrying total momentum q. To compute the DSF through $S(q, \omega > 0) = -2\mathrm{Im}\chi(q, \omega)$, we use the Lehmann representation (see Appendix E.2.1)

$$S(q, \omega > 0) = \frac{1}{N} \sum_{k_i} \frac{|\langle GS \,|n_q|\, k_i + q \rangle|^2}{\omega - \omega_{k_i}(q) + i0^+} \,, \tag{7.31}$$

where $\omega_{k_i}(q) = \epsilon(k_i + q) - \epsilon(k_i)$ is the particle-hole excitation spectrum. At zero temperature, the sum is restricted by the Pauli principle to initially occupied states and finally empty states, $|k_i| < k_F < |k_i + q|$.

The particle-hole excitation spectrum form a continuum in the thermodynamic limit ($N \to \infty$) generally referred to as the two-particle continuum. At half-filling, the boundaries of this continuum are $\omega_L(q) = v_F |\sin(q)|$ and $\omega_U(q) = 2v_F |\sin(q/2)|$, where $v_F = 2t$ is the Fermi velocity. Because of time-reversal symmetry, we can restrict the discussion to $0 \leq q \leq \pi$. The lower threshold is achieved for particle-hole pairs with a deep hole and a low-energy particle ($k_i + q \sim k_F$) or with a finite-energy particle with a low-energy hole ($k_i \sim k_F$). The upper threshold is defined by the symmetric excitations with a hole at $k_F - q/2$ and a particle at $k_F + q/2$ (see Fig. 7.4a) [138].

Using $(x \pm i0^+)^{-1} = \mathcal{P}(1/x) \mp i\pi\delta(x)$, we can evaluate directly the imaginary part of (7.31). In the thermodynamic limit $N \to \infty$ this gives

$$S(q, \omega) = \int_{-\infty}^{\infty} dk_i \delta(\omega - \omega_{k_i}(q)) \theta(\omega - \omega_L(q)) \theta(\omega_U(q) - \omega) \,. \tag{7.32}$$

Equivalently, evaluating the delta function one finds [155]

$$S(q,\omega) = \sum_{\omega_{k_i}(q)=\omega} \left(\frac{d\omega_{k_i}(q)}{dk_i}\right)^{-1} \theta(\omega - \omega_L(q))\theta(\omega_U(q) - \omega)\,. \tag{7.33}$$

Because of particle–hole symmetry [166], for each q and ω there are two degenerate states $|k_1\rangle$ and $|k_2\rangle$ satisfying $\omega_{k_i}(q) = \omega$ (except at $\omega_U(q)$). Hence, the sum provides an overall factor 2 [155, 167] and the result can be written in terms of the joint density of states of the two-particle continuum $D(q,\omega)$ as

$$S(q,\omega) = \frac{4\pi}{N} D(q,\omega)\theta(\omega - \omega_L(q))\theta(\omega_U(q) - \omega)\,, \tag{7.34}$$

where

$$\frac{4\pi}{N} D(q,\omega) = 2\left(\frac{d\omega(q)}{dk_i}\right)^{-1} = 2\left(\omega_U(q)^2 - \omega^2\right)^{-\frac{1}{2}}\,. \tag{7.35}$$

Thus, as shown in Fig. 7.4b, $D(q,\omega)$ exhibits an inverse square-root divergence at the upper boundary which stems from the van Hove singularity of an electron and a hole with the same velocity. Indeed, from Eq. (7.35) one has $D(q,\omega) \propto (v_f - v_i)^{-1}$, with $v_{i(f)} = \partial_k \epsilon(k_{i(f)})$ the velocity of the hole (particle) [168].

Open boundary conditions (OBC) To treat open boundary conditions (OBC), we evaluate the DSF from the real-space admittance as (see Appendix E.3.2) [169]

$$\chi_{lm}(\omega) = -\frac{1}{\pi}\int_{-\infty}^{0} d\varepsilon \mathrm{Im} G^R_{lm}(\varepsilon)\left(G^R_{lm}(\varepsilon+\omega) + \bar{G}^R_{lm}(\varepsilon-\omega)\right)\,, \tag{7.36}$$

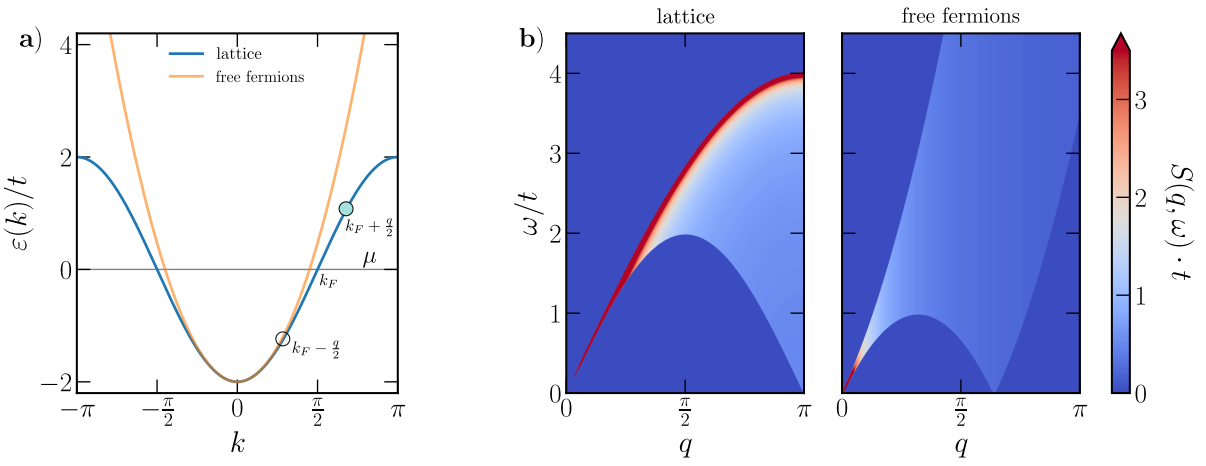

Figure 7.4: One-particle spectrum and DSF for a tight-binding chain and for free fermions. a) One-particle spectrum at chemical potential $\mu = 0$, which corresponds to half-filling in the chain. For the free case we choose the mass so that the continuum dispersion matches the second-order Taylor expansion of the lattice dispersion near $k = 0$. The cosine-shaped band supports particle–hole pairs whose group velocities coincide, which produce a van Hove singularity. b) Because the spectrum in the chain is bounded, the particle-hole excitation continuum is also bounded with van Hove singularity appearing at its upper boundary.

where $G^R_{lm}(t) = -i\theta(t)\langle\{c_l(t), c^\dagger_m\}\rangle$. To construct the OBC Green's function, we first compute the OBC single-particle eigenstates via the method of images. An N-open chain is then equivalent to a ring of length $2N+2$ with hard walls at 0 and $N+1$. The states that satisfy these boundaries are the antisymmetric combinations of the ring plane waves

$$\left|k^{OBC}\right\rangle = \frac{1}{\sqrt{2N+2}} \sum_l \left(e^{ikl} - e^{-ikl}\right) |l\rangle \,, \qquad k = \frac{\pi}{N+1} n \qquad n = 1, \ldots, N \,. \tag{7.37}$$

With these eigenfunctions, we construct the Lehmann representation for the Green's functions (see Appendix E.2.2)

$$\begin{aligned} G^{R,OBC}_{lm}(N,\omega) &= \sum_k \frac{\left\langle l|k^{OBC}\right\rangle \left\langle k^{OBC}|m\right\rangle}{\omega - \epsilon(k) + i0^+} \\ &= \frac{1}{N+1} \sum_k \frac{\cos(k(l-m)) - \cos(k(l+m))}{\omega - \epsilon(k) + i0^+} \qquad (7.38) \\ &= G^{R,\mathrm{PBC}}_{l-m}(2N+2,\omega) - G^{R,\mathrm{PBC}}_{l+m}(2N+2,\omega) \,. \qquad (7.39) \end{aligned}$$

Intuitively, the open boundaries act as perfect mirrors that emit an image source at $-m$ with opposite sign. Subtracting the image propagator cancels all paths that would "leak" across the walls and enforces the open boundary conditions. Due to translational invariance and time-reversal symmetry, the PBC Green's functions depend only on the difference $|l-m|$. They are obtained from the Lehmann representation (see Appendix E.2.2)

$$G^{R,PBC}_{l-m} = \sum_k \frac{\langle l|k\rangle \langle k|m\rangle}{\omega - \epsilon(k) + i0^+} = \frac{1}{N} \sum_k \frac{e^{-ik|l-m|}}{\omega - \epsilon(k) + i0^+} \,, \tag{7.40}$$

Evaluating the sum in k with the residue theorem. This yields

$$G^{R,\mathrm{PBC}}_{l-m}(N,\omega) = \frac{4}{t} \frac{1}{r_2 - r_1} \left(\frac{r_1^{|l-m|}}{r_1^N - 1} - \frac{r_2^{|l-m|}}{r_2^N - 1} \right) \,, \tag{7.41}$$

with $r_{1,2} = (-\omega_+ \pm \sqrt{\omega_+^2 - 4t^2})/2t$ and $\omega_+ = \omega + i0^+$.

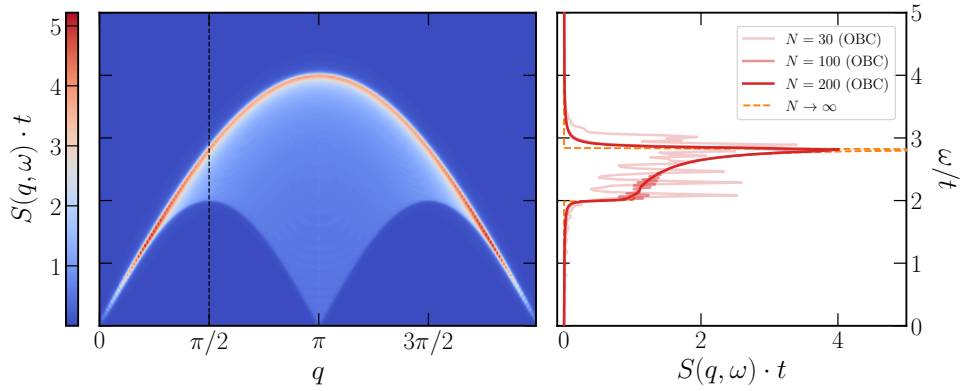

Figure 7.5: Non-interacting DSF at half-filling ($\mu = 0$). The DSF in the thermodynamic limit has a step-function singularity at the lower threshold $\omega_L(q)$ and diverges as an inverse square-root at the upper threshold $\omega_U(q)$. Considering a chain with $N = 200$ dots, finite size effects are negligible and the DSF approaches the predicted behavior in the thermodynamic limit.

Additional fermionic baths coupled to each dot can be included via the substitution $\omega \to \omega + i\Gamma$ in Eq. (7.36), where Γ is the induced linewidth of the system's single-particle eigenstates.

For a chain of $N = 30$ dots at half-filling (Fig. 7.5), the DSF consists of a discrete set of peaks within the two-particle continuum, reflecting the finite number of allowed particle–hole excitations ω_{k_i} in Eq. (7.31).

7.2.2 Interacting gapless regime

In this Section we briefly review non-linear Luttinger liquid theory and its predictions for the edge exponents at the boundaries of the two-particle continuum. Equipped with density-matrix renormalization group (DMRG) simulations, we show that non trivial effects of the interaction and the critical exponents can be extracted from the transmission coefficient in a realistic experimentally relevant scenario.

Exact edge singularities : the Luttinger liquid For $0 < U \leq 2t$ the system remains gapless and its low-energy dynamics are those of a Luttinger liquid with the bare Fermi velocity renormalized to the sound velocity $u = \pi\sqrt{t^2 - 4U^2}/\arccos(2U/t)$ [170]. The particle-hole excitation spectrum still lies in a two-particle continuum whose edges are renormalized by u (see Figs. 7.6) [161]. Its low-energy excitations can be obtained linearizing the dispersion relation near the two Fermi points [170] such that the model becomes equivalent to the Luttinger model [171–173]. At half-filling, charge-density waves that propagate with an effective velocity u are true eigenstates of the Hamiltonian [170]. The low-energy spectrum consists in a linear mode near $q \sim 0$, corresponding to a single boson with infinite lifetime, and a continuum near $q \sim \pi$. The DSF reflects this spectrum: on the mass shell of the boson excitations $\omega = uq$, one finds $S(q,\omega) = Kq\delta(\omega - uq)$ while for $q \sim \pi$ there is a power law singularity at the approximate lower edge of the continuum

$$S(q,\omega) = [\omega^2 - u^2(q-\pi)^2]^{K-1}\,, \tag{7.42}$$

where $K = [2 - 2\arccos(2U)/\pi]^{-1}$ is the parameter of the Luttinger liquid [174–176].

Outside $q = 0, \pi$, the interaction is mapped via bosonization [170] into boson-boson interaction terms in the Luttinger Hamiltonian. If the DSF still presents a step discontinuity at its lower edge due to energy–momentum conservation and Pauli principle, the general behavior of the DSF near the edges can be described considering a Luttinger liquid coupled to mobile impurities [138, 161, 177–181] as in the x-ray edge problem [177, 182, 183]. For the lower threshold

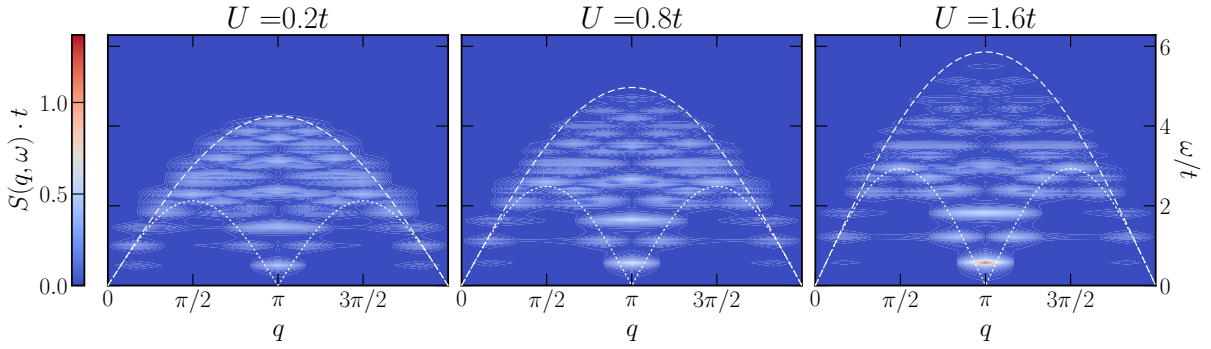

Figure 7.6: $S(q,\omega)$ computed through exact diagonalization (ED) for an open chain of $N = 12$ dots with line-width $\Gamma/t = 0.05$ for different value of the interaction U. The dashed line outlines the boundary of the renormalized two-particle continuum.

$\omega_L(q)$, it is sufficient to consider Fourier modes $\psi_{R/L}$ near $\pm k_F$ and a high energy particle d_1 (either a deep hole or a finite-energy particle). Due to particle-hole symmetry [166], we can consider just the case of a deep hole with $k_1 = k_F + q$. The Fermion field then writes as

$$\psi(x) \sim e^{ik_F x}\psi_R(x) + e^{-ik_F x}\psi_L(x) + e^{ik_1 x_1}d_1(x)\,, \tag{7.43}$$

such that the density operator is

$$\begin{aligned} n_x \sim \psi_R^\dagger\psi_R + \psi_L^\dagger\psi_L + d_1^\dagger d_1 + \Big[e^{i2k_F x}\psi_L^\dagger\psi_R \\ + e^{i(k_1-k_F)x}\psi_R^\dagger d_1 + e^{i(k_1+k_F)x}\psi_L^\dagger d_1 + \text{h.c.}\Big]\,. \end{aligned} \tag{7.44}$$

The component at total momentum $q = k_i - k_F$ is therefore

$$n(x)\big|_q \;\propto\; e^{iqx}\,\psi_R^\dagger d_1 + \text{h.c.}\,,$$

and the only relevant term for the computation of the DSF at q is

$$\langle n_{j+x}(t)n_j\rangle = e^{iqx}\left\langle d_1^\dagger\psi_R(x,t)\psi_R^\dagger d_1\right\rangle\,. \tag{7.45}$$

The evaluation of Eq. (7.45) leads to power law behavior[2]

$$S(q,\omega) \sim [\omega - \omega_L(q)]^{K-1}\,, \tag{7.46}$$

which is in agreement with the predictions of the Bethe-Ansatz solution at the isotropic point $U/t = 2$ [156].

The behavior near the upper threshold is described by the operator d_1, that creates a hole with momentum $k_1 = \pi/2 - q$, and by $d_2^\dagger$, that creates a particle with momentum $k_2 = \pi/2 + q$. The evaluation of relevant correlator in this case, $\langle d_1^\dagger d_2(x,t)d_2^\dagger d_1(0,0)\rangle$, leads to the power law[3]

$$S(q,\omega) \sim \sqrt{\omega_U(q) - \omega}\,, \tag{7.47}$$

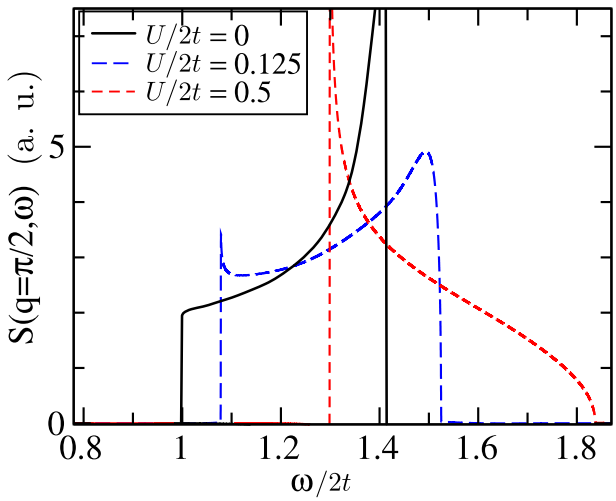

Figure 7.7: $S(q = \pi/2, \omega)$ for several values of U. The line shapes show a divergent x-ray type lower edge and a universal square-root cusp at the upper edge. Figure adapted from Ref. [161].

[2]This is the expression conjectured by Müller [155].
[3]This result contradicts the Müller conjecture [155].

which is in agreement with the predictions of the Bethe Ansatz [155, 156, 159, 184].

To resume, as $U \neq 0$, the van Hove singularity at the upper edge is removed, and as the interaction increases the spectral weight is transferred toward the lower edge, as shown in Fig. 7.7 [161].

Exact diagonalization In Figure 7.6 we compute $S(q,\omega)$ numerically by exact diagonalization for a chain of $N = 12$ dots. After obtaining the full spectrum, we evaluate the real-time correlator

$$\chi_{mm'}(t) = -i\theta(t)\left\langle GS|e^{-iHt}n_m e^{iHt}n_{m'}|GS\right\rangle = e^{-i\varepsilon_{GS}t}\left\langle GS|n_m e^{iHt}n_{m'}|GS\right\rangle \tag{7.48}$$

by applying the matrix exponential e^{iHt} to the state $n_{m'}|GS\rangle$ and then taking the inner product with $n_m|GS\rangle$.

The numerical results indicate that for $0 < U \leq 2t$ the support of $S(q,\omega)$ still lies in a two-particle continuum whose prefactor is renormalized by the interaction. For any $U \neq 0$, the van Hove singularity at the upper edge is removed, and as the interaction increases the spectral weight is transferred toward the lower edge, most prominently at $q = \pi$. Although limited to small system sizes, these simulations provide a robust benchmark for the density-matrix renormalization group simulations presented below.

Density matrix renormalization group To simulate the DSF for longer chains, we perform time-dependent simulations[4] using the density-matrix renormalization group (DMRG) [164]. The DMRG calculation begins with the standard DMRG calculation of the ground state $|GS\rangle$ on a finite system. The ground state is computed from a variational method in the matrix product state (MPS) ansatz.

An MPS is a factorized representation of a many-body wavefunction

$$|\psi\rangle = \sum_{s_1 \ldots s_N} a(s_1,\ldots,s_N)\,|s_1 \ldots s_N\rangle\ . \tag{7.49}$$

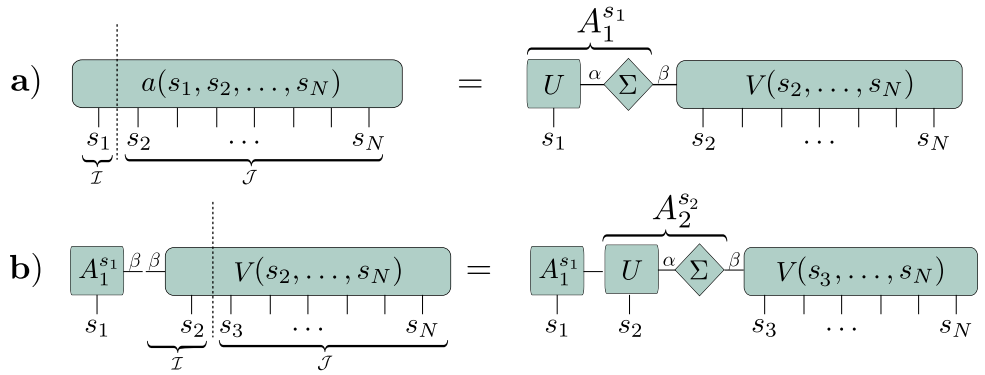

Figure 7.8: Consecutive singular value decompositions (SVD) used to compress a multi-dimensional rank-N tensor into a MPS. a) We consider the index $\mathcal{I} = \{s_1\}$ and the multi-index $\mathcal{J} = \{s_2, \ldots, s_N\}$, and perform an SVD $a_{\mathcal{I}\mathcal{J}} = U_{\mathcal{I}\alpha}\Sigma_{\alpha\beta}V_{\beta\mathcal{J}}$, where U carries $\mathcal{I}$ and a virtual index α contracted with Σ while V carries a virtual index β contracted with Σ and $\mathcal{J}$. For each s_1, $A_1^{s_1}$ is obtained contracting U and Σ. b) $A_2^{s_2}$ is obtained repeating the same procedure with $\mathcal{I} = \{\beta, s_2\}$ and $\mathcal{J} = \{s_3, \ldots, s_N\}$.

[4] We use the package ITensor [185].

As shown in Fig. 7.8, the collection of all the coefficients $a(s_1, \ldots, s_N)$ form a rank-N multi-dimensional tensor with indices $s_1, \ldots, s_N$. By applying consecutive singular value decompositions (SVD) one obtains the matrix-product form

$$|\psi\rangle = \sum_{s_1 \ldots s_N} A_1^{s_1} A_2^{s_2} \ldots A_N^{s_N} |s_1 \ldots s_N\rangle \ , \tag{7.50}$$

where $A_j^{s_j}$ is a $\chi_{j-1} \times \chi_j$ matrix (with $\chi_0 = \chi_N = 1$) and χ_js are called the bond dimensions. A priori, the procedure can reproduce any wavefunction for sufficiently high bond dimension, but in practice a maximum bond dimension χ is chosen to control the size of the variational Ansatz. Concretely, DMRG optimizes locally the A-matrices by sweeping back and forth along the chain at fixed bond dimensions until convergence, then increases the bond dimensions and repeats.

Once the ground state is available in MPS form, we need a compatible way to apply operators to it. Following a construction similar to Fig. 7.8, we represent any operator

$$\mathcal{O} = \sum_{s_1 s_1' \ldots s_N s_N'} \mathcal{O}(s_1, s_1' \ldots, s_N, s_N') \, |s_1 \ldots s_N\rangle \langle s_1' \ldots s_N'| \tag{7.51}$$

in the matrix product operator form (MPO)

$$\mathcal{O} = \sum_{s_1 s_1' \ldots s_N s_N'} W_1^{s_1 s_1'} W_2^{s_2 s_2'} \ldots W_N^{s_N s_N'} |s_1 \ldots s_N\rangle \langle s_1' \ldots s_N'| \ , \tag{7.52}$$

where each $W_j^{s_j s_j'}$ is a matrix for each value of the physical indices (s_j, s_j'). Acting with an MPO on an MPS is a site-wise contraction that yields another MPS after compression.

With this representation, we apply the local density operator $n_{m'}$ to the ground state to obtain $|\phi\rangle = n_{m'} |GS\rangle$. We then evolve $|\phi\rangle$ in real-time using the Time-Evolving Block Decimation (TEBD) algorithm [186].

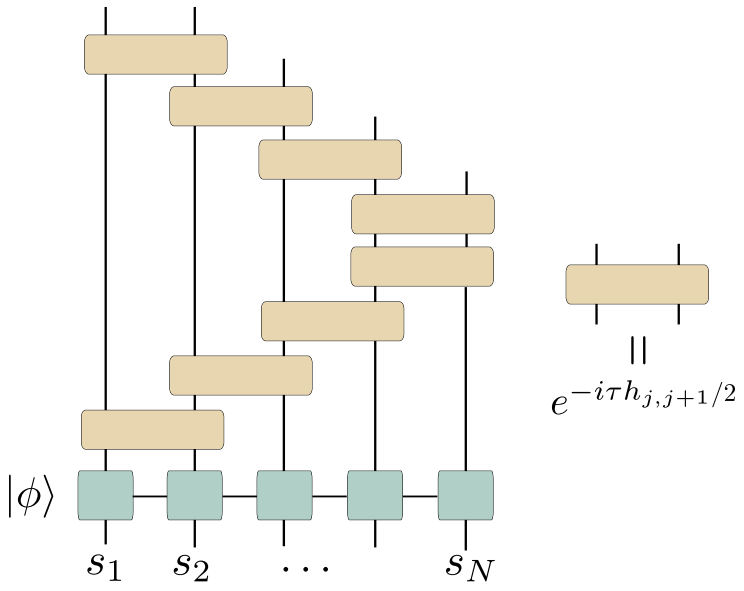

Figure 7.9: Time-Evolving Block Decimation (TEBD) algorithm. The one-step time evolution operator is decomposed into two-site gates using the Trotter decomposition in Eq. (7.53). Each gate is applied sequentially to $|\phi\rangle = n_{m'} |GS\rangle$ first from left to right and then from right to left, according to Eq. (7.53).

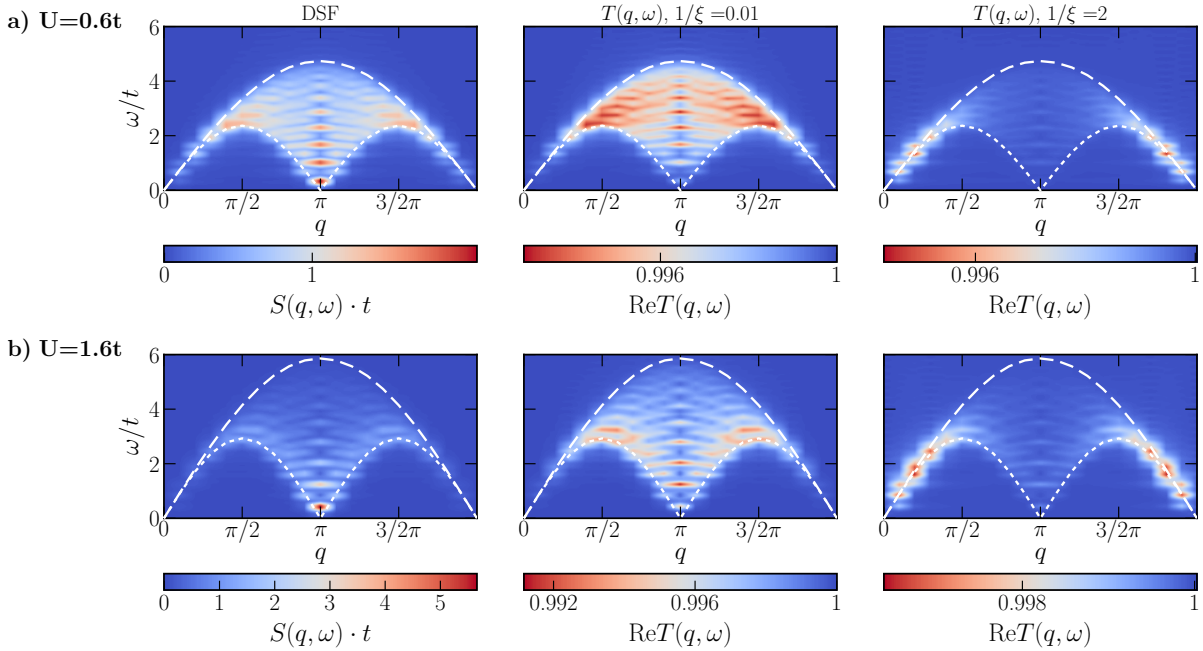

Figure 7.10: DMRG results for $S(q,\omega)$ and $T(q,\omega)$ for a chain of $N = 20$ dots with line-width $\Gamma/t = 0.1$. The time evolution is computed with a time step $\tau/t = 0.005$ up to $t_{\text{final}}/t = 25$. The dashed line outlines the boundary of the renormalized two-particle continuum.

Time evolution using the TEBD algorithm Since direct application of $e^{-it\mathcal{H}_{\text{sys}}}$ typically causes rapid bond-dimension growth, we divide the total time interval into steps τ and use a second order Trotter decomposition of $\mathcal{H}_{\text{sys}} = \sum_j h_{j,j+1}$

$$e^{-i\tau\mathcal{H}_{\text{sys}}} \approx e^{-ih_{1,2}\tau/2} \ldots e^{-ih_{N-1,N}\tau/2}\, e^{-ih_{N-1,N}\tau/2}\, e^{-ih_{N-2,N-1}\tau/2} \ldots e^{-ih_{1,2}\tau/2}\,. \tag{7.53}$$

At each substep we apply the corresponding two-site gate as shown in Fig. 7.9. We then compress the final MPS and truncate back to the target bond dimension, monitoring the discarded weight. The procedure is repeated m times until $t_{\text{final}} = m\tau$.

Finally, we compute the inner product of $|\phi(t)\rangle$ with $n_m\,|GS\rangle$ as an MPS-MPS contraction. Multiplying by $e^{-i\varepsilon_{GS}t}$ yields the density-density correlator.

In Fig. 7.10 we show the result for a chain of $N = 20$ dots. For any $U \neq 0$ the upper-edge divergence is removed by interactions. As U increases, spectral weight shifts toward the lower threshold, most prominently at $q = \pi$. Although the same trend is visible in $T(q,\omega)$, the couplings $\lambda_{lm} = e^{-\xi|l-m|}$ largely suppress the signal at $q = \pi$. At this point, $\lambda(q=\pi) = \sum_{lm}\lambda_{lm}(-1)^{l-m}$ so contributions from even/odd separations cancel. As the characteristic length $1/\xi$ increases, many alternating-sign terms contribute, and the cancellation is strong. Overall, these finite-size features are consistent with the Luttinger-liquid description.

Figure (7.11) investigates further the qualitative effects of the interaction in a finite size chain of $N = 40$ dots. As $U \neq 0$, the intensity peak at the upper edge due to the van Hove singularity is suppressed and transfered to the lower edge of the two particle-continuum. The sudden change in the slope of the transmission coefficient is therefore a clear experimental signature of the interactions.

Figure 7.121a,b shows that beyond the spectral-weight transfer, $T(q,\omega)$ directly reveals the true power-law scaling at the upper boundary in chains as small as $N = 20$ dots, in quantitative agreement with the nonlinear Luttinger-liquid prediction, Eq. (7.47). As the system size

increases, signatures of the power-law singularity at the lower edge, Eq. (7.46), are also captured by $T(q,\omega)$.

The universal Luttinger behavior at $q = \pi$ is clearly manifest in the DSF for $N = 60$ dots, but it is not captured by the transmission coefficient. This singularity lies at small ω, where the behavior of the transmission coefficient is dominated by the by the line's effective density of states $\Gamma(\omega) \sim \omega$, which masks the divergence in $T(q,\omega)$, leaving the leading behavior $T(q,\omega) \sim 1-\Gamma(\omega) \sim 1-\omega$. Optical buses with different density of states could restore visibility of this singularity.

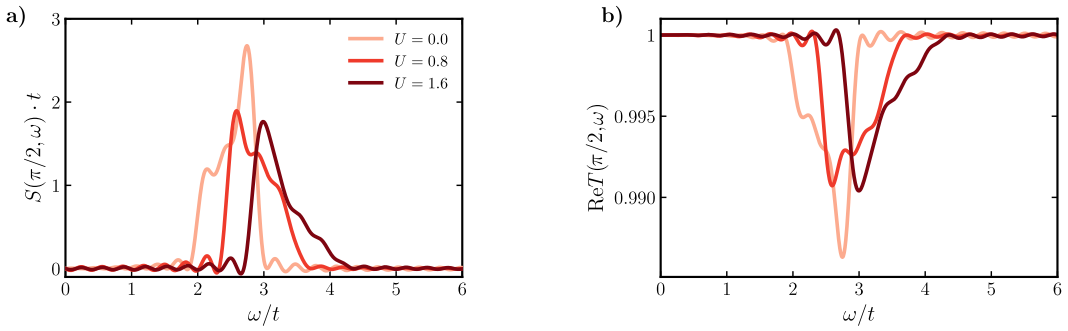

Figure 7.11: DMRG results for $S(q,\omega)$ and $T(q,\omega)$ for open chain with $N = 40$ dots show the weight transfer of the DSF toward the lower edge of the two particle continuum. Temporal evolution obtained with a time step $\tau/t = 0.01$ up to $t_{\mathrm{final}}/t = 20$. Parameters considered to generate the plots: $\mathcal{Z} = 0.01$, $\alpha = 0.7$, $\omega_c/t = 10$, $\Gamma/t = 0.05$.

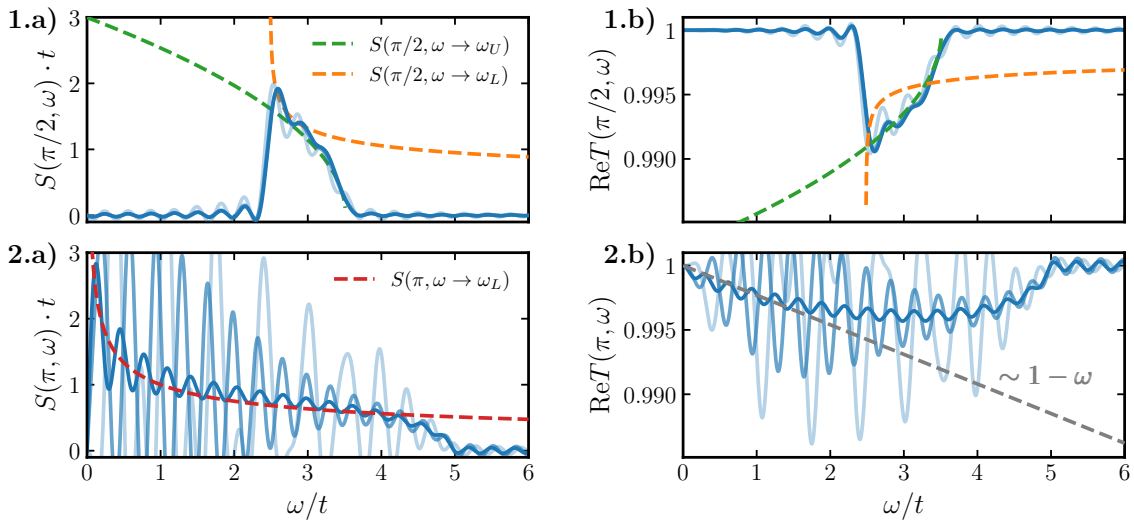

Figure 7.12: DMRG results for $S(q,\omega)$ and $T(\omega,q)$ for open chain with $N = 20$, 40 and 60 dots (opacity increases with N) and with interaction $U = 0.8t$. The orange, green and red dashed lines correspond to the edge exponents given by Eqs. (7.46),(7.47) and (7.42), respectively. Temporal evolution obtained with a time step $\tau/t = 0.01$ up to $t_{\mathrm{final}}/t = 20$. Parameters considered to generate the plots: $\mathcal{Z} = 0.01$, $\alpha = 0.7$, $\omega_c/t = 10$, $\Gamma/t = 0.05$.

7.3 Chapter 7 in a nutshell

In this chapter we proposed many-body admittance spectroscopy (MADS) as a route to access dynamical properties of solid-state quantum simulators. For a network of transmission lines coupled to a lattice system, the measured transmission directly probes the DSF linking an experimentally accessible quantity to the many-body spectrum.

We benchmarked the protocol on a one-dimensional spinless tight-binding chain. In the non-interacting limit, the DSF occupies a particle-hole continuum bounded below and above. The lower edge appears as a step, while the upper edge hosts an inverse square-root (van Hove) singularity. For finite chains this structure resolves into discrete peaks that sharpen as the size grows. Turning on interactions, exact diagonalization and time-dependent DMRG reveal a clear qualitative change: the non-interacting upper-edge divergence disappears, the boundary of the continuum renormalizes and spectral weight shifts toward the lower edge, especially at $q \approx \pi$. In transmission, however, the build-up expected at $q = \pi$ is partly hidden by two factors: small-frequency behavior is dominated by the line's effective density of states, and the spatial coupling profile produces strong even/odd cancellations which suppress the signal in the presence of cross-talks.

For $q \neq \pi$ the behavior towards the edge can be explained in the thermodynamic liquid by a non-linear Luttinger theory which predicts a square-root cusp at the upper threshold and a lower-edge power law governed by the Luttinger parameter. We showed that the experimentally accessible transmission coefficient extracted via MADS are consistent with these edge trends for chains as small as $N = 40$ dots.

In short, MADS provides a controllable route to $S(q, \omega)$ in quantum-dot arrays. It reproduces the non-interacting continuum and its singularities, tracks the renormalization of the continuum due to the interactions, and, within realistic system sizes, potentially resolves the Luttinger-liquid edge physics directly from transmission data.

Since the hybrid cQED platform introduced at the beginning of this chapter is not inherently restricted to one dimensional quantum simulators, a natural direction is to apply MADS to investigate two-dimensional materials.

Chapter

8 Conclusions and perspectives

In this thesis, we explore the limits of fast, efficient single and many-body readout in cQED. Two guiding questions motivated our work: is longitudinal coupling an universal mechanism that can be placed on a theoretical footing that remains predictive beyond state of the art limitations? Can the cQED toolbox be repurposed to read out non-trivial effects of interactions in quantum simulators?

To answer the first question, we devised a Floquet formalism that connects the AC Stark shift of a driven qubit with its longitudinal coupling. We find that if dispersive coupling originates from second-order variation of the Floquet spectrum, longitudinal coupling is tied to its first-order variation, and it is proportional to the static curvature (or quantum capacitance) only in the weak drive limit. Our approach provides a simple and seamless description of various regimes within a unifying framework, extending previous approaches [29, 73–77, 80, 81, 100, 187, 188]. We provide new analytical results, supported by exact numerics, which straightforwardly generalize to various cQED platforms, ranging from hybrid to purely superconducting devices. The method readily incorporates polarizability effects and clarifies the limits of the curvature coupling picture for $g_{\parallel}$.

Our work opens new perspectives to engineer longitudinal coupling by shaping the Floquet spectrum while preserving its static spectrum and thus the device's resilience to low-frequency noise. In particular, we established a new connection beween readout degradation at large drives and the flattening of the Floquet spectrum. Open questions concern how such Floquet methods can provide insight in strongly driven-regimes [189], where photons are strongly entangled to the system and perturbative approaches fail.

Beyond few-level systems, we introduced Many-Body Admittance Spectroscopy (MADS) as a weak, scalable spectroscopic probe of collective excitations using hybrid cQED platforms. Considering experimentally relevant scenarios [36], we derived an input–output relation connecting the measured transmission matrix to the dynamical structure factor (DSF) [138]. By driving one line at a time and recording all outputs, one reconstructs and filters the many-body admittance in momentum and frequency, which is strictly related to the DSF. Applied to a one-dimensional spinless-fermion chain, MADS reproduces the two-particle continuum and its van Hove upper-edge singularity in the non-interacting limit. When interactions are turned on, MADS reveals the removal of the upper-edge divergence, renormalized boundaries, and a shift of weight toward the lower edge, trends already visible for chains of modest length. These features are the finite-size signatures of the edge power laws predicted by interacting Luttinger-liquid theory [138, 161, 190, 191], which are in agreement with our exact diagonalization and DMRG simulations, and can be resolved by MADS on large enough chains.

Building on this one-dimensional validation, the same framework could extend beyond one dimension systems, with recent advances in two-dimensional simulators opening a route to use MADS to probe the Hubbard model and contributing to ongoing efforts to establish whether it captures cuprate physics.

Overall, these results advance readout along two axes. For single qubits, Floquet-engineered

longitudinal coupling provides a fast and flexible path to QND measurement. For many-body simulators, MADS offers a protocol to monitor strongly correlated dynamics in quantum simulators.

Bibliography

[1] 1956 nobel prize in physics. *Physics Today*, 10(1):16–17, 1957.

[2] Ed Hinds and Rainer Blatt. Manipulating individual quantum systems. en. *Nature*, 492(7427):55–55, 2012.

[3] The nobel prize in physics 2012. *Low Temperature Physics*, 38(12):1153–1153, 2012.

[4] Serge Haroche. Nobel lecture: controlling photons in a box and exploring the quantum to classical boundary. *Rev. Mod. Phys.*, 85:1083–1102, 3, 2013.

[5] Serge Haroche and Jean-Michel Raimond. *Exploring the Quantum: Atoms, Cavities, and Photons*. Oxford University Press, 2006.

[6] Richard P. Feynman. Simulating physics with computers. en. *International Journal of Theoretical Physics*, 21(6):467–488, 1982.

[7] Peter W. Shor. Polynomial-time algorithms for prime factorization and discrete logarithms on a quantum computer. *SIAM Journal on Computing*, 26(5):1484–1509, 1997.

[8] Peter W. Shor. Scheme for reducing decoherence in quantum computer memory. *Phys. Rev. A*, 52:R2493–R2496, 4, 1995.

[9] Isaac L. Chuang, Neil Gershenfeld, and Mark Kubinec. Experimental implementation of fast quantum searching. *Phys. Rev. Lett.*, 80:3408–3411, 15, 1998.

[10] Lieven M. K. Vandersypen, Matthias Steffen, Gregory Breyta, Costantino S. Yannoni, Mark H. Sherwood, and Isaac L. Chuang. Experimental realization of Shor's quantum factoring algorithm using nuclear magnetic resonance. en. *Nature*, 414(6866):883–887, 2001.

[11] J. I. Cirac and P. Zoller. Quantum Computations with Cold Trapped Ions. en. *Physical Review Letters*, 74(20):4091–4094, 1995.

[12] Thomas Monz, Daniel Nigg, Esteban A. Martinez, Matthias F. Brandl, Philipp Schindler, Richard Rines, Shannon X. Wang, Isaac L. Chuang, and Rainer Blatt. Realization of a scalable Shor algorithm. en. *Science*, 351(6277):1068–1070, 2016.

[13] M. Saffman, T. G. Walker, and K. Mølmer. Quantum information with Rydberg atoms. en. *Reviews of Modern Physics*, 82(3):2313–2363, 2010.

[14] M. H. Devoret and R. J. Schoelkopf. Superconducting circuits for quantum information: an outlook. *Science*, 339(6124):1169–1174, 2013.

[15] Daniel Loss and David P. DiVincenzo. Quantum computation with quantum dots. *Phys. Rev. A*, 57:120–126, 1, 1998.

[16] Dolev Bluvstein, Simon J. Evered, Alexandra A. Geim, Sophie H. Li, Hengyun Zhou, Tom Manovitz, Sepehr Ebadi, Madelyn Cain, Marcin Kalinowski, Dominik Hangleiter, J. Pablo Bonilla Ataides, Nishad Maskara, Iris Cong, Xun Gao, Pedro Sales Rodriguez, Thomas Karolyshyn, Giulia Semeghini, Michael J. Gullans, Markus Greiner, Vladan Vuletić, and Mikhail D. Lukin. Logical quantum processor based on reconfigurable atom arrays. en. *Nature*, 626(7997):58–65, 2024.

[17] Rajeev Acharya, Dmitry A. Abanin, Laleh Aghababaie-Beni, Igor Aleiner, Trond I. Andersen, Markus Ansmann, Frank Arute, Kunal Arya, Abraham Asfaw, Nikita Astrakhantsev, Juan Atalaya, Ryan Babbush, Dave Bacon, Brian Ballard, Joseph C. Bardin, Johannes Bausch, Andreas Bengtsson, Alexander Bilmes, Sam Blackwell, Sergio Boixo, Gina Bortoli, Alexandre Bourassa, Jenna Bovaird, Leon Brill, Michael Broughton, David A. Browne, Brett Buchea, Bob B. Buckley, David A. Buell, Tim Burger, Brian Burkett, Nicholas Bushnell, Anthony Cabrera, Juan Campero, Hung-Shen Chang, Yu Chen, Zijun Chen, Ben Chiaro, Desmond Chik, Charina Chou, Jahan Claes, Agnetta Y. Cleland, Josh Cogan, Roberto Collins, Paul Conner, William Courtney, Alexander L. Crook, Ben Curtin, Sayan Das, Alex Davies, Laura De Lorenzo, Dripto M. Debroy, Sean Demura, Michel Devoret, Agustin Di Paolo, Paul Donohoe, Ilya Drozdov, Andrew Dunsworth, Clint Earle, Thomas Edlich, Alec Eickbusch, Aviv Moshe Elbag, Mahmoud Elzouka, Catherine Erickson, Lara Faoro, Edward Farhi, Vinicius S. Ferreira, Leslie Flores Burgos, Ebrahim Forati, Austin G. Fowler, Brooks Foxen, Suhas Ganjam, Gonzalo Garcia, Robert Gasca, Élie Genois, William Giang, Craig Gidney, Dar Gilboa, Raja Gosula, Alejandro Grajales Dau, Dietrich Graumann, Alex Greene, Jonathan A. Gross, Steve Habegger, John Hall, Michael C. Hamilton, Monica Hansen, Matthew P. Harrigan, Sean D. Harrington, Francisco J. H. Heras, Stephen Heslin, Paula Heu, Oscar Higgott, Gordon Hill, Jeremy Hilton, George Holland, Sabrina Hong, Hsin-Yuan Huang, Ashley Huff, William J. Huggins, Lev B. Ioffe, Sergei V. Isakov, Justin Iveland, Evan Jeffrey, Zhang Jiang, Cody Jones, Stephen Jordan, Chaitali Joshi, Pavol Juhas, Dvir Kafri, Hui Kang, Amir H. Karamlou, Kostyantyn Kechedzhi, Julian Kelly, Trupti Khaire, Tanuj Khattar, Mostafa Khezri, Seon Kim, Paul V. Klimov, Andrey R. Klots, Bryce Kobrin, Pushmeet Kohli, Alexander N. Korotkov, Fedor Kostritsa, Robin Kothari, Borislav Kozlovskii, John Mark Kreikebaum, Vladislav D. Kurilovich, Nathan Lacroix, David Landhuis, Tiano Lange-Dei, Brandon W. Langley, Pavel Laptev, Kim-Ming Lau, Loïck Le Guevel, Justin Ledford, Joonho Lee, Kenny Lee, Yuri D. Lensky, Shannon Leon, Brian J. Lester, Wing Yan Li, Yin Li, Alexander T. Lill, Wayne Liu, William P. Livingston, Aditya Locharla, Erik Lucero, Daniel Lundahl, Aaron Lunt, Sid Madhuk, Fionn D. Malone, Ashley Maloney, Salvatore Mandrà, James Manyika, Leigh S. Martin, Orion Martin, Steven Martin, Cameron Maxfield, Jarrod R. McClean, Matt McEwen, Seneca Meeks, Anthony Megrant, Xiao Mi, Kevin C. Miao, Amanda Mieszala, Reza Molavi, Sebastian Molina, Shirin Montazeri, Alexis Morvan, Ramis Movassagh, Wojciech Mruczkiewicz, Ofer Naaman, Matthew Neeley, Charles Neill, Ani Nersisyan, Hartmut Neven, Michael Newman, Jiun How Ng, Anthony Nguyen, Murray Nguyen, Chia-Hung Ni, Murphy Yuezhen Niu, Thomas E. O'Brien, William D. Oliver, Alex Opremcak, Kristoffer Ottosson, Andre Petukhov, Alex Pizzuto, John Platt, Rebecca Potter, Orion Pritchard, Leonid P. Pryadko, Chris Quintana, Ganesh Ramachandran, Matthew J. Reagor, John Redding, David M. Rhodes, Gabrielle Roberts, Eliott Rosenberg, Emma Rosenfeld, Pedram Roushan, Nicholas C. Rubin, Negar Saei, Daniel Sank, Kannan Sankaragomathi, Kevin J. Satzinger, Henry F. Schurkus, Christopher Schuster, Andrew W. Senior, Michael J. Shearn, Aaron Shorter, Noah Shutty, Vladimir Shvarts, Shraddha Singh, Volodymyr

Sivak, Jindra Skruzny, Spencer Small, Vadim Smelyanskiy, W. Clarke Smith, Rolando D. Somma, Sofia Springer, George Sterling, Doug Strain, Jordan Suchard, Aaron Szasz, Alex Sztein, Douglas Thor, Alfredo Torres, M. Mert Torunbalci, Abeer Vaishnav, Justin Vargas, Sergey Vdovichev, Guifre Vidal, Benjamin Villalonga, Catherine Vollgraff Heidweiller, Steven Waltman, Shannon X. Wang, Brayden Ware, Kate Weber, Travis Weidel, Theodore White, Kristi Wong, Bryan W. K. Woo, Cheng Xing, Z. Jamie Yao, Ping Yeh, Bicheng Ying, Juhwan Yoo, Noureldin Yosri, Grayson Young, Adam Zalcman, Yaxing Zhang, Ningfeng Zhu, Nicholas Zobrist, and Google Quantum AI and Collaborators. Quantum error correction below the surface code threshold. en. *Nature*, 638(8052):920–926, 2025.

[18] Jerry Chow, Oliver Dial, and Jay Gambetta. Ibm quantum breaks the 100-qubit processor barrier.

[19] Austin G. Fowler, Matteo Mariantoni, John M. Martinis, and Andrew N. Cleland. Surface codes: towards practical large-scale quantum computation. *Phys. Rev. A*, 86:032324, 3, 2012.

[20] R. Maurand, X. Jehl, D. Kotekar-Patil, A. Corna, H. Bohuslavskyi, R. Laviéville, L. Hutin, S. Barraud, M. Vinet, M. Sanquer, and S. De Franceschi. A CMOS silicon spin qubit. en. *Nature Communications*, 7(1):13575, 2016.

[21] L. M. K. Vandersypen, H. Bluhm, J. S. Clarke, A. S. Dzurak, R. Ishihara, A. Morello, D. J. Reilly, L. R. Schreiber, and M. Veldhorst. Interfacing spin qubits in quantum dots and donors—hot, dense, and coherent. en. *npj Quantum Information*, 3(1):1–10, 2017.

[22] A. Wallraff, D. I. Schuster, A. Blais, L. Frunzio, R.-S. Huang, J. Majer, S. Kumar, S. M. Girvin, and R. J. Schoelkopf. Strong coupling of a single photon to a superconducting qubit using circuit quantum electrodynamics. en. *Nature*, 431(7005):162–167, 2004.

[23] V. Bouchiat, D. Vion, P. Joyez, D. Esteve, and M. H. Devoret. Quantum Coherence with a Single Cooper Pair. en. *Physica Scripta*, T76(1):165, 1998.

[24] Alexandre Blais, Ren-Shou Huang, Andreas Wallraff, S. M. Girvin, and R. J. Schoelkopf. Cavity quantum electrodynamics for superconducting electrical circuits: an architecture for quantum computation. *Phys. Rev. A*, 69:062320, 6, 2004.

[25] K. D. Petersson, L. W. McFaul, M. D. Schroer, M. Jung, J. M. Taylor, A. A. Houck, and J. R. Petta. Circuit quantum electrodynamics with a spin qubit. *Nature*, 490:380–, 2012.

[26] Cécile X Yu, Simon Zihlmann, José C Abadillo-Uriel, Vincent P Michal, Nils Rambal, Heimanu Niebojewski, Thomas Bedecarrats, Maud Vinet, Étienne Dumur, Michele Filippone, et al. Strong coupling between a photon and a hole spin in silicon. *Nature Nanotechnology*:1–6, 2023.

[27] Xin-Lei Hei, Xing-Liang Dong, Jia-Qiang Chen, Cai-Peng Shen, Yi-Fan Qiao, and Peng-Bo Li. Enhancing spin-photon coupling with a micromagnet. *Phys. Rev. A*, 103:043706, 4, 2021.

[28] Nicolas Piot, B Brun, Vivien Schmitt, Simon Zihlmann, VP Michal, A Apra, JC Abadillo-Uriel, Xavier Jehl, Benoit Bertrand, H Niebojewski, et al. A single hole spin with enhanced coherence in natural silicon. *Nature Nanotechnology*, 17(10):1072–1077, 2022.

[29] Nicolas Didier, Jérôme Bourassa, and Alexandre Blais. Fast quantum nondemolition readout by parametric modulation of longitudinal qubit-oscillator interaction. *Phys. Rev. Lett.*, 115:203601, 20, 2015.

[30] Susanne Richer and David DiVincenzo. Circuit design implementing longitudinal coupling: a scalable scheme for superconducting qubits. *Phys. Rev. B*, 93:134501, 13, 2016.

[31] Susanne Richer, Nataliya Maleeva, Sebastian T. Skacel, Ioan M. Pop, and David DiVincenzo. Inductively shunted transmon qubit with tunable transverse and longitudinal coupling. *Phys. Rev. B*, 96:174520, 17, 2017.

[32] C. Eichler and J. R. Petta. Realizing a circuit analog of an optomechanical system with longitudinally coupled superconducting resonators. *Phys. Rev. Lett.*, 120:227702, 22, 2018.

[33] J. G. Bednorz and K. A. Müller. Possible high-tc superconductivity in the la-ba-cu-o system. en. *Zeitschrift für Physik B Condensed Matter*, 64(2):189–193, 1986.

[34] Christie Shinglei Chiu. Quantum simulation of the Hubbard model. en, 2019.

[35] Anton Mazurenko, Christie Chiu, Geoffrey Ji, Maxwell Parsons, Márton Kanász-Nagy, Richard Schmidt, Fabian Grusdt, Eugene Demler, Daniel Greif, and Markus Greiner. A cold-atom fermi-hubbard antiferromagnet. *Nature*, 545:462–466, 2017.

[36] T. Hensgens, T. Fujita, L. Janssen, Xiao Li, C. J. Van Diepen, C. Reichl, W. Wegscheider, S. Das Sarma, and L. M. K. Vandersypen. Quantum simulation of a fermi–hubbard model using a semiconductor quantum dot array. en. *Nature*, 548(7665):70–73, 2017.

[37] William D. Phillips and Harold J. Metcalf. Cooling and trapping atoms. *Scientific American*, 256:50–56, 1987.

[38] David E. Pritchard. Cooling neutral atoms in a magnetic trap for precision spectroscopy. *Phys. Rev. Lett.*, 51:1336–1339, 15, 1983.

[39] Peter T. Brown, Debayan Mitra, Elmer Guardado-Sanchez, Reza Nourafkan, Alexis Reymbaut, Charles-David Hébert, Simon Bergeron, A.-M. S. Tremblay, Jure Kokalj, David A. Huse, Peter Schauß, and Waseem S. Bakr. Bad metallic transport in a cold atom fermi-hubbard system. *Science*, 363(6425):379–382, 2019.

[40] Thomas Hartke, Botond Oreg, Carter Turnbaugh, Ningyuan Jia, and Martin Zwierlein. Direct observation of nonlocal fermion pairing in an attractive Fermi-Hubbard gas. en. *Science*, 381(6653):82–86, 2023.

[41] Thomas Chalopin, Petar Bojović, Si Wang, Titus Franz, Aritra Sinha, Zhenjiu Wang, Dominik Bourgund, Johannes Obermeyer, Fabian Grusdt, Annabelle Bohrdt, Lode Pollet, Alexander Wietek, Antoine Georges, Timon Hilker, and Immanuel Bloch. Probing the magnetic origin of the pseudogap using a fermi-hubbard quantum simulator, 2024.

[42] Muqing Xu, Lev Haldar Kendrick, Anant Kale, Youqi Gang, Chunhan Feng, Shiwei Zhang, Aaron W. Young, Martin Lebrat, and Markus Greiner. A neutral-atom hubbard quantum simulator in the cryogenic regime. en. *Nature*, 642(8069):909–915, 2025.

[43] Francesco Borsoi, Nico W. Hendrickx, Valentin John, Marcel Meyer, Sayr Motz, Floor van Riggelen, Amir Sammak, Sander L. de Snoo, Giordano Scappucci, and Menno Veldhorst. Shared control of a 16 semiconductor quantum dot crossbar array. en. *Nature Nanotechnology*, 19(1):21–27, 2024.

[44] Xiqiao Wang, Ehsan Khatami, Fan Fei, Jonathan Wyrick, Pradeep Namboodiri, Ranjit Kashid, Albert F. Rigosi, Garnett Bryant, and Richard Silver. Experimental realization of an extended Fermi-Hubbard model using a 2D lattice of dopant-based quantum dots. en. *Nature Communications*, 13(1):6824, 2022.

[45] Pierre-André Mortemousque, Baptiste Jadot, Emmanuel Chanrion, Vivien Thiney, Christopher B auerle, Arne Ludwig, Andreas D. Wieck, Matias Urdampilleta, and Tristan Meunier. Enhanced Spin Coherence while Displacing Electron inf a Two-Dimensional Array of Quantum Dots. en. *PRX Quantum*, 2(3):030331, 2021.

[46] J. P. Dehollain, U. Mukhopadhyay, V. P. Michal, Y. Wang, B. Wunsch, C. Reichl, W. Wegscheider, M. S. Rudner, E. Demler, and L. M. K. Vandersypen. Nagaoka ferromagnetism observed in a quantum dot plaquette. en. *Nature*, 579(7800):528–533, 2020.

[47] V. Champain, S. Zihlmann, A. Chessari, B. Bertrand, H. Niebojewski, É. Dumur, X. Jehl, V. Schmitt, B. Brun, C. Winkelmann, Y.M. Niquet, M. Filippone, S. De Franceschi, and R. Maurand. Parametric longitudinal coupling of a semiconductor charge qubit and an rf resonator. *Phys. Rev. Appl.*, 23:034067, 3, 2025.

[48] A. Chessari, E. A. Rodríguez-Mena, J. C. Abadillo-Uriel, V. Champain, S. Zihlmann, R. Maurand, Y.-M. Niquet, and M. Filippone. Unifying floquet theory of longitudinal and dispersive readout. *Phys. Rev. Lett.*, 134:037003, 3, 2025.

[49] A. Chessari and M. Filippone. Many-body admittance spectroscopy. *in preparation*, 2025.

[50] Alexandre Blais, Arne L. Grimsmo, S. M. Girvin, and Andreas Wallraff. Circuit quantum electrodynamics. *Rev. Mod. Phys.*, 93:025005, 2, 2021.

[51] Edward M. Purcell. Spontaneous emission probabilities at radio frequencies. *Physical Review D*, 69:839–839, 1995.

[52] E.T. Jaynes and F.W. Cummings. Comparison of quantum and semiclassical radiation theories with application to the beam maser. *Proceedings of the IEEE*, 51(1):89–109, 1963.

[53] M. Brune, F. Schmidt-Kaler, A. Maali, J. Dreyer, E. Hagley, J. M. Raimond, and S. Haroche. Quantum rabi oscillation: a direct test of field quantization in a cavity. *Phys. Rev. Lett.*, 76:1800–1803, 11, 1996.

[54] Benjamin Schumacher. Quantum coding. *Phys. Rev. A*, 51:2738–2747, 4, 1995.

[55] Michael A. Nielsen and Isaac L. Chuang. *Quantum Computation and Quantum Information: 10th Anniversary Edition*. Cambridge University Press, 2010.

[56] C. Monroe, D. M. Meekhof, B. E. King, W. M. Itano, and D. J. Wineland. Demonstration of a fundamental quantum logic gate. *Phys. Rev. Lett.*, 75:4714–4717, 25, 1995.

[57] Herbert Goldstein, Charles P. Poole, and John L. Safko. *Classical mechanics*. eng. Pearson, Harlow, San Fransisco, third edition. Edition, 2011. OCLC: 960166650.

[58] David M. Pozar. *Microwave engineering*. eng. John Wiley & Sons, Inc, Hoboken, NJ, fourth edition edition, 2012.

[59] Adrian Parra-Rodriguez and Iñigo L. Egusquiza. Canonical quantisation of telegrapher's equations coupled by ideal nonreciprocal elements. en. *Quantum*, 6:681, 2022.

[60] Carlo Forestiere and Giovanni Miano. A δ-free approach to quantization of transmission lines connected to lumped circuits. *Physica Scripta*, 99(4):045123, 2024.

[61] A. Parra-Rodriguez and I. L. Egusquiza. Exact quantization of nonreciprocal quasilumped electrical networks. *Phys. Rev. X*, 15:011072, 1, 2025.

[62] C. W. Gardiner and P. Zoller. *Quantum Noise*. 2000.

[63] A. Cottet, T. Kontos, and B. Dou çot. Electron-photon coupling in mesoscopic quantum electrodynamics. *Phys. Rev. B*, 91:205417, 20, 2015.

[64] Olesia Dmytruk and Marco Schiró. Gauge fixing for strongly correlated electrons coupled to quantum light. *Phys. Rev. B*, 103:075131, 7, 2021.

[65] Heinz-Peter Breuer and Francesco et al. Petruccione. *The theory of open quantum systems*. Oxford University Press, 2002.

[66] AA Clerk, KW Lehnert, P Bertet, JR Petta, and Y Nakamura. Hybrid quantum systems with circuit quantum electrodynamics. *Nature Physics*, 16(3):257–267, 2020.

[67] H. Toida, T. Nakajima, and S. Komiyama. Vacuum rabi splitting in a semiconductor circuit qed system. *Phys. Rev. Lett.*, 110:066802, 6, 2013.

[68] Yanko Todorov and Carlo Sirtori. Few-electron ultrastrong light-matter coupling in a quantum lc circuit. *Phys. Rev. X*, 4:041031, 4, 2014.

[69] D. F. Walls and G. J. Milburn. *Quantum Optics*. Springer Berlin Heidelberg, Berlin, Heidelberg, 1994.

[70] Andrew J Kerman. Quantum information processing using quasiclassical electromagnetic interactions between qubits and electrical resonators. *New Journal of Physics*, 15(12):123011, 2013.

[71] P.-M. Billangeon, J. S. Tsai, and Y. Nakamura. Circuit-qed-based scalable architectures for quantum information processing with superconducting qubits. *Phys. Rev. B*, 91:094517, 9, 2015.

[72] J. R. Schrieffer and P. A. Wolff. Relation between the anderson and kondo hamiltonians. *Phys. Rev.*, 149:491–492, 2, 1966.

[73] Rusko Ruskov and Charles Tahan. Quantum-limited measurement of spin qubits via curvature couplings to a cavity. *Phys. Rev. B*, 99:245306, 24, 2019.

[74] Rusko Ruskov and Charles Tahan. Modulated longitudinal gates on encoded spin qubits via curvature couplings to a superconducting cavity. *Phys. Rev. B*, 103:035301, 3, 2021.

[75] Sunghun Park, C. Metzger, L. Tosi, M. F. Goffman, C. Urbina, H. Pothier, and A. Levy Yeyati. From adiabatic to dispersive readout of quantum circuits. *Phys. Rev. Lett.*, 125:077701, 7, 2020.

[76] V. P. Michal, J. C. Abadillo-Uriel, S. Zihlmann, R. Maurand, Y.-M. Niquet, and M. Filippone. Tunable hole spin-photon interaction based on g-matrix modulation. *Phys. Rev. B*, 107:L041303, 4, 2023.

[77] Rusko Ruskov and Charles Tahan. Longitudinal (curvature) couplings of an N-level qudit to a superconducting resonator at the adiabatic limit and beyond. *Phys. Rev. B*, 109:245303, 24, 2024.

[78] Joni Ikonen, Jan Goetz, Jesper Ilves, Aarne Keränen, Andras M. Gunyho, Matti Partanen, Kuan Y. Tan, Dibyendu Hazra, Leif Grönberg, Visa Vesterinen, Slawomir Simbierowicz, Juha Hassel, and Mikko Möttönen. Qubit measurement by multichannel driving. *Phys. Rev. Lett.*, 122:080503, 8, 2019.

[79] C. C. Bultink, B. Tarasinski, N. Haandbæk, S. Poletto, N. Haider, D. J. Michalak, A. Bruno, and L. DiCarlo. General method for extracting the quantum efficiency of dispersive qubit readout in circuit qed. *Applied Physics Letters*, 112(9):092601, 2018.

[80] J. Corrigan, Benjamin Harpt, Nathan Holman, Rusko Ruskov, Piotr Marciniec, D. Rosenberg, D. Yost, R. Das, William D. Oliver, R. McDermott, Charles Tahan, Mark Friesen, and M.A. Eriksson. Longitudinal coupling between a $Si/Si_{1-x}Ge_x$ double quantum dot and an off-chip TiN resonator. *Phys. Rev. Appl.*, 20:064005, 6, 2023.

[81] S. Touzard, A. Kou, N. E. Frattini, V. V. Sivak, S. Puri, A. Grimm, L. Frunzio, S. Shankar, and M. H. Devoret. Gated conditional displacement readout of superconducting qubits. *Phys. Rev. Lett.*, 122:080502, 8, 2019.

[82] Benjamin Harpt, J. Corrigan, Nathan Holman, Piotr Marciniec, D. Rosenberg, D. Yost, R. Das, Rusko Ruskov, Charles Tahan, William D. Oliver, R. McDermott, Mark Friesen, and M. A. Eriksson. Ultra-dispersive resonator readout of a quantum-dot qubit using longitudinal coupling. en. *npj Quantum Information*, 11(1):1–4, 2025.

[83] CGL Bøttcher, SP Harvey, Saeed Fallahi, GC Gardner, MJ Manfra, Uri Vool, SD Bartlett, and Amir Yacoby. Parametric longitudinal coupling between a high-impedance superconducting resonator and a semiconductor quantum dot singlet-triplet spin qubit. *Nature Communications*, 13(1):4773, 2022.

[84] T. Bédécarrats, B. Cardoso Paz, B. Martinez Diaz, H. Niebojewski, B. Bertrand, N. Rambal, C. Comboroure, A. Sarrazin, F. Boulard, E. Guyez, J.-M. Hartmann, Y. Morand, A. Magalhaes-Lucas, E. Nowak, E. Catapano, M. Cassé, M. Urdampilleta, Y.-M. Niquet, F. Gaillard, S. De Franceschi, T. Meunier, and M. Vinet. A new FDSOI spin qubit platform with 40nm effective control pitch:1–4, 2021. ISSN: 2156-017X.

[85] G. Floquet. Sur les équations différentielles linéaires à coefficients périodiques. fr. *Annales scientifiques de l'École Normale Supérieure*, 2e série, 12:47–88, 1883.

[86] Jon H. Shirley. Solution of the schrödinger equation with a hamiltonian periodic in time. *Phys. Rev.*, 138:B979–B987, 4B, 1965.

[87] Hideo Sambe. Steady states and quasienergies of a quantum-mechanical system in an oscillating field. *Phys. Rev. A*, 7:2203–2213, 6, 1973.

[88] Milena Grifoni and Peter Hänggi. Driven quantum tunneling. *Physics Reports*, 304(5):229–354, 1998.

[89] Shih-I Chu and Dmitry A. Telnov. Beyond the floquet theorem: generalized floquet formalisms and quasienergy methods for atomic and molecular multiphoton processes in intense laser fields. *Physics Reports*, 390(1):1–131, 2004.

[90] Mark S. Rudner and Netanel H. Lindner. The floquet engineer's handbook.

[91] L. Mirsky, F. R. Gantmacher, and Kurt A. Hirsch. The theory of matrices. *The Mathematical Gazette*, 45:267–267, 1961.

[92] Konrad Viebahn. Introduction to floquet theory. In 2020.

[93] Neil W. Ashcroft and N. David Mermin. *Solid state physics*. eng. Saunders College Publ. [u.a.], Fort Worth, internat. ed., 21. print edition, 1995.

[94] S.N. Shevchenko, S. Ashhab, and Franco Nori. Landau–zener–stückelberg interferometry. *Physics Reports*, 492(1):1–30, 2010.

[95] Johannes Hausinger and Milena Grifoni. Dissipative two-level system under strong ac driving: a combination of floquet and van vleck perturbation theory. *Phys. Rev. A*, 81:022117, 2, 2010.

[96] Chunqing Deng, Jean-Luc Orgiazzi, Feiruo Shen, Sahel Ashhab, and Adrian Lupascu. Observation of floquet states in a strongly driven artificial atom. *Phys. Rev. Lett.*, 115:133601, 13, 2015.

[97] Chunqing Deng, Feiruo Shen, Sahel Ashhab, and Adrian Lupascu. Dynamics of a two-level system under strong driving: quantum-gate optimization based on floquet theory. *Phys. Rev. A*, 94:032323, 3, 2016.

[98] J. V. Koski, A. J. Landig, A. Pályi, P. Scarlino, C. Reichl, W. Wegscheider, G. Burkard, A. Wallraff, K. Ensslin, and T. Ihn. Floquet spectroscopy of a strongly driven quantum dot charge qubit with a microwave resonator. *Phys. Rev. Lett.*, 121:043603, 4, 2018.

[99] S. P. Harvey, C. G. L. Bøttcher, L. A. Orona, S. D. Bartlett, A. C. Doherty, and A. Yacoby. Coupling two spin qubits with a high-impedance resonator. *Phys. Rev. B*, 97:235409, 23, 2018.

[100] Stefano Bosco, Pasquale Scarlino, Jelena Klinovaja, and Daniel Loss. Fully tunable longitudinal spin-photon interactions in si and ge quantum dots. *Phys. Rev. Lett.*, 129:066801, 6, 2022.

[101] J.R. Johansson, P.D. Nation, and Franco Nori. Qutip 2: a python framework for the dynamics of open quantum systems. *Computer Physics Communications*, 184(4):1234–1240, 2013.

[102] Stephan G. J. Philips, Mateusz T. Mądzik, Sergey V. Amitonov, Sander L. de Snoo, Maximilian Russ, Nima Kalhor, Christian Volk, William I. L. Lawrie, Delphine Brousse, Larysa Tryputen, Brian Paquelet Wuetz, Amir Sammak, Menno Veldhorst, Giordano Scappucci, and Lieven M. K. Vandersypen. Universal control of a six-qubit quantum processor in silicon. en. *Nature*, 609(7929):919–924, 2022.

[103] Guido Burkard, Thaddeus D. Ladd, Andrew Pan, John M. Nichol, and Jason R. Petta. Semiconductor spin qubits. *Rev. Mod. Phys.*, 95:025003, 2, 2023.

[104] N. Samkharadze, G. Zheng, N. Kalhor, D. Brousse, A. Sammak, U. C. Mendes, A. Blais, G. Scappucci, and L. M. K. Vandersypen. Strong spin-photon coupling in silicon. *Science*, 359(6380):1123–1127, 2018.

[105] Patrick Harvey-Collard, Guoji Zheng, Jurgen Dijkema, Nodar Samkharadze, Amir Sammak, Giordano Scappucci, and Lieven M. K. Vandersypen. On-chip microwave filters for high-impedance resonators with gate-defined quantum dots. *Physical Review Applied*, 14:034025, 3, 2020.

[106] X. Mi, M. Benito, S. Putz, D. M. Zajac, J. M. Taylor, Guido Burkard, and J. R. Petta. A coherent spin–photon interface in silicon. en. *Nature*, 555(7698):599–603, 2018.

[107] Jarryd J. Pla, Kuan Y. Tan, Juan P. Dehollain, Wee H. Lim, John J. L. Morton, David N. Jamieson, Andrew S. Dzurak, and Andrea Morello. A single-atom electron spin qubit in silicon. en. *Nature*, 489(7417):541–545, 2012.

[108] Vitaly N. Golovach, Massoud Borhani, and Daniel Loss. Electric-dipole-induced spin resonance in quantum dots. *Phys. Rev. B*, 74:165319, 16, 2006.

[109] S. Nadj-Perge, S. M. Frolov, E. P. a. M. Bakkers, and L. P. Kouwenhoven. Spin–orbit qubit in a semiconductor nanowire. en. *Nature*, 468(7327):1084–1087, 2010.

[110] M. D. Schroer, K. D. Petersson, M. Jung, and J. R. Petta. Field tuning the g factor in inas nanowire double quantum dots. *Phys. Rev. Lett.*, 107:176811, 17, 2011.

[111] Xuedong Hu, Yu-xi Liu, and Franco Nori. Strong coupling of a spin qubit to a superconducting stripline cavity. *Physical Review B*, 86(3):035314, 2012.

[112] X. Mi, M. Benito, S. Putz, D. M. Zajac, J. M. Taylor, Guido Burkard, and J. R. Petta. A coherent spin-photon interface in silicon. *Nature*, 555:599, 2018.

[113] Pei Qing Jin, Michael Marthaler, Alexander Shnirman, and Gerd Schön. Strong coupling of spin qubits to a transmission line resonator. *Physical Review Letters*, 108(19):190506, 2012.

[114] T. Frey, P. J. Leek, M. Beck, A. Blais, T. Ihn, K. Ensslin, and A. Wallraff. Dipole coupling of a double quantum dot to a microwave resonator. *Phys. Rev. Lett.*, 108:046807, 4, 2012.

[115] JJ Viennot, MC Dartiailh, Audrey Cottet, and Takis Kontos. Coherent coupling of a single spin to microwave cavity photons. *Science*, 349(6246):408–411, 2015.

[116] F. Borjans, X. G. Croot, X. Mi, M. J. Gullans, and J. R. Petta. Resonant microwave-mediated interactions between distant electron spins. *Nature*, 577(7789):195–198, 2019.

[117] L. Childress, A. S. Sørensen, and M. D. Lukin. Mesoscopic cavity quantum electrodynamics with quantum dots. *Physical Review A*, 69(4):042302, 2004.

[118] Guido Burkard and Atac Imamoglu. Ultra-long-distance interaction between spin qubits. *Physical Review B*, 74(4):041307(R), 2006.

[119] Mircea Trif, Vitaly N. Golovach, and Daniel Loss. Spin dynamics in inas nanowire quantum dots coupled to a transmission line. *Phys. Rev. B*, 77:045434, 4, 2008.

[120] Audrey Cottet and Takis Kontos. Spin quantum bit with ferromagnetic contacts for circuit qed. *Phys. Rev. Lett.*, 105:160502, 16, 2010.

[121] Philipp M. Mutter and Guido Burkard. Natural heavy-hole flopping mode qubit in germanium. *Phys. Rev. Res.*, 3:013194, 1, 2021.

[122] Frank Arute, Kunal Arya, Ryan Babbush, Dave Bacon, Joseph Bardin, Rami Barends, Rupak Biswas, Sergio Boixo, Fernando Brandao, David Buell, Brian Burkett, Yu Chen, Jimmy Chen, Ben Chiaro, Roberto Collins, William Courtney, Andrew Dunsworth, Edward Farhi, Brooks Foxen, Austin Fowler, Craig Michael Gidney, Marissa Giustina, Rob Graff, Keith Guerin, Steve Habegger, Matthew Harrigan, Michael Hartmann, Alan Ho, Markus Rudolf Hoffmann, Trent Huang, Travis Humble, Sergei Isakov, Evan Jeffrey, Zhang Jiang, Dvir Kafri, Kostyantyn Kechedzhi, Julian Kelly, Paul Klimov, Sergey Knysh, Alexander Korotkov, Fedor Kostritsa, Dave Landhuis, Mike Lindmark, Erik Lucero, Dmitry Lyakh, Salvatore Mandrà, Jarrod Ryan McClean, Matthew McEwen, Anthony Megrant, Xiao Mi, Kristel Michielsen, Masoud Mohseni, Josh Mutus, Ofer Naaman, Matthew Neeley, Charles Neill, Murphy Yuezhen Niu, Eric Ostby, Andre Petukhov, John Platt, Chris Quintana, Eleanor G. Rieffel, Pedram Roushan, Nicholas Rubin, Daniel Sank, Kevin J. Satzinger, Vadim Smelyanskiy, Kevin Jeffery Sung, Matt Trevithick, Amit Vainsencher, Benjamin Villalonga, Ted White, Z. Jamie Yao, Ping Yeh, Adam Zalcman, Hartmut Neven, and John Martinis. Quantum supremacy using a programmable superconducting processor. *Nature*, 574:505–510, 2019.

[123] Audrey Cottet. *Implementation of a quantum bit in a superconducting circuit.* PhD thesis, PhD Thesis, Université Paris 6, 2002.

[124] M. H. Devoret, A. Wallraff, and J. M. Martinis. Superconducting qubits: a short review, 2004.

[125] Jens Koch, Terri M. Yu, Jay Gambetta, A. A. Houck, D. I. Schuster, J. Majer, Alexandre Blais, M. H. Devoret, S. M. Girvin, and R. J. Schoelkopf. Charge-insensitive qubit design derived from the cooper pair box. *Phys. Rev. A*, 76:042319, 4, 2007.

[126] Vladimir E Manucharyan, Jens Koch, Leonid I Glazman, and Michel H Devoret. Fluxonium: single cooper-pair circuit free of charge offsets. *Science*, 326(5949):113–116, 2009.

[127] Aaron Somoroff, Quentin Ficheux, Raymond A. Mencia, Haonan Xiong, Roman Kuzmin, and Vladimir E. Manucharyan. Millisecond coherence in a superconducting qubit. *Phys. Rev. Lett.*, 130:267001, 26, 2023.

[128] D. Vion, A. Aassime, A. Cottet, P. Joyez, H. Pothier, C. Urbina, D. Esteve, and M. H. Devoret. Manipulating the quantum state of an electrical circuit. *Science*, 296(5569):886–889, 2002.

[129] Peter Groszkowski and Jens Koch. Scqubits: a python package for superconducting qubits. *Quantum*, 5:583, 2021.

[130] Sai Pavan Chitta, Tianpu Zhao, Ziwen Huang, Ian Mondragon-Shem, and Jens Koch. Computer-aided quantization and numerical analysis of superconducting circuits. *New Journal of Physics*, 24(10):103020, 2022.

[131] Aaron Somoroff, Quentin Ficheux, Raymond A. Mencia, Haonan Xiong, Roman Kuzmin, and Vladimir E. Manucharyan. Millisecond coherence in a superconducting qubit. *Phys. Rev. Lett.*, 130:267001, 26, 2023.

[132] R Kubo. The fluctuation-dissipation theorem. *Reports on Progress in Physics*, 29(1):255, 1966.

[133] Bella Lake, D. Alan Tennant, Chris D. Frost, and Stephen E. Nagler. Quantum criticality and universal scaling of a quantum antiferromagnet. en. *Nature Materials*, 4(4):329–334, 2005.

[134] A. Scheie, P. Laurell, B. Lake, S. E. Nagler, M. B. Stone, J.-S. Caux, and D. A. Tennant. Quantum wake dynamics in Heisenberg antiferromagnetic chains. en. *Nature Communications*, 13(1):5796, 2022.

[135] G. T. Rado and H. Suhl. *Magnetism*, volume III. 1963.

[136] J. Villain M. Steiner and C.G. Windsor. Theoretical and experimental studies on one-dimensional magnetic systems. *Advances in Physics*, 25(2):87–209, 1976.

[137] I. U. Heilmann, G. Shirane, Y. Endoh, R. J. Birgeneau, and S. L. Holt. Neutron study of the line-shape and field dependence of magnetic excitations in Cu Cl 2 · 2N(C 5 D 5). en. *Phys. Rev. B*, 18(7):3530–3536, 1978.

[138] Adilet Imambekov, Thomas L. Schmidt, and Leonid I. Glazman. One-dimensional quantum liquids: Beyond the Luttinger liquid paradigm. en. *Rev. Mod. Phys.*, 84(3):1253–1306, 2012.

[139] J. Steinhauer, R. Ozeri, N. Katz, and N. Davidson. Excitation Spectrum of a Bose-Einstein Condensate. en. *Phys. Rev. Lett.*, 88(12):120407, 2002.

[140] Chen-Lung Hung, Xibo Zhang, Nathan Gemelke, and Cheng Chin. Accelerating evaporative cooling of atoms into Bose-Einstein condensation in optical traps. en. *Phys. Rev. A*, 78(1):011604, 2008.

[141] N. Fabbri, M. Panfil, D. Clément, L. Fallani, M. Inguscio, C. Fort, and J.-S. Caux. Dynamical structure factor of one-dimensional bose gases: experimental signatures of beyond-luttinger-liquid physics. *Phys. Rev. A*, 91:043617, 4, 2015.

[142] J. M. Pino, R. J. Wild, P. Makotyn, D. S. Jin, and E. A. Cornell. Photon counting for Bragg spectroscopy of quantum gases. en. *Phys. Rev. A*, 83(3):033615, 2011.

[143] Renate Landig, Ferdinand Brennecke, Rafael Mottl, Tobias Donner, and Tilman Esslinger. Measuring the dynamic structure factor of a quantum gas undergoing a structural phase transition. en. *Nat Commun*, 6(1):7046, 2015.

[144] T.L. Yang, P. Grišins, Y.T. Chang, Z.H. Zhao, C.Y. Shih, T. Giamarchi, and R.G. Hulet. Measurement of the Dynamical Structure Factor of a 1D Interacting Fermi Gas. en. *Phys. Rev. Lett.*, 121(10):103001, 2018.

[145] Hauke Biss, Lennart Sobirey, Niclas Luick, Markus Bohlen, Jami J. Kinnunen, Georg M. Bruun, Thomas Lompe, and Henning Moritz. Excitation Spectrum and Superfluid Gap of an Ultracold Fermi Gas. en. *Phys. Rev. Lett.*, 128(10):100401, 2022.

[146] Annabelle Bohrdt, Eugene Demler, Frank Pollmann, Michael Knap, and Fabian Grusdt. Parton theory of angle-resolved photoemission spectroscopy spectra in antiferromagnetic Mott insulators. en. *Phys. Rev. B*, 102(3):035139, 2020.

[147] Peter T. Brown, Elmer Guardado-Sanchez, Benjamin M. Spar, Edwin W. Huang, Thomas P. Devereaux, and Waseem S. Bakr. Angle-resolved photoemission spectroscopy of a Fermi–Hubbard system. en. *Nat. Phys.*, 16(1):26–31, 2020.

[148] A. Bohrdt, E. Demler, and F. Grusdt. Rotational Resonances and Regge-like Trajectories in Lightly Doped Antiferromagnets. en. *Phys. Rev. Lett.*, 127(19):197004, 2021.

[149] Maria Laura Baez, Marcel Goihl, Jonas Haferkamp, Juani Bermejo-Vega, Marek Gluza, and Jens Eisert. Dynamical structure factors of dynamical quantum simulators. *Proceedings of the National Academy of Sciences*, 117(42):26123–26134, 2020.

[150] Saverio Bocini, Filippo Caleca, Fabio Mezzacapo, and Tommaso Roscilde. Nonlocal quench spectroscopy of fermionic excitations in quantum spin chains. en. *Phys. Rev. B*, 111(12):L121114, 2025.

[151] E. Altuntas, R. G. Lena, S. Flannigan, A. J. Daley, and I. B. Spielman. Dynamical structure factor from weak measurements, 2024.

[152] Lucia Vilchez-Estevez, Raul A. Santos, Sabrina Wang, and Filippo Maria Gambetta. Extracting the spin excitation spectrum of a fermionic system using a quantum processor, 2025.

[153] R. Hanson, L. P. Kouwenhoven, J. R. Petta, S. Tarucha, and L. M. K. Vandersypen. Spins in few-electron quantum dots. en. *Rev. Mod. Phys.*, 79(4):1217–1265, 2007.

[154] C.J. Van Diepen, T.-K. Hsiao, U. Mukhopadhyay, C. Reichl, W. Wegscheider, and L.M.K. Vandersypen. Quantum Simulation of Antiferromagnetic Heisenberg Chain with Gate-Defined Quantum Dots. en. *Phys. Rev. X*, 11(4):041025, 2021.

[155] Gerhard Müller, Harry Thomas, Hans Beck, and Jill C. Bonner. Quantum spin dynamics of the antiferromagnetic linear chain in zero and nonzero magnetic field. en. *Phys. Rev. B*, 24(3):1429–1467, 1981.

[156] Michael Karbach, Gerhard Müller, A. Hamid Bougourzi, Andreas Fledderjohann, and Karl-Heinz Mütter. Two-spinon dynamic structure factor of the one-dimensional s= Heisenberg antiferromagnet. *Phys. Rev. B*, 55(18):12510–12517, 1997. Publisher: American Physical Society.

[157] Jean-Sébastien Caux and Jean Michel Maillet. Computation of Dynamical Correlation Functions of Heisenberg Chains in a Magnetic Field. en. *Physical Review Letters*, 95(7):077201, 2005.

[158] Jean-Sébastien Caux and Rob Hagemans. The four-spinon dynamical structure factor of the Heisenberg chain. *Journal of Statistical Mechanics: Theory and Experiment*, 2006(12):P12013–P12013, 2006.

[159] Jean-Sébastien Caux, Hitoshi Konno, Mark Sorrell, and Robert Weston. Tracking the Effects of Interactions on Spinons in Gapless Heisenberg Chains. en. *Phys. Rev. Lett.*, 106(21):217203, 2011.

[160] Jean-Sébastien Caux, Hitoshi Konno, Mark Sorrell, and Robert Weston. Exact form-factor results for the longitudinal structure factor of the massless XXZ model in zero field. *Journal of Statistical Mechanics: Theory and Experiment*, 2012(01):P01007, 2012.

[161] Rodrigo G. Pereira, Steven R. White, and Ian Affleck. Exact Edge Singularities and Dynamical Correlations in Spin- 1 / 2 Chains. en. *Phys. Rev. Lett.*, 100(2):027206, 2008.

[162] Rodrigo Gonçalves Pereira. *Dynamical correlations of S=1/2 quantum spin chains*. PhD thesis, University of British Columbia, 2008.

[163] Alexander Weiße and Holger Fehske. *Exact diagonalization techniques*. In *Computational Many-Particle Physics*. H. Fehske, R. Schneider, and A. Weiße, editors. Springer Berlin Heidelberg, Berlin, Heidelberg, 2008, pages 529–544.

[164] Steven R. White. Density matrix formulation for quantum renormalization groups. en. *Phys. Rev. Lett.*, 69(19):2863–2866, 1992.

[165] Nicola Marzari, Arash A. Mostofi, Jonathan R. Yates, Ivo Souza, and David Vanderbilt. Maximally localized wannier functions: theory and applications. *Rev. Mod. Phys.*, 84:1419–1475, 4, 2012.

[166] Jozef Sznajd and Klaus W Becker. Spinless fermion chains with weak interchain hopping. en. *J. Phys.: Condens. Matter*, 17(46):7359–7370, 2005.

[167] G Muller and H Beck. Dynamical correlation functions for linear spin systems. en. *J. Phys. C: Solid State Phys.*, 11(3):483–495, 1978.

[168] R G Pereira, K Penc, S R White, P D Sacramento, and J M P Carmelo. Charge dynamics in half-filled Hubbard chains with finite on-site interaction. en. *PHYSICAL REVIEW B*, 2012.

[169] Bruus Henrik; Flensberg Karsten. *Many-body quantum theory in condensed matter physics : an introduction*. Oxford Uni. press, New York, 2018.

[170] Thierry Giamarchi. *Quantum Physics in One Dimension*. Oxford University Press, 2003.

[171] Sin-itiro Tomonaga. Remarks on Bloch's Method of Sound Waves applied to Many-Fermion Problems. *Progress of Theoretical Physics*, 5(4):544–569, 1950.

[172] J. M. Luttinger. An Exactly Soluble Model of a Many-Fermion System. *Journal of Mathematical Physics*, 4(9):1154–1162, 1963.

[173] Daniel C Mattis and Elliott H Lieb. Exact Solution of a Many-Fermion System and Its Associated Boson Field. en, 1965.

[174] A. Luther and I. Peschel. Calculation of critical exponents in two dimensions from quantum field theory in one dimension. en. *Phys. Rev. B*, 12(9):3908–3917, 1975.

[175] F. D. M. Haldane. General Relation of Correlation Exponents and Spectral Properties of One-Dimensional Fermi Systems: Application to the Anisotropic S = 1 2 Heisenberg Chain. en. *Phys. Rev. Lett.*, 45(16):1358–1362, 1980.

[176] H. J. Schulz. Phase diagrams and correlation exponents for quantum spin chains of arbitrary spin quantum number. en. *Phys. Rev. B*, 34(9):6372–6385, 1986.

[177] K. D. Schotte and U. Schotte. Tomonaga's Model and the Threshold Singularity of X-Ray Spectra of Metals. en. *Phys. Rev.*, 182(2):479–482, 1969.

[178] Leon Balents. X-ray-edge singularities in nanotubes and quantum wires with multiple subbands. en. *Phys. Rev. B*, 61(7):4429–4432, 2000.

[179] M. Pustilnik, M. Khodas, A. Kamenev, and L. Glazman. Dynamic Response of One-Dimensional Interacting Fermions. en. *Phys. Rev. Lett.*, 96(19):196405, 2006.

[180] Rodrigo G. Pereira, Steven R. White, and Ian Affleck. Spectral function of spinless fermions on a one-dimensional lattice. en. *Phys. Rev. B*, 79(16):165113, 2009.

[181] Adilet Imambekov and Leonid I. Glazman. Phenomenology of One-Dimensional Quantum Liquids Beyond the Low-Energy Limit. en. *Phys. Rev. Lett.*, 102(12):126405, 2009.

[182] G. D. Mahan. Excitons in metals: infinite hole mass. *Physical Review*, 163(3):612–617, 1967. Publisher: American Physical Society.

[183] P. Nozières and C. T. De Dominicis. Singularities in the x-ray absorption and emission of metals. iii. one-body theory exact solution. *Phys. Rev.*, 178:1097–1107, 3, 1969.

[184] A. H. Bougourzi, M. Couture, and M. Kacir. Exact two-spinon dynamical correlation function of the one-dimensional Heisenberg model. en. *Phys. Rev. B*, 54(18):R12669–R12672, 1996.

[185] Matthew Fishman, Steven R. White, and E. Miles Stoudenmire. The ITensor Software Library for Tensor Network Calculations. *SciPost Phys. Codebases*:4, 2022.

[186] Guifré Vidal. Efficient classical simulation of slightly entangled quantum computations. *Phys. Rev. Lett.*, 91:147902, 14, 2003.

[187] Sigmund Kohler. Dispersive readout of adiabatic phases. *Phys. Rev. Lett.*, 119:196802, 19, 2017.

[188] Sigmund Kohler. Dispersive readout: universal theory beyond the rotating-wave approximation. *Phys. Rev. A*, 98:023849, 2, 2018.

[189] Ross Shillito, Alexandru Petrescu, Joachim Cohen, Jackson Beall, Markus Hauru, Martin Ganahl, Adam G.M. Lewis, Guifre Vidal, and Alexandre Blais. Dynamics of transmon ionization. *Phys. Rev. Appl.*, 18:034031, 3, 2022.

[190] R. G. Pereira, J. Sirker, J.-S. Caux, R. Hagemans, J. M. Maillet, S. R. White, and I. Affleck. Dynamical spin structure factor for the anisotropic spin- 1 / 2 heisenberg chain. *Physical Review Letters*, 96(25):257202, 2006.

[191] R G Pereira, J Sirker, J-S Caux, R Hagemans, J M Maillet, S R White, and I Affleck. Dynamical structure factor at small q for the XXZ spin-1/2 chain. *Journal of Statistical Mechanics: Theory and Experiment*, 2007(8):P08022–P08022, 2007.

[192] Roland Winkler. *Spin—Orbit Coupling Effects in Two-Dimensional Electron and Hole Systems*. en, volume 191 of *Springer Tracts in Modern Physics*. Springer Berlin Heidelberg, Berlin, Heidelberg, 2003.

[193] Edward B. Saff and Arthur David Snider. *Fundamentals of complex analysis with applications for engineering and science*. eng. Prentice Hall Pearson Education Inc, Upper Saddle River, NJ, 3. ed edition, 2003.

[194] Alexander L. Fetter and John Dirk Walecka. *Quantum Theory of Many-Particle Systems*. eng. Dover Books on Physics. Dover Publications, Newburyport, 2012.

Appendix

A Input-output theory

In this section we invert the relations (2.36-2.37)

$$Q_{\rm tml} = \frac{\partial \mathcal{L}}{\partial\left(\partial_t \Phi_{\rm tml}\right)} = Q_{\rm tml}^{\rm bare} + \kappa(x) q_k(x)\,, \qquad Q_{\rm tml}^{\rm bare} = \frac{\partial \mathcal{L}_{\rm tml}}{\partial\left(\partial_t \Phi_{\rm tml}\right)} = c\dot{\Phi}_{\rm tml}\,, \tag{A.1}$$

$$Q_{\rm res} = \frac{\partial \mathcal{L}}{\partial\left(\partial_t \Phi_{\rm res}\right)} = Q_{\rm res}^{\rm bare} - \int_0^\infty dx \kappa(x) q_k(x)\,, \qquad Q_{\rm res}^{\rm bare} = \frac{\partial \mathcal{L}_{\rm res}}{\partial\left(\partial_t \Phi_{\rm res}\right)} = C\dot{\Phi}_{\rm res}\,, \tag{A.2}$$

where

$$q_\kappa(x) = C_\kappa\left(\dot{\Phi}_{\rm tml}(x) - \dot{\Phi}_{\rm res}\right)\,, \tag{A.3}$$

$$= \frac{C_\kappa}{c} Q_{\rm tml}^{\rm bare} - \frac{C_\kappa}{C} Q_{\rm res}^{\rm bare}\,. \tag{A.4}$$

Solving Eq. (A.1) for $Q_{\rm tml}^{\rm bar}$

$$Q_{\rm tml}^{\rm bar} = \frac{c}{c + C_\kappa \kappa(x)}\left(Q_{\rm tml} + \kappa(x)\frac{C_\kappa}{C} Q_{\rm res}^{\rm bare}\right) \tag{A.5}$$

and substituting into Eq. (A.1) gives

$$Q_{\rm res} = Q_{\rm res}^{\rm bare} - \int_0^\infty dx \kappa(x)\left(\frac{C_\kappa}{c + C_\kappa \kappa(x)}\left(Q_{\rm tml} + \kappa(x)\frac{C_\kappa}{C + C_\kappa} Q_{\rm res}^{\rm bare}\right) - \frac{C_\kappa}{C} Q_{\rm res}^{\rm bare}\right)\,, \tag{A.6}$$

which we solve for $Q_{\rm res}^{\rm bare}$ up to linear order in C_κ

$$Q_{\rm res}^{\rm bare} = C\dot{\Phi}_{\rm res} = C\frac{Q_{\rm res} + C_\kappa I_1}{C + C_\kappa}\,, \qquad I_1 = \int_0^\infty dx \kappa(x)\frac{Q_{\rm tml}(x)}{c + C_\kappa \kappa(x)}\,, \tag{A.7}$$

from which we obtain

$$\dot{\Phi}_{\rm res} = \frac{Q_{\rm res} + C_\kappa I_1}{C + C_\kappa}\,. \tag{A.8}$$

We then plug (A.7) into (A.5) to obtain up to linear order in C_κ

$$Q_{\rm tml}^{\rm bar} = c\dot{\Phi}_{\rm tml} = \frac{c}{c + C_\kappa \kappa(x)}\left(Q_{\rm tml} + \kappa(x)\frac{C_\kappa}{C + C_\kappa} Q_{\rm res}\right)\,, \tag{A.9}$$

from which we obtain

$$\dot{\Phi}_{\rm tml} = \frac{1}{c + C_\kappa \kappa(x)}\left(Q_{\rm tml} + \kappa(x)\frac{C_\kappa}{C + C_\kappa} Q_{\rm res}\right)\,. \tag{A.10}$$

Appendix

B Active and passive transformations in physics

Physicists often do not explicitly distinguish between an operator (tensor) and its matrix representation in a given basis. While this is generally accepted practice, it can lead to ambiguities. In this Appendix, I will take care to clearly differentiate between the two wherever necessary.

B.1 Active and passive transformations

Any rotation can be interpreted in two distinct but equivalent ways. As an illustrative example, consider the matrix equation

$$\begin{pmatrix} v^1 \\ v^2 \end{pmatrix} = \mathcal{R}(\theta) \begin{pmatrix} \tilde{v}^1 \\ \tilde{v}^2 \end{pmatrix}, \qquad \mathcal{R}(\theta) = \begin{pmatrix} \cos(\theta) & \sin(\theta) \\ -\sin(\theta) & \cos(\theta) \end{pmatrix}. \tag{B.1}$$

B.1.1 Active interpretation

Consider a canonical basis $\{\vec{e}_1, \vec{e}_2\}$ for the vectors and the corresponding dual basis $\{\vec{e}^1, \vec{e}^2\}$ for covectors[1], defined such that $\vec{e}^i(\vec{e}_j) = \delta_{ij}$. We consider the tensor

$$\boldsymbol{\mathcal{R}}(\theta) = \sum_{ij} \mathcal{R}(\theta)^i_j \vec{e}_i \otimes \vec{e}^j, \tag{B.2}$$

where i denotes the row (covariant index, which transforms as a vector) and j the column (contravariant index), [2]. Let $\vec{v} = v^1\vec{e}_1 + v^2\vec{e}_2$ be a vector. Then Eq. (B.1) expresses an active

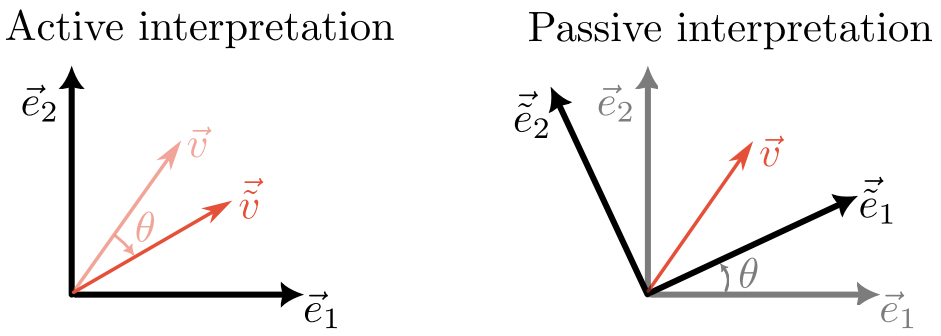

Figure B.1: An active transformation involves the rotation of the vector itself within a fixed coordinate system. A passive transformation involves rotating the coordinate system (basis) while keeping the vector fixed. Only its components change relative to the new basis.

[1] Maybe the reader is more familiar to the concepts of "kets" and "bras".

[2] Maybe the reader is more familiar to the expression in quantum mechanics $\mathcal{R}^i_j(\theta) = \langle i | \boldsymbol{\mathcal{R}}(\theta) | j \rangle$and $\boldsymbol{\mathcal{R}}(\theta) = \sum_{ij} \mathcal{R}(\theta)^i_j |i\rangle \langle j|$

transformation

$$\vec{v} = \boldsymbol{\mathcal{R}}(\theta)\vec{\tilde{v}} \tag{B.3}$$

where the vector $\vec{v}$ has been rotated by an angle $-\theta$ and has been *actively* transformed into the vector $\vec{\tilde{v}} = \tilde{v}^1\vec{e}_1 + \tilde{v}^2\vec{e}_2$, as shown in Fig. B.1.

B.1.2 Passive interpretation

Alternatively, we can define a new basis $\left\{\vec{\tilde{e}}_1, \vec{\tilde{e}}_2\right\}$ by rotating the original one as $\vec{\tilde{e}}_j = \mathcal{R}(\theta)^i{}_j\vec{e}_i$. The new basis is obtained by rotating the original basis by an angle θ, see Fig. B.1. Since $\mathcal{R}^{-1}(\theta) = \mathcal{R}(-\theta)$, we also have $\vec{e}_j = \mathcal{R}(-\theta)^i{}_j\vec{\tilde{e}}_i$, then

$$\vec{v} = \sum_j v^j\vec{e}_j = \sum_{ij}\mathcal{R}(\theta)^i{}_j v^j\vec{\tilde{e}}_i = \sum_j \tilde{v}^j\vec{\tilde{e}}_i\,, \tag{B.4}$$

from which

$$\tilde{v}^j = \sum_i \mathcal{R}(\theta)^i{}_j v^j\,, \tag{B.5}$$

which is Eq. (B.1). In this case Eq. (B.1) represents how the coordinates of the vector $\vec{v}$ changes upon the change of basis $\mathcal{B} = \{\vec{e}_1, \vec{e}_2\} \to \tilde{\mathcal{B}} = \left\{\vec{\tilde{e}}_1, \vec{\tilde{e}}_2\right\}$. The matrix $\mathcal{R}(\theta)$ thus serves as the change-of-basis matrix $\mathcal{M}_{\mathcal{B}\to\tilde{\mathcal{B}}}$, which represents the identity tensor as $\mathbf{1} = \sum_{ij}\mathcal{R}^i{}_j(\theta)\vec{\tilde{e}}_i \otimes \vec{e}^j$, with the tensor expressed in the mixed basis: $\tilde{\mathcal{B}}$ as the covariant basis (basis for the vectors) and the canonical basis $\mathcal{B}$ as the contravariant basis (basis for the covectors). Eq. (B.1) then is interpreted as

$$\vec{v}_{\tilde{\mathcal{B}}} = \mathcal{M}_{\mathcal{B}\to\tilde{\mathcal{B}}}\vec{v}_{\mathcal{B}}\,, \tag{B.6}$$

where $\vec{v}_{\mathcal{B}}$ is just a column whose elements are the coordinates of the vector $\vec{v}$ in the basis $\mathcal{B}$.

Application to the spin

B.1.2.1 Application to the dipole operator

Here, we want to derive Eq. (6.29). Let

$$\mathcal{B}' = \{|\bar{0}\rangle, |\bar{1}\rangle, |1\rangle, |0\rangle\}\,, \tag{B.7}$$

be the eigenbasis at $\varepsilon_0 = 0$ of the spin qubit Hamiltonian. Denote by $\mathcal{M}_{\mathcal{B}'\to\mathcal{B}}$ the change-of-basis matrix that maps coordinate vectors in $\mathcal{B}'$ to coordinate vectors in $\mathcal{B}$.

By construction, the columns of $\mathcal{M}_{\mathcal{B}'\to\mathcal{B}}$ are the coordinates of the vectors of $\mathcal{B}'$ written in $\mathcal{B}$. Indeed, if $e_1 = \begin{pmatrix}1 & 0 & 0 & 0\end{pmatrix}^T$ is the coordinate vector of $|\bar{0}\rangle$ in $\mathcal{B}'$, then $\mathcal{M}_{\mathcal{B}'\to\mathcal{B}}e_1$ simply picks out the first column and give and, by the definition of the change-of-basis matrix, yields the coordinates of $|\bar{0}\rangle$ in $\mathcal{B}$

$$\mathcal{M}_{\mathcal{B}'\to\mathcal{B}}\begin{pmatrix}1\\0\\0\\0\end{pmatrix} = \begin{pmatrix}\cos\frac{\theta}{2}\\0\\0\\-\sin\frac{\theta}{2}\end{pmatrix}\,. \tag{B.8}$$

To write τ_z in the eigenbasis $\mathcal{B}'$, we use the change of basis matrix diagram

$$\begin{array}{ccc}\mathcal{B} & \xrightarrow{\tau_z} & \mathcal{B}\\ {\scriptstyle\mathcal{M}_{\mathcal{B}\to\mathcal{B}'}}\downarrow & & \uparrow{\scriptstyle\mathcal{M}_{\mathcal{B}'\to\mathcal{B}}}\\ \mathcal{B}' & \xrightarrow[\tau_z]{} & \mathcal{B}'\end{array}\,, \tag{B.9}$$

which implies $(\tau_z)_{\mathcal{B}'} = \mathcal{M}_{\mathcal{B}\to\mathcal{B}'}\,(\tau_z)_{\mathcal{B}}\,\mathcal{M}_{\mathcal{B}'\to\mathcal{B}}$. Carrying out the multiplication, we obtain τ_z in the eigenbasis $\mathcal{B}'$

$$\tau_z = \begin{pmatrix} 0 & \sin\left(\frac{\phi-\theta}{2}\right) & -\cos\left(\frac{\phi-\theta}{2}\right) & 0 \\ \sin\left(\frac{\phi-\theta}{2}\right) & 0 & 0 & \cos\left(\frac{\phi-\theta}{2}\right) \\ -\cos\left(\frac{\phi-\theta}{2}\right) & 0 & 0 & \sin\left(\frac{\phi-\theta}{2}\right) \\ 0 & \cos\left(\frac{\phi-\theta}{2}\right) & \sin\left(\frac{\phi-\theta}{2}\right) & 0 \\ |\bar{0}\rangle & |\bar{1}\rangle & |1\rangle & |0\rangle \end{pmatrix} \begin{matrix} \langle\bar{0}| \\ \langle\bar{1}| \\ \langle 1| \\ \langle 0| \end{matrix} \quad . \tag{B.10}$$

To express τ_z in the eigenbasis we remind our notations for the *intra-doublets* (τ') and *inter-doublets* (σ') operators

$$\tau'_x = |0\rangle\langle 1| + |1\rangle\langle 0| \;, \qquad \sigma'_x = |0\rangle\langle\bar{1}| + |\bar{1}\rangle\langle 0| \;, \tag{B.11}$$

$$\bar{\tau}'_x = |\bar{0}\rangle\langle\bar{1}| + |\bar{1}\rangle\langle\bar{0}| \;, \qquad \bar{\sigma}'_x = |\bar{0}\rangle\langle 1| + |1\rangle\langle\bar{0}| \;. \tag{B.12}$$

With these notations

$$\tau_z = \sin\left(\frac{\phi-\theta}{2}\right)(\tau'_x + \bar{\tau}'_x) + \cos\left(\frac{\phi-\theta}{2}\right)(\sigma'_x - \bar{\sigma}'_x) \;. \tag{B.13}$$

This form makes the selection rules explicit: the $\sin\left(\frac{\phi-\theta}{2}\right)$ term couples $|0\rangle \longleftrightarrow |1\rangle$ and $|\bar{0}\rangle \longleftrightarrow |\bar{1}\rangle$, while the $\cos\left(\frac{\phi-\theta}{2}\right)$ term couples $|0\rangle \longleftrightarrow |\bar{1}\rangle$ and $|\bar{0}\rangle \longleftrightarrow |1\rangle$.

B.2 Diagonalization of an operator

When dealing with a time-independent Hamiltonian, the Schrödinger equation reduces to an eigenvalue problem

$$\mathbf{H}\left|\tilde{\lambda}_k\right\rangle = \lambda_k \left|\tilde{\lambda}_k\right\rangle \;, \tag{B.14}$$

implying that the Hamiltonian is diagonal in the basis formed by its eigenvectors

$$\mathbf{H} = \sum_k \lambda_k \left|\tilde{\lambda}_k\right\rangle\left\langle\tilde{\lambda}_k\right| \;. \tag{B.15}$$

Considering the canonical basis $\{|l\rangle\}$ of the Hilbert space, The standard procedure to diagonalize $H_{mn} = \langle m|\mathbf{H}|n\rangle$ is to construct the matrix U, where the columns of $U^\dagger$ are the coordinates of the eigenvectors of $\mathbf{H}$ expressed in the canonical basis of the Hilbert space. The matrix constructed in this way is nothing else than the matrix that change the basis from the basis of the eigenvectors to the canonical basis. The matrix U thus serves as the change-of-basis matrix from the eigenbasis of H to the canonical basis. The diagonalization then reads

$$UHU^\dagger = D \,, \tag{B.16}$$

with $D_{kl} = \lambda_k \delta_{kl}$.

Passive interpretation We can again distinguish between an active and a passive interpretation of the diagonalization equation (B.16). In the passive interpretation, we understand the transformation as a change of basis. Given that $U^\dagger_{mn} = \left\langle m|\tilde{\lambda}_n \right\rangle$ and $U_{mn} = \left\langle \tilde{\lambda}_m|n \right\rangle$, we can write the canonical basis vectors in terms of the eigenbasis as

$$|m\rangle = \sum_l U_{lm} \left|\tilde{\lambda}_l\right\rangle . \tag{B.17}$$

Then

$$\mathbf{H} = \sum_n H_{mn} |m\rangle \langle n| = \sum_{kl} U_{lm} H_{mn} U^\dagger_{nk} \left|\tilde{\lambda}_l\right\rangle \left\langle \tilde{\lambda}_k\right| = \sum_{kl} \lambda_n \delta_{kl} \left|\tilde{\lambda}_l\right\rangle \left\langle \tilde{\lambda}_k\right| , \tag{B.18}$$

which gives (B.16)

$$\sum_n U_{lm} H_{mn} U^\dagger_{nk} = \lambda_n \delta_{nk} . \tag{B.19}$$

Active interpretation On the other hand, we can adopt an active interpretation by considering the operator

$$\mathbf{U} = \sum_{mn} U_{mn} |m\rangle \langle n| , \tag{B.20}$$

which actively transform vectors from the canonical basis into the eigenstates of $\mathbf{H}$, that is $\left|\tilde{\lambda}_n\right\rangle = \mathbf{U}|n\rangle$. In this framework, the transformation

$$\mathbf{U}\mathbf{H}\mathbf{U}^\dagger = \sum_n \lambda_n |n\rangle \langle n| = \mathbf{H}' , \tag{B.21}$$

produces a new operator $\mathbf{H}'$ that is the diagonal in the canonical basis. The matrix representation of this transformation in the canonical basis is precisely Eq. (B.16). In essence, we have constructed a new operator $\mathbf{H}'$ that corresponds to the diagonal matrix D when expressed in the canonical basis.

It is important to note that, in this active interpretation, the Hamiltonian itself has changed. Therefore, if one wishes to compute time-dependent expectation values such as

$$\langle \mathbf{O}(t) \rangle = \langle \psi(t)|\mathbf{O}|\psi(t)\rangle = \left\langle \psi|e^{-i\mathbf{H}t}\mathbf{O}e^{i\mathbf{H}t}|\psi\right\rangle , \tag{B.22}$$

this must be consistently expressed in terms of the transformed Hamiltonian $\mathbf{H}'$. In particular, the state vectors must also be rotated accordingly. This leads to the expression

$$\langle \mathbf{O}(t) \rangle = \left\langle \psi|\mathbf{U}^\dagger e^{-i\mathbf{H}'t}\mathbf{O}e^{i\mathbf{H}'t}\mathbf{U}|\psi\right\rangle \tag{B.23}$$

A useful perspective to transition between the active and passive interpretations is to rewrite the original Hamiltonian using projectors in the rotated basis. Define the projectors $\mathbf{P}_n = |n\rangle \langle n|$. Then, the original Hamiltonian can be written as

$$\mathbf{H} = \sum_n \lambda_n \mathbf{U}^\dagger \mathbf{P}_n \mathbf{U} = \sum_n \lambda_n \tilde{\mathbf{P}}_n , \tag{B.24}$$

where the transformed projectors $\tilde{\mathbf{P}}_n$ are given by

$$\tilde{\mathbf{P}}_n = \mathbf{U}^\dagger \mathbf{P}_n \mathbf{U} = \left|\tilde{\lambda}_n\right\rangle \left\langle \tilde{\lambda}_n\right| . \tag{B.25}$$

This decomposition will prove particularly helpful in the example that follows.

Example Consider the basis $\mathcal{B} = \{|\downarrow\rangle, |\uparrow\rangle\}$ and the Hamiltonian

$$\mathbf{H} = t_c \boldsymbol{\sigma_x} , \tag{B.26}$$

with$\boldsymbol{\sigma_x} = |\downarrow\rangle\langle\uparrow| + |\uparrow\rangle\langle\downarrow|$ being Pauli matrix σ_x in the basis $\mathcal{B}$. The eigenstates of $\mathbf{H}$ are $|\pm\rangle = (|\uparrow\rangle \pm |\downarrow\rangle)/\sqrt{2}$, defining the new basis $\tilde{\mathcal{B}} = \{|\pm\rangle\}$.

This Hamiltonian is diagonalized by $\mathbf{U} = \exp\left(-i\frac{\pi}{4}\boldsymbol{\sigma_y}\right)$ so that $\mathbf{H}' = \mathbf{U}\mathbf{H}\mathbf{U}^\dagger = t_c\boldsymbol{\sigma_z}$. This implies

$$\mathbf{H} = t_c\boldsymbol{\sigma_x} = t_c\tilde{\boldsymbol{\sigma}}_{\boldsymbol{z}} , \tag{B.27}$$

where $\tilde{\boldsymbol{\sigma}}_{\boldsymbol{z}} = \mathbf{U}^\dagger\boldsymbol{\sigma_x}\mathbf{U} = |+\rangle\langle+| - |-\rangle\langle-|$

$$\tilde{\boldsymbol{\sigma}}_{\boldsymbol{z}} = \begin{pmatrix} 1 & 0 \\ 0 & -1 \end{pmatrix}_{\tilde{\mathcal{B}}} = \begin{pmatrix} 0 & 1 \\ 1 & 0 \end{pmatrix}_{\mathcal{B}} . \tag{B.28}$$

B.3 Schrödinger, Heisenberg and interacting picture

Schrödinger picture n the Schrödinger picture, time evolution is typically understood as an active transformation of the quantum state. The time evolution operator $\mathcal{U}(t)$ evolves an initial state $|\psi\rangle$ into a time-dependent state $|\psi(t)\rangle = \boldsymbol{\mathcal{U}}(t)|\psi\rangle$. For any Hermitian operator $\boldsymbol{\Lambda} = \sum_j \lambda_j |\lambda_j\rangle\langle\lambda_j|$, satisfying the eigenvalue equation

$$\boldsymbol{\Lambda}|\lambda_j\rangle = \lambda_j|\lambda_j\rangle , \tag{B.29}$$

the expectation value at time t is obtained as

$$\langle\boldsymbol{\Lambda}(t)\rangle = \langle\psi(t)|\boldsymbol{\Lambda}|\psi(t)\rangle . \tag{B.30}$$

Heisenberg picture In contrast to the Schrödinger picture, the Heisenberg picture offers a passive viewpoint on time evolution. This means that we could see the time evolution as a rotation of the reference frame whereas the state $|\psi\rangle$ stays the same. Consider the wave function at time t, expressed in the position basis

$$\psi(x,t) = \langle x|\psi(t)\rangle = \langle x(-t)|\psi\rangle , \tag{B.31}$$

This suggests that the time dependence can be transferred from the state to the basis, leading us to define $|x(-t)\rangle = \boldsymbol{\mathcal{U}}^\dagger(t)|x\rangle$ [3], where $\boldsymbol{\mathcal{U}}(t)$ is the time-evolution operator. While in the Schrödinger picture the state evolves through the action of $\boldsymbol{\mathcal{U}}(t)$, , in the Heisenberg picture the basis vectors evolve in the opposite direction through the adjoint transformation $\boldsymbol{\mathcal{U}}^\dagger(t)$, keeping the state fixed.

Indeed, to ensure that physical predictions remain invariant between the Schrödinger and Heisenberg pictures, the expectation values of observables must coincide in both descriptions. Specifically, we require that

$$\langle\boldsymbol{\Lambda}(t)\rangle = \langle\psi(t)|\boldsymbol{\Lambda}|\psi(t)\rangle = \left\langle\psi|\boldsymbol{\mathcal{U}}^\dagger(t)\boldsymbol{\Lambda}\boldsymbol{\mathcal{U}}(t)|\psi\right\rangle = \langle\psi|\boldsymbol{\Lambda}(t)|\psi\rangle , \tag{B.32}$$

where we have defined $\Lambda(t) = \mathcal{U}^\dagger(t)\Lambda\mathcal{U}(t)$. This construction guarantees that the Heisenberg-evolved operator satisfies

$$\Lambda(t)|\lambda_j(-t)\rangle = \lambda_j|\lambda_j(-t)\rangle . \tag{B.33}$$

preserving the eigenstructure of the observable under time evolution.

[3]This definition could be ambigous for a coherent state since we have defined $|\alpha(t)\rangle = \mathbf{D}(\alpha(t))|0\rangle \neq U(t)|\alpha\rangle$.

Interacting picture Sometimes it is useful to leave part of the time dependence in the state and the rest to the basis. In certain situations, particularly when the Hamiltonian takes the form $\mathbf{H} = \mathbf{H_0} + \mathbf{V}$, it is advantageous to separate the time evolution in two contributions. Consider $\mathcal{U}_0(t) = e^{-iH_0 t}$. In this case the vector $|\psi(t)\rangle = \boldsymbol{\mathcal{U}_0}(t) \left|\tilde{\psi}(t)\right\rangle$ can be seen as a rotation of $\left|\tilde{\psi}(t)\right\rangle$ that only evolves with V. Looking at the wave function we see that part of the time dependence is in the state and part in the basis

$$\psi(x,t) = \langle x|\psi(t)\rangle = \left\langle x|\boldsymbol{\mathcal{U}_0}(t)\tilde{\psi}(t)\right\rangle = \left\langle \tilde{x}(-t)|\tilde{\psi}(t)\right\rangle . \tag{B.34}$$

This is the Dirac or interacting picture, in which the basis rotates only through $\boldsymbol{\mathcal{U}_0}^\dagger(t)$. Consequently, in this picture

$$\langle \mathbf{\Lambda}(t)\rangle = \langle\psi(t)|\mathbf{\Lambda}|\psi(t)\rangle = \left\langle \tilde{\psi}(t)|\boldsymbol{\mathcal{U}}_0^\dagger(t)\mathbf{\Lambda}\boldsymbol{\mathcal{U}}_0(t)|\tilde{\psi}(t)\right\rangle = \left\langle \tilde{\psi}(t)|\tilde{\mathbf{\Lambda}}(t)|\tilde{\psi}(t)\right\rangle , \tag{B.35}$$

with $\tilde{\mathbf{\Lambda}}(t) = \boldsymbol{\mathcal{U}}_0^\dagger(t)\mathbf{\Lambda}\boldsymbol{\mathcal{U}}_0(t)$. Since $\left|\tilde{\psi}(t)\right\rangle$ still carries a residual time dependence, it is instructive to determine its equation of motion $\left|\tilde{\psi}(t)\right\rangle$. Substituting the definition of $\left|\tilde{\psi}(t)\right\rangle$ into the Schrödinger equation leads to

$$\boldsymbol{\mathcal{U}}_0^\dagger(t)\mathbf{V}\boldsymbol{\mathcal{U}}_0(t)\left|\tilde{\psi}(t)\right\rangle = i\partial_t \left|\tilde{\psi}(t)\right\rangle . \tag{B.36}$$

B.4 Rotating frame

In this section, we clarify the interpretation of rotating frames in quantum mechanics, using the intuitive example of an observer on a carousel watching a spring-mass oscillator. The goal is to describe how physics appears to an observer rotating at a fixed angular velocity relative to an inertial (lab) frame. This analysis distinguishes between active and passive transformations and explains their roles in quantum mechanical calculations. Again, there are two mathematically equivalent but conceptually distinct ways to describe the same physical system in a rotating frame.

Passive interpretation In the passive interpretation, the state vector remains fixed, but we change the coordinates (basis) used to describe observables. This corresponds to switching from the lab frame to a rotating frame by rotating the operators (rotating the basis). If $\mathbf{\Lambda} = \sum_j \lambda_j |\lambda_j\rangle \langle\lambda_j|$ is an observable in the lab frame and $\mathbf{U}(t)$ is the unitary transformation associated with rotation at angular frequency ω_r, then the rotated operator is

$$\tilde{\mathbf{\Lambda}}(t) = \mathbf{U}(t)\mathbf{\Lambda}\mathbf{U}^\dagger(t) = \sum_j \lambda_j |\lambda_j(t)\rangle \langle\lambda_j(t)| , \tag{B.37}$$

The expectation value in the rotating frame is then given by:

$$\left\langle \tilde{\mathbf{\Lambda}}(t)\right\rangle = \langle\psi(t)|\tilde{\mathbf{\Lambda}}(t)|\psi(t)\rangle = \left\langle \psi(t)|\mathbf{U}(t)\mathbf{\Lambda}\mathbf{U}^\dagger(t)|\psi(t)\right\rangle , \tag{B.38}$$

and describe the perspective of an observer rotating with the system.

Active interpretation Alternatively, we may adopt an active interpretation by "unwinding" the dynamics of the state vector while keeping the basis fixed (see Fig. B.1). This corresponds to applying a unitary transformation that rotates the state vector by an angle $-\omega_{\mathrm{r}} t$

$$|\tilde{\psi}(t)\rangle = \mathbf{U}^\dagger(t)|\psi(t)\rangle . \tag{B.39}$$

The expectation value of $\mathbf{\Lambda}$ is computed using the transformed state

$$\left\langle \tilde{\mathbf{\Lambda}}(t) \right\rangle = \langle \tilde{\psi}(t) | \mathbf{\Lambda} | \tilde{\psi}(t) \rangle = \left\langle \psi(t) | \mathbf{U}(t) \mathbf{\Lambda} \mathbf{U}^\dagger(t) | \psi(t) \right\rangle . \tag{B.40}$$

The time evolution of $\left| \tilde{\psi}(t) \right\rangle$ follows from the Schrödinger equation

$$\left(\mathbf{U}^\dagger \mathbf{H} \mathbf{U} + i(\partial_t \mathbf{U}^\dagger)\mathbf{U} \right) \left| \tilde{\psi}(t) \right\rangle = i\partial_t \left| \tilde{\psi}(t) \right\rangle , \tag{B.41}$$

with the effective Hamiltonian

$$\mathbf{H}_{\text{eff}} = \mathbf{U}^\dagger \mathbf{H} \mathbf{U} + i(\partial_t \mathbf{U}^\dagger)\mathbf{U} . \tag{B.42}$$

Appendix

C Schrieffer-Wolff transformations

Schrieffer-Wolff transformation [72] was introduced to relate the Anderson impurity model and the Kondo model. In Semiconductor physics it is called $k \cdot p$ perturbation theory [192] and is used to obtain a low-energy effective Hamiltonian by a unitary transformation decoupling the low-energy and high-energy sectors. Since it is a unitary transformation, it can be understood as a method to block-diagonalize the Hamiltonian to some desired perturbative order.

To set the stage for the Schrieffer--Wolff transformation, we consider a system whose Hilbert space factorizes as $\mathcal{H} = \mathcal{H}_A \otimes \mathcal{H}_B$. The Hamiltonian is written as $H = H_0 + V$, where the unperturbed Hamiltonian H_0 is diagonal in the canonical basis of $\mathcal{H}_B$ and commutes with a complete set of mutually commuting operators $\{q_i\}$ acting on $\mathcal{H}_A$, i.e., $[H_0, q_i \otimes \mathbf{1}_B] = 0$ for all i. This allows us to label the eigenstates of H_0 by the joint eigenvalues $\vec{q} = (q_1, q_2, \dots)$ of q_i, and to write the Hilbert space as a direct sum of sectors $\mathcal{H}_A = \bigoplus_{\vec{q}} \mathcal{H}_{\vec{q}}$, each invariant under H_0. As illustrated in Fig. C.1, we decompose the perturbation V as

$$V = H_1 + H_2 \,, \tag{C.1}$$

where H_1 preserves each sector $\mathcal{H}_{\vec{q}}$ while acting nontrivially in $\mathcal{H}_B$. In contrast, H_2 contains the components of V that couple different $\vec{q}$-labeled sectors. This separation of V is particularly convenient when constructing a Schrieffer-Wolff transformation, as H_2 defines the part of the perturbation to be eliminated (to leading order), while H_1 contributes directly to the effective Hamiltonian without mixing the sectors of $\mathcal{H}_A$.

The full Hamiltonian is thus decomposed as

$$H = H_0 + H_1 + H_2 \,. \tag{C.2}$$

The Schrieffer-Wolff transformation is the operator $U = e^{i\mathcal{S}}$ such that the effective Hamiltonian

$$H_{\text{eff}} = U H U^\dagger = \sum_{j=0}^{\infty} \frac{1}{j!} [i\mathcal{S}, H]^j \,, \qquad \text{with} \quad [A,B]^j = \underbrace{[A,[\dots,[A}_{j \text{ times}},B]]] \,, \tag{C.3}$$

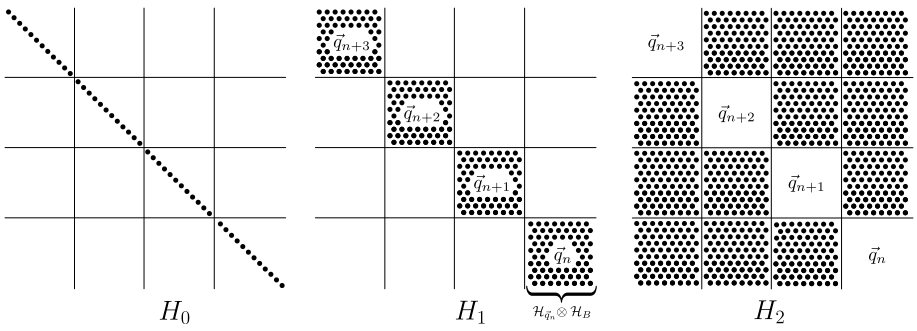

Figure C.1: Illustration of the components of H_0, H_1 and H_2. While each $\vec{q}$-labeled sector is invariant under the action of H_1 which acts non-trivially only in $\mathcal{H}_B$, H_2 couples different $\vec{q}$-labeled sectors.

does not couple different $\vec{q}$-sectors. The Schrieffer-Wolff transformation can be decomposed in successive orders as $\mathcal{S} = \mathcal{S}^{(1)} + \mathcal{S}^{(2)} + \ldots$, where the first order is obtained imposing

$$i\left[\mathcal{S}^{(1)}, H_0\right] = -H_2\,, \tag{C.4}$$

and gives rise to the second-order terms

$$i\left[\mathcal{S}^{(1)}, H_1 + H_2\right] - \frac{1}{2}\left[\mathcal{S}^{(1)}, \left[\mathcal{S}^{(1)}, H_0\right]\right] = i\left[\mathcal{S}^{(1)}, H_1\right] + \frac{i}{2}\left[\mathcal{S}^{(1)}, H_2\right] \tag{C.5}$$

in the effective Hamiltonian. From C.4 we can see that $\mathcal{S}^{(1)}$ is defined up to terms that commute with H_0. We can then choose $\mathcal{S}^{(1)}$ up to these terms such that it contains only terms that couples different $\vec{q}$-sectors. Then $i\left[\mathcal{S}^{(1)}, H_1\right]$ contains only off-diagonal terms in $\mathcal{H}_A$ while $i\left[\mathcal{S}^{(1)} H_2\right]$ contains both diagonal and off-diagonal terms. Defining the projector on the $\vec{q}$-sector $P_{\vec{q}}$, the second order term in $\mathcal{S}$ is constructed through

$$i\left[\mathcal{S}^{(2)}, \mathcal{H}_0\right] = i\left[\mathcal{S}^{(1)}, H_1\right] - \frac{i}{2}\sum_{\vec{s}\neq\vec{q}} P_{\vec{s}}\,[\mathcal{S}, H_2]\,P_{\vec{q}}\,, \tag{C.6}$$

and so on.

C.1 The dispersive Hamiltonian

We consider the case of the dispersive Hamiltonian in (3.3)

$$H = H_0 + \frac{\varepsilon_0}{\omega_{\mathrm{q}}(\varepsilon_0)} g_\perp \left(a + a^\dagger\right)\sigma_z + \frac{2t_c}{\omega_{\mathrm{q}}(\varepsilon_0)} g_\perp \left(a + a^\dagger\right)\sigma_x\,. \tag{C.7}$$

The unperturbed part of the Hamiltonian is $H_0 = \omega_q/2\sigma_z + \omega_r a^\dagger a$ which is diagonal in the basis of the total Hilbert space $\mathcal{H}_A \otimes \mathcal{H}_B$, which factorizes into a qubit space $\mathcal{H}_A = \mathrm{span}\{|-\rangle, |+\rangle\}$ and a bosonic Fock space $\mathcal{H}_B$ spanned by photon number states $\{|n\rangle\}$.

To organize the Hilbert space, we consider the operator $q = \sigma_z$, which commutes with H_0, and use it to subdivide the Hilbert space into eigenspace of q as $\mathcal{H}_A = \mathcal{H}_+ \oplus \mathcal{H}_-$ where $\mathcal{H}_\pm = \mathrm{span}\{|\pm\rangle\}$. Introduicng $g'_\perp = 2g_\perp t_c/\omega_{\mathrm{q}}(\varepsilon_0)$, the perturbation V comprises $H_1 = \varepsilon_0 g_\perp \left(a + a^\dagger\right)\sigma_z/\omega_{\mathrm{q}}(\varepsilon_0)$ and $H_2 = g'_\perp \left(a + a^\dagger\right)\sigma_x$. In this case, the first order of $\mathcal{S}$ is

$$i\mathcal{S}^{(1)} = \frac{g'_\perp}{\omega_{\mathrm{q}} - \omega_{\mathrm{r}}}(a\sigma_+ - a^\dagger\sigma_-) + \frac{g'_\perp}{\omega_{\mathrm{q}} + \omega_{\mathrm{r}}}(a^\dagger\sigma_+ - a\sigma_-)\,, \tag{C.8}$$

and the second order corrections to the Hamiltonian is composed by the contribution diagonal in $\mathcal{H}_A$

$$\frac{i}{2}\left[\mathcal{S}^{(1)}, H_2\right] = \chi a^\dagger a\sigma_z + \frac{\chi}{2}\sigma_z + g'^2_\perp \frac{\omega_{\mathrm{r}}}{\omega_{\mathrm{q}}^2 - \omega_{\mathrm{r}}^2}\left(a^2 + a^{\dagger 2}\right)\sigma_z + g'^2_\perp \frac{\omega_{\mathrm{r}}}{\omega_{\mathrm{q}}^2 - \omega_{\mathrm{r}}^2}\,, \tag{C.9}$$

with χ given by

$$\chi = 2g'^2_\perp \frac{\omega_{\mathrm{q}}}{\omega_{\mathrm{q}}^2 - \omega_{\mathrm{r}}^2}\,,$$

which is (3.6) at the sweet spot $\varepsilon_0 = 0$, where $g'_\perp = g_\perp$. The static longitudinal term gives rise to the off-diagonal term in $\mathcal{H}_A$

$$\begin{aligned} i\left[\mathcal{S}^{(1)}, \mathcal{H}_1\right] = &-2g_\perp \frac{\varepsilon_0}{\omega_q}\left[\left(\frac{g'_\perp}{\omega_q - \omega_r}\,\sigma_+ + \frac{g'_\perp}{\omega_q + \omega_r}\,\sigma_-\right)\right] a^2 \\ &- 2g_\perp \frac{\varepsilon_0}{\omega_q}\left[\left(\frac{g'_\perp}{\omega_q + \omega_r}\,\sigma_+ + \frac{g'_\perp}{\omega_q - \omega_r}\,\sigma_-\right)\right] a^{\dagger 2} \\ &- g_\perp \frac{\varepsilon_0}{\omega_q}\left[\left(\frac{g'_\perp}{\omega_q - \omega_r} + \frac{g'_\perp}{\omega_q + \omega_r}\right)\right](2a^\dagger a + 1)\sigma_x\,. \end{aligned}$$

The second order in $\mathcal{S}$ is constructed through (C.6) to eliminate this latter off-diagonal term as

$$i\left[\mathcal{S}^{(2)}, \mathcal{H}_0\right] = -\left[\mathcal{S}^{(1)}, \mathcal{H}_1\right]\,,$$

and reads

$$\begin{aligned} \mathcal{S}^{(2)} = \quad & 2\left(\frac{\varepsilon_0}{\omega_q} g_\perp\right)\left(\frac{2t_c}{\omega_q} g_\perp\right)\left[\frac{a^2\sigma_+}{(\omega_q - \omega_r)(\omega_q - 2\omega_r)} - \frac{a^2\sigma_-}{(\omega_q + \omega_r)(\omega_q + 2\omega_r)}\right. \\ & \left. + \frac{a^{\dagger 2}\sigma_+}{(\omega_q + \omega_r)(\omega_q + 2\omega_r)} - \frac{a^{\dagger 2}\sigma_-}{(\omega_q - \omega_r)(\omega_q - 2\omega_r)}\right] \\ & + \left(\frac{\varepsilon_0}{\omega_q} g_\perp\right)\left(\frac{2t_c}{\omega_q} g_\perp\right)\left(\frac{1}{\omega_q - \omega_r} + \frac{1}{\omega_q + \omega_r}\right)\frac{(2a^\dagger a + 1)}{\omega_q}\, i\,\sigma_y\,. \end{aligned}$$

C.2 The Floquet Hamiltonian

In this section we consider the Hamiltonian (5.76)

$$\mathcal{H}_\mathcal{F} = \mathbf{p}\,\omega_\mathrm{r} + \frac{\omega_\mathrm{q}}{2}\sigma_z + \frac{1}{2}\left(\mathcal{A}\, f_- + \mathcal{A}^*\, f_+\right)\sigma_x\,.$$

and we perform a SW transformation to find perturbatively the transformation $\mathcal{U}$, up to third order in $\mathcal{A}$, that diagonalize $\mathcal{H}_\mathcal{F}$. We use this result to compute the quasi-energies up to fourth order in $\mathcal{A}$. We then generalize the transformation to diagonalize also $\bar{\mathcal{H}}_\mathcal{F}$ perturbatively both in $g_\perp$ and A_q, up to fourth order.

The unperturbed part of the Hamiltonian is $H_0 = \mathbf{p}\,\omega_\mathrm{r} + \omega_\mathrm{q}\sigma_z/2$ and is diagonal in the basis of $\mathcal{H}_A$, which is the Hilbert space tensor product of the qubit space and the Sambe space. In particular, we split the Hilbert space $\mathcal{H}_A$ into the sectors $\vec{q} = (p, j)$ where p labels the eigenvalues of $q_1 = \mathbf{p} = \sum_p p\,|p)\,(p|$ and j labels the eigenvalues of $q_2 = \sigma_z$. The off-diagonal term coupling different sectors of $\mathcal{H}_A$ is $H_2 = (\mathcal{A}\, f_- + \mathcal{A}^*\, f_+)\,\sigma_x/2$. We computed $\mathcal{S}$ up to third order as

$$\begin{aligned} i\mathcal{S}^{(1)} &= \frac{1}{2}\frac{1}{\omega_\mathrm{q} - \omega_\mathrm{r}}(\mathcal{A}\sigma_+ - \mathcal{A}^*\sigma_-) + \frac{1}{2}\frac{1}{\omega_\mathrm{q} + \omega_\mathrm{r}}(\mathcal{A}^*\sigma_+ - \mathcal{A}\sigma_-) \\ i\mathcal{S}^{(2)} &= \frac{1}{8\omega_\mathrm{r}}\frac{\omega_\mathrm{q}}{\omega_\mathrm{q}^2 - \omega_\mathrm{r}^2}\left(\mathcal{A}^{*2} - \mathcal{A}^2\right)\sigma_z \\ i\mathcal{S}^{(3)} &= \frac{1}{8}\frac{\omega_\mathrm{q}}{\omega_\mathrm{q}^2 - \omega_\mathrm{r}^2}(\lambda_1\left(\mathcal{A}^3\sigma_+ - \mathcal{A}^{*3}\sigma_-\right) + \lambda_2(\mathcal{A}^{*3}\sigma_+ - \mathcal{A}^3\sigma_-) \\ &\quad + \lambda_3(-\mathcal{A}\mathcal{A}^*\mathcal{A}\sigma_+ + \mathcal{A}^*\mathcal{A}\mathcal{A}^*\sigma_-) + \lambda_4(\mathcal{A}^*\mathcal{A}\mathcal{A}^*\sigma_+ - \mathcal{A}\mathcal{A}^*\mathcal{A}\sigma_-)) \end{aligned} \tag{C.10}$$

where

$$\begin{aligned}
\lambda_1 &= \frac{\omega_\mathrm{r}-3\omega_\mathrm{q}}{\omega_\mathrm{q}-3\omega_\mathrm{r}}\frac{1}{6\omega_\mathrm{r}}\frac{1}{\omega_\mathrm{q}-\omega_\mathrm{r}}\\
\lambda_2 &= \frac{\omega_\mathrm{r}+3\omega_\mathrm{q}}{\omega_\mathrm{q}+3\omega_\mathrm{r}}\frac{1}{6\omega_\mathrm{r}}\frac{1}{\omega_\mathrm{q}+\omega_\mathrm{r}}\\
\lambda_3 &= \frac{1}{\omega_\mathrm{q}-\omega_\mathrm{r}}\left(\frac{(\omega_\mathrm{q}+3\omega_\mathrm{r})\,(\omega_\mathrm{r}+3\omega_\mathrm{q})}{6\omega_\mathrm{r}(\omega_\mathrm{q}^2-\omega_\mathrm{r}^2)}+\frac{4}{3}\frac{1}{(\omega_\mathrm{q}-\omega_\mathrm{r})}\right)\\
\lambda_4 &= -\frac{1}{\omega_\mathrm{q}+\omega_\mathrm{r}}\left(\frac{(\omega_\mathrm{q}-3\omega_\mathrm{r})\,(\omega_\mathrm{r}-3\omega_\mathrm{q})}{6\omega_\mathrm{r}(\omega_\mathrm{q}^2-\omega_\mathrm{r}^2)}+\frac{4}{3}\frac{1}{(\omega_\mathrm{q}+\omega_\mathrm{r})}\right).
\end{aligned} \tag{C.11}$$

The effective Hamiltonian is diagonal in $\mathcal{H}_A$ and reads $\mathcal{D}=\mathbf{p}\,\omega_\mathrm{r}+\varepsilon(\omega_\mathrm{q},\omega_\mathrm{r},|\mathcal{A}|)\,\sigma_z$, with the ε given by

$$\varepsilon=\frac{\omega_\mathrm{q}}{2}+\frac{|\mathcal{A}|^2}{4}\left(2\frac{\omega_\mathrm{q}}{(\omega_\mathrm{q}^2-\omega_\mathrm{r}^2)}\right)+\frac{|\mathcal{A}|^4}{16}\left(\frac{\omega_\mathrm{q}}{\omega_r}\left(\frac{1}{(\omega_\mathrm{q}+\omega_\mathrm{r})^3}-\frac{1}{(\omega_\mathrm{q}-\omega_\mathrm{r})^3}\right)\right). \tag{C.12}$$

Considering now the Hamiltonian 5.77

$$\bar{\mathcal{H}}_\mathcal{F}=\mathbf{p}\,\omega_\mathrm{r}+\frac{\omega_\mathrm{q}}{2}\sigma_z+\frac{1}{2}\left(\mathcal{A}\,f_-+\mathcal{A}^\dagger\,f_+\right)\sigma_x\,,$$

with $\mathcal{A}=A_\mathrm{q}+2g_\perp a$, we have that the total Hilbert space is now $\mathcal{H}_A\otimes\mathcal{H}_B$ with $\mathcal{H}_B$ spanned by the photon number states $\{|n\rangle\}$. The off-diagonal terms are now $H_1=g_\perp\left(a\,f_-+a^\dagger\,f_+\right)\sigma_x$ and $H_2=(A_\mathrm{q}f_-+A_\mathrm{q}f_+)\,\sigma_x/2$. We computed the first three order of $\mathcal{S}$, and the result is still Eq. (C.10) where one needs to perform the substitution $\mathcal{A}^*\to\mathcal{A}^\dagger$, without modifying the order of $\mathcal{A}$, $\mathcal{A}^*$ in the products.

The effective Hamiltonian reads, up to fourth order in $\mathcal{A}$

$$\begin{aligned}
\mathcal{H}'_\mathcal{F}=&\frac{\omega_\mathrm{q}}{2}\sigma_z+\omega_\mathrm{r}n+\frac{1}{8}\left(\frac{1}{(\omega_\mathrm{q}+\omega_\mathrm{r})}+\frac{1}{(\omega_\mathrm{q}-\omega_\mathrm{r})}\right)\left(\mathcal{A}^\dagger\mathcal{A}+\mathcal{A}\mathcal{A}^\dagger\right)\sigma_z\\
&+\frac{1}{8}\left(\frac{1}{(\omega_\mathrm{q}+\omega_\mathrm{r})}-\frac{1}{(\omega_\mathrm{q}-\omega_\mathrm{r})}\right)\left(\mathcal{A}^\dagger\mathcal{A}-\mathcal{A}\mathcal{A}^\dagger\right)\\
&+\frac{1}{32}\frac{\omega_\mathrm{q}}{\omega_r}\left(\frac{1}{(\omega_\mathrm{q}+\omega_\mathrm{r})^3}-\frac{1}{(\omega_\mathrm{q}-\omega_\mathrm{r})^3}\right)\left(\left(\mathcal{A}^\dagger\mathcal{A}\right)^2+\left(\mathcal{A}\mathcal{A}^\dagger\right)^2\right)\sigma_z\\
&+\frac{1}{32}\frac{\omega_q}{\omega_r}\left(\frac{1}{(\omega_\mathrm{q}+\omega_\mathrm{r})^3}+\frac{1}{(\omega_\mathrm{q}-\omega_\mathrm{r})^3}\right)\left(\left(\mathcal{A}^\dagger\mathcal{A}\right)^2-\left(\mathcal{A}\mathcal{A}^\dagger\right)^2\right)
\end{aligned}$$

from which we obtain the longitudinal coupling

$$g_\parallel=\frac{A_\mathrm{q}}{2}\left(2g_\perp\frac{\omega_\mathrm{q}}{(\omega_\mathrm{q}^2-\omega_\mathrm{r}^2)}\right)+\frac{A_\mathrm{q}^3}{4}g_\perp\frac{\omega_\mathrm{q}}{\omega_r}\left(\frac{1}{(\omega_\mathrm{q}+\omega_\mathrm{r})^3}-\frac{1}{(\omega_\mathrm{q}-\omega_\mathrm{r})^3}\right),$$

and the dispersive shift

$$\chi=2g_\perp^2\frac{\omega_\mathrm{q}}{(\omega_\mathrm{q}^2-\omega_\mathrm{r}^2)}+g_\perp^2\frac{\omega_\mathrm{q}}{\omega_r}A_\mathrm{q}^2\left(\frac{1}{(\omega_\mathrm{q}+\omega_\mathrm{r})^3}-\frac{1}{(\omega_\mathrm{q}-\omega_\mathrm{r})^3}\right),$$

which, together with the spectrum in (C.12), confirm explicitely Eq. 5.75 up to fourth order in A_q.

Appendix

D Kubo linear response

The Kubo formalism is used to calculate the first order linear approximation of the expectation value of a generic observable A in the presence of a time-dependent perturbative term $H'(t)$ applied starting from a time t_0. Given an Hamiltonian $H(t) = H_0 + H'(t)$, the key idea is to consider the interaction picture of H_0.

D.1 The interaction picture

This picture is usually used to separate the time evolution due to H_0 from the intricate one due to $H'(t)$. In the interacting picture (see Appendix B.3), we "unwind" the time evolution of the free Hamiltonian from the state, while we make the operators evolve with the free Hamiltonian H_0

$$\begin{cases} |\psi(t)\rangle_I &= e^{iH_0 t} |\psi(t)\rangle \,, \\ A_I(t) &= e^{iH_0 t} A e^{-iH_0 t} \,. \end{cases} \tag{D.1}$$

The interaction picture coincide with the Heisenberg picture when $V = 0$. The time evolution operator in this representation is obtained considering

$$|\psi(t)\rangle_I = e^{iH_0 t} |\psi(t)\rangle = e^{iH_0 t} \mathcal{U}(t, t_0) e^{-iH_0 t_0} |\psi(t_0)\rangle_I = \mathcal{U}_I(t, t_0) |\psi(t_0)\rangle_I \,, \tag{D.2}$$

and reads

$$\mathcal{U}_I(t, t_0) = e^{iH_0 t} \mathcal{U}(t, t_0) e^{-iH_0 t_0} \,. \tag{D.3}$$

The state follows the Schrödinger equation

$$i\partial_t |\psi(t)\rangle_I = \left(i\partial_t e^{iH_0 t}\right) \left|\hat{\psi}(t)\right\rangle + e^{iH_0 t} \left(i\partial_t \left|\hat{\psi}(t)\right\rangle\right) = H'_I \left|\hat{\psi}(t)\right\rangle_I \,, \tag{D.4}$$

with an Hamiltonian given by $H'_I(t) = e^{iH_0 t} H'(t) e^{-iH_0 t}$. Inserting Eq. D.2 into Eq. D.4, we obtain that the time evolution operator follows the same Schrödinger equation

$$i\partial_t \mathcal{U}_I(t, t_0) = H'_I(t) \mathcal{U}_I(t, t_0) \,. \tag{D.5}$$

D.2 The Dyson series

The integral form of (D.5) reads

$$\mathcal{U}_I(t, t_0) = 1 - i \int_{t_0}^{t} dt' H'_I(t') \mathcal{U}_I(t', t_0) \,, \tag{D.6}$$

and can be solved iteratively for $\mathcal{U}_I(t, t_0)$, starting from $\mathcal{U}_I(t', t_0) = 1$, as

$$\mathcal{U}_I(t, t_0) = 1 - i \int_{t_0}^{t} dt_1 H'_I(t_1) + (-i)^2 \int_{t_0}^{t} dt_1 H'_I(t_1) \int_{t_0}^{t_1} dt_2 H'_I(t_2) + \dots \tag{D.7}$$

We decompose each term in the series in the following way

$$\begin{aligned}\int_{t_0}^{t} dt_1 H'_I(t_1) \int_{t_0}^{t_1} dt_2 H'_I(t_2) &= \frac{1}{2}\int_{t_0}^{t} dt_1 H'_I(t_1) \int_{t_0}^{t_1} dt_2 H'_I(t_2) \\ &\quad + \frac{1}{2}\int_{t_0}^{t} dt_2 H'_I(t_2) \int_{t_0}^{t_2} dt_1 H'_I(t_1) \\ &= \frac{1}{2}\int_{t_0}^{t} dt_1 H'_I(t_1) \int_{t_0}^{t} dt_2 H'_I(t_2)\theta(t_1 - t_2) \\ &\quad + \frac{1}{2}\int_{t_0}^{t} dt_2 H'_I(t_2) \int_{t_0}^{t} dt_1 H'_I(t_1)\theta(t_2 - t_1) \\ &= \frac{1}{2}\int_{t_0}^{t}\int_{t_0}^{t} dt_1 dt_2 \mathbb{T}\left(H'_I(t_1)H'_I(t_2)\right) , \end{aligned} \tag{D.8}$$

(D.9)

where we have introduced the time-ordering operator

$$\mathbb{T}\left(\hat{A}(t_1)\hat{B}(t_2)\right) = \begin{cases} \hat{A}(t_1)\hat{B}(t_2) & \text{if } t_1 > t_2 \\ \hat{B}(t_2)\hat{A}(t_1) & \text{if } t_2 > t_1 \end{cases} . \tag{D.10}$$

Equation D.7 can then be rewritten as

$$\hat{U}_I(t, t_0) = \mathbb{T} e^{-i\int_{t_0}^{t} dt' \hat{H}'_I(t')} , \tag{D.11}$$

that consitutes the so-called Dyson series.

D.3 The linear response function

Let's imagine now that a perturbation of the form $H' = gV\theta(t - t_0)$, applied at t_0, drives the system out of equilibrium. Our aim is to express average values that evolve according to the full Hamiltonian as average values that evolve according $H_{g=0}$=H_0 .

First, we could express the average value of the generic observable A in the interacting picture. The evolution of the density matrix in the interacting picture is given by $\rho_I(t) = \mathcal{U}_I(t, t_0)\rho_I(t_0)\mathcal{U}_I^\dagger(t, t_0)$. Through Eq. D.11 we can express the expectation value of A up to linear order in g as

$$\begin{aligned}\langle A(t)\rangle &= \mathrm{Tr}\left\{\rho_I(t)A_I(t)\right\} = \langle A(t)\rangle_{g=0} - i\int_{t_0}^{t} dt' \langle [A(t), V(t')]\rangle_{g=0} \\ &= \langle A(t)\rangle_{g=0} + g\int_{-\infty}^{t} dt' \chi_{AV}(t - t') , \end{aligned} \tag{D.12}$$

where we have introduced the so-called Kubo linear response formula

$$\chi_{AV}(t - t') = -i\theta(t - t')\langle [A(t), V(t')]\rangle_{g=0} , \tag{D.13}$$

where the average $\langle \dots \rangle_{g=0}$ indicates that the density matrix evolves with the Hamiltonian $H_{g=0}$.

At equilibrium, the density matrix is $\rho(t_0) = \rho_I(t_0) = e^{-\beta H_0}/\mathrm{Tr}\left\{\rho_0\right\}$, and the linear response depends only on the difference $t - t'$, since

$$\begin{aligned}\langle A(t)V(t')\rangle_{g=0} &= \frac{\mathrm{Tr}\left\{e^{itH_0}Ae^{-itH_0}e^{it'H_0}Ve^{-it'H_0}e^{-\beta H_0}\right\}}{\mathrm{Tr}\left\{\hat{\rho}_0\right\}} \\ &= \frac{\mathrm{Tr}\left\{Ae^{i(t'-t)H_0}Ve^{i(t-t')H_0}e^{-\beta H_0}\right\}}{\mathrm{Tr}\left\{\rho_0\right\}} . \end{aligned} \tag{D.14}$$

Appendix

E Supplementary material for Chapter 7

E.1 Change of basis in second quantization

In second quantization the action of a one-body operator A can always be expressed in terms of its matrix elements in a chosen basis. If $\{|l\rangle\}$ denotes a complete set of single-particle states, we can write

$$A = \sum_{l,m} \langle m|A|l\rangle \, c_m^\dagger c_l \, . \tag{E.1}$$

Now consider a change of basis, for example to the set $\{|k\rangle\}$ of crystal momentum eigenstates. Inserting resolutions of the identity gives

$$\begin{aligned} A &= \sum_{\alpha,\beta,k,k'} \langle m|k'\rangle \langle k'|A|k\rangle \langle k|l\rangle \, c_m^\dagger c_l \\ &= \sum_{k,k'} \langle k'|A|k\rangle \, c_{k'}^\dagger c_k \, . \end{aligned} \tag{E.2}$$

From the latter we obtain that the change of basis for the annihilation operator reads

$$c_k = \sum_n \langle k|l\rangle \, c_l \, . \tag{E.3}$$

For the density operator $n_l = |l\rangle \langle l|$, we can use Eq. (E.1) in position representation, using the set of localized states $\{|l\rangle\}$

$$n_l = \sum_{l,m} \langle m|n_l|l\rangle \, c_m^\dagger c_l = c_l^\dagger c_l \, , \tag{E.4}$$

or the set of crystal momentum eigenstates. In this case we obtain

$$n_l = \frac{1}{N} \sum_{k,k'} e^{iql} c_{k'+q}^\dagger c_{k'} = \frac{1}{N} \sum_q e^{iql} n_q \, , \tag{E.5}$$

where we introduced the density operator in momentum representation

$$n_q = \sum_{k'} c_{k'+q}^\dagger c_{k'} = \sum_l e^{-iql} n_l \, . \tag{E.6}$$

E.2 The Lehmann representation

An important way to write Green's functions is the so-called Lehman representation. We first introduce the greater and lesser Green's functions for two bosonic or fermionic operators A and B [169]

$$\begin{aligned} G_{AB}^{>}(t,t') &= -i \langle A(t)B(t')\rangle \, , \\ G_{AB}^{<}(t,t') &= i(\pm 1) \langle B(t')A(t)\rangle \, , \end{aligned} \tag{E.7}$$

with ± 1 for bosons (fermions). The retarded Green's function is defined as

$$G^R_{AB}(t,t')) = -i\theta(t)\left\langle \left[A(t),B(t')\right]_{\mp}\right\rangle ,$$

where $[A(t),B(t')]_{\mp}$ is a commutator (anticommutator). It can be rewritten using the greater and lesser Green's functions as

$$G^R_{AB}(t,t') = \theta(t-t')\left[G^>_{AB}(t,t') - G^<_{AB}(t,t')\right]. \tag{E.8}$$

We now consider the eigenstates $\{|n\rangle\}$ and eigenvalues $\{E_n\}$ of the Hamiltonian of the system. Inserting the completeness relation $\mathbf{1} = \sum_n |n\rangle\langle n|$, we rewrite the greater Green's function as

$$\begin{aligned} G^>_{AB}(t,t') &= -i\frac{1}{Z}\sum_n \langle n|e^{-\beta H}A(t)B(t')|n\rangle \\ &= -i\frac{1}{Z}\sum_{nn'} e^{-\beta E_n}\langle n|A|n'\rangle\langle n'|B|n\rangle e^{i(E_n-E_{n'})(t-t')}, \end{aligned} \tag{E.9}$$

where β is the Boltzmann factor and $Z = \mathrm{Tr}\left\{e^{-\beta H}\right\}$ is the partition function. Similarly, we obtain for the lesser

$$\begin{aligned} G^<_{AB}(t,t') &= \mp i\frac{1}{Z}\sum_n \langle n|e^{-\beta H}B(t')A(t)|n\rangle \\ &= \mp i\frac{1}{Z}\sum_{nn'} e^{-\beta E_n}\langle n|B|n'\rangle\langle n'|A|n\rangle e^{-i(E_n-E_{n'})(t-t')}. \end{aligned} \tag{E.10}$$

Inserting these expressions in Eq. (E.8), we obtain that $G^R_{AB}(t,t')$ depends only on the difference $t-t'$ and can be rewritten as

$$G^R_{AB}(t-t') = -i\theta(t-t')\frac{1}{Z}\sum_{nn'} e^{-\beta E_n}\langle n|A|n'\rangle\langle n'|B|n\rangle\left(e^{i(E_n-E_{n'})(t-t')} \mp e^{-i(E_n-E_{n'})(t-t')}\right). \tag{E.11}$$

In the frequency domain, Eq. (E.11) provides the Lehmann representation of the retarded Green's function

$$\begin{aligned} G^R_{AB}(\omega) &= \int_{-\infty}^{\infty} dt e^{i(\omega+i\eta)t}G^R_{AB}(t) \\ &= -\frac{i}{Z}\int_0^{\infty} dt e^{i(\omega+i\eta)t}\sum_{n,n'}\langle n|A|n'\rangle\langle n'|B|n\rangle e^{-\beta E_n} \\ &\quad \left(e^{i(E_n-E_{n'})(t-t')} \mp e^{-i(E_n-E_{n'})(t-t')}\right) \\ &= \frac{1}{Z}\sum_{nn'}\frac{\langle n|A|n'\rangle\langle n'|B|n\rangle}{\omega+E_n-E_{n'}+i\eta}\left(e^{-\beta E_n} \mp e^{-\beta E_{n'}}\right). \end{aligned} \tag{E.12}$$

Similarly, one can obtain $G^>_{AB}(\omega)$, $G^<_{AB}(\omega)$ and shows the following relations [169]

$$iG^>_{AB}(\omega) = -2\mathrm{Im}G^R_{AB}(\omega)\left[1 \pm n_{B/F}(\omega)\right], \tag{E.13}$$

$$-iG^<_{AB}(\omega) = -2\mathrm{Im}G^R_{AB}(\omega)n_{B/F}(\omega), \tag{E.14}$$

where $n_{B/F}(\omega)$ is the Bose (Fermi) distribution. With these expressions, the DSF reduces to

$$S(q,\omega) = \frac{1}{N}\sum_{lm} e^{-iq(l-m)}\int dt e^{i\omega t}\langle n_l(t)n_m(0)\rangle = -\frac{2}{N}\sum_{lm} e^{-iq(l-m)}\mathrm{Im}\chi^R_{lm}(\omega)\left[1+n_B(\omega)\right]. \tag{E.15}$$

At zero temperature, $n_B(\omega > 0) = 0$ and $n_B(\omega < 0) = -1$, so that

$$S(q, \omega > 0) = -2\mathrm{Im}\chi^R_{lm}(\omega)\,, \qquad S(q, \omega < 0) = 0\,, \tag{E.16}$$

which gives Eq. (7.2) . In the same limit, the retarded Green's function (E.12) reduces to

$$G^R_{AB}(\omega) = \sum_n \left[\frac{\langle GS|A|n\rangle\langle n|B|GS\rangle}{\omega + E_{GS} - E_n + i\eta} \mp \frac{\langle n|A|GS\rangle\langle GS|B|n\rangle}{\omega + E_n - E_{GS} + i\eta}\right]. \tag{E.17}$$

E.2.1 Application to the DSF

We compute now the Lehmann representation of admittance $\chi_{lm}(t) = -i\theta(t)\,\langle[n_l(t), n_m]\rangle$, which is the retarded Green's function of the density operator. Using Eq. (E.5), Equation (E.17) yields

$$\chi_{lm}(\omega) = \frac{1}{N^2}\sum_{qq'k'}\left[\frac{\langle GS|n_q|k'\rangle\langle k'|n_{q'}|GS\rangle}{\omega + E_{GS} - E_{k'} + i\eta} - \frac{\langle k'|n_q|GS\rangle\langle GS|n_{q'}|k'\rangle}{\omega + E_{k'} - E_{GS} + i\eta}\right] e^{iql + iq'm}\,. \tag{E.18}$$

For translational invariant systems, $\chi_{lm}(t) = -i\theta(t)\,\langle[n_l(t), n_m]\rangle$ depends only on $l - m$. Therefore, introducing $\delta = l - m$, we require $q' = -q$ so that the exponential $e^{iql+iq'm} = e^{iq\delta}e^{im(q+q')}$ is m-independent. The admittance then reads

$$\chi_{lm}(\omega) = \frac{1}{N}\sum_q \underbrace{\sum_{k'}\frac{1}{N}\left[\frac{|\langle GS|n_q|k'\rangle|^2}{\omega + E_{GS} - E_{k'} + i\eta} - \frac{|\langle GS|n_{-q}|k'\rangle|^2}{\omega + E_{k'} - E_{GS} + i\eta}\right]}_{\chi(q,\omega)} e^{iq(l-m)}\,.$$

Equation (E.16) yields

$$S(q, \omega > 0) = -\frac{2}{N}\sum_{k'}\mathrm{Im}\left[\frac{|\langle GS|n_q|k'\rangle|^2}{\omega + E_{GS} - E_{k'} + i\eta} - \frac{|\langle GS|n_{-q}|k'\rangle|^2}{\omega + E_{k'} - E_{GS} + i\eta}\right], \tag{E.19}$$

and can be further simplified using the identity [193]

$$\lim_{\varepsilon\to 0}\frac{1}{x - x_0 - i\varepsilon} = \mathcal{P}\left[\frac{1}{x - x_0}\right] + i\pi\delta(x - x_0)\,. \tag{E.20}$$

We obtain that the second term in (E.19) is proportional to $\delta(\omega + E_{k'} - E_{GS} + i\eta)$, which always vanishes for $\omega > 0$ since, by the definition of ground state, $E_{k'} - E_{GS} > 0$. We are thus left with

$$S(q, \omega > 0) = -\frac{2}{N}\sum_{k'}\mathrm{Im}\left[\frac{|\langle GS|n_q|k'\rangle|^2}{\omega + E_{GS} - E_{k'} + i\eta}\right], \tag{E.21}$$

which, for the tight-binding chain, reduced to Eq. (7.31).

E.2.2 Application to the fermionic Green's function in the tight-binding chain

We compute now the Lehmann representation of the fermionic Green's function in momentum representation $G^R_{kk'}(t) = -i\theta(t)\left\langle\left\{c_k(t), c^\dagger_{k'}\right\}\right\rangle$

$$G^R_{kk'}(\omega) = \sum_q\left[\frac{\langle GS|c_k|q\rangle\langle q|c^\dagger_{k'}|GS\rangle}{\omega + E_{GS} - E_q + i\eta} + \frac{\langle q|c_k|GS\rangle\langle GS|c^\dagger_{k'}|q\rangle}{\omega + E_q - E_{GS} + i\eta}\right]. \tag{E.22}$$

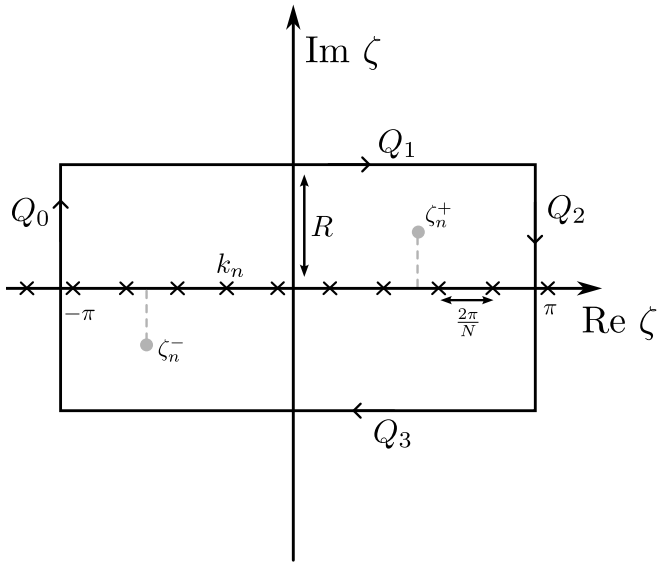

Figure E.1: The contour $Q = Q_1 + Q_2 + Q_3 + Q_4$ used for integration for the Matsubara sum in Eq. (E.29).

For non-interacting fermions, $|GS\rangle$ is the Fermi sea and the first sum is non-zero only for the many-body state $|k\rangle$ with a particle with momentum k above the Fermi sea $|k\rangle = c_k^\dagger |GS\rangle$. On the other hand, the second sum is non-zero only for the many-body state $\left|\bar{k}\right\rangle$ with a hole in the Fermi sea $\left|\bar{k}\right\rangle = c_k |GS\rangle$. Hence, since the one-particle spectrum is $\epsilon(k)$ and the system is non-interacting, $E_k = E_{GS} + \epsilon(k)$ and $E_{\bar{k}} = E_{GS} - \epsilon(k)$. We obtain that the fermionic Green's function is non-zero only for $k = k'$ and its Lehmann representation reads

$$G_k^R(\omega) = \frac{1 - n_F(\epsilon(k))}{\omega - \epsilon(k) + i\eta} + \frac{n_F(\epsilon(k))}{\omega - \epsilon(k) + i\eta} = \frac{1}{\omega - \epsilon(k) + i\eta}\,, \tag{E.23}$$

where $n_F(\epsilon(k))$ here is the Fermi function at zero temperature, $n_F(\epsilon(k)) = \theta(\epsilon(k))$.

We remark that the same result can be obtained using the Heisenberg equation

$$i\partial_t c_k(t) = i\,[H, c_k] = \epsilon(k) c_k \qquad \rightarrow \qquad c_k(t) = c_k e^{-i\epsilon(k)t}\,, \tag{E.24}$$

from which we find immediately

$$G_k^R(\omega) = \int_{-\infty}^{\infty} dt e^{i(\omega + i\eta)t} G_{kk}^R(t) = \frac{1}{\omega - \epsilon(k) + i\eta}\,. \tag{E.25}$$

Finally, from $G_{lm}^R(t) = -i\theta(t) \left\langle \left\{ c_l(t), c_m^\dagger \right\} \right\rangle = -i\theta(t) \sum_k \langle l|k\rangle \langle k|m\rangle \left\langle \left\{ c_k(t), c_k^\dagger \right\} \right\rangle$ we obtain Eqs. (7.39),(7.40).

E.2.3 Analytical evaluation of the Green's functions in coordinate space

Here we are interested in evaluating the Green's functions

$$G_{l-m}^{R,PBC} = \frac{1}{N} \sum_k \frac{e^{-ik|l-m|}}{\omega - \epsilon(k) + i0^+}\,, \tag{E.26}$$

where $\epsilon(k) = -2t\cos(k)$ and $k = 2\pi n/N$.

We begin by introducing two functions

$$f(\zeta) = \frac{e^{i\zeta|\delta|}}{e^{i\zeta N}-1}\,, \qquad \text{with poles in} \qquad k_n = \frac{2\pi}{N}n\,, \tag{E.27}$$

$$g(\zeta) = \frac{1}{\omega + 2t\cos\zeta + i0^+}\,, \qquad \text{with poles in} \qquad e^{i\zeta_n^\pm} = -\frac{\omega}{2t} \pm i\frac{\sqrt{\omega_+^2 - 4t^2}}{2t}\,, \tag{E.28}$$

with $\omega_+ = \omega + i0^+$. We now consider the contour Q_R in Fig. (E.1). Since $\zeta_n^\pm$ is 2π periodic, we can always find n such that $\zeta_n^\pm$ is encircled by Q_R. Using the residue theorem, we have [193]

$$\lim_{R\to\infty}\int_{Q_R} d\zeta f(\zeta)g(\zeta) = 2\pi i \sum_{n=-N/2}^{N/2-1} \mathrm{Res}\left(f(\zeta)g(\zeta), k_n\right) + 2\pi i \sum_{\sigma=\pm} \mathrm{Res}\left(f(\zeta)g(\zeta), \zeta_n^\pm\right)\,. \tag{E.29}$$

The residues are given by

$$\begin{cases} \mathrm{Res}_{\zeta\to k_n} f(\zeta) = \lim_{\zeta\to k_n} f(\zeta)(\zeta - k_n) = \lim_{\eta\to 0} f(k_n+\eta)\eta = \frac{e^{ik_n|m|}}{iN}\,, \\ \mathrm{Res}_{\zeta\to\zeta_n^\pm} g(\zeta) = \lim_{\zeta\to\zeta_n^\pm} g(\zeta)(\zeta - \zeta_n^\pm) = \lim_{\eta\to 0} g(\zeta_n^\pm+\eta)\eta = -\frac{1}{2t\sin\zeta_n^\sigma}\,, \end{cases} \tag{E.30}$$

where we used

$$\cos\left(\zeta_n^\pm + \eta\right) = \cos\left(\zeta_n^\pm\right) - i\eta\sin\left(\zeta_n^\pm\right)\,. \tag{E.31}$$

Pluggin Eq. (E.30) into (E.29), we obtain

$$\begin{aligned} \lim_{R\to\infty}\int_{Q_R} d\zeta f(\zeta)g(\zeta) &= \frac{2\pi}{N}\sum_{n=-N/2}^{N/2-1} e^{ik_n|m|}g(k_n) - \sum_{\sigma=\pm}\frac{f(\zeta_n^\sigma)}{2t\sin\zeta_n^\sigma} \\ &= 2\pi G_{l-m}^{R,PBC} - \sum_{\sigma=\pm}\frac{f(\zeta_n^\sigma)}{2t\sin\zeta_n^\sigma}\,. \end{aligned} \tag{E.32}$$

We will now show that the integral on the left hand side vanish. First, we show that the integral vanishes on the contour $Q_1 \cup Q_3$ using the estimation lemma [193]

$$\lim_{R\to\infty}\left|\int_{Q_1\cup Q_3} d\zeta f(\zeta)g(\zeta)\right| < \lim_{R\to\infty}\sup_{\zeta\in Q_1\cup Q_3}|f(\zeta)g(\zeta)|\, l(Q_1\cup Q_3) = 0\,, \tag{E.33}$$

where $l(Q_1 \cup Q_3) = 4R$ is the length of $Q_1 \cup Q_3$. For $Q_0 \cup Q_2$ it is sufficient to notice that

$$\int_{Q_0\cup Q_2} d\zeta f(\zeta)g(\zeta) = \int_{Q_0} d\zeta f(\zeta)g(\zeta) - \int_{Q_0} d\zeta f(\zeta+2\pi)g(\zeta+2\pi)\,, \tag{E.34}$$

which, using the 2π-periodicity of f and g, gives

$$\int_{Q_0\cup Q_2} d\zeta f(\zeta)g(\zeta) = 0\,. \tag{E.35}$$

Hence, Eq. (E.32) yields

$$G_{l-m}^{R,PBC} = \frac{1}{2\pi}\sum_n \frac{f(\zeta_n)}{2t\sin\zeta_n} = \frac{4}{t}\frac{1}{r_2 - r_1}\left(\frac{r_1^{|l-m|}}{r_1^N - 1} - \frac{r_2^{|l-m|}}{r_2^N - 1}\right)\,, \tag{E.36}$$

where with $r_{1,2} = (-\omega_+ \pm \sqrt{\omega_+^2 - 4t^2})/2t$.

E.3 The Matsubara formalism

To compute retarded Green's functions, for technical reason, it is convenient to use a mapping to a more general Green's function, where time and frequencies are imaginary quantities. This is a powerful method since it allows to compute the retarded Green's functions from the more compact time-ordered ones, to which Wick's theorem [194] can be applied. Moreover, switching to imaginary time permits to treat both the time-evolution operator and the density matrix on the same footstep, since they share the general structure of exponential of the Hamiltonian.

To start, the time argument is replaced by an imaginary quantity $t \to -i\tau$ where τ is real and has the dimensions of time. As for real time we can define an imaginary-time interaction picture by substituting it by τ. The time-evolution operator, in the interacting picture then reads

$$\mathcal{U}(\tau,\tau') = e^{\tau H_0} e^{-(\tau-\tau')H} e^{-\tau' H_0} \,. \tag{E.37}$$

It follows that the density matrix of the whole system can be seen as an evolution of the equilibrium density matrix through the imaginary time-evolution operator,

$$e^{-\beta H} = e^{-\beta H_0}\,\mathcal{U}(\beta,0) = e^{-\beta H_0}\,\mathbb{T}_\tau \exp\left(-\int_0^\beta d\tau_1 V(\tau_1)\right) , \tag{E.38}$$

where the time-evolution operator in the interacting picture has been expressed as in Sec. D.

The so-called Matsubara Green's functions are defined in the following way

$$\mathcal{G}_{AB}(\tau,\tau') := -\langle \mathbb{T}_\tau(A(\tau)B(\tau'))\rangle \,, \tag{E.39}$$

where the time-ordering operator in imaginary time has been introduced. Its behaviour is identical to the one in real time

$$\mathbb{T}_\tau(A(\tau)B(\tau')) = \theta(\tau-\tau')A(\tau)B(\tau') \pm \theta(\tau'-\tau)B(\tau')A(\tau) \,, \quad \begin{cases} + & \text{for bosons,} \\ - & \text{for fermions.} \end{cases} \tag{E.40}$$

The Matsubara Green's function $\mathcal{G}_{AB}(\tau,\tau')$ has several properties. First, it is a function of the time difference only, i.e. $\mathcal{G}_{AB}(\tau,\tau') = \mathcal{G}_{AB}(\tau-\tau')$. Indeed, for $\tau > \tau'$

$$\begin{aligned} \mathcal{G}_{AB}(\tau,\tau') &= -\frac{1}{Z}\mathrm{Tr}\left[e^{-\beta H} e^{\tau H} A e^{-\tau H} e^{\tau' H} B e^{-\tau' H}\right] \\ &= -\frac{1}{Z}\mathrm{Tr}\left[e^{-\beta H} e^{(\tau-\tau')H} A e^{-(\tau-\tau')H} B\right] \\ &= \mathcal{G}_{AB}(\tau-\tau') \,, \end{aligned}$$

and similarly for $\tau < \tau'$.

Secondly, it is a periodic function with period 2β. Indeed, for $\tau < 0$, we have

$$\begin{aligned} \mathcal{G}_{AB}(\tau+\beta) &= -\frac{1}{Z}\mathrm{Tr}\left[e^{-\beta H} e^{(\tau+\beta)H} A e^{-(\tau+\beta)H} B\right] \\ &= -\frac{1}{Z}\mathrm{Tr}\left[e^{\tau H} A e^{-\tau H} e^{-\beta H} B\right] \\ &= -\frac{1}{Z}\mathrm{Tr}\left[e^{-\beta H} B e^{\tau H} A e^{-\tau H}\right] \\ &= -\frac{1}{Z}\mathrm{Tr}\left[e^{-\beta H} B A(\tau)\right] \\ &= \mp\frac{1}{Z}\mathrm{Tr}\left[e^{-\beta H}\mathbb{T}_\tau\left(B A(\tau)\right)\right] \\ &= \mp\mathcal{G}_{AB}(\tau) \,, \end{aligned} \tag{E.41}$$

and similarly for $\tau > 0$.

Because of this property, we can just define the Matsubara Green's function in the interval $-\beta < \tau < \beta$. According to the theory of Fourier transformations we have a discrete Fourier series on that interval that reads

$$\mathcal{G}_{AB}(i\omega_n) = \int_{-\beta}^{\beta} d\tau e^{i\pi n\tau/\beta}\mathcal{G}_{AB}(\tau)\,, \tag{E.42}$$

$$\mathcal{G}_{AB}(\tau) = \frac{1}{\beta}\sum_{n=-\infty}^{\infty} e^{-i\pi n\tau/\beta}\mathcal{G}_{AB}(i\omega_n)\,. \tag{E.43}$$

Due to Eq. (E.41), we can further rewrite

$$\begin{aligned}\mathcal{G}_{AB}(i\omega_n) &= \frac{1}{2}\int_0^{\beta} d\tau e^{i\pi n\tau/\beta}\mathcal{G}_{AB}(\tau) + \frac{1}{2}\int_{-\beta}^{0} d\tau e^{i\pi n\tau/\beta}\mathcal{G}_{AB}(\tau)\\ &= \frac{1}{2}\int_0^{\beta} d\tau e^{i\pi n\tau/\beta}\mathcal{G}_{AB}(\tau) + e^{-in\pi}\frac{1}{2}\int_{-\beta}^{0} d\tau e^{i\pi n\tau/\beta}\mathcal{G}_{AB}(\tau-\beta)\\ &= \frac{1}{2}\left(1 \pm e^{-i\pi n}\right)\int_0^{\beta} d\tau e^{i\pi n\tau/\beta}\mathcal{G}_{AB}(\tau)\,,\end{aligned} \tag{E.44}$$

which gives

$$\mathcal{G}_{AB}(i\omega_n) = \int_0^{\beta} d\tau e^{i\omega_n\tau}\mathcal{G}_{AB}(\tau)\,, \quad \begin{cases}\omega_n = \frac{2n\pi}{\beta}\,, & \text{for bosons,}\\ \omega_n = \frac{(2n+1)\pi}{\beta}\,, & \text{for fermions,}\end{cases} \tag{E.45}$$

and

$$\mathcal{G}_{AB}(\tau) = \frac{1}{\beta}\sum_{i\omega_n} e^{-i\omega_n\tau}\mathcal{G}_{AB}(i\omega_n)\,, \quad \begin{cases}\omega_n = \frac{2n\pi}{\beta}\,, & \text{for bosons,}\\ \omega_n = \frac{(2n+1)\pi}{\beta}\,, & \text{for fermions.}\end{cases} \tag{E.46}$$

E.3.1 Connection between Matsubara and retarded functions

The relation between the two functions $\mathcal{G}_{AB}$ and $\mathcal{G}^R_{AB}$ is proven by use of the Lehmann representation. For $\tau > 0$ the Matsubara function the Lehmann representation reads

$$\begin{aligned}\mathcal{G}_{AB}(\tau) &= -\frac{1}{Z}\mathrm{Tr}\left[e^{-\beta H}e^{\tau H}Ae^{-\tau H}B\right]\\ &= -\frac{1}{Z}\sum_{nn'} e^{-\beta E_n}\langle n|A|n'\rangle\langle n'|B|n\rangle e^{\tau(E_n - E_{n'})}\,.\end{aligned} \tag{E.47}$$

Hence, in the frequency domain we have

$$\begin{aligned}\mathcal{G}_{AB}(i\omega_n) &= -\frac{1}{Z}\int_0^{\beta} d\tau e^{i\omega_n\tau}\sum_{mm'} e^{-\beta E_m}\langle m|A|m'\rangle\langle m'|B|m\rangle e^{\tau(E_m - E_{m'})}\\ &= -\frac{1}{Z}\sum_{mm'} e^{-\beta E_m}\frac{\langle m|A|m'\rangle\langle m'|B|m\rangle}{i\omega_n + E_m - E_{m'}}\left(e^{i\omega_n\beta}e^{\beta(E_m - E_{m'})} - 1\right)\\ &= -\frac{1}{Z}\sum_{mm'}\frac{\langle m|A|m'\rangle\langle m'|B|m\rangle}{i\omega_n + E_m - E_{m'}}\left(e^{-\beta E_m} - (\pm)\,e^{-\beta E_{m'}}\right)\,.\end{aligned} \tag{E.48}$$

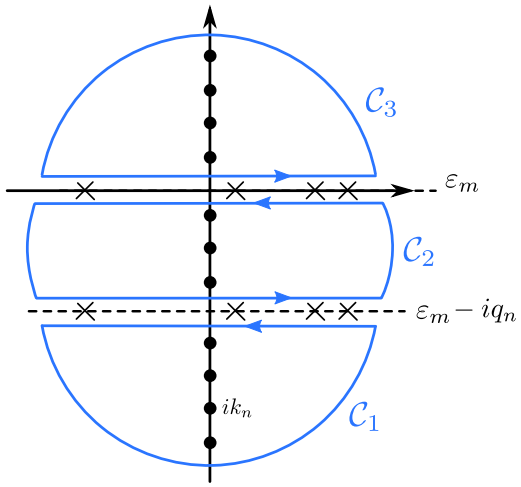

Figure E.2: The contour $\mathcal{C} = \mathcal{C}_1 + \mathcal{C}_2 + \mathcal{C}_3$ used for integration for the Matsubara sum in Eq. E.58.

Eq. (E.48) and (E.12) show that we can generate both $\mathcal{G}_{AB}(i\omega_n)$ and $\mathcal{G}^R_{AB}(\omega)$ from the following function, defined in the entire complex plane except for the real axis,

$$\mathcal{G}_{AB}(z) = -\frac{1}{Z}\sum_{mm'} \frac{\langle m|\, A\, |m'\rangle \langle m'|\, B\, |m\rangle}{z + E_m - E_{m'}} \left(e^{-\beta E_m} - (\pm)\, e^{-\beta E_{m'}}\right) . \tag{E.49}$$

This function is analytic in the upper (or lower) half plane, but has a series of poles at $E_m - E_{m'}$ along the real axis. Thus, according to the theory of analytic functions, since $\mathcal{G}_{AB}(i\omega_n)$ and $\mathcal{G}^R_{AB}(z)$ coincide in an infinite set of points (the whole imaginary axis expect for zero), they are fully identical functions within the entire domain where at least one of them is analytical. Therefore, we can obtain the retarded function through the analytic continuation

$$G^R_{AB}(\omega) = \mathcal{G}_{AB}(z \to \omega + i0^+) = \mathcal{G}_{AB}(i\omega_n \to \omega + i0^+) . \tag{E.50}$$

E.3.2 Derivation of Eq. (7.36)

Here we want here to express $\chi_{lm}(\omega)$ in terms of one-particle Green's functions. In the Matsubara formalism, we write $\chi_{lm}(\omega)$ as

$$\chi_{lm}(iq_n) = \int_0^\beta d\tau e^{iq_n\tau}\chi_{lm}(\tau) = -\int_0^\beta d\tau e^{iq_n\tau}\langle \mathbb{T}_\tau c_l^\dagger(\tau_1^+ + \tau) c_l(\tau_1 + \tau) c_m^\dagger(\tau_1^+) c_m(\tau_1)\rangle_0 . \tag{E.51}$$

Applying Wick's theorem in Fourier space, we obtain

$$\chi_{lm}(iq_n) = \int_0^\beta d\tau e^{iq_n\tau}\left(\mathcal{G}_{lm}(0^-)\mathcal{G}_{lm}(0^-) + \mathcal{G}_{lm}(\tau)\mathcal{G}_{lm}(-\tau)\right) = \frac{1}{\beta}\sum_{ik_n} g(ik_n) , \tag{E.52}$$

where we have defined the function $g(\zeta)$,

$$g(\zeta) = \mathcal{G}_{lm}(\zeta)\mathcal{G}_{lm}(\zeta + iq_n) . \tag{E.53}$$

If $\mathcal{G}_{lm}(\zeta)$ has poles in $\zeta = \varepsilon_m$, then $g(\zeta)$ has poles in ε_m and $\varepsilon_m - iq_n$. To evaluate χ_{lm}, the trick is to rewrite the sum as an integral over a complex variable and to use residue theory. To do so, we consider the Fermi distribution

$$n_F(\zeta) = \frac{1}{e^{\beta\zeta} + 1} , \tag{E.54}$$

that has poles in $ik_n = i(2n+1)\pi/\beta$. This way, for a contour that encloses $\zeta = ik_n$ but no singularity of g (see Fig. E.2), we have

$$\oint d\zeta n_F(\zeta)g(\zeta) = 2\pi i \mathrm{Res}_{\zeta\to ik_n}\left[n_F(\zeta)g(ik_n)\right] = -\frac{2\pi i}{\beta}g(ik_n)\,, \tag{E.55}$$

where we have used

$$\mathrm{Res}_{\zeta\to ik_n}\frac{\zeta - ik_n}{e^{\beta z}+1} = \lim_{\delta\to 0}\frac{\delta}{e^{\beta i k_n}e^{\beta\delta}+1} = -\frac{1}{\beta}\,. \tag{E.56}$$

Now, in order to compute the sum over all ik_n, we consider the contour $\mathcal{C} = \mathcal{C}_1 + \mathcal{C}_2 + \mathcal{C}_3$ illustrated in Fig. E.2. This contour encloses all the ik_n singularities of n_F, but no singularity of g. Therefore,

$$\chi_{lm}(iq_n) = \frac{1}{\beta}\sum_{ik_n} g(ik_n) = -\int_{\mathcal{C}}\frac{d\zeta}{2\pi i}n_F(\zeta)g(\zeta)\,. \tag{E.57}$$

To evaluate the complex integral, we remark that by the estimation lemma we only need to compute

$$\begin{aligned}
-\int_{\mathcal{C}}\frac{d\zeta}{2\pi i}n_F(\zeta)g(\zeta) &= -\lim_{\eta\to 0}\int_{-\infty}^{\infty}\frac{d\varepsilon}{2\pi i}n_F(\varepsilon)\left(g(\varepsilon+i\eta)+g(\varepsilon-i\eta)\right)\\
&\quad -\int_{-\infty}^{\infty}\frac{d\varepsilon}{2\pi i}n_F(\varepsilon-iq_n)\left(g(\varepsilon-iq_n+i\eta)+g(\varepsilon-iq_n-i\eta)\right)\\
&= -\int_{-\infty}^{\infty}\frac{d\varepsilon}{2\pi i}n_F(\varepsilon-iq_n)\left(\mathcal{G}_{lm}(\varepsilon-iq_n)\mathcal{G}_{lm}(\varepsilon+i\eta)\right.\\
&\quad \left.-\mathcal{G}_{lm}(\varepsilon-iq_n)\mathcal{G}_{lm}(\varepsilon-i\eta)\right)\,.
\end{aligned} \tag{E.58}$$

At the end of the computation, we continue iq_n analytically to $\omega + i0^+$ and find

$$\chi_{lm}(\omega) = -\frac{1}{\pi}\int_{-\infty}^{\infty}d\varepsilon n_F(\varepsilon-\mu)\mathrm{Im}G^R_{lm}(\varepsilon)\left(G^R_{lm}(\varepsilon+\omega)+\bar{G}^R_{lm}(\varepsilon-\omega)\right)\,. \tag{E.59}$$

Finally, at zero temperature and at half filling ($\mu = 0$), we obtain Eq. (7.36)

$$\chi_{lm}(\omega) = -\frac{1}{\pi}\int_{-\infty}^{0}d\varepsilon\mathrm{Im}G^R_{lm}(\varepsilon)\left(G^R_{lm}(\varepsilon+\omega)+\bar{G}^R_{lm}(\varepsilon-\omega)\right)\,. \tag{E.60}$$